Clouds and Hazes in Planetary Atmospheres

Thesis by
Peter Gao

In Partial Fulfillment of the Requirements for the
degree of
Doctor of Philosophy

CALIFORNIA INSTITUTE OF TECHNOLOGY
Pasadena, California

2017
Defended September 8th, 2016

Peter Gao
ORCID: 0000-0002-8518-9601

Live Long and Prosper

TABLE OF CONTENTS

ACKNOWLEDGEMENTS

Here we are at last.

It's hard to believe that it has almost been six years since I crossed the border between Canada and the United States to start my journey at Caltech. These past six years have been an extraordinary time in my life, filled with both the highest of highs, and the lowest of lows. There were lots of struggles and tough times, but also incredible experiences that I will cherish forever. None of this would've mattered though, if it were not for the people here, those who shared in my experiences, those who helped me with my problems, who listened to both my complaints and my good news, and above all, those who cared. It's tough to be away from family, and that's why many here have become a second one for me.

I would like to begin by thanking the unsung heroes of the office, the admin and tech staff. I thank Irma Black, Margaret Carlos, and Ulrika Terrones for helping me deal with the simplest of bureaucratic nightmares that would drive me up the wall. I have always said that they keep us alive, and I maintain that. I also thank Mike Black, Scott Dungan, and Ken Ou for keeping our science machines running, our data safe, and our brains from exploding whenever we need to do anything remotely tech-related.

I would also like to thank my distant (and not so distant) collaborators. David Crisp advised me on my second paper (Chapter 2 of this thesis), and I thank him for his unending knowledge of Venus and radiative transfer, which he is able to rattle off at no less than 10% the speed of light. I thank Ty Robinson, who helped me with my third paper about exoplanet photochemistry, for his calm demeanor, patience with my ignorance, and unlimited skill set. I thank Vikki Meadows and the VPL team for their support, both financially and academically, and for their encouragements throughout the years. I thank Danie "from Taiwan" Liang for his insights into my ideas, and his dedication to his old research group. Finally, I thank my current collaborator, Bj$'$orn Benneke, for being the most patient man alive.

I want to especially thank Peter Plavchan, Jonathan Gagné, and Elise Furlan for their guidance and help on the NIR RV project, which has lasted longer than any project in this thesis. I started working with Peter in early 2011, and our relationship since then has been extremely helpful for my professional career. I thank Peter for his patience, perseverance, mentorship, and calm in the face of a limitless number

of coding issues and data problems. I thank Jonathan and Elise for breaking Peter and I out of our endless struggle for answers with fresh views and skillful solutions; if it weren't for them I would not have been able to publish.

The funny thing about being in a small department is that you can end up "working" with everyone. This can range from actual advising, to being in the same reading class. Thus, I would like to thank the Professors, postdocs, and research staff of the Planetary Science option. I thank Mike Brown for putting up with my loudness, for always being open to questions as long as his door is open, and for putting together a very interesting class for me to TA. I thank Bethany Ehlmann for answering some of my dumb Mars questions, for leading a very informative Mars reading class, and for being one of the architects of the amazing Iceland trip. I thank Andy Ingersoll for always asking the best questions during any seminar, for indulging my attempts at doing Enceladus research (see Chapter 4 of this thesis), and for his pure Awesomeness. Although he is not Planetary, I thank Paul Asimow for being just an incredible Professor, orchestra conductor, evil mustache wearer, and all around fun dude.

I thank my thesis committee, Geoff Blake, Heather Knutson, Dave Stevenson, and Yuk Yung. I thank Geoff for always wearing a smile in the hallway and for always giving out sound advice. I thank Heather for being extraordinarily patient with me when I attempted to analyze that one phase curve that I just didn't have time for, and for being totally ok with me switching to another project when it seemed right. I also thank Heather for teaching me the importance of when to say "enough" when the project doesn't seem to be working out. I thank Dave for his unrelenting dedication to Planetary Science. He intimidated me at first, and though that still may be true sometimes, I know that Dave is just a big teddy bear with a heart of metallic hydrogen (in a good way). Though we did not continue publishing papers together after our first, I thank Dave for always having the patience to entertain my questions, for always answering questions precisely, and for critiquing questions that aren't asked correctly.

Yuk. What I can I say. Yuk Yung has his own style, #yukyungstyle, if you will. There are not enough words for me to truly spell out the ways that I have appreciated his support and help as my advisor. I'll try anyway though. Yuk's style is unique, and it may not be everyone's tea. It was mine, though. It was good tea. It is still good tea. I thank Yuk for his absolute dedication to his students. I thank him for the way he is willing to set aside his nights to make sure that we are on the right track.

I thank him for his high standards for us; it's no secret that working with Yuk is like doing 2 (or more) PhD's. I thank Yuk for his rambling thoughts on poetry, politics, and life. I thank him for his tireless efforts in writing proposals so that we can all have food to eat. I thank him for trying his hardest to send all of us to conferences so that we may all get a chance to become famous. I thank him for treating me like a colleague as I near the end of my PhD. I thank him for being Yuk.

Beyond Yuk, there is the Yuk Army. I thank Dr. Run-Lie Shia for being the best problem solver, for always entertaining my questions, and for his tireless dedication to keeping our models intact and running. I thank Dr. Sally Newman for her work in trying to save the planet, and for helping my fiancée when she needed work. I will never forget what she and Yuk did for us in our time of need. Finally, I thank Dr. Renyu Hu for his advising on my third paper, for his great insights on photochemistry, and his and his wife's friendship.

I also thank the postdocs that have shared with me their experiences and their advice, Hao Cao, Kat Deck, Courtney Dressing, and Erik Petigura. I hope a faculty job with their name on it is right around the corner!

Even though I have grown up in the west, I still value the Chinese culture instilled in me by my family. I would therefore like to thank the CaltechC for building a sense of community among Chinese people at Caltech, and welcoming me within this community despite my upbringing and my inability to speak Chinese (at first). I would also like to thank the many Chinese friends I've made, with whom I've had lots of fun hiking, having delicious food, and just hanging out, including Zhihong Tan, Jinqing Chen, Xuan Zhang, Qiuyu Peng, Wentao Huang, Lucy Yin, Hank Yu, Wen Yan, Boyu Li, Alex Teng, and ZB.

I thank Ernies for keeping me alive these last 2 years. I would either be dead, starving, poor, or frustrated if it were not for his Awesome burritos. Long may he reign.

Being a grad student is a funny thing. Every single one will know how it feels to be the youngest in the pack and eventually, the oldest. Each one of us is the focal point for more than a decade of grad students and their friendships. I am lucky that the grad students in my department have been some of the kindest, smartest, and funniest people I've ever known. I would like to start off by thanking the "old guard" – grad students who were already senior by the time I started, including Alex Hayes, Kuai Le, Alejandro Soto, Aaron Walf, King-Fai Li, Da Yang, and Meg

Rosenberg. Though our interactions were brief (and some not so brief), they were always a valuable source of advice and guidance. I would also like to thank Xi Zhang, my office mate, and spiritual leader of the Yuk Army during my first years in the service. I think Xi (Arthur) for helping me on my first projects, for offering words of comfort in times of stress, and for introducing me to Tai Chi.

Those first years of grad school were fun and wild. It was my first time away from family, but it turns out that a new family was right in front of me. The older grad students welcomed us with open arms and made sure that we felt right at home. I thank Alex Lockwood, Mike Line, Konstantin Batygin, Ajay Limaye, and Jeff Thompson for always being up for hanging out and having fun, for always organizing little get togethers, for giving us the Rules, and for just being Awesome people. I also thank the other party peoples, Tobias Bischoff, Xavier Levine, CHRRRRIIIIIIISSSSS Rollins, Bryan Riel, Howard Hui, Stephen Perry, Becky Schwantes, and Rob Wills for all the good times.

In particular, I would like to thank those of my year, Miki Nakajima, Josh Kammer, Adam Waszczak (and Kelley!), Masha Kleshcheva, Zhan Su, and Hilary Martens for all their support throughout the years and their friendship. It felt like we all grew up together, and though we have already spread out across the country, we will continue to share that bond that was formed when we all started this journey six years ago.

Those first years passed, and soon more grad students arrived. I went from being one of youngest of the pack to one of the old ones. Luckily, those new grad students followed in the footsteps of the kind, warmhearted individuals who came before. I thank Cheng Li for all the interesting conversations we've had about numerical modeling and atmospheric dynamics; I thank Henry Ngo (and Laura!) for sticking by me for 10 years and still willing to help me with my ignorance about life in general; I thank Mike Wong for aaaalllllllll the Star Trek things and for being an Awesome person and roommate; I thank Pan Lu for all the Chinese gossip; I thank Joe O'Rourke for his smart ass remarks about lots of things; I thank Danielle Piskorz for putting up with the nonstop Trek talk in her office; I thank Qiong Zhang for more Chinese gossip; I thank Pushkar Kopparla for his exasperation at our shenanigans; I thank Dana Anderson for wanting to claim my dilapidated desks; I thank Chris Spalding for the acknowledgement in his paper and the brilliant dynamics conversations; I thank Ian Wong for all the dank memes; I thank Peter Buhler for the hilarious banter; I thank Nancy Thomas for always lighting up

a room; I thank Elizabeth Bailey for the WAR; I thank Sam Trumbo for coming out to see The Martian with us; I thank Nathan Stein for schooling us on the Curiosity knowledge; I thank Ana Lobo for all the Yuks; and I thank Siteng Fan for allowing me to advise him even though I clearly don't know what I'm doing.

I thank Caltech for giving me the opportunity to study what I have always wanted and for allowing me to travel to so many places, like Hawaii, Iceland, Spain, Switzerland, and Japan. It has opened up my future and supplied me with the skills and connections needed have a successful career in Planetary Science.

Of course, I would not be here if it were not for my family. My Mom had set out first, moving from China to Canada to make a life for herself and for my Dad and I. It would be three long years before I saw her again. We also gained a new family member in my Uncle, who helped my Mom with our immigration. I owe so much to all of them; they had uprooted their entire lives to give me a chance at success in the west. I remember my Mom and Dad saying that they did not come here for nothing when I told them that I had gotten into Caltech. It was all worth it.

Then, in my second year, I found out that my Mom had cancer, and that it was terminal. The few months that followed were agonizing, punctuated by brief distractions thanks to my Caltech family. She passed away on December 31st, 2012. I thank her for dedicating her life to me, for creating my future, and for teaching me a valuable life lesson in dealing with loss. I thank my Dad for watching out for my safety and health all my life, for keeping tabs on me and my affairs to make sure I'm not screwing things up, and for his total focus on my wellbeing even when he is in pain. I thank my Uncle for driving me to school everyday during my undergrad, for saying yes any time I needed help, for looking after my Dad during the dark times, and for having the best life stories. I thank them for everything.

Last, but definitely not least, I thank my honey, my love, Hao Zhang. She was the first to know about my Mom's illness and she stuck by me. She was by my side as I faced the worst life has to offer, and she picked me up. I thank her for all her support; I would not be who I am today without her. Her dedication, her kindness, her laughter, her love, I thank her for being her and for being here. I thank her for traveling with me, for putting up with my crap, for introducing me to Chinese historic dramas (Lang Ya Bang!!), for being the cutest, for buying me clothes, for teaching me what it means to be a partner in life, and for agreeing to marry me.

These last six years have been a blast. Thank you all for the memories.

ABSTRACT

Clouds and hazes are found in every significant planetary atmosphere in the Solar System, from the sulfuric acid clouds of Venus and the water clouds of Earth and Mars, to the photochemical hazes that pervade the giant planets, ice giants, Titan, and even Pluto. Beyond the Solar System, transmission spectroscopy of exoplanets have found that many are also bound in clouds and hazes, though their higher temperatures give rise to clouds of salts, rocks, and metals, and hazes of soots and sulfurs. Understanding the behavior and role of clouds and hazes in planetary atmospheres is instrumental in understanding atmospheres as a whole, as they are strongly coupled to other atmospheric processes. For example, highly reflective clouds can reduce the effective temperature of a planet, while UV absorbing hazes can increase local atmospheric temperatures. Clouds and hazes also act as reservoirs for important trace species and can be crucial to atmospheric chemical cycles.

In this Ph.D thesis, I use modeling and comparisons to observations to understand cloud and haze processes on multiple worlds within and beyond the Solar System. I use the Community Aerosol and Radiation Model for Atmospheres (CARMA) to simulate the sulfuric acid clouds of Venus in an attempt to find the cause of the spatial and temporal variability in the Venus upper haze, as observed by Venus Express. I show that the variability is likely caused by sustained updrafts lofting large cloud particles into the haze. I then modify CARMA to include fractal aggregate particles to investigate the properties of the photochemical haze on Pluto as observed by New Horizons, and find that the haze particles must be porous, and that they may act as nucleation cites for simple hydrocarbons. Finally, I add exotic condensates to CARMA to model clouds on exoplanets, where their existence has led to difficulties in finding the atmospheric compositions of these worlds. I show that not all species that can condense will, due to their material properties, and that the cloud optical depth is largely controlled by the rate of particle production via homogeneous nucleation. In addition, I investigate the effect a sulfur haze would have on the reflected light spectrum of giant exoplanets to prepare for upcoming direct imaging missions, and find that sulfur hazes significantly brighten these planets at long wavelengths, while darkening them at short wavelengths due to UV absorption. Finally, I retrieve the properties of water ice particles from Cassini observations of the plumes of Enceladus assuming that they are aggregates rather than spheres, and thereby unifying forward scattering observations with in situ measurements.

LIST OF ILLUSTRATIONS

LIST OF TABLES

PUBLISHED CONTENT AND CONTRIBUTIONS

Gao, P., S. Fan, et al. (Accepted). "Constraints on the Microphysics of Pluto's Photochemical Haze from New Horizons Observations". In: *Icarus*. DOI: 10.1016/j.icarus.2016.09.030.

P. Gao participated in the conception of the project, conducted the numerical simulations, analyzed the results, and wrote the manuscript.

Gao, P., P. Kopparla, et al. (2016). "Aggregate particles in the plumes of Enceladus". In: *Icarus* 264, pp. 227–238. DOI: 10.1016/j.icarus.2015.09.030.

P. Gao conceived of and led the project, conducted the data retrievals, analyzed the results, and wrote the majority of the manuscript.

Gao, P., X. Zhang, et al. (2014). "Bimodal distribution of sulfuric acid aerosols in the upper haze of Venus". In: *Icarus* 231, pp. 83–98. DOI: 10.1016/j.icarus.2013.10.013.

P. Gao participated in the conception of the project, conducted the numerical simulations, analyzed the results, and wrote the manuscript.

Chapter 1

SPACE: THE FINAL FRONTIER

Every world in the Solar System that has an atmosphere has within it some form of aerosol, be it clouds, hazes, or dust. Venus, for example, is enveloped in a thick cloud and haze system that is mostly made up of sulfuric acid (Hansen and Hovenier, 1974). Earth's atmosphere is rife with water/water ice clouds, as well as high altitude sulfuric acid hazes (Junge, 1963) and organic hazes from surface sources. Mars sees frequent appearances of water and CO_2 ice clouds, which may use the abundant dust in its atmosphere as nucleation sites (Colaprete, Toon, and Magalhães, 1999; Listowski et al., 2014). Jupiter is almost entirely covered in clouds of water, ammonia and possibly ammonium hydrosulfide, with overlying hydrocarbon photochemical hazes (Atreya et al., 1999; Zhang et al., 2013). Saturn is also covered in a photochemical haze (West, Baines, et al., 2009), with evidence of water and ammonia clouds beneath (Li and Ingersoll, 2015). Like planet like moon, Saturn's largest natural satellite, Titan, is also enveloped in a photochemical haze, with hydrocarbon clouds at lower altitudes (Lavvas, Yelle, and Griffith, 2010; Barth and Toon, 2006). The Ice Giants, Uranus and Neptune, possess hydrocarbon clouds and hazes derived from photochemistry and condensation (Moses, Allen, and Yung, 1992; Lunine, 1993). Even the relatively thin atmosphere of Pluto (surface pressure $\sim$10 μbar) contains intricately layered photochemical hazes (Gladstone et al., 2016).

Aerosols are plentiful even beyond the Solar System. Recent observations by the Wide Field Camera 3 onboard the Hubble Space Telescope of exoplanets in transmission– when the planets passes in front of their host stars such that stellar light can penetrate the planets' upper atmospheres and pick up signatures of molecular absorption– show that many of these planets' transmission spectra are featureless in the near–infrared (e.g. Knutson, Benneke, et al., 2014; Knutson, Dragomir, et al., 2014; Kreidberg et al., 2014), suggesting either a high metallicity atmosphere or optically thick clouds and/or hazes. Equilibrium chemistry calculations show these clouds to be composed of exotic materials, such as salts, sulfides, rocks, and metals (Morley et al., 2012).

Clouds and hazes are important components of planetary atmospheres. First and

foremost, they are radiatively active, and can heat or cool their surroundings depending on their optical properties. For example, unknown contaminants in the clouds of Venus strongly absorbs UV, such that the heating rates associated with them can be up to a few K day^{-1}; at the same time, the clouds themselves are extremely reflective, so that Venus' equilibrium temperature is actually lower than that of Earth (Crisp, 1986; Haus, Kappel, and Arnold, 2015; Haus, Kappel, Tellmann, et al., 2016). Similarly, dust in Mars' atmosphere absorbs thermal IR such that temperatures in a dusty atmosphere can be tens of K higher than in a clear one (Pollack et al., 1979). Meanwhile, the photochemical haze particles in Titan's atmosphere is an important contributor to radiative cooling of its stratosphere (McKay, Pollack, and Courtin, 1989; Tomasko et al., 2008). Clouds and hazes can also act as reservoir for key chemical species in a planet's atmosphere. On Venus, sulfuric acid acts as the ultimate sink for sulfur freed from SO_2 and OCS photolysis above the cloud deck, though elemental sulfur can also exist in small amounts; transport of sulfuric acid particles to the deep atmosphere by sedimentation then causes their evaporation and thermal decomposition back into H_2O and SO_3, ultimately completing the sulfur cycle (Mills, Esposito, and Yung, 2007).

In this thesis, I explore some important examples of cloud and haze systems within the Solar System and beyond, and attempt to answer several questions that have arisen recently due to observations from spacecrafts and ground–based and space–based observatories. A key tool of my work is the Community Aerosol and Radiation Model for Atmospheres, a cloud microphysics code developed in the late 1970s to study Earth's stratospheric aerosols (Turco et al., 1979; Toon et al., 1979). It calculates the equilibrium cloud particle distribution based on rates of nucleation, condensation, evaporation, coagulation/coalescence, and transport. I elaborate on CARMA's internal workings in Appendix A.

This thesis is composed of three parts split into five major chapters. Each part has a specific focus on an aspect of clouds and hazes that is explored through the pertinent questions of the chapter(s). The first part, **DROPPING ACID**, contains Chapter 2 and focuses on the planet–wide sulfuric acid clouds and hazes of Venus. It explores the full suite of cloud/haze processes mentioned previously and investigates the question, *what controls the cloud and haze distribution seen on Venus, and what causes the temporal variations in abundance and size distribution of particles in the Venus upper haze?* I use CARMA to simulate the full sulfuric acid cloud and haze system, assuming that photochemically produced sulfuric acid heteroge-

neously nucleate onto prescribed sulfur condensation nuclei; the sulfuric acid cloud particles are then allowed to be transported throughout the atmosphere and grow by condensation and coagulation, and shrink by evaporation. I then investigate how to generate two size modes in the upper haze, as observed by Venus Express. I evaluate two processes: (1) the interaction of upwelled cloud particles and sulfuric acid particles nucleated in situ on meteoric dust, and (2) advection of cloud particles into the upper haze due to sustained subsolar cloud top convection. Process (2) is able to reproduce the time scales associated with the temporal variability and the two size modes.

In Part 2, **FROZEN FRACTALS ALL AROUND**, which contains Chapters 3 and 4, I tackle the importance of fractal aggregates, which is the shape that most photochemical haze particles take in the Solar System (West and Smith, 1991). Specifically, I investigate the photochemical haze of Pluto, and invoke aggregates in the plumes of Enceladus–the closest thing this tiny Saturnian moon has to an atmosphere. Chapter 3 asks the straightforward question, *is Pluto's haze composed of fractal aggregates and how do they interact with the condensing hydrocarbon species in Pluto's atmosphere?* For this chapter I modify CARMA to include coagulation and sedimentation of aggregate particles, and compare the extinction coefficients calculated from equilibrium haze distributions with solar occultation observations from the New Horizons spacecraft. In order to match the observations, the rate of haze particle formation must be close to the methane photolysis rate, and that the haze particles must be aggregates, or at least porous. The haze particles can also act as nucleation sites for HCN and C_2 hydrocarbons. Chapter 4 considers the very specific question, *can aggregate ice particles explain the difference in the derived mass of solids in the Enceladus plumes between forward scattering and in situ detection?* Estimates of the total particulate mass of the plumes of Enceladus are important to constrain theories of particle formation and transport at the surface and interior of the satellite. In previous models of the plumes, the water ice particles have always been assumed to be spherical, which led to high values of the solid–to–vapor mass ratio of the plumes (IE11) derived from forward scattering observations. However, in situ measurements of the plume solids led to a value an order of magnitude lower. A possible solution is if the solid particles are aggregates, which, like spheres of similar sizes, forward scatters strongly, but are lower in mass due to their porosity. Using the same forward scattering observations as in Ingersoll and Ewald (IE11) and the Monte Carlo Markov Chain method, I find two possible solutions for mass of the solids in the plume, one where the particles are spheri-

cal, in which case the mass matched previous works, and one where the particles are aggregates, which resulted in masses matching that of the in situ observations. Using the MCMC method, I am also able to constrain the aggregate radius and the aggregate monomer radius, which can be tested by analysis of polarimetry data.

Part 3 contains Chapters 5 and 6 and is called, **STRANGE NEW WORLDS**. As the name suggests, I move beyond the Solar System into the wild world of exoplanets. Here, the focus is on applying what we have learned in the Solar System to these newly discovered planets, and see whether I can make sense of the exotic clouds and hazes that seem to pervade their atmospheres. In Chapter 5, I ask the simple question, *can the salt and sulfide clouds in exoplanet atmospheres be treated like water clouds on Earth, and if so, how do they vary with changes in the eddy mixing and metallicity in the atmosphere?* I use CARMA to simulate the potassium chloride (KCl) and zinc sulfide (ZnS) clouds of the Super Earth GJ 1214 b and subject them to changes in atmospheric conditions. Contrary to popular belief, pure ZnS clouds cannot form from homogeneous nucleation due to its high surface energy, limiting it to heterogeneous nucleation only, which requires some external surface. High eddy diffusivities promote high rates of nucleation due to increased upwelling of KCl vapor from depth and generate more massive, vertically extended clouds, while high metallicities drastically increase the cloud mass due to higher supersaturations leading to high nucleation rates, and thus even moderately supersolar metallicities ($0 < [Fe/H] < 1$) may produce optically thick clouds at high altitudes. In Chapter 6, I pose the question, *how does the appearance of a sulfur haze on giant exoplanets change its geometric albedo spectrum, and can this be detected?* With the prioritization of direct imaging in upcoming exoplanet observation missions, such as WFIRST, it is importance to predict what these missions will see. Just as sulfuric acid is the sink for photolysis of sulfur compounds in oxidizing atmospheres, elemental sulfur can play the same rule in reducing atmospheres, such as those of giant exoplanets (Zahnle et al., 2016). I use an established model to simulate the geometric albedo spectrum of a giant exoplanet with a sulfur haze in its atmosphere, and investigate how the albedo changes as a function parameters. The albedo spectrum is most sensitive to changes in the haze optical depth, but the strong absorption band of sulfur at wavelengths <0.45 μm is robust even at very low optical depths. Detection of such a haze by WFIRST is possible, though discriminating between a sulfur haze and any other reflective material will require observations of the short wavelength absorption band, which is currently beyond WFIRST's grasp.

References

Atreya, S. K. et al. (1999). "A comparison of the atmospheres of Jupiter and Saturn: deep atmospheric composition, cloud structure, vertical mixing, and origin". In: *Planetary and Space Science* 47, p. 1243.

Barth, E. L. and O. B. Toon (2006). "Methane, ethane, and mixed clouds in Titan's atmosphere: Properties derived from microphysical modeling". In: *Icarus* 182, pp. 230–250.

Colaprete, A., O. B. Toon, and J. A. Magalhães (1999). "Cloud formation under Mars Pathfinder conditions". In: *Journal of Geophysical Research* 104, pp. 9043–9054.

Crisp, D. (1986). "Radiative forcing of the Venus mesosphere". In: *Icarus* 514, pp. 484–514.

Gladstone, G. R. et al. (2016). "The atmosphere of Pluto as observed by New Horizons." In: *Science* 351, p. 1280.

Hansen, J. E. and J. W. Hovenier (1974). "Interpretation of the polarization of Venus." In: *Journal of the Atmospheric Sciences* 21, pp. 1137–1160.

Haus, R., D. Kappel, and G. Arnold (2015). "Radiative heating and cooling in the middle and lower atmosphere of Venus and responses to atmospheric and spectroscopic parameter variations". In: *Planetary and Space Science* 117, pp. 262–294.

Haus, R., D. Kappel, S. Tellmann, et al. (2016). "Radiative energy balance of Venus based on improved models of the middle and lower atmosphere". In: *Icarus* 272, pp. 178–205.

Ingersoll, A. P. and S. P. Ewald (2011). "Total particulate mass in Enceladus plumes and mass of Saturn's E ring inferred from Cassini ISS images". In: *Icarus* 216, pp. 492–506.

Junge, C. E. (1963). "Sulfur in the atmosphere". In: *Journal of Geophysical Research* 65, p. 227.

Knutson, H. A., B. Benneke, et al. (2014). "A featureless transmission spectrum for the Neptune-mass exoplanet GJ436b". In: *Nature* 505, p. 66. arXiv: 1401.3350.

Knutson, H. A., D. Dragomir, et al. (2014). "Hubble Space Telescope Near-Ir Transmission Spectroscopy of the Super-Earth Hd 97658B". In: *The Astrophysical Journal* 794, p. 155. arXiv: 1403.4602.

Kreidberg, L. et al. (2014). "Clouds In The Atmosphere Of The Super-Earth Exoplanet GJ1214b". In: *Nature* 505, pp. 69–72. arXiv: arXiv:1401.0022v1.

Lavvas, P., R. V. Yelle, and C. A. Griffith (2010). "Titan's vertical aerosol structure at the Huygens landing site: Constraints on particle size, density, charge, and refractive index". In: *Icarus* 210, pp. 832–842.

Li, C. and A. P. Ingersoll (2015). “Moist convection in hydrogen atmospheres and the frequency of Saturn’s giant storms”. In: *Nature Geoscience* 8, pp. 398–403.

Listowski, C. et al. (2014). “Modeling the microphysics of CO_2 ice clouds within wave-induced cold pockets in the martian mesosphere”. In: *Icarus* 237, pp. 239–261.

Lunine, J. I. (1993). “The atmospheres of Uranus and Neptune”. In: *Annual review of astronomy and astrophysics* 31, pp. 217–263.

McKay, C. P., J. B. Pollack, and R. Courtin (1989). “The thermal structure of Titan’s atmosphere”. In: *Icarus* 80, pp. 23–53.

Mills, F. P., L. W. Esposito, and Y. L. Yung (2007). “Atmospheric composition, chemistry, and clouds.” In: *Exploring Venus as a Terrestrial Planet*. Ed. by L. W. Esposito, E. R. Stofan, and T. E. Cravens. Washington D.C., USA: American Geophysical Union, pp. 73–100.

Morley, C. V. et al. (2012). “Neglected Clouds in T and Y Dwarf Atmospheres”. In: *The Astrophysical Journal* 756, p. 172.

Moses, J. I., M. Allen, and Y. L. Yung (1992). “Hydrocarbon nucleation and aerosol formation in Neptune’s atmosphere”. In: *Icarus* 99, pp. 318–346.

Pollack, J. B. et al. (1979). “Properties and Effects of Dust Particles Suspended in the Martian Atmosphere ”. In: *Journal of Geophysical Research* 84, pp. 2929–2945.

Tomasko, M. G. et al. (2008). “Heat balance in Titan’s atmosphere”. In: *Planetary and Space Science* 56, pp. 648–659.

Toon, O. B. et al. (1979). “A one-dimensional model describing aerosol formation and evolution in the stratosphere: II. Sensitivity studies and comparison with observations”. In: *Journal of the Atmospheric Sciences* 36, pp. 718–736.

Turco, R. P. et al. (1979). “A one-dimensional model describing aerosol formation and evolution in the stratosphere: I. Physical processes and mathematical analogs.” In: *Journal of the Atmospheric Sciences* 36, pp. 699–717.

West, R. A., K. H. Baines, et al. (2009). “Clouds and Aerosols and Saturn’s Atmosphere”. In: *Saturn from Cassini–Huygens*. Ed. by M. Dougherty, L. Esposito, and S. Krimigis. Springer Netherlands, pp. 161–179.

West, R. A. and P. H. Smith (1991). “Evidence for aggregate particles in the atmospheres of Titan and Jupiter”. In: *Icarus* 90, pp. 330–333.

Zahnle, K. et al. (2016). “Photolytic Hazes in the Atmosphere of 51 Eri B”. In: *The Astrophysical Journal* 824, p. 137.

Zhang, X. et al. (2013). “Stratospheric aerosols on Jupiter from Cassini observations”. In: *Icarus* 226, pp. 159–171.

PART I: DROPPING ACID

Chapter 2

BIMODAL DISTRIBUTION OF SULFURIC ACID AEROSOLS IN THE UPPER HAZE OF VENUS

Gao, P. et al. (2014). "Bimodal distribution of sulfuric acid aerosols in the upper haze of Venus". In: *Icarus* 231, pp. 83–98. DOI: 10.1016/j.icarus.2013.10.013.

2.1 Abstract

Observations by the SPICAV/SOIR instruments aboard Venus Express have revealed that the upper haze (UH) of Venus, between 70 and 90 km, is variable on the order of days and that it is populated by two particle modes. We use a 1–dimensional microphysics and vertical transport model based on the Community Aerosol and Radiation Model for Atmospheres to evaluate whether interaction of upwelled cloud particles and sulfuric acid particles nucleated in situ on meteoric dust are able to generate the two observed modes, and whether their observed variability are due in part to the action of vertical transient winds at the cloud tops. Nucleation of photochemically produced sulfuric acid onto polysulfur condensation nuclei generates mode 1 cloud droplets, which then diffuse upwards into the UH. Droplets generated in the UH from nucleation of sulfuric acid onto meteoric dust coagulate with the upwelled cloud particles and therefore cannot reproduce the observed bimodal size distribution. By comparison, the mass transport enabled by transient winds at the cloud tops, possibly caused by sustained subsolar cloud top convection, are able to generate a bimodal size distribution in a time scale consistent with Venus Express observations. Below the altitude where the cloud particles are generated, sedimentation and vigorous convection causes the formation of large mode 2 and mode 3 particles in the middle and lower clouds. Evaporation of the particles below the clouds causes a local sulfuric acid vapor maximum that results in upwelling of sulfuric acid back into the clouds. In the case where the polysulfur condensation nuclei are small and their production rate is high, coagulation of small droplets onto larger droplets in the middle cloud may set up an oscillation in the size modes of the particles such that precipitation of sulfuric acid "rain" may be possible immediately below the clouds once every few Earth months. Reduction of the polysulfur condensation nuclei production rate destroys this oscillation and reduces

the mode 1 particle abundance in the middle cloud by two orders of magnitude. However, it better reproduces the sulfur-to-sulfuric-acid mass ratio in the cloud and haze droplets as constrained by fits to UV reflectivity data. In general we find satisfactory agreement between our nominal and transient wind results and observations from Pioneer Venus, Venus Express, and Magellan, though improvements could be made by incorporating sulfur microphysics.

2.2 Introduction

Sulfuric acid aerosols make up most of the global cloud deck and accompanying hazes that shroud the surface of Venus (Esposito et al., 1983). As a result, the radiation environment and energy budget at the surface and throughout the atmosphere is strongly affected by the vertical extent, size distribution, and mean optical properties of these particles. These aerosols also serve as a reservoir for sulfur and oxygen, and thus play a major part of the global sulfur oxidation cycle (F. P. Mills, Esposito, and Yung, 2007). Furthermore, recent studies by Zhang, Liang, Montmessin, et al. (2010) and Zhang, Liang, F. P. Mills, et al. (2012) have hypothesized that the upper haze layer could provide the source of sulfur oxides above 90 km. Therefore, studying aerosols is a crucial step in understanding the climate and chemistry on Venus.

Observations from the Pioneer Venus atmospheric probes (Knollenberg and Hunten, 1980) helped constrain the number density and size distribution of the aerosols in the cloud deck, and revealed the possibility of two size modes with mean radii ~0.2 μm (mode 1) and ~1 μm (mode 2), along with a third, controversial mode with radius ~3.5 μm whose existence has been challenged (Toon, Ragent, et al., 1984). The clouds were also vertically resolved into three distinct regions: the upper cloud, from 58 to 70 km; the middle cloud, from 50 to 58 km; and the lower cloud, from 48 to 50 km. Mode 1 particles have the largest number densities at all altitudes, while modes 2 and 3 particles are relatively more abundant in the middle and lower clouds than in the upper cloud (Knollenberg and Hunten, 1980). Both entry probe (Knollenberg and Hunten, 1980; Esposito et al., 1983) and remote sensing (Crisp, Sinton, et al., 1989; Crisp, McMuldroch, et al., 1991; Carlson et al., 1993; Grinspoon et al., 1993; Hueso et al., 2008) indicate that the middle and lower clouds are much more variable than the upper cloud. This variability may be associated with strong convective activity within the middle cloud, where downdrafts with amplitudes as large as 3 m s^{-1} and updrafts as large as 1 m s^{-1} were measured in situ by the VEGA Balloons (Ingersoll, Crisp, and VEGA Balloon Science Team., 1987;

Crisp, Ingersoll, et al., 1990).

These observations of the Venus clouds have been interpreted using numerical models that account for transport and/or aerosol microphysics. Toon, Turco, and Pollack (1982) showed that sulfur could be present in the upper cloud under low oxygen conditions in sufficient amounts to form mode 1 particles, with mode 2 particles arising from the coagulation of these particles and sulfuric acid droplets. However, they did not model any other interactions between sulfuric acid and the sulfur particles beside coagulation. Krasnopolsky and Pollack (1994), meanwhile, showed that the lower cloud is formed by upwelling and subsequent condensation of sulfuric acid vapor due to the strong gradient in sulfuric acid mixing ratio below the clouds. James, Toon, and Schubert (1997) showed that this process is very sensitive to the local eddy diffusion coefficient, and suggested that the variability of the lower and middle clouds was tied to the dynamical motions of the atmosphere in this region. This conclusion was also reached by McGouldrick and Toon (2007); they showed that organized downdrafts from convection and other dynamic processes could produce holes in the clouds. Indeed, observations from Pioneer Venus indicated that this region of the atmosphere has a lapse rate close to adiabatic, with parts of the middle cloud region being superadiabatic Seiff, Kirk, et al. (1980) and Schubert et al. (1980). Imamura and Hashimoto (2001) modeled the entire cloud deck, and reached many of the same conclusions as James, Toon, and Schubert (1997) and Krasnopolsky and Pollack (1994) regarding the lower and middle clouds, and Toon, Turco, and Pollack (1982) regarding the upper cloud. They also concluded that an upward wind may be necessary in order to reproduce the observations.

The clouds lie below an upper haze (UH), which extends from 70 to 90 km (F. P. Mills, Esposito, and Yung, 2007). In Imamura and Hashimoto (2001), small cloud particles are lofted by upward winds out of the top of the model domain, which would place them in this UH. This demonstrates that regional and/or global dynamical processes will lead to some mixing of the haze with the clouds, resulting in variability of the particle populations in the UH, especially if these processes vary with space and time. Though the variability of winds at the clouds-haze boundary has never been measured directly, we do observe the particle population variability. For instance, data from the Pioneer Venus Orbiter Cloud Photopolarimeter (OCPP) revealed latitudinal variations of an order of magnitude in haze optical thickness from the polar region (where it is more abundant) to the tropics, as well as temporal variations on the order of hundreds of days (Kawabata et al., 1980). More recently,

Wilquet, Fedorova, et al. (2009) and Wilquet, Drummond, et al. (2012) used Venus Express SPICAV/SOIR solar occultation observations to show the existence of bimodality in the size distribution of the UH, with a small mode of radius 0.1–0.3 μm, and a large mode of radius 0.4–1.0 μm. These modes are not to be confused with the aforementioned modes 1, 2, and 3 in the cloud deck, even though they might be physically connected. Interestingly, the mean size of the haze particles as reported by Kawabata et al. (1980) from OCPP measurements 30 years earlier (0.23 ± 0.04 μm) lies well within the small mode size range. In addition, Wilquet, Fedorova, et al. (2009) find that the extinction of the haze was observed to vary by as much as an order of magnitude in a matter of days. The degree of variability also changed, as observations a few months later (Wilquet, Drummond, et al., 2012) showed variability in the magnitude of the haze extinction of only a factor of two. Time variability of the haze was also observed in infrared images of the Venus southern hemisphere, where the appearance of the haze changed dramatically across tens of degrees of latitude in the span of a few days (Markiewicz et al., 2007). The three studies above also showed that the haze optical depth can exceed unity, making it an active participant in the regulation of solar radiation reaching lower altitudes, and its variability a property that requires better understanding. However, numerical models with adequate microphysics that include the UH are rare. Yamamoto and Tanaka (1998) and Yamamoto and Takahashi (2006) included the UH in their simulations of aerosol transport via global atmospheric dynamics and reproduced much of the observations satisfactorily. However, the aerosol microphysics in both studies is inadequate due to the lack of a detailed treatment of nucleation.

In this study, we investigate the formation and evolution of the UH and the cloud decks by constructing a 1–dimensional (1D) microphysical and vertical transport model that couples the clouds to the haze with a more detailed treatment of the microphysics. We propose two possible causes for the bimodal size distribution and time variability of the haze: (1) the two modes are produced from two separate processes—one mode is derived from the in situ nucleation of sulfuric acid onto meteoric dust, a possibility discussed by Turco, Toon, et al. (1983) for terrestrial atmospheres, and the other mode is made up of cloud particles that have been lofted into the UH via winds and eddy diffusion, and (2) the two modes and the time variability are entirely due to strong transient winds at the cloud tops lofting both mode 1 and mode 2 cloud particles into the UH.

We describe our basic model in §2.3, with emphasis on the model attributes unique

to our investigation of aerosols in the Venus atmosphere. In §2.4 we present our model results, along with comparisons with data from Pioneer Venus and Venus Express. We also discuss our results in the context of physical processes involved in our model. We summarize our work and state our conclusions in §2.5.

2.3 Model

We use version 3.0 of the Community Aerosol and Radiation Model for Atmospheres (CARMA) as our base microphysical and vertical transport code. The model is an upgrade from the original CARMA (Turco, Hamill, et al., 1979; Toon, Turco, Westphal, et al., 1988) by Bardeen, Toon, et al. (2008) and Bardeen, Conley, et al. (2011). We describe our model setup and departures from the base model below, and we refer the reader to Turco, Hamill, et al. (1979), Toon, Turco, Westphal, et al. (1988), and Toon, Turco, Jordan, et al. (1989) and Jacobson and Turco (1994) for detailed descriptions of the basic microphysics and vertical transport and English et al. (2011) for the sulfate microphysics in CARMA.

2.3.1 Model Setup

The microphysical and dynamical processes included in the model are the nucleation of liquid sulfuric acid droplets on sulfur and meteoric dust condensation nuclei; the condensational growth, evaporation, and coagulation of these particles; and their transport by sedimentation, advection, and diffusion.

Table 2.1 summarizes the simulation parameters. The model atmosphere extends from 40 to 100 km, covering the altitudes of the cloud deck and UH. This vertical range is split into 300 levels of 200 m thickness each in our model. Our model time step is 10 seconds, and we found that a total simulation time on the order of 2×10^8 seconds, or about 2000 Earth days, was necessary for the model to reach steady state. This is similar to the characteristic vertical diffusion time of the lower clouds as calculated from the eddy diffusion coefficient in §2.3.4 and far greater than that of the Venus mesosphere (i.e. the altitudes of the upper cloud and upper haze) calculated by Imamura (1997).

In order to cover the size range from meteoric dust to large droplets and represent both volatile and involatile particles, we use two groups of particle bins, each covering the radius range from 1.3 nm to ~30 μm. The lower radius limit corresponds to the size of meteoric dust as described in Kalashnikova et al. (2000), while the upper radius limit mirrors the upper limit used in Imamura and Hashimoto (2001). The inclusion of multiple bins for involatile particles differs from the approach by Ima-

Table 2.1: Model Parameters

	Nominal Model	Other Values Used
Surface Gravity	887.0 cm s^{-1}	
Atmospheric Molecular Weight	43.45 g mol^{-1} (CO_2)	
Condensable Molecular Weight	98.08 g mol^{-1} (H_2SO_4)	
Atmospheric Viscosity[a]	1.496×10^{-4} g cm^{-1} s^{-1}	
Sulfuric Acid Surface Tension[b]	72.4 erg cm^{-2}	
T-P Profile	Figure 2.1	
Water Vapor Profile	Figure 2.3	
Production Rates		
Meteoric Dust	4800 cm^{-2} s^{-1} (Figure 2.5)	
Photochemical CNs	1.75×10^6 cm^{-2} s^{-1} (Figure 2.2)	Nominal/10[c], Nominal/100[c]
Sulfuric Acid Vapor	6×10^11 cm^{-2} s^{-1} (Figure 2.2)	
Time Domain		
Time Step	10 s	
Total Simulation Time	2×10^8 s	5×10^4 s[d], 5×10^5 s[d]
Altitude Domain		
Thickness of Altitude Level	200 m	
Total Altitude Levels	300	
Size Domain		
Mass Ratio Between Bins	2	
Number of Bins	45	
Smallest Bin Size	1.3 nm	
Photochemical CN Size	10.4 nm[e]	
Initial Conditions		
Meteoric Dust	0 cm^{-3}	
Photochemical CNs	0 cm^{-3}	
Sulfuric Acid Vapor	0 ppm	
Boundary Conditions		
Meteoric Dust (Top)	Zero Flux	
Photochemical CNs (Top)	Zero Flux	
Sulfuric Acid Vapor (Top)	Zero Flux	
Meteoric Dust (Bottom)	0 cm^{-3}	
Photochemical CNs (Bottom)[f]	40 cm^{-3}	
Sulfuric Acid Vapor (Bottom)	3 ppm	
Wind Speed	0 cm s^{-1}	Figure 2.6[d]

[a] Value at 300 K. Viscosity dependence on temperature is calculated using Sutherland's equation and parameters from White (1974).

[b] Value for a flat surface at ~60 km, where temperature ~260 K and sulfuric acid weight percentage of sulfuric acid droplets ~80%.

[c] See §2.4.3.

[d] For transient wind tests (§2.3.6 and §2.4.4).

[e] We use 10.4 nm instead of 10 nm as 10.4 nm corresponds to the radius represented by one of the discrete size bins in our model (bin 10).

[f] These photochemical CNs have radius ~0.17 μm, consistent with the mean size of the particles at ~40 km observed by Pioneer Venus LCPS (Knollenberg and Hunten, 1980).

mura and Hashimoto (2001), which only had the smallest particle size bin allocated to involatile particles.

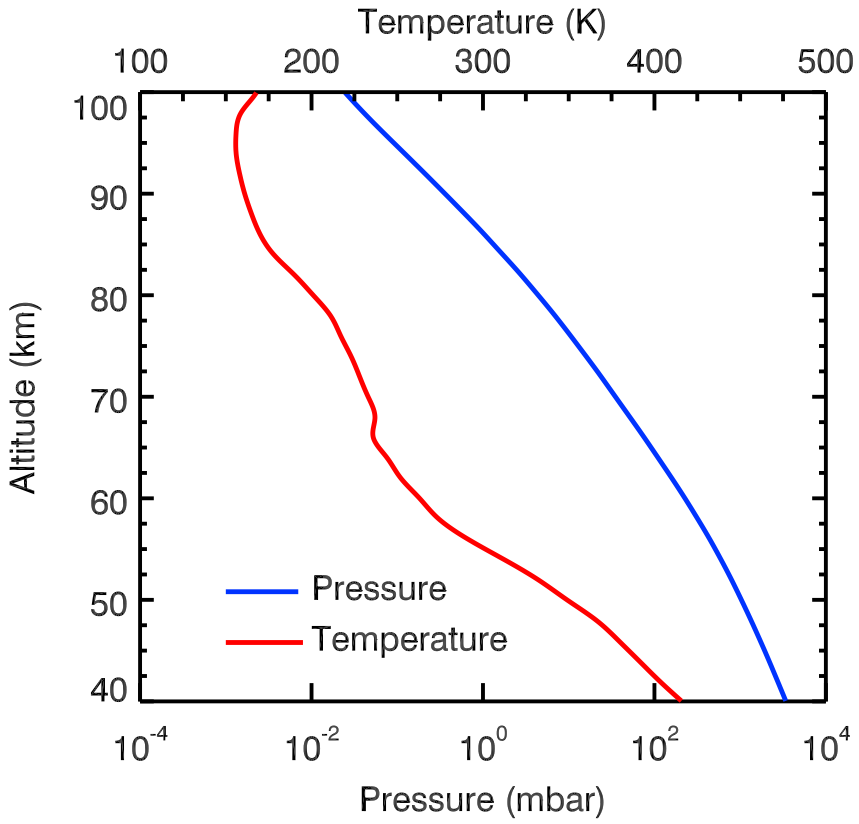

Figure 2.1: Model temperature (rectangles) and pressure (short lines) profiles taken from the Venus International Reference Atmosphere (Seiff, Schofield, et al., 1985).

Figure 2.1 shows the temperature and pressure profiles used (Seiff, Schofield, et al., 1985), which were fixed in the model. This is a simplification, as episodic increases in the temperatures of the Venus upper mesosphere and lower thermosphere have been known to exist since they were first observed by Clancy and Muhleman (1991). Such temperature increases have also been seen more recently by the Venus Express SPICAV and SOIR instruments (Bertaux et al., 2007) and the VeRa experiment (Tellmann et al., 2009). An increase in temperatures will suppress H_2SO_4 aerosol formation and enhance particle evaporation near the top of the domain studied here. These temperature fluctuations will have little direct impact on the particle populations at lower altitudes, but may indicate the presence of substantial changes in the dynamics of the mesosphere, which could affect particle transport.

The production rates of sulfur and sulfuric acid depend on the chemical pathways that lead to their production. Imamura and Hashimoto (2001) used

$$3SO_2 + 2H_2O \longrightarrow S + 2H_2SO_4 \qquad [R2.1]$$

(Yung and DeMore, 1982; Krasnopolsky and Parshev, 1983) as their primary reaction. However, Yung and DeMore (1982) suggests that the main scheme for production of sulfuric acid is actually

$$SO_2 + 1/2O_2 + 2H_2O \longrightarrow H_2SO_4, \qquad [R2.2]$$

where the sulfur produced during the reaction is converted to SO via reaction with O_2, though their model still shows a net production of S. Furthermore, [R2.1] is derived from Model A of Yung and DeMore (1982), which is more appropriate for a Venus early in its evolution than the current Venus. Meanwhile, Krasnopolsky and Parshev (1983) note that the reaction that would normally generate S, SO + SO, could also go on to produce S_2O instead. All of these considerations suggest that the production rate of S is likely to be lower than half the production rate of sulfuric acid, as suggested by [R2.1]. On the other hand, Yung and DeMore (1982) also showed that polysulfur can be produced and that sulfuric acid production ([R2.2]) can be suppressed via $(SO)_2$ dimer chemistry, while Toon, Turco, and Pollack (1982) suggested that the primary reaction can switch between [R2.1] and [R2.2] depending on the local O_2 content, which may be variable. Therefore, it is uncertain what the sulfur production rate actually is. For simplicity, we will use [R2.1] as a basis for the production of sulfuric acid and sulfur, but we will also test the effect of decreasing the sulfur production rate (see §2.4.3).

We begin each model run with no model-relevant species in the model box, e.g. no sulfuric acid vapor or condensation nuclei of any kind. As each model run progresses, mass is injected into the model atmosphere in the form of sulfuric acid vapor and involatile condensation nuclei. The latter is split into two populations, one corresponding to photochemical products (sulfur), and one corresponding to meteoric dust. Here, we assume a density of 1.9 g cm^{-3} for the condensation nuclei, as an average between the density of sulfur (1.8 g cm^{-3}, Imamura and Hashimoto, 2001) and meteoric dust (2.0 g cm^{-3}, Hunten, Turco, and Toon, 1980). We use the same production profiles of sulfuric acid vapor and photochemical condensation

nuclei as Imamura and Hashimoto (2001) for the production rates $P_{H_2SO_4}$ and P_{CN}, respectively:

$$P_{H_2SO_4} = \Phi_p g(z) \quad \text{cm}^{-3}\,\text{s}^{-1}, \tag{2.1}$$

$$P_{CN} = \frac{1}{2}\Phi_p g(z)\left(\frac{\rho_{CN}}{M_s}\frac{4}{3}\pi r_{CN}^3\right)^{-1} \quad \text{cm}^{-3}\,\text{s}^{-1}, \tag{2.2}$$

where Φ_p is the column-integrated production rate of sulfuric acid vapor; the function $g(z)$ is a Gaussian with a peak at 61 km altitude and full-width-half-max of 2 km such that

$$\int_0^\infty g(z)dz = 1, \tag{2.3}$$

ρ_{CN} is the density of the condensation nuclei, 1.9 g cm^{-3}; r_{CN} is the radius of the condensation nuclei; and M_s is the mass of a sulfur atom, 5.34×10^{-23} g. Our results showed that agreement between model and data was best if Φ_p was decreased from the nominal value of Imamura and Hashimoto (2001) of 10^{12} cm^{-2} s^{-1} to 6×10^{11} cm^{-2} s^{-1}, consistent with the suppression of the sulfuric acid production rate discussed in Yung and DeMore (1982). Our nominal production profiles are plotted in Figure 2.2.

The exact mechanics of how sulfuric acid nucleates onto condensation nuclei is not well understood and this is made worse by the complexities of the chemistry in the Venus atmosphere. As previously stated, we assume that the photochemical condensation nuclei are made of sulfur, similar to the strategy of Imamura and Hashimoto (2001). However, this is a simplification, as sulfur would likely exist in the form of polysulfur in the Venus clouds. Polysulfur would also undergo the processes of nucleation, condensation, and evaporation similar to sulfuric acid aerosols (Toon, Turco, and Pollack, 1982), with the only difference being that the polysulfur aerosols would likely be solid at the temperatures of the upper cloud (Lyons, 2008; Zhang, Liang, F. P. Mills, et al., 2012) and therefore would not coagulate as efficiently as liquid aerosol droplets. Furthermore, as sulfuric acid cannot actually wet sulfur (Young, 1983), polysulfur cannot act as condensation nuclei in the sense that they form cores that are completely encased within a layer of sulfuric acid. Instead, it is more likely that sulfuric acid will only condense on a fraction of the total surface of a polysulfur particle, and it is this small "drop" of condensed acid that then acts as the nucleation site for more sulfuric acid. Thus, the actual particles would be

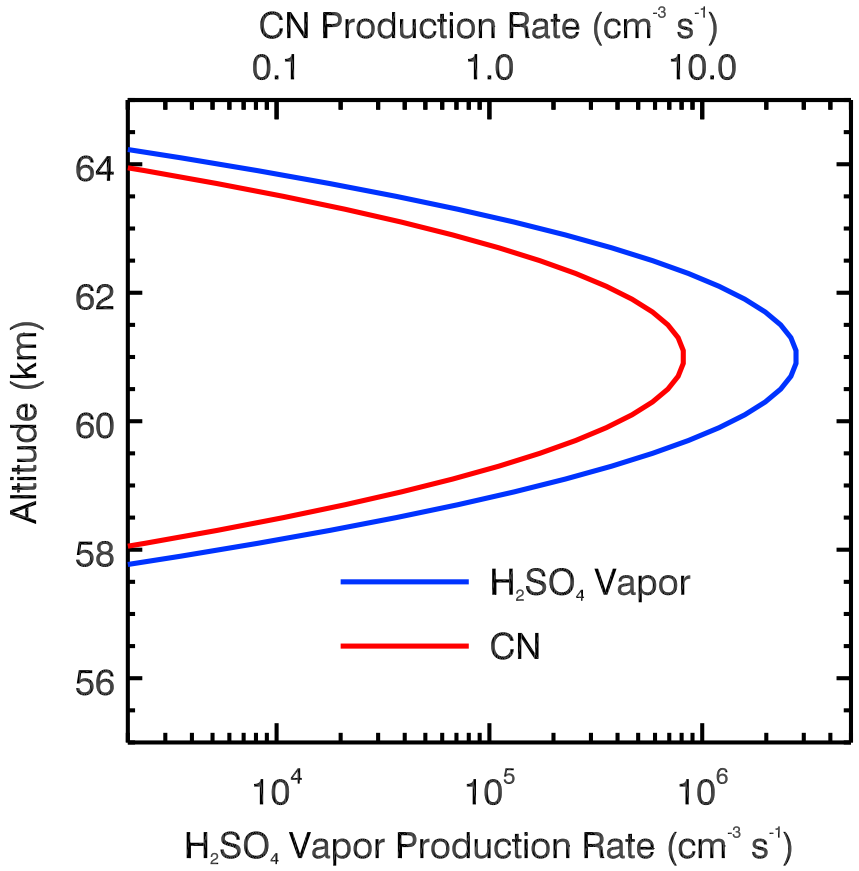

Figure 2.2: Model production rate profiles for sulfuric acid vapor (short lines) and photochemical condensation nuclei (rectangles), based on that of Imamura and Hashimoto (2001) with the peak rates adjusted to fit LCPS data.

made up of a polysulfur particle stuck to the side of a droplet of sulfuric acid, with part of the polysulfur particle exposed to the atmosphere. As Young (1983) elucidates, this has the effect of decreasing the efficiency of coagulation in the growth of these sulfuric acid aerosols, as now part of the surface is covered by polysulfur and will not be able to participate in coagulation. In addition, as coagulation occurs, more of the sulfuric acid particle's surface area will be covered by polysulfur (from particles it coagulated with), further decreasing its coagulation rate. This has the effect of eventually stopping coagulation altogether when the particle reaches a radius of $\sim$10 μm. While our model does not distinguish whether the polysulfur "core" is within the sulfuric acid or attached to its side, it does assume, for coagulation, that the entire surface is "available". We will discuss the effect of this in §2.4.1.

Further complicating the picture is the process opposite to the one we are modeling: the nucleation of polysulfur onto sulfuric acid particles (Young, 1983; Lyons,

2008). Whether one process dominates the other is determined by which particles homogeneously nucleates, i.e. which one appears "first" to act as the condensation nuclei for the other. In this case, as the saturation vapor pressure of most species of S_x is an order of magnitude or more lower than that of sulfuric acid in the cloud top region (Young, 1983; Lyons, 2008), we can safely assume that polysulfur will homogeneously nucleate before sulfuric acid does so as to act as its condensation nuclei and that we may ignore the opposite process. However, future studies should take into account the aerosol physics of the polysulfur nuclei to investigate its effects on the cloud distribution.

In our model, nucleation of sulfuric acid vapor onto the polysulfur condensation nuclei occurs when the ambient sulfuric acid vapor concentration reaches a critical supersaturation. This is determined by the sulfuric acid weight percent of the liquid that would form upon condensation (see §2.3.2) and the curvature of the surface on which the vapor will condense. That is, we assume that the accommodation coefficient is unity. The curvature effect is determined by the Kelvin equation (Seinfeld and Pandis, 2006):

$$\ln \frac{p}{p_o} = \frac{2\gamma M}{\rho r RT}. \tag{2.4}$$

For our case, p_o is the saturation vapor pressure over a flat surface; p is the saturation vapor pressure over a surface with curvature r; γ, M, and ρ are the surface tension, molar mass, and density of sulfuric acid, respectively; R is the universal gas constant; and T is the temperature. For reasonable values of these parameters corresponding to ~61 km in the Venus atmosphere, where we use the parameterization of M. J. Mills (1996) for the surface tension, we find that the actual saturation vapor pressure over condensation nuclei becomes an order of magnitude greater than the saturation vapor pressure over a flat surface when the radius of the particle is ~2 nm. However, given Eq. 2.1, it will take on the order of hours for the sulfuric acid to build to such concentrations, during which time the polysulfur condensation nuclei will also be growing, thus increasing its radius of curvature and decreasing the saturation vapor pressure over its surface. Therefore, there may exist an equilibrium point where the sulfuric acid concentration is just high enough to begin nucleation onto the growing polysulfur particles. The calculation of this equilibrium point is beyond the scope of this work, however, as our knowledge of the kinetics of sulfur reactions is poor and thus we have ignored all microphysics (nucleation, condensation, coagulation) associated with the condensation nuclei. Therefore, we will

make a simplification and assign a radius of ∼10 nm to the polysulfur condensation nuclei that are injected into the model. Toon, Turco, and Pollack (1982) simulated the microphysics of sulfur particles, but did not take into account the effects of background sulfuric acid vapor or nucleation of said vapor on the sulfur particles. It would be ideal to combine these processes to create a more complete picture of the Venus clouds and hazes.

We adopt similar lower boundary conditions as those of Imamura and Hashimoto (2001), where involatile (sulfur) particles of size ∼0.17 μm (mode 1) are fixed to have a number density of 40 cm^{-3} in accordance with LCPS data (Knollenberg and Hunten, 1980). We set the mixing ratio of H_2SO_4 to be 3 ppm at the lower boundary, within the 0–4 ppm estimates from analysis of Magellan radio occultation observations by Kolodner and Steffes (1998). We adopt a zero flux boundary condition for the top boundary, as we assume that no particles or H_2SO_4 vapor escape the mesosphere above 100 km.

2.3.2 Thermodynamics of H_2SO_4

Of particular importance in this model is the treatment of certain thermodynamic properties of H_2SO_4, such as its saturation vapor pressure and surface tension. Both of these quantities control whether a sulfuric acid droplet is growing by condensation or evaporating.

The saturation vapor pressure $p_{H_2SO_4}$, in units of atm, is calculated via the equation of Ayers, Gillett, and Gras (1980), modified by Kulmala and Laaksonen (1990):

$$\ln p_{H_2SO_4} = \ln p^0_{H_2SO_4} + 10156 \left[-\frac{1}{T} + \frac{1}{T_0} + \frac{0.38}{T_c - T_0} \left(1 + \ln \frac{T_0}{T} - \frac{T_0}{T} \right) \right] - \frac{H}{RT}, \quad (2.5)$$

where $T_0 = 340$ K is a reference temperature, $T_c = 905$ K is the critical temperature, $p^0_{H_2SO_4}$ is a reference pressure given by:

$$\ln p^0_{H_2SO_4} = -\frac{10156}{T_0} + 16.259, \quad (2.6)$$

and H is the enthalpy associated with the mixing of water and sulfuric acid, given by the parameterization of Giauque et al. (1959):

$$H = 4.184{\times}10^7 \left[23624.8 - \frac{1.14208 \times 10^8}{4798.69 + (W_{H_2SO_4} - 105.315)^2} \right] \quad \text{erg mol}^{-1}, \quad (2.7)$$

where $W_{H_2SO_4}$ is the weight percentage of H_2SO_4 in the aerosol droplet calculated from Tabazadeh et al. (1997) as a parameterization to temperature and background water vapor concentration.

The surface tension is derived from data collected by Sabinina and Turpugow (1935) parameterized linearly with respect to temperature by M. J. Mills (1996). The value of the surface tension at ~61 km is given in Table 2.1.

2.3.3 Water Vapor Profile

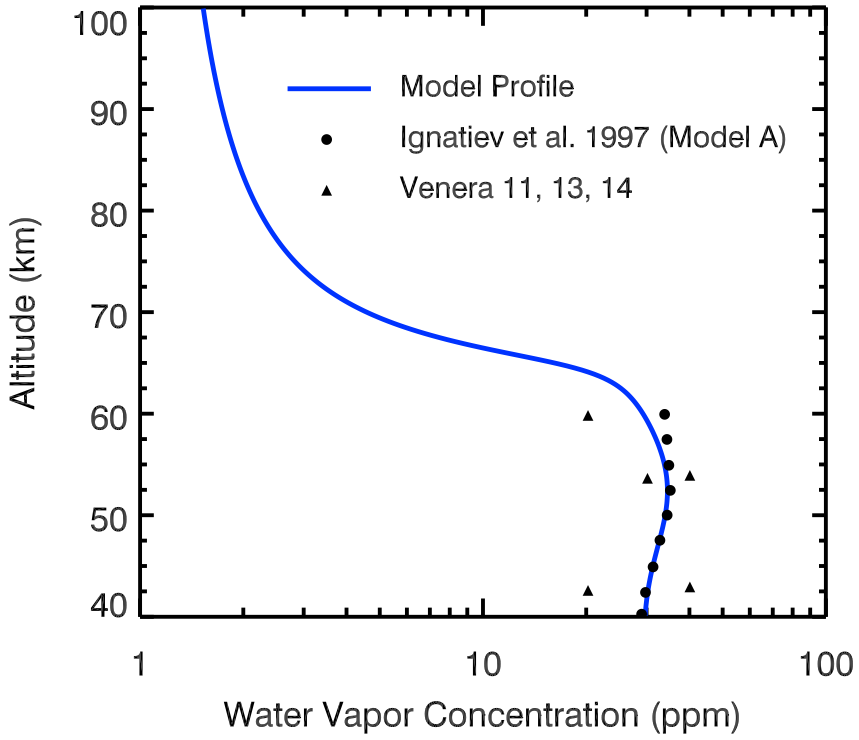

Figure 2.3: Model water vapor profile (rectangles) plotted with the Model A (filled circles) and Venera 11, 13, and 14 data (triangles) from Ignatiev et al. (1997). The water vapor concentration in the upper haze is taken to be ~1 ppm from observations by Bertaux et al. (2007).

The base CARMA model does not treat the exchange of water between the background water vapor concentration and the water taken up in the sulfuric acid cloud particles as they grow. Instead, the weight percentage of water and sulfuric acid is always such that there is equilibrium between the particle and the background water vapor concentration. In other words, the model assumes the equilibrium aerosol growth regime (Zhang, Pandis, and Seinfeld, 2012). However, this may not necessary be true given the low water vapor concentration in the Venus atmosphere (Ignatiev et al., 1997). Therefore, we will assume an equilibrium background water

vapor profile that is fixed in time. Figure 2.3 shows this profile. Above 60 km, we assume a water vapor concentration of ~1 ppm in accordance with observations by Bertaux et al. (2007). Below 60 km, we model our profile after Model A of Ignatiev et al. (1997) and data from Venera 11, 13, and 14 (also taken from Ignatiev et al., 1997). The profile is empirically determined using an arctangent function to connect the region above 60 km to the region below, and a Gaussian function to take into account the water vapor concentration maximum at ~53 km in Model A of Ignatiev et al. (1997). The formula for the water vapor mixing ratio, f_{H_2O}, is then

$$f_{H_2SO_4} = 6\exp\left[-\left(\frac{z-52}{8}\right)^2\right] - 14.5\left(\frac{2}{\pi}\right)\tan^{-1}(0.5z - 32.5) + 15.5 \quad ppm, \quad (2.8)$$

where z is in kilometers.

2.3.4 Eddy Diffusion

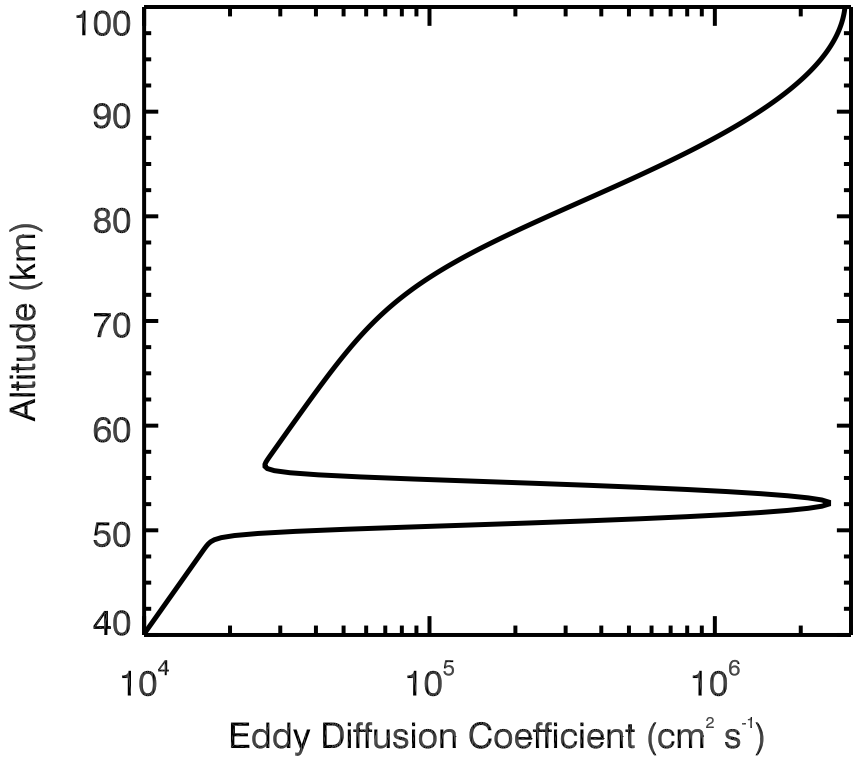

Figure 2.4: Model eddy diffusion coefficient profile, with the 40–70 km section based on Imamura and Hashimoto (2001), and the 70–100 km section based on Krasnopolsky (1983).

The eddy diffusion coefficient profile is shown in Figure 2.4. The values between 40 and 70 km altitude are approximated from Imamura and Hashimoto (2001) by

fitting a function consisting of the sum of an exponential and a Gaussian function. The large increase in eddy diffusion coefficient at ~53 km simulates the convective overturning present in the middle cloud as inferred from Schubert et al. (1980) and measured in situ by the VEGA Balloons (Ingersoll, Crisp, and VEGA Balloon Science Team., 1987; Crisp, Ingersoll, et al., 1990). The eddy diffusion coefficient above 70 km is approximated as a Gaussian from Figure 11 of Krasnopolsky (1983), which itself is generated from continuity arguments with respect to the aerosol distribution observed in this region at the time. The empirical formula of the eddy diffusion coefficient, K_{zz} , as a function of altitude z in kilometers above 40 km is then:

$$K_{zz} = 10^{\frac{4z-160}{38.55}} + 2500000 \left\{ \exp\left[-\left(\frac{z-52.5}{1.201} \right)^2 \right] + \exp\left[-\left(\frac{z-100}{12.01} \right)^2 \right] \right\} \quad \mathrm{cm^2\,s^{-1}}. \tag{2.9}$$

2.3.5 Meteoric Dust

Turco, Toon, et al. (1983) discussed the properties of meteoric dust in the Venus atmosphere and concluded that it is similar to meteoric dust in the atmosphere of Earth and could act as condensation nuclei to water vapor, forming thin ice hazes. We propose that meteoric dust could also serve as condensation nuclei to sulfuric acid vapor, as its saturation vapor pressure is extremely low at the altitude of the UH, on the order of 10^{-19} mbars for pure sulfuric acid, and 10^{-31} mbars for a water-sulfuric acid mixture with 75 wt% sulfuric acid (Kulmala and Laaksonen, 1990) that is typical of the UH (Kawabata et al., 1980). Thus, any sulfuric acid vapor that is lofted into the UH by diffusion or winds could potentially condense on the meteoric dust present in this region.

The Kelvin effect may play a large role in limiting the efficiency of meteoric dust as condensation nuclei due to their small size. However, if we use the appropriate values for sulfuric acid in the UH and a typical condensation nuclei size of 1.3 nm (Kalashnikova et al., 2000), then Eq. 2.4 yields an approximate increase of 2.4 orders of magnitude in the saturation vapor pressure. This gives a resulting saturation vapor pressure of $\sim 10^{-29}$–10^{-28} mbars, which is far less than recent upper limits on the abundance of H_2SO_4 in the UH, e.g. 3 ppb, or about 3×10^{-9} mbar at 80 km, from Sandor, Clancy, and Moriarty-Schieven (2012). Therefore, meteoric dust should act as very efficient condensation nuclei as long as the actual H_2SO_4

mixing ratio is not significantly lower than this upper limit, even if the Kelvin effect is considered.

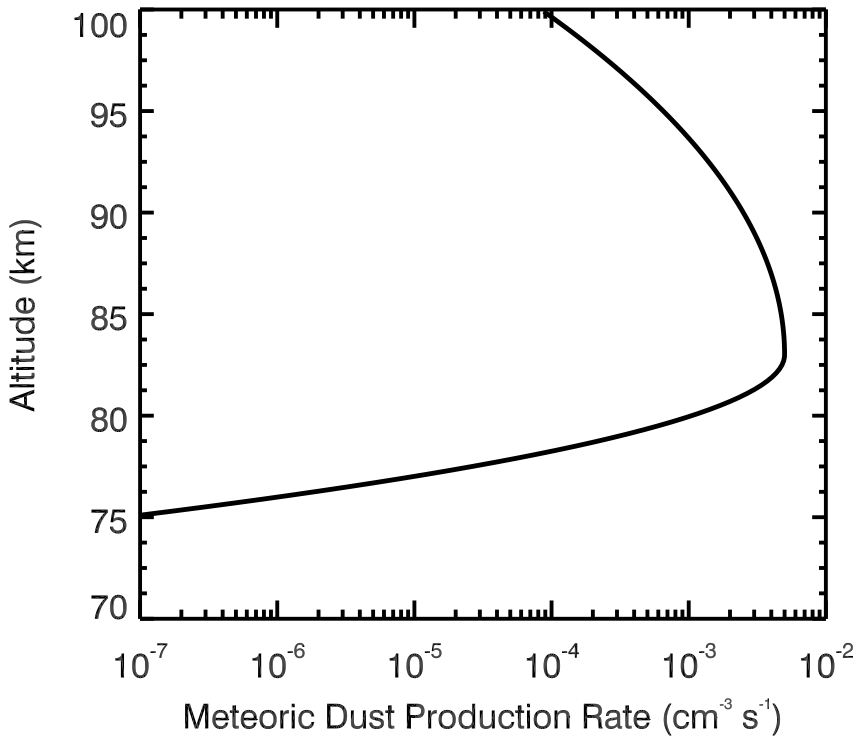

Figure 2.5: Model meteoric dust production rate profile, based on Kalashnikova et al. (2000), normalized to 1.3 nm particles, and shifted down from the original distribution by 4 km in order for the maximum of this profile to match that of the number density profile of the small mode particles in the UH, as retrieved from solar occultation data by Wilquet, Fedorova, et al. (2009).

Meteoric dust is treated in the same way in our model as the sulfur condensation nuclei. However, it is clear that meteoric dust, which is typically made of silicates (Hunten, Turco, and Toon, 1980), may react differently to sulfuric acid than sulfur. For example, Saunders et al. (2012) showed that silicates dissolve in sulfuric acid on a timescale of an Earth week at the temperatures of the cloud tops. However, once the sulfuric acid droplet becomes much larger than the nucleus it condensed on, the dissolution of said nucleus should have very little effect on the rest of the particle. The production profile of meteoric dust we use in our model is shown in Figure 2.5 as an empirical approximation of the profile calculated by Kalashnikova et al. (2000). All meteoric dust particles are assumed to have a radius of 1.3 nm. We have shifted the profile maximum from 87 km to 83 km in order to match the maximum in the small mode curve in Figure 9 of Wilquet, Fedorova, et al. (2009). The parameterization of the profile is given by

$$P_{md} = 5 \times 10^{-3} e^{-\left(\frac{z-83}{2.402}\right)^2} \quad \mathrm{cm}^{-3}\,\mathrm{s}^{-1}, \tag{2.10}$$

below 83 km altitude, and

$$P_{md} = 5 \times 10^{-3} e^{-\left(\frac{z-83}{8.407}\right)^2} \quad \mathrm{cm}^{-3}\,\mathrm{s}^{-1}, \tag{2.11}$$

above 83 km. z has units of km.

Though this profile was applied to Earth only, we will assume that it is also applicable to Venus due to the two planets' similarities. However, if atmospheric density is the determining factor of the altitude of peak meteoric dust ablation (e.g. Gadsden, 1968) then our profile may be too low in the atmosphere. This is due to the fact that the altitude on Venus with the same atmospheric density as that of the peak ablation altitude on Earth is actually ~110 km.

2.3.6 Winds

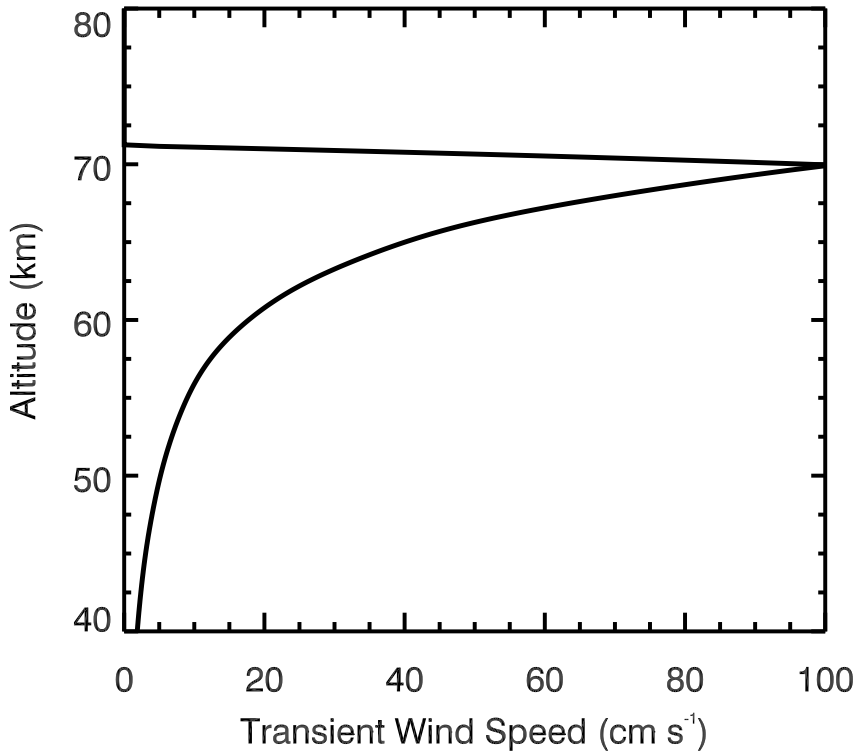

Figure 2.6: Model wind speed profile with the portion below 70 km taken from Imamura and Hashimoto (2001), and the cut-off above 70 km representing the turning over of the upwelling.

In addition to testing the effects of the nucleation of sulfuric acid droplets on meteoric dust on the UH particle size distribution, we will also test the effects of transient gusts at the cloud tops. These are a separate set of simulations from the nominal runs described in §2.3.1, though they do use the results of the nominal runs as initial conditions. Figure 2.6 shows the wind profile we use to test the effects of transient upward winds on the number density and size distribution of the cloud and haze aerosols. The wind beneath 70 km is a constant flux wind similar to that of Imamura and Hashimoto (2001) but increased in strength by two orders of magnitude to simulate a gust as opposed to a branch of the global circulation:

$$w = \frac{8 \times 10^{-3}}{\rho} \quad \mathrm{cm\,s^{-1}}, \tag{2.12}$$

where w is upward wind speed and ρ is atmospheric density, both in cgs units. In order to adhere to our top boundary condition and simulate turning over of the wind currents, we allow the upward wind to fall off linearly above 70 km so that it vanishes at 75 km. This is consistent with the strong static stability above that altitude.

Recent Venus Express observations of the Venus southern polar vortex at the altitude of the upper cloud (63–69 km) show divergent and convergent circulations that imply vertical velocities of ∼0.2 m s^{-1} (Garate-Lopez et al., 2013), roughly consistent with the lower limits of our upper cloud wind velocities, though most of the vertical motions were downward rather than upward. In addition, convective cells at the cloud tops have been observed at and downwind of the Venus subsolar point (Belton et al., 1976; Titov et al., 2012). These have been interpreted using 2D convection simulations as the incursion of the convective region in the middle cloud into the stably stratified upper cloud (Baker, Schubert, and Jones, 1998; Baker, Schubert, and Jones, 1999), though some recent observations suggest that the convective layer is thin enough that it may only occupy the upper cloud itself (Markiewicz et al., 2007). The results of Baker, Schubert, and Jones (1998) suggest that gravity waves originating from the enlarged convective region could produce vertical velocities of 1–2 m s^{-1} at and above 60 km, matching our wind velocities at those altitudes.

Nevertheless, there are clear differences between our vertical advection scheme and the actual advection processes in the Venus clouds. For instance, a realistic treatment of the gust "turning over" above 70 km requires horizontal transport, which

is beyond the scope of this study. Thus, for the purpose of this work we will only examine qualitatively the effects of such a gust on the cloud profile, such as the formation of a detached haze due to upwelled cloud particles, its destruction due to sedimentation and diffusion, the time scales involved, and the changes in particle size distributions. In order to better evaluate these effects, we will magnify them by considering gusts that last for 5×10^4 seconds, or ~14 Earth hours. Gusts in the polar vortex may last as long, though as Venus Express orbits Venus on the same time scale (~1 Earth day), the actual duration is uncertain. Winds caused by subsolar point convection may also be able to last 14 hours, as convective features were seen up to 50° latitude away from the equator (Titov et al., 2012). This should also apply to longitude, and a distance of 50° longitude away from the subsolar point can be covered by the ~100 m s^{-1} planet-encircling zonal winds at the cloud tops (Schubert et al., 1980) in about 14 hours. In other words, each parcel of air could have 14 hours during which gusts arising from subsolar convection can disrupt the aerosol particle distributions therein before the convective cells give way to stably stratified regions. Nevertheless, not only is the wind unlikely to be constant given the turbulent nature of its origin, but Wilquet, Fedorova, et al. (2009) observed the haze at ~ 50°, a full 20° latitude away from the convective region. In short, we are not looking for exact agreement between our particle number density and size distributions and one that is retrieved from observations, but rather whether we can qualitatively reproduce the chaotic behavior of the UH.

2.4 Results & Discussion

Our steady state results do not show a stable equilibrium distribution, but rather a quasi-periodically varying distribution. Thus, we will proceed to compare to observations our results from a single time step near the end of our nominal model run that best match them (§2.4.1), and then describe the mechanisms that could allow for such dynamics to occur despite a constant background atmospheric state (§2.4.2). In §2.4.3 we discuss the effect of decreasing the sulfur production rate, and in §2.4.4 we will describe our transient wind results.

2.4.1 Nominal Results

Figure 2.7 shows the number density predictions from our model for particles with radii greater than ~0.1 μm, which we choose as the lower size boundary of mode 1/small mode particles (Wilquet, Fedorova, et al., 2009). We see that it is largely consistent with LCPS cloud data (Knollenberg and Hunten, 1980), though the mid-

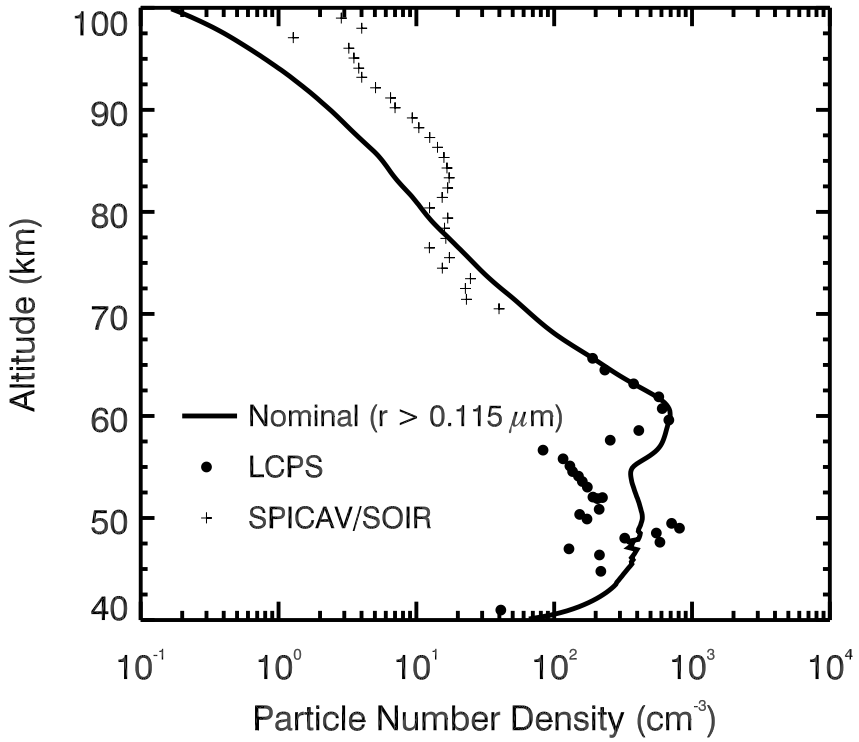

Figure 2.7: Number density of cloud and haze particles with radius r > 0.115 μm (solid line) from the nominal model compared to total number density data from LCPS (filled circles) (Knollenberg and Hunten 1980) and Venus Express (pluses) (Wilquet, Fedorova, et al. 2009).

dle cloud is overestimated by a factor of 3 and the lower cloud is underestimated by a factor of <2. These differences are well within the range of variability seen at these levels by the Pioneer Venus entry probes (Esposito et al., 1983), or in near infrared observations of the Venus night side (Crisp, Ingersoll, et al., 1990; Grinspoon et al., 1993). Figure 2.8 shows the size distributions of the cloud and haze particles at various altitudes. It reproduces both the high number density of mode 1 particles in the upper cloud and the distinct multi-modal nature of the middle and lower clouds' particle size distributions as seen by Pioneer Venus (Knollenberg and Hunten, 1980), including mode 1 at ~0.2 μm, mode 2 at ~1.4 μm, and mode 3 (near the cloud base) at ~3.5 μm. Comparison of this size distribution with Pioneer Venus observations at 54.2 km (Knollenberg and Hunten, 1980) shows clear agreement between the model mode radii and that of the data, though a discrepancy exists in the mode abundances, as there is an order of magnitude less mode 3 particles and ~3 times more mode 2 particles in our model than in the observations. These discrepancies could be caused by the lack of transient gusts in the middle and lower clouds

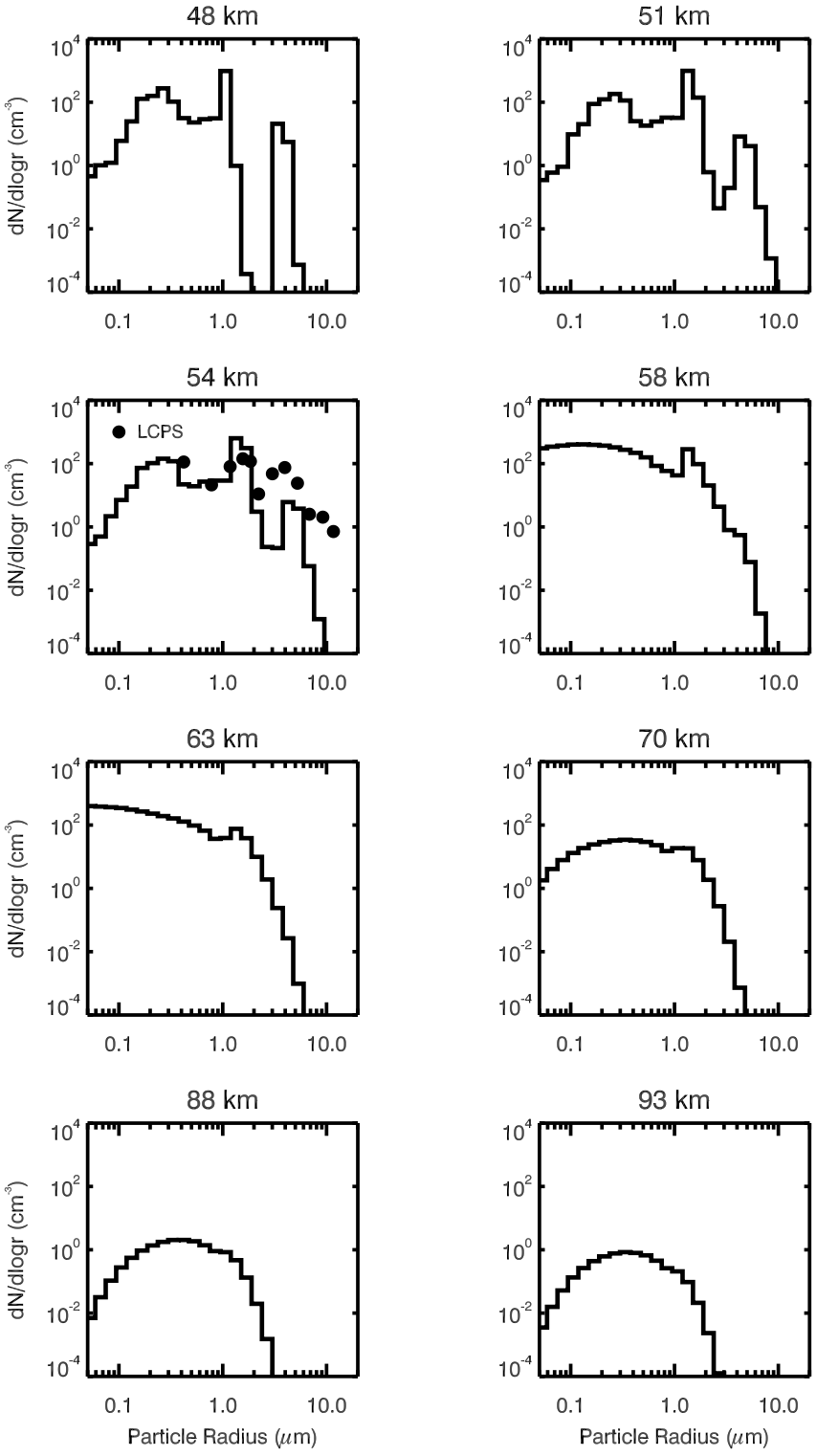

Figure 2.8: Particle size distributions at various altitudes from the nominal model. LCPS size data at 54.2 km (dots) (Knollenberg and Hunten 1980) is plotted for comparison.

of our steady state model, which Imamura and Hashimoto (2001) showed could be used to produce a multi-modal structure in their model. Physically, vertical gusts such as those detected in the middle cloud by the VEGA balloons (Crisp, Ingersoll, et al., 1990) would both aid in the growth of mode 2 particles into mode 3 particles by introducing "fresh" sulfuric acid from below (updrafts) and in the depletion of the middle cloud by downwelling the cloud particles (downdrafts); the depletion of the middle cloud is also a natural consequence of the growth of particles, as these larger particles would have a faster sedimentation time. Therefore, a series of vertical updrafts and downdrafts could lead to fewer mode 2 particles, more mode 3 particles, and fewer particles in the middle cloud, resulting in better agreement with data.

We assume that mode 3 particles are just larger versions of mode 2 particles, i.e. they are liquid sulfuric acid droplets with a solid polysulfur component, but this need not be the case. In fact, (Knollenberg and Hunten, 1980) discussed the possibility that mode 3 is made up of solid, crystalline particles. On the other hand, Toon, Ragent, et al. (1984) suggested that mode 3 is in fact a large particle tail of mode 2; our results support this latter interpretation, as the mode 3 particle peak blends into the mode 2 peak somewhere between 54 and 58 km (Figure 2.8). In light of the results of Young (1983), however, we must consider the effect of solid polysulfur "patches" on the surface of our sulfuric acid particles, which may make them seem like solid, crystalline particles if the polysulfur coverage is high enough. As previously stated, the effect of these patches is the decrease in the efficiency of coagulation in the removal of smaller particles, creating a smaller number of larger particles. This could explain our underestimation of the lower cloud particle number density, though it would also further overestimate our middle cloud particle number density. Thus, a combination of decreased coagulation efficiency in larger particles and the addition of middle cloud vertical gusts may be necessary to improve our model's agreement with the Pioneer Venus Sounder Probe observations.

In the UH, our model predicts a steady state size distribution that is roughly monomodal, with a small "bump" at radii > 1 μm corresponding to upwelled mode 2 particles that is largely insignificant compared to the rest of the distribution. The lack of distinct bimodality despite the two different sources of particles is likely due to the effects of coagulation. In Figure 2.9, we follow the time evolution of the upper haze at an altitude of 84 km during the first $\sim$4 months of the model run, long before steady state is reached. The green "bar" at 0.01 μm is caused by

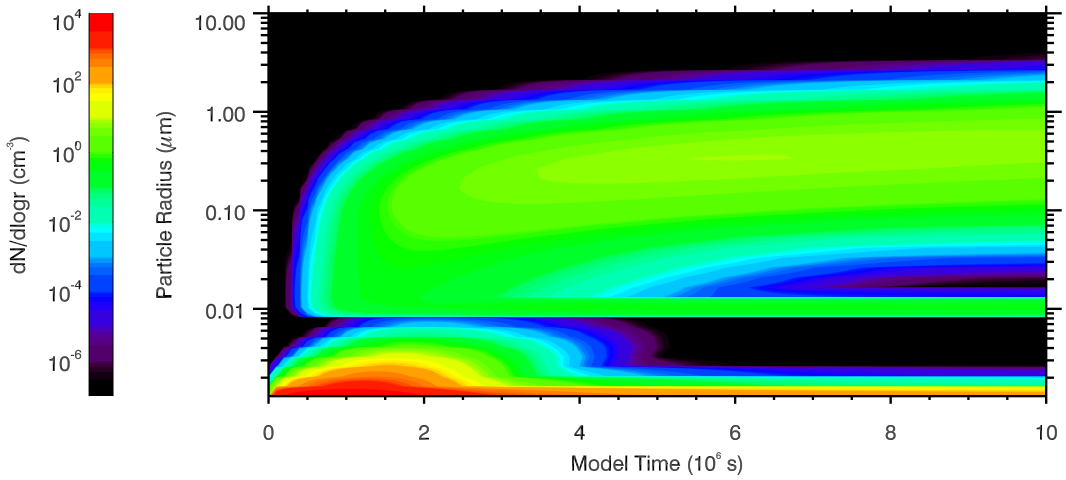

Figure 2.9: Time evolution of the UH particle size distribution at 84 km at the beginning of the nominal model run, from t = 0 to t = 10^7 s. The green "bar" at 10 nm is a result of the artificial injection of 10 nm particles into the model domain as photochemical condensation nuclei and should be ignored. The black regions represent parts of the phase space where $dN/dLnr < 10^{-7}$ cm^{-3}.

the artificial injection of 10 nm photochemical condensation nuclei into the model domain and should be ignored. Immediately after the start of the simulation, a haze population emerges with particle radii < 10 nm. Such small particles could have only resulted from the nucleation of sulfuric acid onto meteoric dust and subsequent condensational growth. Cloud droplets reach 84 km one week later due to upward diffusion, which is followed by the disappearance of the original meteoric-dust-derived haze population about a month afterwards. This suggests a coagulation timescale of about a month to decrease the original population by about 2–3 orders of magnitude, if indeed coagulation is the cause of this result. We can test whether this is physically viable using the simplified solution to the discrete coagulation equation $N(t)$:

$$N(t) = \frac{N_0}{1 + t/\tau_c}, \tag{2.13}$$

where

$$\tau_c = \frac{2}{KN_0} \tag{2.14}$$

is a coagulation timescale. Here, N_0 is the original number density, and K is the coagulation kernel. For simplicity we use the continuum regime kernel, as particle

number density is small, and assume that the particle radii $R_2 \gg R_1$:

$$K \sim \frac{2kT}{3\mu}\frac{R_2}{R_1} \tag{2.15}$$

(Seinfeld and Pandis, 2006). For a Boltzmann's constant k = 1.38×10^{-16} erg K^{-1}, temperature T ~ 160 K, atmospheric viscosity $\mu \sim 8 \times 10^{-5}$ g cm^{-1} s^{-1} and particle radii R_1 = 1 nm and R_2 = 100 nm, we get a coagulation time needed to reduce the number density by ~2–3 orders of magnitude of a few months, similar to our model results. Therefore we can conclude that the UH is likely a combination of upwelled cloud particles and particles nucleated in situ on meteoric dust, but that the latter population has "fused" with the former, resulting in a mono-modal size distribution in steady state. Thus, two separate sources of particles—one upwelled from below, and one nucleated in situ cannot explain the bimodality detected by Kawabata et al. (1980) and Wilquet, Fedorova, et al. (2009). However, our peak model cloud top haze particle radius, ~0.3 μm at 70 km, is fairly close to the average haze particle radius originally detected by Kawabata et al. (1980) (0.23 ± 0.04 μm). Furthermore, our UH size distribution covers the size range of both the small and the large mode detected by Wilquet, Fedorova, et al. (2009). Therefore, we propose that our results represent both modes, and that something else is responsible for the splitting of the particle population into two distinct modes. Figure 2.7 shows a comparison between the model number density and the sum of the number densities of the two modes detected by Wilquet, Fedorova, et al. (2009). The agreement between model and data is satisfactory up to 80 km, above which the model underestimates the number density by about half an order of magnitude.

Alternatively, the meteoric dust production profile could be at a much higher altitude (see §2.3.5) such that they are above the upwelled cloud particles; the sulfuric acid droplets that nucleate onto these meteoric dust particles would then have time to grow before they sediment into the altitudes dominated by cloud droplets, with which they will coagulate as before. In this scenario, the small mode would consist of both the upwelled cloud particles and the sedimenting particles that nucleated in situ onto meteoric dust, while the larger mode would be made up of the products of small mode coagulation. However, the resulting smaller R_2/R_1 ratio (Eq. 2.15) would increase the coagulation time scale and decrease the amount of large mode particles that can be produced. Ultimately, the particles that nucleate from meteoric dust may be inconsequential due to the lower flux of meteoric dust as compared to the flux of sulfuric acid vapor and sulfur.

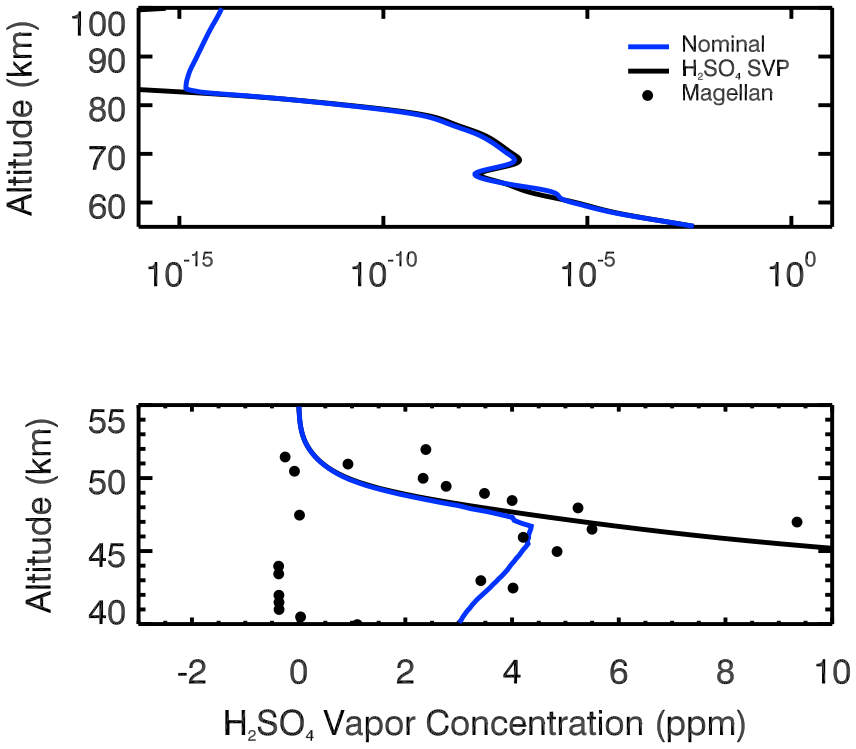

Figure 2.10: Sulfuric acid vapor mixing ratio from the nominal model (short lines) compared with the sulfuric acid saturation vapor pressure over a flat surface (solid) (§2.3.2) and Magellan radio occultation data analyzed by Kolodner and Steffes (1998) (filled circles).

Figure 2.10 shows a comparison between the predicted mixing ratio of sulfuric acid vapor and the observed mixing ratio from Magellan radio occultation data as analyzed by Kolodner and Steffes (1998). Though the large dispersion in the data from 0–6 ppm allows for a wide variety of results to "fit" it, the physically relevant results are likely those that exhibit a local sulfuric acid maximum below the clouds, and which also fit the nonzero data points. Indeed, our model results show a satisfactory fit to the data points. While the bottom boundary condition fixes the vapor concentration to 3 ppm at 40 km, the vapor concentration peak of ~4.5 ppm at the cloud base is entirely due to sedimenting particles evaporating and depositing their sulfuric acid vapor at that altitude. The peak value reflects a balance between the rate of vapor deposition and the upward and downward vapor diffusion, and also imposes a constraint on the altitude of the cloud base, below which any sulfuric acid droplets will be evaporating. Our results show that the cloud base is at ~47 km, consistent with the model results of Krasnopolsky and Pollack (1994). Above the cloud base, the vapor profile largely follows the saturation vapor pressure curve

except at (1) 61 km, where sulfuric acid vapor is photochemically produced, and (2) above 80 km. This latter deviation may be caused by numerical instabilities caused by the low saturation vapor pressure ($\sim 10^{-31}$ mbars) or the phase properties of sulfuric acid and water solutions in this region (McGouldrick, Toon, and Grinspoon, 2011).

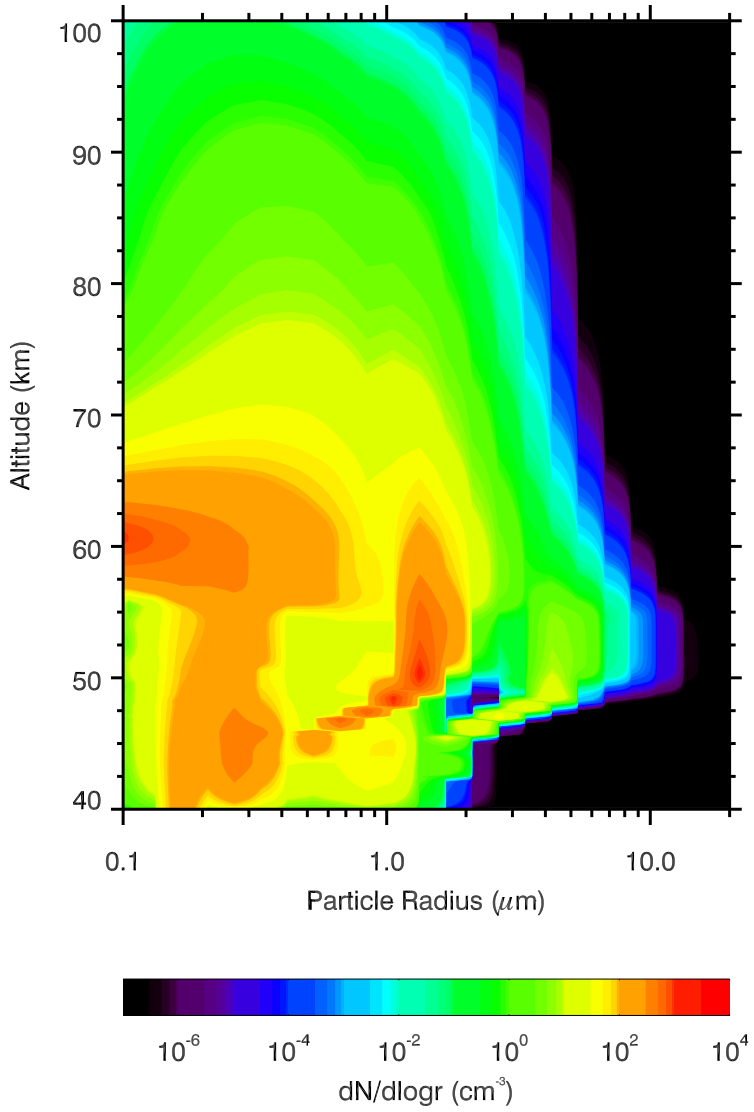

Figure 2.11: The nominal particle number density as a function of particle size and altitude. The black regions represent parts of the phase space where $dN/dlogr < 10^{-7}$ cm^{-3}.

Figure 2.11 shows number density as a function of both altitude and particle radius, while Figure 2.12 shows the sulfuric acid and particle mass fluxes for the middle cloud (top) and the other altitudes (bottom); together they give a summary of the processes occurring in the clouds and UH of Venus. The production of involatile

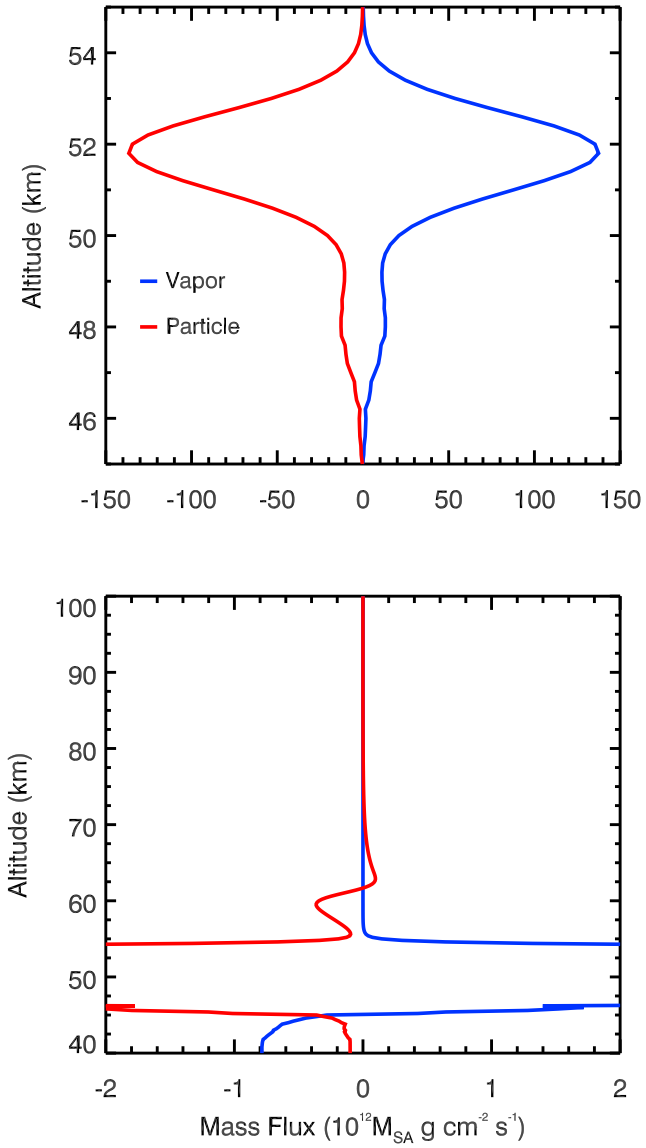

Figure 2.12: The nominal sulfuric acid vapor (dashes) and particle (short lines) mass fluxes at steady state at the same time step as in figures 7, 8, 10, and 11 expressed in units of mass equivalent to 10^12 sulfuric acid molecules per unit area per second, where each molecule has mass $M_{SA} \sim 1.6 \times 10^{-22}$ g. Note the different axes scales between the top and bottom panels: the top panel shows the high flux values of the middle cloud, while the bottom panel shows the lower flux values at the other altitudes.

sulfur condensation nuclei causes the nucleation and condensational growth of liquid sulfuric acid droplets at 61 km, resulting in a high number density of mode 1 particles. These particles then diffuse upwards and sediment downwards. The positive divergence in the particle flux (in units of mass equivalent to 10^{12} sulfuric acid molecules per unit area per second, where each molecule has mass $\sim 1.6 \times 10^{-22}$ g)

in this region is clearly shown by the positive slope at ~61 km in the lower panel of Figure 2.12—particles higher up has a smaller downward flux (i.e. a less negative flux) than the particles lower down. There is no corresponding slope in the vapor flux curve as all the vapor is condensing onto the particles. In the UH, the upward diffusion of particles appears to balance the sedimentation, leading to a near zero particle flux; the sulfuric acid vapor flux is also very close to zero, but it is likely due to the small amount of vapor at these altitudes.

Below 61 km, the vigorous convection in the middle cloud drives the large upward flux of sulfuric acid vapor (top panel of Figure 2.12), resulting in enhanced production of mode 2 particles as well as a tail of even larger particles resulting from coagulation. These particles, like the upper cloud particles, are transported downwards by sedimentation and upwards by diffusion. The latter process leads to a small large particle bump in the UH. These particles evaporate upon reaching the cloud base, leading to the regeneration of mode 1 particles and the deposition of sulfuric acid vapor beneath the clouds. The regenerated mode 1 is larger than the mode 1 of the upper cloud due to the coagulation of the droplets higher up in the clouds—the cores of these droplets are in effect added together, leading to the generation of larger involatile particles as the larger cores are exposed upon droplet evaporation. This may not be what actually happens if the "cores" are instead patches of polysulfur decorating the outside of the sulfuric acid droplets, as per the "gumdrop" model of Young (1983). In this case, the "cores" would not be added together and would remain the same size as their upper cloud counterparts upon the evaporation of the sulfuric acid. Meanwhile, the tail of large particles forms a distinct third mode upon evaporation due to its slower evaporation rate as compared to that of the smaller mode 2 particles, which is a product of the Kelvin effect (Eq. 2.4).

Below the clouds, the sulfuric acid vapor exhibits a negative flux as discussed previously, while the particle flux is similarly negative, as the particles are sedimenting out of the bottom of the model domain. The absolute value of the sum of the two fluxes at the bottom of the model domain is $\sim 9 \times 10^{11}$ cm^{-2} s^{-1}, slightly higher than the sum of the input flux of meteoric dust ($\sim 5 \times 10^{5}$ cm^{-2} s^{-1}), photochemical condensation nuclei ($\sim 10^{11}$ cm^{-2} s^{-1}), and sulfuric acid vapor ($6 \sim 10^{11}$ cm^{-2} s^{-1}). This is due to the quasi-periodically varying nature of our results, i.e. we have examined our simulated Venus cloud-haze system at a time when the flux out of the lower model boundary is higher than what it should be for a steady state ($\sim 6.835^{11}$ cm^{-2} s^{-1}).

2.4.2 Periodic Behavior and Precipitation on Venus

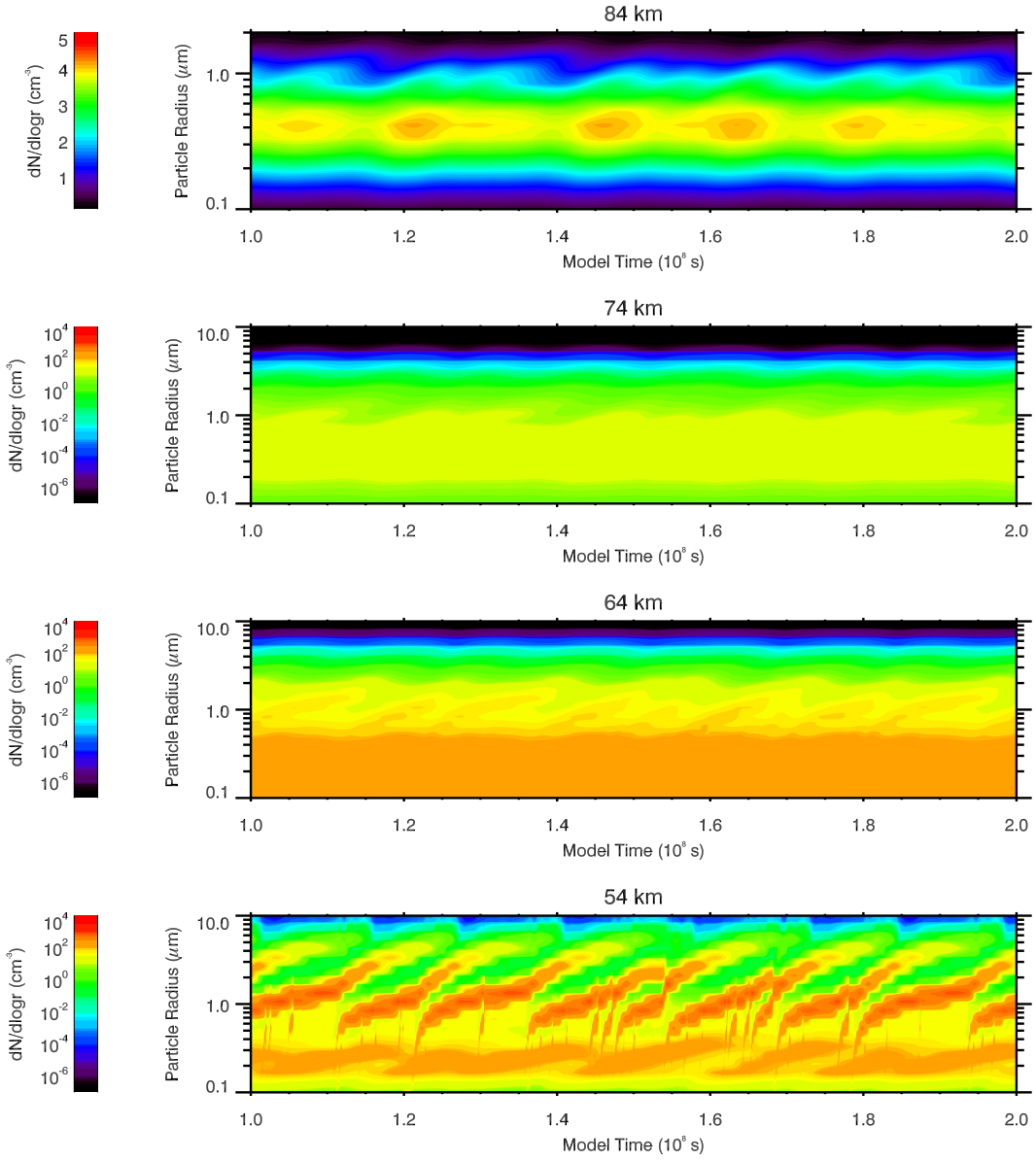

Figure 2.13: Time evolution of the nominal particle size distribution at 84, 74, 64, and 54 km from t = 10^8 s to t = 2×10^8 s. Note the different number density contour and y axis scale for the 84 km plot. The black regions represent parts of the phase space where $dN/dlogr < 10^{-7}$ cm^{-3} at 74, 64, and 54 km, and < 0.1 cm^{-3} at 84 km.

Figure 2.13 shows the time evolution of the particle size distribution at various altitudes. Above the clouds, the quasi-periodic variations are very small, with amplitudes of no more than 10%. In the upper cloud, the variations are larger with small hints of quasi-periodicity in the mode 2 particle abundances apparent, but the size distribution is dominated by mode 1 particles, which are fairly stable. In con-

trast, the middle cloud shows variations in particle abundances of several orders of magnitude. All three modes appear to grow in radii with time and are subsequently replaced with smaller particles on a time scale of ~6 Earth months. In particular, mode 1 slowly grows to larger radii via coagulation and condensation until reaching ~0.25 μm, where there is a rapid growth of particles to mode 2. This actually occurs at several points during the slow migration of mode 1 particles to larger radii, as the intense eddy diffusion at 54 km will allow any particles large enough to overcome the Kelvin barrier to grow rapidly. The upward diffusion of mode 1 particles from below then "resets" the mean mode 1 particle radius back to ~0.2 μm. Mode 2 then also grow slowly with time before growing somewhat rapidly into mode 3 particles, which then proceed to sediment into lower altitudes. The increase in mode 2 particle growth rate occurs at nearly the same time as the rapid growth of mode 1 particles into mode 2 particles, possibly due to the coagulation of the "new" mode 2 particles among themselves and with the "old" mode 2 particles, leading to the creation of the larger mode 3 particles.

Figure 2.13 also shows that, in comparison with the nominal/best-fit results in §2.4.1, the "usual state" of the Venus clouds is actually not those observed by the LCPS—for the majority of the time, mode 2 has a mean radius of ~1.2 μm instead of the observed 1.4 μm (Knollenberg and Hunten, 1980), and it only grows to such a size right before the emergence of a "new" mode 2.

This oscillation is apparently perpetuated by the growth of mode 1 particles into sizes capable of overcoming the Kelvin Barrier, as that leads to the perturbation of the established mode 2 particles which in turn leads to their growth into mode 3 particles. The growth of mode 1 particles can occur via coagulation among themselves, though it is more likely that the majority of coagulation events are with the large number of smaller particles we use in our model as photochemical condensation nuclei and which grew from those nuclei but have not yet reached the sizes of the mode 1 particles, as coagulation between particles of vastly difference sizes is faster than coagulation between similarly sized particles (Seinfeld and Pandis, 2006). As such, since each coagulation event would only add a very small amount of mass to each mode 1 particle, the growth would be gradual but steady, matching what we see in our model results. It is interesting to note that this does not happen when we use a larger particle as our photochemical condensation nuclei (e.g. Imamura and Hashimoto, 2001), as coagulation would be much slower and "random" in time. These variations also do not happen to such an extent in the UH, as both

the coagulation kernel (Eq. 2.15) and condensational growth rate are much lower there.

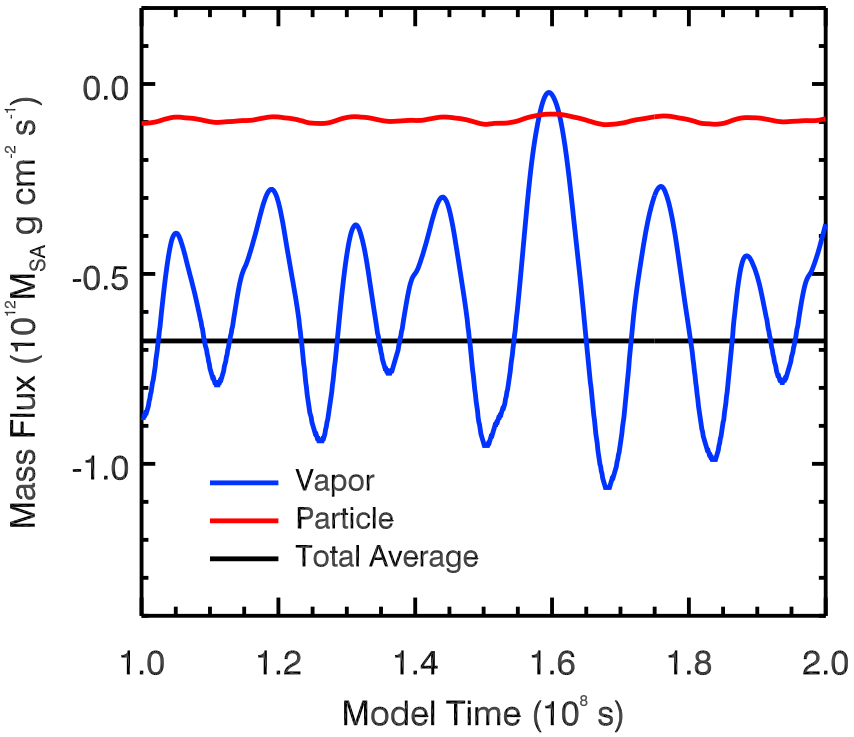

Figure 2.14: The time evolution of the nominal sulfuric acid vapor (dashes) and particle (short lines) mass fluxes at the bottom of the model domain from t = 10^8 s to t = 2×10^8 s plotted with the average of the total flux during this time period (solid), all expressed in units of mass equivalent to 10^{12} sulfuric acid molecules per unit area per second, where each molecule has mass $M_{SA} \sim 1.6 \times 10^{-22}$ g. The negative values indicate downward fluxes.

The quasi-periodic variability of the middle cloud leads to a quasi-periodic sedimentation flux for the largest particles, which leads to the larger-than-expected bottom boundary flux in Figure 2.12. Figure 2.14 shows the time evolution of the sulfuric acid vapor and particle flux out of the bottom boundary of the model domain, expressed in the same units as Figure 2.12. The average of these oscillations, 6.765×10^{11} cm^{-2} s^{-1} matches the injection rate of mass into the model domain, 6.835×10^{11} cm^{-2} s^{-1} fairly well, indicating that we are indeed at an equilibrium state. Finally, we note that the particle and vapor flux oscillations are in phase with each other, and that the latter has greater amplitude than the former. This is explained by the evaporation of the particles below the cloud deck at ~47 km, such that the sulfuric acid variations from the middle cloud are mostly expressed in the resulting vapor.

The possibility of such long term, quasi-periodic particle size variations provide tantalizing hints towards possible sulfuric acid "rain" below the cloud decks of Venus, though we use the term loosely as the downward mass fluxes associated with the "rain" in our model results are far smaller than that of typical rain events on Earth. Nonetheless, it would be interesting to search for evidence of their existence in VIRTIS observations of the Venus night side, which are sensitive to such variations in particle population.

2.4.3 Variations in the Sulfur Production Rate

As discussed in §2.3.1, the production rate of sulfur in the Venus atmosphere may be much lower than half the production rate of sulfuric acid as implied by [R2.1] due to reactions of S with O_2 and the formation of S_2O instead of SO_2 and S from the reaction SO + SO. To address the effect decreasing the sulfur production would have on our results we rerun our model with both one order of magnitude less sulfur produced and two orders of magnitude less sulfur produced. Figure 2.15 shows our results in terms of the number density (top) and size distribution at 54 km in the middle cloud (bottom). Decreasing the sulfur condensation nuclei production rate decreases the number of cloud droplets produced at all altitudes, but also increases the average size of the droplets, since there are fewer nuclei for the same amount of gas to condense on. Mode 1 particle abundances also decrease significantly in the middle cloud when sulfur production is reduced, as the relative fraction of mode 1 particles that grow to mode 2 particles is now much larger. The disagreement between the observed size distribution and the results of the reduced sulfur cases suggest that either (1) the primary reaction in the production of sulfur is indeed [R2.1] (§2.3.1), and that O_2 is relatively scarce in the upper cloud, or (2) Pioneer Venus took data during a period of time when SO_2 abundance exceeded O_2 abundance, perhaps due to an updraft (Toon, Turco, and Pollack, 1982), and that the "steady state" size distribution in the middle cloud is more akin to the reduced sulfur cases, with a low mode 1 abundance, or (3) our model is missing several pieces of essential physics, such as the microphysics of the sulfur particles, which would otherwise result in greater mode 1 abundance even when sulfur production is reduced. Option (3) is unfortunate but likely, given recent modeling results by Carlson (2010), which showed that the ratio between total sulfur mass and total sulfuric acid mass in the cloud droplets is on the order of 0.1–1%. We can calculate the same ratio for our model by adding up the masses of the bare condensation nuclei and the sulfur cores of the sulfuric acid droplets and dividing it by the mass of the sulfuric acid in

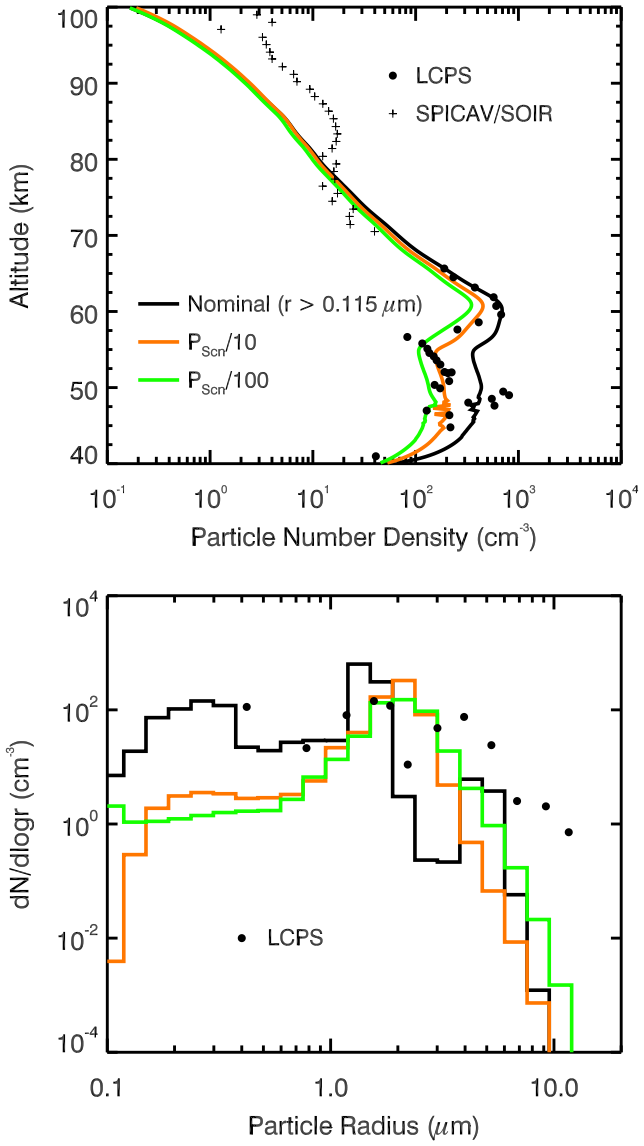

Figure 2.15: The number density (top) and size distribution at 54 km (bottom) of the nominal (black), one order of magnitude reduction in sulfur production (orange), and two orders of magnitude reduction in sulfur production (green) cases. The curves in the top figure are compared to total number density data from LCPS (filled circles) (Knollenberg and Hunten 1980) and Venus Express (pluses) (Wilquet, Fedorova, et al. 2009). The histograms in the bottom figure are compared to LCPS size data at 54.2 km (filled circles) (Knollenberg and Hunten 1980).

the droplets. Figure 2.16 shows this ratio for our three sulfur production rate cases. The sulfur-to-sulfuric-acid mass ratio steadily decreases with altitude until the middle cloud, where it quickly decreases due to the turbulence in the region causing increased condensation of sulfuric acid onto the droplets; the ratio increases below the middle cloud as sulfuric acid begins evaporating from the droplets. The best

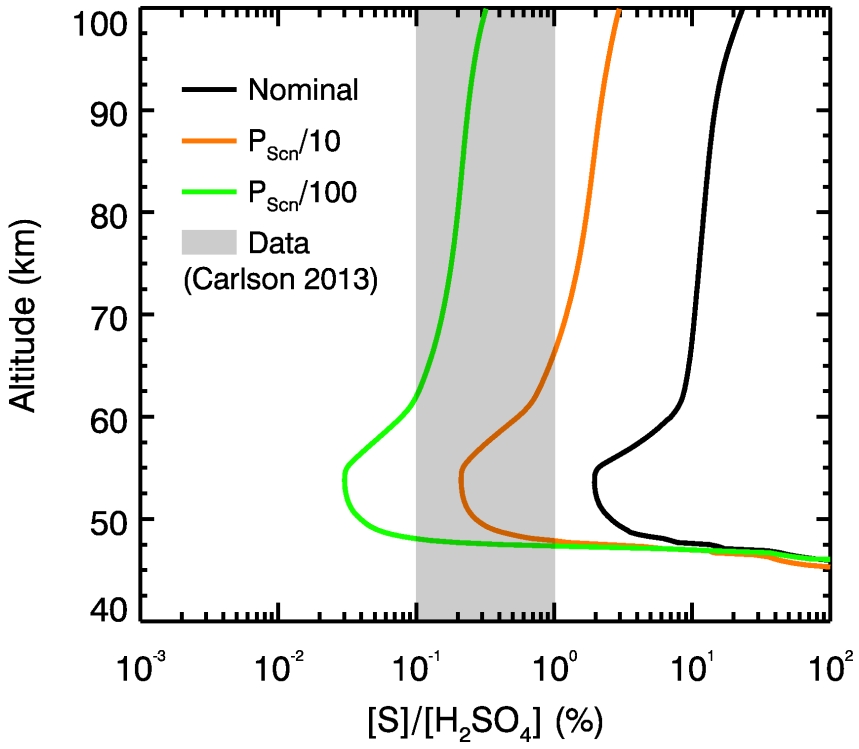

Figure 2.16: The average mass ratio of sulfur to sulfuric acid in cloud and haze droplets as a function of altitude for the nominal (black), one order of magnitude reduction in sulfur production (orange), and two orders of magnitude reduction in sulfur production (green) cases. The two red dashed lines show the range of mass ratios as constrained by fits to UV data (Barker et al. 1975) produced by Carlson (2010).

fit case is evidently one where the sulfur production rate is one order of magnitude less than that of our nominal case, but this contradicts Figure 2.15, where that case did not yield enough mode 1 particles in the middle cloud to match the observations. This discrepancy may be avoided if sulfur microphysics were included in the model, as the small sulfur particles could then grow to larger sizes via condensation of sulfur vapor, perhaps to sizes comparable to that of mode 1 particles. In other words, the mass would be concentrated in mode 1 particles rather than the "sea" of smaller condensation nuclei, even for the cases with reduced sulfur production.

Finally, it should be noted that the periodic behavior of the nominal case disappears in the reduced sulfur cases. This is consistent with our hypothesis that the oscillation is caused by slow growth of mode 1 particles due to coagulation with the background "sea" of much smaller particles—if the "sea" is reduced, then coagulation may not be enough to allow mode 1 particles to grow past the Kelvin barrier.

This further suggests that the reduced sulfur cases match the true state of the Venus clouds more closely than the nominal case, as no periodic behavior similar to those in the nominal case has yet been observed.

2.4.4 Transient Wind Results

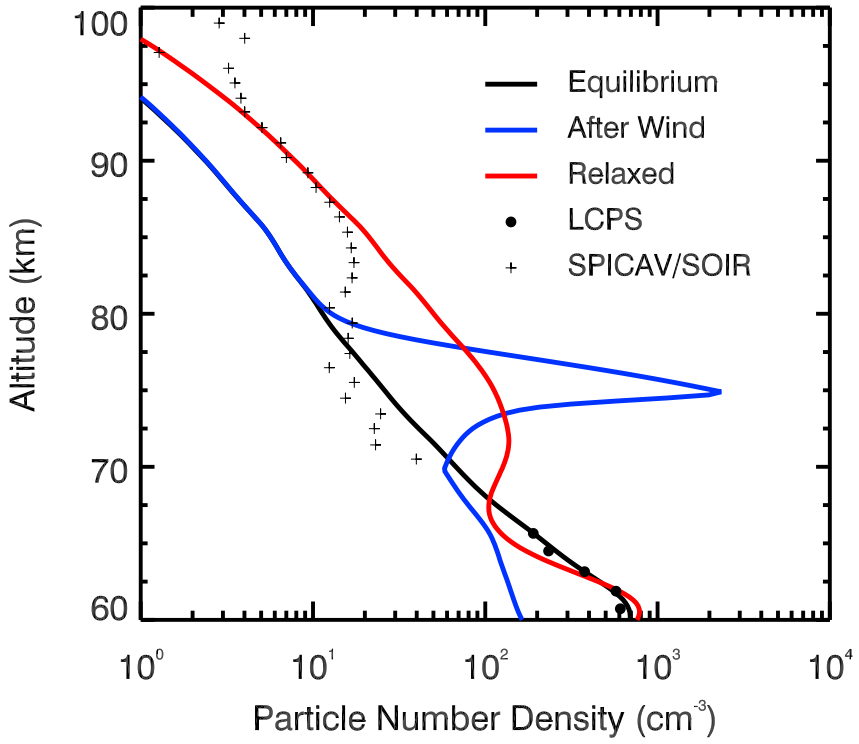

Figure 2.17: Number density profiles of the upper cloud and haze before (black), immediately after (blue), and 5×10^5 s after (red) a 5×10^4 s transient wind event. The total number density data from LCPS (filled circles) (Knollenberg and Hunten et al. 1980) and Venus Express (pluses) (Wilquet, Fedorova, et al. 2009) are plotted for comparison. The wind speed profile is shown in Figure 6.

Figure 2.17 gives the number density results before (black), immediately after (blue), and about an Earth week after a transient updraft event lasting ~14 Earth hours (5×10^4 s) (red), using the wind speed profile given in Figure 2.6. We see that a detached haze layer forms at 75 km with a peak number density 2 orders of magnitude greater than the number density at that altitude before the wind event. The altitude of the detached haze is likely artificial given our wind profile and the actual maximum detached haze number density is likely overestimated due to the lack of horizontal diffusion aiding (the already present) vertical diffusion in smoothing out the number density profile. However, the occurrence of an increase in number density at the altitude of the turn-over should be profile-independent. In the week that

follows, the detached haze layer diffuses away so that the peak number density is more than an order of magnitude lower than its maximum immediately following the wind event. This shows that such a wind event produces the right time scales for the observed haze variability from Wilquet, Drummond, et al. (2012), on the order of days. Furthermore, the diffusion of the detached haze particles upwards results in an increase in the number density of the UH such that there is now a much better agreement between the Wilquet, Fedorova, et al. (2009) UH number density observations and that of our model above 80 km. It is clear, however, that the agreement between data and model would be even better if the relaxed distribution was shifted up by 10 km. This suggests that the turnover was actually 10 km higher in the actual observations, though it is unlikely that such large gusts existed at such high altitudes.

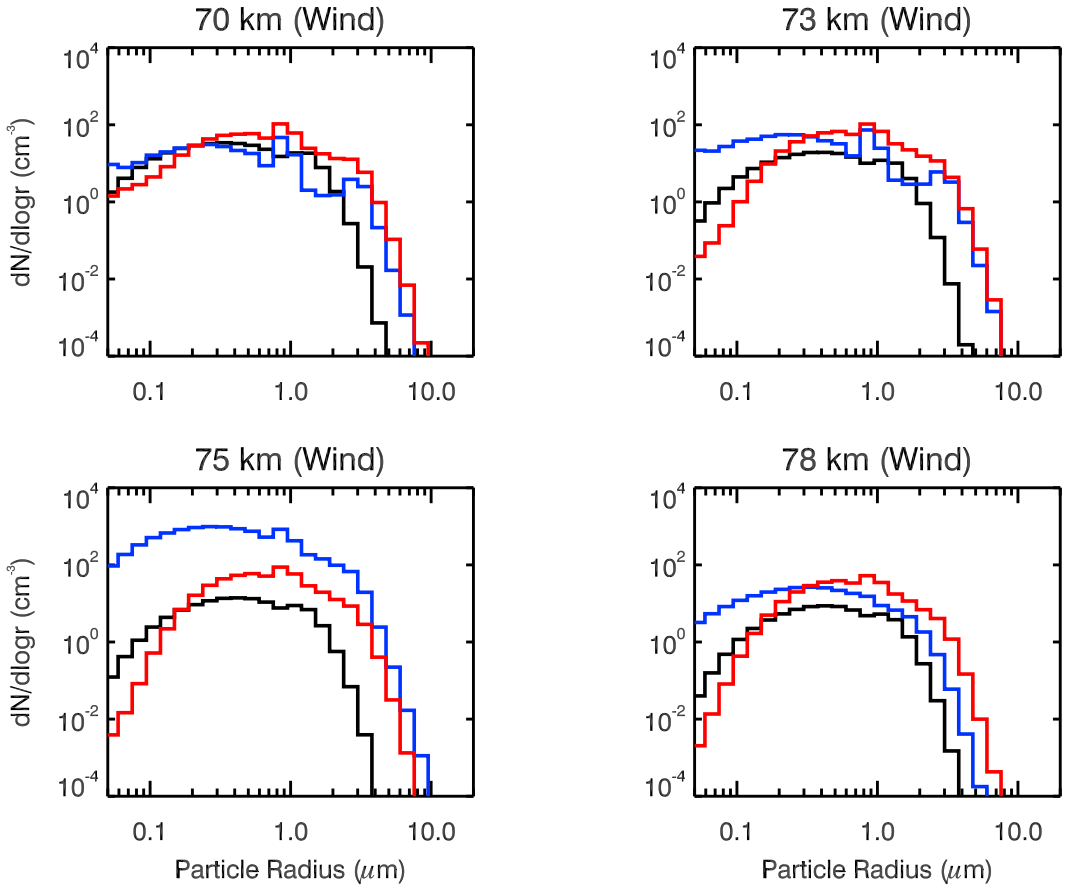

Figure 2.18: Particle size distribution before (black), immediately after (blue), and 5×10^5 s after (red) a 5×10^4 s transient wind event, plotted for various altitudes close to the turnover altitude of the transient wind. The wind speed profile is shown in Figure 6.

Figure 2.18 shows the size distributions at altitudes close to the detached haze layer at the same times as Figure 2.17. Multiple size modes form below the turnover of the wind immediately following the wind event (blue). The small mode at ~0.2 μm is largely unchanged from the equilibrium distribution for altitudes below the detached haze, but is much more abundant within the detached haze itself at 75 km; this is caused by the advection of these small particles up to the altitude of the detached haze. The "bump" associated with the high altitude tail of the mode 2 cloud particles in the equilibrium distribution (black) becomes much more distinct due to upward advection of more mode 2 particles; this feature is much more prominent below the detached haze, which matches the observations of Wilquet, Fedorova, et al. (2009) where the large UH particle mode (mode 2 cloud particles) number density drops off with altitude much faster than the small UH particle mode (mode 1 cloud particles). The small mode radii covers sizes < 0.6 μm, which is a larger range than the Wilquet, Fedorova, et al. (2009) result of 0.1–0.3 μm; the large mode radii covers the sizes between 0.6 and 1 μm, similar to their results. Beyond 1 μm, the particle abundance drops by over an order of magnitude, though a third mode does appear resulting from advected mode 3 cloud particles; however, it is insignificant compared to the small and large modes. Above the turnover, the size distribution remains largely mono-modal.

Below the detached haze, the large mode becomes less distinct following the relaxation period (red), though both modes increase in number density. This is due to the sedimentation of large mode particles from the detached haze, as we see a large decrease in number density at the altitude of the detached haze itself. There is also an increase in number density above the turnover, as the detached haze particles diffuse upwards from the number density maximum. Thus, if the bimodality observed by Wilquet, Fedorova, et al. (2009) was caused by winds, then it was likely transient in nature. This is supported by the order of magnitude variability between extinction profiles of the UH taken only days apart presented in Wilquet, Drummond, et al. (2012). It is unlikely that condensational and coagulational growth play any important role here, as their timescales are far greater than the observed variability timescale (James, Toon, and Schubert, 1997; Seinfeld and Pandis, 2006).

In §2.3.6 we noted the unrealistic long gust duration we have used (~14 Earth hours). However, we see that the UH size distribution is still visibly disturbed almost a full Earth week after the wind event in question. If we suppose that our wind event is caused by subsolar convection near 50° N that lasted for a full 14

hours and that the wind was constantly upwards with velocity $\sim$1 m s^{-1} at the cloud top, then given poleward meridional velocities of $\sim$5 m s^{-1} (Rossow, Del Benio, and Eichler, 1990) (a high estimate), it would take $\sim$1 Earth week for this parcel of air to reach 70° N, the latitude where the measurements of Wilquet, Fedorova, et al. (2009) were taken. It may not be surprising then that our "relaxed" UH number density profile matches the Wilquet, Fedorova, et al. (2009) number density data so well. However, most of these assumptions are highly optimistic and it is much more likely that our results show an exaggeration of what transient winds at the cloud tops can really do to the steady state aerosol distribution.

2.5 Summary & Conclusions

In this study we simulated the clouds and upper haze of Venus using version 3.0 of the microphysical and vertical transport model CARMA. We showed that appropriate choices of initial, boundary, and model atmospheric conditions can not only satisfactorily reproduce the number density and size distributions of the Venus clouds as seen in Pioneer Venus data (Knollenberg and Hunten, 1980), including the bimodal and possible trimodal particle size spectrum and the three separate cloud layers, but also generate a quasi-periodically varying system rather than a system with a stable equilibrium distribution. The disagreements between our results and the observations—the overestimation of the particle number density and abundance of mode 2 particles in the middle cloud and the underestimation of the lower cloud and the abundance of mode 3 particles—are all within the range of variability seen in other observations, though the addition of transient gusts in the middle cloud, which would both deplete the middle cloud of particles and create a greater number of larger particles, may improve our agreement with the Pioneer Venus Sounder Probe data.

We also simulated the upper haze as a mixture of droplets formed from in situ nucleation of sulfuric acid vapor on meteoric dust and droplets upwelled from the cloud decks below. We showed that the former population rapidly coagulates with the latter population, resulting in a mono-modal size distribution. Meanwhile, for altitudes below 80 km there is good agreement between our model particle number densities and the sum of the small mode (mode 1) and large mode (mode 2) number densities from Wilquet, Fedorova, et al. (2009); above 80 km, we underestimate the number density by about half an order of magnitude. These particles are likely those originally observed by the Pioneer Venus OCPP (Kawabata et al., 1980), and could represent the haze under stable atmospheric conditions. These discrepancies

were reduced upon the application of a transient updraft, which created a detached haze layer at the altitude of turnover. The diffusion of the detached haze upwards increased the particle number density of the UH such that the results agreed with the UH number densities derived by Wilquet, Fedorova, et al. (2009) above 80 km. The resulting size distribution showed a clear bimodal structure below the detached haze immediately after the wind event, with the small mode (mode 1) particles having radii < 0.6 μm, and the large mode having radii between 0.6 and 1 μm, similar to the results of Wilquet, Fedorova, et al. (2009). The relaxation of the multi-modal structures in the size distribution back to a mono-modal distribution had a timescale of roughly an Earth week, similar to the time scales of haze variability observed by Venus Express (Luz et al., 2011; Markiewicz et al., 2007). The duration and strength of the updraft were likely exaggerations of what actually takes place in the Venus atmosphere, though subsolar convection could be a viable candidate for the generation of these events under optimistic assumptions.

We noted a quasi-periodic variability in our results with a rough period of ~6 Earth months despite a stable background atmospheric state and constant input of sulfuric acid vapor and condensation nuclei. This variability is most apparent in the middle cloud, where steady coagulation of small particles (~10 nm) with mode 1 particles lead to a slow increase in the mean mode 1 particle radii. Upon reaching the Kelvin barrier, the mode 1 particles rapidly grow to mode 2 particles via condensational growth, while upward diffusion of mode 1 particles from below replenish the mode 1 population. The cycle then repeats and a new wave of mode 2 particles appear; these new mode 2 particles coagulate with the old mode 2 particles, resulting in mode 3 particles that then sediment out of the model domain. This process does not occur if the sulfur condensation nuclei production rate is decreased by an order of magnitude or more, nor does it occur if the condensation nuclei are larger. Comparison between model results and Pioneer Venus observations (Knollenberg and Hunten, 1980) suggests that the LCPS data may have been taken during one of the unstable "growth phases" rather than the much more long-lived stable phases. These episodic variations also leads to periodicity in the magnitude of the sulfuric acid flux out of the bottom boundary of the model domain and suggests possible sulfuric acid "rain events" that could occur immediately below the cloud deck. Such long term variability in particle population should be detectable by VIRTIS observations of the Venus night side.

The sulfur production rate in the upper cloud is uncertain and could be much lower

than half of the sulfuric acid production rate as assumed in Imamura and Hashimoto (2001) and in our nominal model. Comparisons with sulfur-to-sulfuric-acid mass ratios of the cloud droplets derived from UV data (Carlson, 2010) shows that the best fit case is one where the sulfur production rate is reduced by an order of magnitude from that of the nominal case. However, comparison of this case with LCPS particle size distributions shows that the model predicts mode 1 particle abundances in the middle cloud two orders of magnitude less what is observed. This discrepancy could be caused by the lack of sulfur microphysics in our model, which could allow the sulfur condensation nuclei to grow to mode 1 particles ($\sim$0.2 μm) instead of being fixed at a size of $\sim$10 nm.

It is necessary for future models to include both sulfur and sulfuric acid microphysics in order to provide a more complete picture of the processes occurring within the Venus clouds and hazes. Interactions between aerosols formed from these species and their gas phases are diverse and only a subset has been tested. Furthermore, the production rates of these two species, particularly sulfur and its allotropes, require better constraints from both chemical models that take into account sinks due to aerosol formation and observations that are able to probe down to the altitudes where photochemistry dominates. Finally, continuous observation of the Venus hazes and clouds is essential in constraining their time evolution, especially after transient events.

We thank S. Garimella and R. L. Shia for assistance with the setting up and running of the CARMA code. We thank R. W. Carlson and C. Parkinson for their valuable inputs. We thank C. Li for his help in speeding up our model runs by more than a factor of 10. This research was supported in part by the Venus Express program via NASA NNX10AP80G grant to the California Institute of Technology, and in part by an NAI Virtual Planetary Laboratory grant from the University of Washington to the Jet Propulsion Laboratory and California Institute of Technology. Part of the research described here was carried out at the Jet Propulsion Laboratory, California Institute of Technology, under a contract with the National Aeronautics and Space Administration.

References

Ayers, G. P., R. W. Gillett, and J. L. Gras (1980). “On the vapor pressure of sulfuric acid.” In: *Geophysics Research Letters* 7, pp. 433–436.

Baker, R. D., G. Schubert, and P. W. Jones (1998). "Cloud-level penetrative compressible convection in the Venus atmosphere." In: *Journal of the Atmospheric Sciences* 55, pp. 3–18.

– (1999). "High Rayleigh number compression convection in Venus' atmosphere: Penetration, entrainment, and turbulence." In: *Journal of Geophysical Research* 104, pp. 3815–3832.

Bardeen, C. G., A. Conley, et al. (2011). "The CARMA 3.0 microphysics package in CESM." Presented at the *Whole Atmosphere Working Group Meeting*, Boulder, USA.

Bardeen, C. G., O. B. Toon, et al. (2008). "Numerical simulations of the three dimensional distribution of meteoric dust in the mesosphere and upper stratosphere." In: *Journal of Geophysical Research* 113, p. D17202.

Belton, M. J. S. et al. (1976). "Cloud patterns, waves and convection in the Venus atmosphere." In: *Journal of the Atmospheric Sciences* 33, pp. 1394–1417.

Bertaux, J-L. et al. (2007). "A warm layer in Venus' cryosphere and high-altitude measurements of HF, HCl, H2O, and HDO." In: *Nature* 450, pp. 646–649.

Carlson, R. W. (2010). "Venus's ultraviolet absorber and sulfuric acid droplets". Presented at the *International Venus Conference*, Aussois, France.

Carlson, R. W. et al. (1993). "Variations in Venus cloud properties: A new view of Venus's cloud morphology as observed by the Galileo Near-Infrared Mapping Spectrometer." In: *Planetary and Space Science* 41, pp. 477–485.

Clancy, R. T. and D. O. Muhleman (1991). "Long-term (1979-1990) changes in the thermal, dynamical, and compositional structure of the Venus mesosphere as inferred from microwave spectral line observations of 12CO, 13CO, and C18O." In: *Icarus* 89, pp. 129–146.

Crisp, D., A. P. Ingersoll, et al. (1990). "VEGA Balloon meteorological measurements." In: *Advances in Space Research* 10, pp. 109–124.

Crisp, D., S. McMuldroch, et al. (1991). "Ground-based near-infrared imaging observations of Venus during the Galileo encounter." In: *Science* 253, pp. 1538–1541.

Crisp, D., W. M. Sinton, et al. (1989). "The nature of the near-infrared features on the Venus night side." In: *Science* 246, pp. 506–509.

English, J. M. et al. (2011). "Microphysical simulations of new particle formation in the upper troposphere and lower stratosphere." In: *Atmospheric Chemistry and Physics* 11, pp. 9303–9322.

Esposito, L. W. et al. (1983). "The clouds and hazes of Venus." In: *Venus*. Ed. by D. M. Hunten et al. Tucson, USA: University of Arizona Press, pp. 484–564.

Gadsden, M. (1968). "Sodium in the upper atmosphere: Meteoric origin." In: *Journal of Atmospheric and Solar-Terrestrial Physics* 30, pp. 151–161.

Garate-Lopez, I. et al. (2013). "A chaotic long-lived vortex at the southern pole of Venus." In: *Nature Geoscience* 6, pp. 254–257.

Giauque, W. F. et al. (1959). "The thermodynamic properties of aqueous sulfuric acid solutions and hydrates from 15 to 300 K." In: *Journal of the American Chemical Society* 82, pp. 62–70.

Grinspoon, D. H. et al. (1993). "Probing Venus's cloud structure with Galileo NIMS." In: *Planetary and Space Science* 41, pp. 515–542.

Hueso, R. et al. (2008). "Morphology and dynamics of Venus oxygen airglow from Venus Express/Visible and Infrared Thermal Imaging Spectrometer observations." In: *Journal of Geophysical Research* 113, E00B02.

Hunten, D. M., R. P. Turco, and O. B. Toon (1980). "Smoke and dust particles of meteoric origin in the mesosphere and stratosphere." In: *Journal of the Atmospheric Sciences* 37, pp. 1342–1357.

Ignatiev, N. I. et al. (1997). "Water vapour in the lower atmosphere of Venus: A new analysis of optical spectra measured by entry probes." In: *Planetary and Space Science* 45, pp. 427–438.

Imamura, T. (1997). "Momentum balance of the Venusian midlatitude mesosphere." In: *Journal of Geophysical Research* 102, pp. 6615–6620.

Imamura, T. and G. L. Hashimoto (2001). "Microphysics of Venusian clouds in rising tropical air." In: *Journal of the Atmospheric Sciences* 55, pp. 3597–3612.

Ingersoll, A. P., D. Crisp, and the VEGA Balloon Science Team. (1987). "Estimates of convective heat fluxes and gravity wave amplitudes in the Venus middle cloud layer from VEGA balloon measurements." In: *Advances in Space Research* 7, pp. 343–349.

Jacobson, M. Z. and R. P. Turco (1994). "Modeling coagulation among particles of different composition and size." In: *Atmospheric Environment* 28, pp. 1327–1338.

James, E. P., O. B. Toon, and G. Schubert (1997). "A numerical microphysical model of the condensational Venus cloud." In: *Icarus* 129, pp. 147–171.

Kalashnikova, O. et al. (2000). "Meteoric smoke production in the atmosphere." In: *Geophysical Research Letters* 27, pp. 3293–3296.

Kawabata, K. et al. (1980). "Cloud and haze properties from Pioneer Venus polarimetry." In: *Journal of Geophysical Research* 85, pp. 8129–8140.

Knollenberg, R. G. and D. M. Hunten (1980). "The microphysics of the clouds of Venus: Results of the Pioneer Venus particle size spectrometer experiment." In: *Journal of Geophysical Research* 85, pp. 8039–8058.

Kolodner, M. A. and P. G. Steffes (1998). "The microwave absorption and abundance of sulfuric acid vapor in the Venus atmosphere based on new laboratory measurements." In: *Icarus* 132, pp. 151–169.

Krasnopolsky, V. A. (1983). “Venus spectroscopy in the 3000–8000 Åregion by Veneras 9 and 10.” In: *Venus*. Ed. by D. M. Hunten et al. Tucson, USA: University of Arizona Press, pp. 459–483.

Krasnopolsky, V. A. and V. A. Parshev (1983). “Photochemistry of the Venus atmosphere.” In: *Venus*. Ed. by D. M. Hunten et al. Tucson, USA: University of Arizona Press, pp. 431–458.

Krasnopolsky, V. A. and J. B. Pollack (1994). “H2O - H2SO4 system in Venus’ clouds and OCS, CO, and H2SO4 profiles in Venus’ troposphere.” In: *Icarus* 109, pp. 58–78.

Kulmala, M. and A. Laaksonen (1990). “Binary nucleation of water-sulfuric acid system: Comparison of classical theories with different H2SO4 saturation vapor pressures.” In: *Journal of Chemical Physics* 93, pp. 696–701.

Luz, D. et al. (2011). “Venus’s southern polar vortex reveals precessing circulation.” In: *Science* 332, pp. 577–580.

Lyons, J. R. (2008). “An estimate of the equilibrium speciation of sulfur vapor over solid sulfur and implications for planetary atmospheres.” In: *Journal of Sulfur Chemistry* 29, pp. 269–279.

Markiewicz, W. J. et al. (2007). “Morphology and dynamics of the upper cloud layer of Venus.” In: *Nature* 450, pp. 633–636.

McGouldrick, K. and O. B. Toon (2007). “An investigation of possible causes of the holes in the condensational Venus cloud using a microphysical cloud model with a radiative-dynamical feedback.” In: *Icarus* 191, pp. 1–24.

McGouldrick, K., O. B. Toon, and D. H. Grinspoon (2011). “Sulfuric acid aerosols in the atmosphere of the terrestrial planets.” In: *Planetary and Space Science* 59, pp. 934–941.

Mills, F. P., L. W. Esposito, and Y. L. Yung (2007). “Atmospheric composition, chemistry, and clouds.” In: *Exploring Venus as a Terrestrial Planet*. Ed. by L. W. Esposito, E. R. Stofan, and T. E. Cravens. Washington D.C., USA: American Geophysical Union, pp. 73–100.

Mills, M. J. (1996). “Stratospheric sulfate aerosol: A microphysical model.” PhD thesis. University of Colorado, Department of Astrophysical, Planetary, and Atmospheric sciences.

Rossow, W. B., A. D. Del Benio, and T. Eichler (1990). “Cloud-tracked winds from Pioneer Venus OCPP images.” In: *Journal of the Atmospheric Sciences* 47, pp. 2053–2084.

Sabinina, L. and L. Turpugow (1935). “The surface tension of the system sulfuric acid/water.” In: *Zeitschrift für Physikalische Chemie* A173, pp. 237–241.

Sandor, B. J., R. T. Clancy, and G. Moriarty-Schieven (2012). “Upper limits for H2SO4 in the mesosphere of Venus.” In: *Icarus* 217, pp. 839–844.

Saunders, R. W. et al. (2012). “Interactions of meteoric smoke particles with sulphuric acid in the Earth’s stratosphere.” In: *Atmospheric Chemistry and Physics* 12, pp. 4387–4398.

Schubert, G. et al. (1980). “Structure and circulation of the Venus atmosphere.” In: *Journal of Geophysical Research* 85, pp. 8007–8025.

Seiff, A., D. B. Kirk, et al. (1980). “Measurements of thermal structure and thermal contrasts in the atmosphere of Venus and related dynamical observations: Results from the four Pioneer Venus probes.” In: *Journal of Geophysical Research* 85, pp. 7903–7933.

Seiff, A., J. T. Schofield, et al. (1985). “Models of the structure of the atmosphere of Venus from the surface to 100 kilometers altitude.” In: *Advances in Space Research* 5, pp. 3–58.

Seinfeld, J. H. and S. N. Pandis (2006). *Atmospheric chemistry and physics: From air pollution to climate change, 2nd edition.* John Wiley & Sons, Inc. Hoboken, New Jersey, USA.

Tabazadeh, A. et al. (1997). “A new parameterization of H2SO4/H2O aerosol composition: Atmospheric implications.” In: *Geophysical Research Letters* 24, pp. 1931–1934.

Tellmann, S. et al. (2009). “Structure of the Venus neutral atmosphere as observed by the Radio Science experiment VeRa on Venus Express.” In: *Journal of Geophysical Research* 114, E00B36.

Titov, D. V. et al. (2012). “Morphology of the cloud tops as observed by the Venus Express Monitoring Camera.” In: *Icarus* 217, pp. 682–701.

Toon, O. B., B. Ragent, et al. (1984). “Large, solid particles in the clouds of Venus: Do they exist?” In: *Icarus* 57, pp. 143–160.

Toon, O. B., R. P. Turco, J. Jordan, et al. (1989). “Physical processes in polar stratospheric ice clouds.” In: *Journal of Geophysical Research* 94, pp. 11359–11380.

Toon, O. B., R. P. Turco, and J. B. Pollack (1982). “The ultraviolet absorber on Venus: Amorphous sulfur.” In: *Icarus* 51, pp. 358–373.

Toon, O. B., R. P. Turco, D. Westphal, et al. (1988). “A multidimensional model for aerosols: Description of computational analogs.” In: *Journal of the Atmospheric Sciences* 45, pp. 2123–2143.

Turco, R. P., P. Hamill, et al. (1979). “A one-dimensional model describing aerosol formation and evolution in the stratosphere: I. Physical processes and mathematical analogs.” In: *Journal of the Atmospheric Sciences* 36, pp. 699–717.

Turco, R. P., O. B. Toon, et al. (1983). “Venus: Mesospheric hazes of ice, dust, and acid aerosols.” In: *Icarus* 53, pp. 18–25.

White, F. M. (1974). *Viscous Fluid Flow.* McGraw-Hill, New York, USA.

Wilquet, V., R. Drummond, et al. (2012). “Optical extinction due to aerosols in the upper haze of Venus: Four years of SOIR/VEX observations from 2006 to 2010.” In: *Icarus* 317, pp. 875–881.

Wilquet, V., A. Fedorova, et al. (2009). “Preliminary characterization of the upper haze by SPICAV/SOIR solar occultation in UV to mid-IR onboard Venus Express.” In: *Journal of Geophysical Research* 114, E00B42.

Yamamoto, M. and M. Takahashi (2006). “An aerosol transport model based on a two-moment microphysical parametrization in the Venus middle atmosphere: Model description and preliminary experiments.” In: *Journal of Geophysical Research* 111, E08002.

Yamamoto, M. and H. Tanaka (1998). “The Venusian Y-shaped cloud pattern based on an aerosol-transport model.” In: *Journal of the Atmospheric Sciences* 55, pp. 1400–1426.

Young, A. T. (1983). “Venus cloud microphysics.” In: *Icarus* 56, pp. 568–577.

Yung, Y. L. and W. B. DeMore (1982). “Photochemistry of the stratosphere of Venus: Implications for atmospheric evolution.” In: *Icarus* 51, pp. 199–247.

Zhang, X., M. C. Liang, F. P. Mills, et al. (2012). “Sulfur chemistry in the middle atmosphere of Venus.” In: *Icarus* 217, pp. 714–739.

Zhang, X., M. C. Liang, F. Montmessin, et al. (2010). “Photolysis of sulphuric acid as the source of sulphur oxides in the mesosphere of Venus.” In: *Nature Geoscience* 3, pp. 834–837.

Zhang, X., S. N. Pandis, and J. H. Seinfeld (2012). “Diffusion-limited versus quasi-equilibrium aerosol growth.” In: *Aerosol Science and Technology* 46, pp. 874–885.

PART II: FROZEN FRACTALS ALL AROUND

Chapter 3

CONSTRAINTS ON THE MICROPHYSICS OF PLUTO'S PHOTOCHEMICAL HAZE FROM NEW HORIZONS OBSERVATIONS

Gao, P. et al. (Accepted). "Constraints on the Microphysics of Pluto's Photochemical Haze from New Horizons Observations". In: *Icarus*. DOI: 10.1016/j.icarus.2016.09.030.

3.1 Abstract

The New Horizons flyby of Pluto confirmed the existence of hazes in its atmosphere. Observations of a large high to low phase brightness ratio, combined with the blue color of the haze (indicative of Rayleigh scattering), suggest that the haze particles are fractal aggregates, perhaps analogous to the photochemical hazes on Titan. Therefore, studying the Pluto hazes can shed light on the similarities and differences between the Pluto and Titan atmospheres. We model the haze distribution using the Community Aerosol and Radiation Model for Atmospheres assuming that the distribution is shaped by downward transport and coagulation of particles originating from photochemistry. Hazes composed of both purely spherical and purely fractal aggregate particles are considered. General agreement between model results and solar occultation observations is obtained with aggregate particles when the downward mass flux of photochemical products is equal to the column-integrated methane destruction rate $\sim 1.2 \times 10^{-14}$ g cm^{-2} s^{-1}, while for spherical particles the mass flux must be 2–3 times greater. This flux is nearly identical to the haze production flux of Titan previously obtained by comparing microphysical model results to Cassini observations. The aggregate particle radius is sensitive to particle charging effects, and a particle charge to radius ratio of 30 e$^-$/μm is necessary to produce $\sim$0.1–0.2 μm aggregates near Pluto's surface, in accordance with forward scattering measurements. Such a particle charge to radius ratio is 2–4 times higher than those previously obtained for Titan. Hazes composed of spheres with the same particle charge to radius ratio have particles that are 4 times smaller at Pluto's surface. These results further suggest that the haze particles are fractal aggregates. We also consider the effect of condensation of HCN, C_2H_2, C_2H_4, and C_2H_6 on the haze particles, which may play an important role in shaping their

altitude and size distributions.

3.2 Introduction

Photochemical hazes naturally arise in reducing atmospheres due to the destruction of methane and higher hydrocarbons by solar UV photons and high-energy ions and neutrals, followed by polymerization of the resulting radical species. Such conditions have been hypothesized to exist in the atmosphere of Pluto from detections of spectral features belonging to methane gas/ice (e.g. Cruikshank and Brown, 1986; Owen et al., 1993), which suggests the possible existence of hazes therein. However, previous attempts at characterizing the lower atmosphere of Pluto by exploiting the "knee" in stellar occultation light curves (where the slope of ingress/egress steepens closer to Pluto's surface) have been inconclusive, as both a strong thermal inversion and a haze layer can produce such an observation (e.g. Elliot, Dunham, et al., 1989; Stansberry, Lunine, Hubbard, et al., 1994; Young et al., 2008; Person et al., 2013; Olkin et al., 2014; Dias-Oliveira et al., 2015; Gulbis et al., 2015).

The July 14th, 2015 flyby of Pluto by the New Horizons probe settled the debate by confirming the existence of optically thin haze layers pervading the lower few hundred kilometers of Pluto's atmosphere, as seen in both forward scattering observations and solar/stellar occultations (Stern et al., 2015; Gladstone et al., 2016). The haze appeared blue, which is likely due to Rayleigh scattering by small particles. However, it also featured a large high to low phase brightness ratio, indicative of large particles. These two observations combined point to the haze particles being fractal aggregates, drawing strong parallels between the Pluto haze and the hazes of Titan (Elliot, Ates, et al., 2003). Thus, studying the Pluto haze can greatly inform comparisons of these two apparently disparate worlds. In addition, the haze particles can act as nucleation sites for condensable species in Pluto's atmosphere, thereby directly affecting atmospheric chemistry. In this work, we compare the observed haze extinction profiles with those calculated by microphysical models, thereby offering insights into the major processes controlling the haze distribution.

We describe our microphysical model in §3.3. In §3.4, we present our model results, compare them to data, and discuss the impact of condensation on the haze distribution.

3.3 Model

We model the Pluto haze as a direct analog of the Titan haze, as the atmospheric chemistry of the two worlds is similar (Wong, Yung, and Gladstone, 2015), and un-

certainties on the processes governing the formation and evolution of Titan's haze are much smaller than that of Pluto's haze owing to 10 years of Cassini observations. Possible differences between the hazes on these two worlds are discussed in §3.4.1.

Titan's haze is composed of fractal aggregates—fluffy, porous particles consisting of smaller subunits, or "monomers" (West and Smith, 1991). The number of monomers, N_m, in an aggregate particle is defined as

$$N_m = \left(\frac{R_f}{r_m}\right)^{D_f}, \tag{3.1}$$

where R_f is the effective particle radius of the aggregate, r_m is the monomer radius, and D_f is the fractal dimension of the aggregate, typically between 1.75 and 2.5 for Titan haze particles (Cabane et al., 1993). For simplicity we use $D_f = 2$ in our modeling. Eq. 3.1 can be used to find the mass M of an aggregate, which for $D_f = 2$ is

$$M = \frac{4}{3}\pi\rho_p r_m R_f^2, \tag{3.2}$$

where $\rho_p = 1$ g cm^{-3} is the monomer mass density (Lavvas, Yelle, and Griffith, 2010). Gladstone et al. (2016) estimated r_m to be ~10 nm for Pluto's haze particles using Rayleigh scattering, and thus we adopt this value for our nominal model. We also consider 5 nm monomers, under the hypothesis that monomers can grow by condensation of simple hydrocarbons and nitriles (Barth, 2014; Wong, Fan, et al., 2016).

We use the same model atmosphere as for the photochemical calculations of Wong, Fan, et al. (2016), though we focus only on altitudes below 500 km to avoid spending computational time on altitudes where data quality is low. Figure 3.1 shows the temperature profile of the model atmosphere, updated from Zhu, Strobel, and Erwin (2014).

We calculate the equilibrium haze particle size and altitude distribution using the 1–dimensional Community Aerosol and Radiation Model for Atmospheres (CARMA; Turco et al., 1979; Toon, Turco, et al., 1988; Jacobson and Turco, 1994; Bardeen et al., 2008; Wolf and Toon, 2010). CARMA is a Eulerian forward model that solves the discretized continuity equation for aerosol particles subject to vertical transport

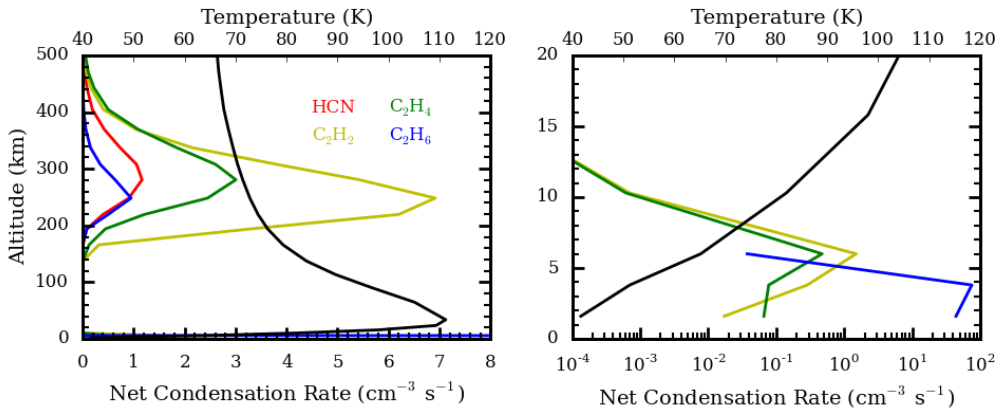

Figure 3.1: (Left) The temperature (black) and net condensation rate profiles for HCN (red), C_2H_2 (yellow), C_2H_4 (green), and C_2H_6 (blue) taken from the photochemical model results of Wong, Fan, et al. (2016). (Right) The same as the left plot but zoomed into the lower 20 km of the atmosphere, where C_2H_6 condensation dominates over the other species. Note the different bottom x-axis scale between the two plots.

and production and loss due to particle nucleation, condensation, evaporation, and coagulation, and has been used to simulate the Titan hazes (e.g. Toon, McKay, et al., 1992; Larson, Toon, and Friedson, 2014; Larson, Toon, West, et al., 2015). Coagulation and transport of Titan's haze particles dominate over nucleation and condensation/evaporation above the troposphere (Lavvas, Yelle, and Griffith, 2010; Larson, Toon, and Friedson, 2014), and thus the change with time of $n_p(z)$, the number density of particles in the pth mass bin at altitude z can be simplified to

$$\frac{\partial n_p}{\partial t} = -\frac{\partial}{\partial z}(w_{sed} n_p) + \frac{1}{2}\sum_{i=1}^{i=p-1} K_{i,p-i} n_i n_{p-i} - n_p \sum_{i=1}^{i=N_b} K_{i,p} n_i, \tag{3.3}$$

where w_{sed} is the sedimentation velocity and $K_{i,j}$ is the Brownian coagulation kernel between particles in mass bins i and j. The mass bins are set such that each bin corresponds to particle masses twice that of the previous bin. We use $N_b = 30$ bins in our model, starting from a minimum radius of $R_f = 20$ nm, which was chosen such that the smallest particles are still fractal in nature. A fixed downward mass flux of these minimum–R_f aggregate particles (with $r_m = 5$ or 10 nm) is imposed at the top boundary of the model atmosphere, while at the lower boundary the aggregates are assumed to sediment out onto the surface.

The first term on the right hand side of Eq. 3.3 represents vertical transport due

to sedimentation of the aerosol particles; the second term represents the increase in n_p due to the coagulation of smaller particles with total mass equal to that of particles in the pth mass bin; and the third term represents the decrease in n_p due to coagulation of particles in the pth mass bin with other particles to generate more massive particles. All variables in Eq. 3.3 are functions of z.

For non-porous spherical particles of radius r_p, w_{sed} is given by

$$w_{sed} = \frac{2}{9}\frac{\rho_p g r_p^2 f_s}{\eta}, \tag{3.4}$$

where g is the gravitational acceleration of Pluto (61.7 cm s^{-1} at the surface; Stern et al., 2015), η is the dynamic viscosity, in units of Poise, calculated using Sutherland's formula as a function of the temperature T and the appropriate constants for pure N_2 gas (White, 1974)

$$\eta = 1.781 \times 10^{-4} \frac{411.55}{T + 111} \left(\frac{T}{300.55}\right)^{1.5}, \tag{3.5}$$

and f_s is the Cunningham slip correction factor given by

$$f_s = 1 + 1.246Kn + 0.42Kne^{-0.87/Kn}, \tag{3.6}$$

(Pruppacher and Klett, 1978), where Kn is the Knudsen number defined as the ratio of the atmospheric mean free path l to r_p, where l can be written as

$$l = \frac{2\eta}{\rho}\sqrt{\frac{\pi\mu}{8RT}}, \tag{3.7}$$

where ρ is the atmospheric mass density, μ is the mean molecular weight of the atmosphere, and R is the universal gas constant. $f_s \sim 1$ in the continuum regime ($Kn \ll 1$); however, at Pluto's surface, where $T \sim 40$ K and the atmospheric pressure ~ 10 μbar (Stern et al., 2015), $Kn \sim 3000$ for $r_p \sim 0.1$ μm, and thus f_s is large and linear with Kn (kinetics regime). Taking this into account, Eq. 3.4 becomes

$$w_{sed} = A\frac{\rho_p g r_p}{\rho}\sqrt{\frac{\pi\mu}{2RT}} \tag{3.8}$$

where A is a constant that is ~0.5. Eq. 3.8 is the dominant form of the sedimentation velocity throughout Pluto's atmosphere for $r_p < 300$ μm.

Transport by diffusion is not included in the model as it is minor in comparison to sedimentation. The eddy diffusion coefficient K_{zz} has been constrained to be ~1000 $cm^2\ s^{-1}$ by Wong, Fan, et al. (2016) for all altitudes, while the Brownian diffusion coefficient D can be defined as

$$D = \frac{B}{r_p^2 n_a}\sqrt{\frac{RT}{2\pi\mu}} \tag{3.9}$$

in the kinetics limit, where n_a is the number density of air molecules and B is a numerical constant that is ~0.25 (Pruppacher and Klett, 1978). To compare transport by sedimentation, eddy diffusion, and Brownian diffusion, we define a time scale τ, defined as the time needed to traverse d = 1 km in the atmosphere. For sedimentation $\tau \sim d/w_{sed}$; for eddy diffusion $\tau \sim d^2/K_{zz} = 10^7$ s; and for Brownian diffusion $\tau \sim d^2/D$. Figure 3.2 shows τ of these three transport processes for R_f = 0.1 μm, r_m = 10 nm, and D_f = 2. It is clear that sedimentation occurs the fastest, and therefore dominates the transport in Pluto's atmosphere. This outcome is not changed when R_f and r_m are altered within the ranges considered in this work.

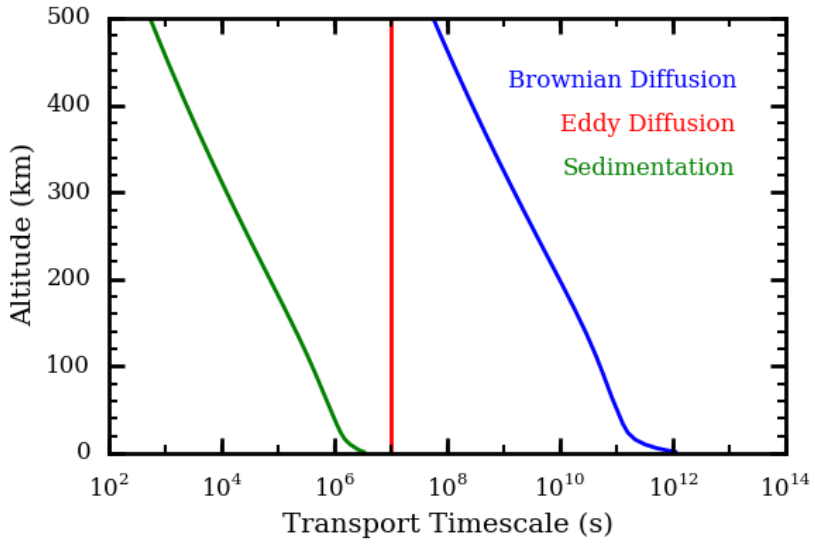

Figure 3.2: The time needed to traverse 1 km in the Pluto atmosphere as a function of altitude for an aggregate particle with R_f = 0.1 μm, r_m = 10 nm, and D_f = 2 undergoing (blue) Brownian diffusion, (red) eddy diffusion, or (green) sedimentation.

The decrease of g with altitude is taken into account in our model, as Pluto's atmosphere is extended with respect to Pluto's radius. The gravitational acceleration

at some altitude z is calculated by multiplying the surface g value by the ratio $R^2/(R+z)^2$, where R is Pluto's radius (1187 km; Stern et al., 2015).

For aggregate particles Eq. 3.8 can also be applied, with R_f in place of r_p, a reduced particle density ρ_p^{agg} in place of ρ_p given by

$$\rho_p^{agg} = \rho_p \left(\frac{R_f}{r_m} \right)^{D_f - 3}, \tag{3.10}$$

and by taking into account porosity by multiplying Eq. 3.8 by a factor Ω (Lavvas, Yelle, and Griffith, 2010)

$$\Omega = \frac{2\beta^2 \left(1 - \frac{\tanh(\beta)}{\beta}\right)}{2\beta^2 + 3\left(1 - \frac{\tanh(\beta)}{\beta}\right)}, \quad \beta = \frac{R_f}{\sqrt{\kappa}}, \tag{3.11}$$

where

$$\kappa = \frac{4r_m^2}{18\psi} \frac{3 - 4.5\psi^{1/3} + 4.5\psi^{5/3} - 3\psi^2}{3 + 2\psi^{5/3}}, \quad \psi = \frac{\rho_p^{agg}}{\rho_p}. \tag{3.12}$$

The standard expression for $K_{i,j}$ (Pruppacher and Klett, 1978; Lavvas, Yelle, and Griffith, 2010) is used in CARMA for both spherical and aggregate particles, where for the latter the radius upon which $K_{i,j}$ depends is R_f instead of r_p. In addition, we assume that coagulation is impeded due to particle charging effects, similar to Titan's aerosols, with the coagulation rate reduced by a factor

$$f_c = \frac{\tau}{e^\tau - 1}, \quad \tau = \frac{q^2 r_i r_j}{kT(r_i + r_j)}, \tag{3.13}$$

where k is Boltzmann constant, and q is the charge density (Fuch, 1964). It is unknown what processes could be responsible for charging aerosols in Pluto's atmosphere, though interactions of the haze particles with ambient ions and electrons created from photolysis and interactions with the Solar wind are likely (Cravens and Strobel, 2015), with the low density of the Pluto atmosphere facilitating charge separation due to differential diffusion of free electrons and positive ions.

As an alternative scenario we also consider spherical haze particles to evaluate the need for low-density aggregates in Pluto's tenuous atmosphere to combat the relatively short sedimentation times. For this simulation we assume that the particles

sedimenting into the model domain from above 500 km are spherical but with the same mass as the aggregate particles, such that they have a radius r_p = 15.87 nm and 12.6 nm, equivalent to the 10 nm and 5 nm aggregate cases, respectively.

Unlike Titan, where condensation of simple hydrocarbons and nitriles onto aerosols only becomes important in the stratosphere (<110 km), far below the altitudes of haze formation (~1000 km; Lavvas, Griffith, and Yelle, 2011; Barth, 2015), condensation of such species on Pluto aerosols may occur at altitudes (~200 km, Figure 3.1) much closer to where the aerosols first form (~500 km; Wong, Fan, et al., 2016), such that it could impact the observed extinction profiles. However, our current model does not take into account condensation onto fractal aggregates. In addition, as the condensation rates can be comparable to reaction rates governing the chemistry of Pluto's atmosphere (Wong, Fan, et al., 2016), a coupled photochemistry-microphysics model will be needed to fully explain the observed extinction profiles of chemical species and aerosols. Despite our limitations, however, we will attempt to quantify the effects of condensation in §3.4.2 using a simple analytic model.

We compare our model results to the solar occultation observations of Pluto's atmosphere obtained by the Alice ultraviolet spectrograph onboard New Horizons during its flyby. The retrieved line of sight (LOS) optical depth is converted into an extinction coefficient α by using the Abel transform (i.e. Kammer et al., 2013) across the full range of altitudes where data was collected, from ~2000 km above the surface to the surface itself. Uncertainties in α at each altitude are computed using a bootstrap Monte Carlo routine. Simulated α profiles are derived from the haze particle size and number density distributions calculated by the model by assuming that these particles have the same optical properties as that of tholins in Titan's atmosphere, with a complex refractive index of $1.65+0.24i$ corresponding approximately to the wavelength range (145–185 nm) of the data (Khare et al., 1984). α is calculated from the product of the number density of haze particles N and the extinction cross section σ of the particles, given by

$$\sigma = Q_e \pi r_p^2 \tag{3.14}$$

for spheres, and

$$\sigma = Q_e \pi r_m^2 N_m^{2/3} \tag{3.15}$$

for aggregates, where Q_e is the extinction efficiency calculated using established Mie scattering codes for aggregates (Tomasko et al., 2008) and spheres (Grainger et al., 2004).

3.4 Results & Discussion

3.4.1 Comparison to Data

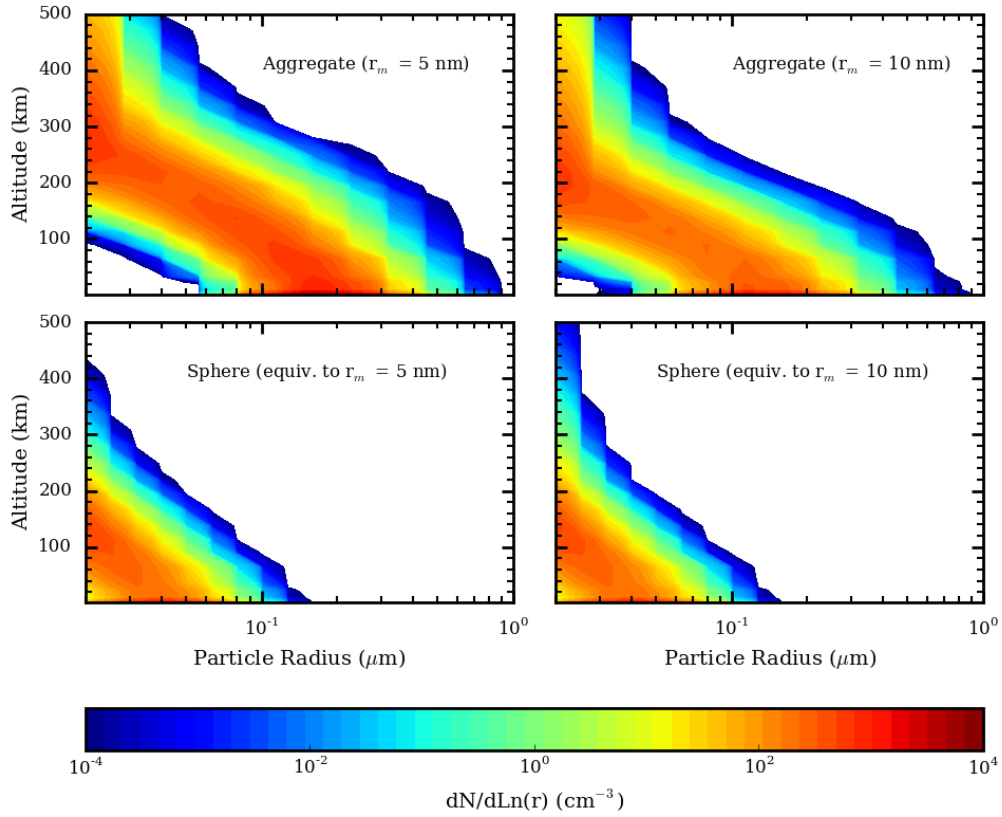

Figure 3.3: Particle number density as functions of altitude and particle radius for the (clockwise from the top left) 5 nm monomer aggregate, 10 nm monomer aggregate, 5 nm monomer-equivalent spherical, and 10 nm monomer-equivalent spherical haze solutions computed by CARMA. Particle radius refers to the true radius r_p for spheres and effective radius R_f for aggregates. Number density is expressed in $dN/dLn(r_p)$ for spheres and $dN/dLn(R_f)$ for aggregates.

Figure 3.3 shows the particle number density, expressed in $dN/dLn(R_f)$ for aggregates and in $dN/dLn(r_p)$ for spheres, as a function of altitude in Pluto's atmosphere and particle radius for the (clockwise from the top left) 5 nm monomer aggregate, 10 nm monomer aggregate, 5 nm monomer-equivalent spherical, and 10 nm monomer-equivalent spherical haze solutions computed by CARMA. The particle size distribution peaks at ~0.1–0.2 μm below 150 km altitude for the aggregate

cases, consistent with particle sizes inferred from forward scattering observations by New Horizons (Gladstone et al., 2016), while for the spherical haze cases the particle radii are smaller by about a factor of 4. The low vertical resolution of our model (~25 km at 50 km altitude) is far too coarse to resolve the low altitude (<80 km), few-km-thick, spatially coherent haze layers that were seen in high phase angle observations (Cheng, Gladstone, and Summers, 2015), which are thought to be generated by gravity waves (Gladstone et al., 2016)—a process not included in our model.

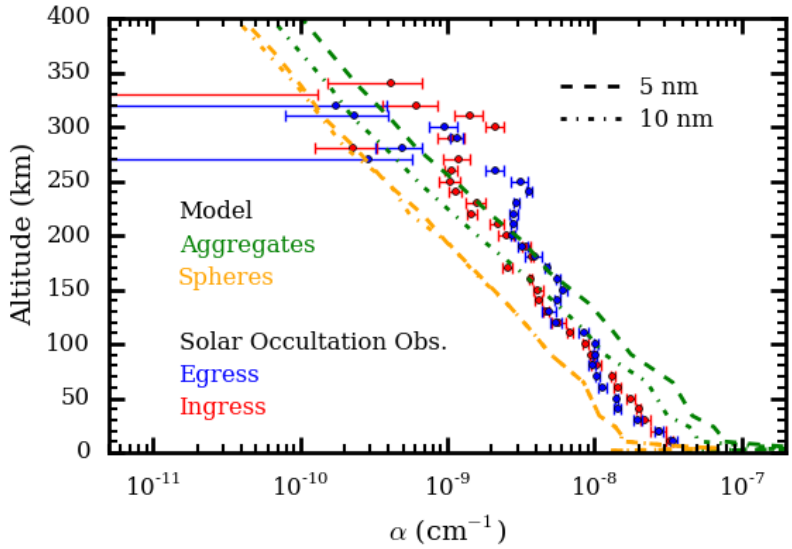

Figure 3.4: The extinction coefficients α as a function of altitude calculated from our model aggregate (green) and spherical (orange) particle haze results, for both the 10 nm monomer (dash dot line) and 5 nm monomer (dashed line) cases (and the equivalent cases for spherical particles), compared to that derived from the ingress (red) and egress (blue) solar occultation observations from New Horizons.

Figure 3.4 compares the extinction coefficients α calculated from our model aggregate (green) and spherical (orange) particle haze results, for both the 10 nm monomer (dash dot line) and 5 nm monomer (dashed line) cases (and the equivalent cases for spherical particles), to that derived from both the ingress (red) and egress (blue) solar occultation observations. We obtain general agreement between the aggregate cases and the data when the downward mass flux of photochemical products is equal to the column-integrated methane destruction rate $\sim 1.2 \times 10^{-14}$ g cm^{-2} s^{-1} computed by the photochemical model of Wong, Fan, et al. (2016). This flux is nearly identical to the haze production flux obtained for Titan using similar microphysical models (Lavvas, Yelle, and Griffith, 2010; Larson, Toon, and

Friedson, 2014), despite Titan being exposed to more solar UV photons, which suggests that haze production may be limited by the availability of haze precursors. By comparison, the same downward mass flux applied to the spherical particle cases underestimates α by a factor of ~3.

It should be noted that, given the significance of condensation and surface deposition as sinks for C_2 hydrocarbons, which prevents them from participating in further photochemistry in the atmosphere that may convert them to tholins Wong, Fan, et al. (2016), the conversion rate of methane to tholins is almost certainly less than 100% (Stansberry, Lunine, and Tomasko, 1989). Thus, the downward mass flux of haze particles should be less than what is presented here. However, the degree of freedom afforded to aggregates by r_m can alleviate this issue. This can be understood by noting that the α profile for the 5 nm aggregate case is almost identical to the 10 nm monomer case, except that the former is greater than the latter by a factor of ~1.5. An alternate case where r_m is set to 1 nm resulted in α values 5 times greater than that of the 10 nm monomer case (not shown). In other words, decreasing r_m has the effect of increasing α, which would compensate for a decrease in α due to a decrease in downward haze particle mass flux. This is because reducing r_m for a fixed R_f increases the porosity of the aggregate and thus decreases its density, which in turn reduces its sedimentation velocity, allowing for more haze particles to stay aloft, increasing α. Thus, the uncertainty in conversion efficiency of methane to tholins prevents us from constraining the aggregate monomer size using occultation observations alone. However, this same degeneracy points strongly to Pluto's haze particles being fractal aggregates, as spherical particles do not have an extra degree of freedom arising from monomers, i.e. decreasing their downward mass flux would just lead to smaller α values.

Figure 3.5 (top) shows variations in the particle size distribution 1.6 km above the surface of Pluto with changes in the particle charge to radius ratio, given in e^-/μm. We find that $q = 30\ e^-/\mu$m offers the best agreement with the retrieved mean particle size (~0.1–0.2 μm) from the forward scattering measurements (Gladstone et al., 2016), which is 2–4 times that obtained from observations of Titan aerosols (Lavvas, Yelle, and Griffith, 2010; Larson, Toon, and Friedson, 2014). This suggests that Pluto's atmosphere may be more amicable to particle charging.

Figure 3.5 (bottom) shows profiles of extinction coefficients corresponding to the particle charge to radius ratios of Figure 3.5 (top), and reveals that α is not significantly perturbed when the charge to radius ratio is varied. This results from the

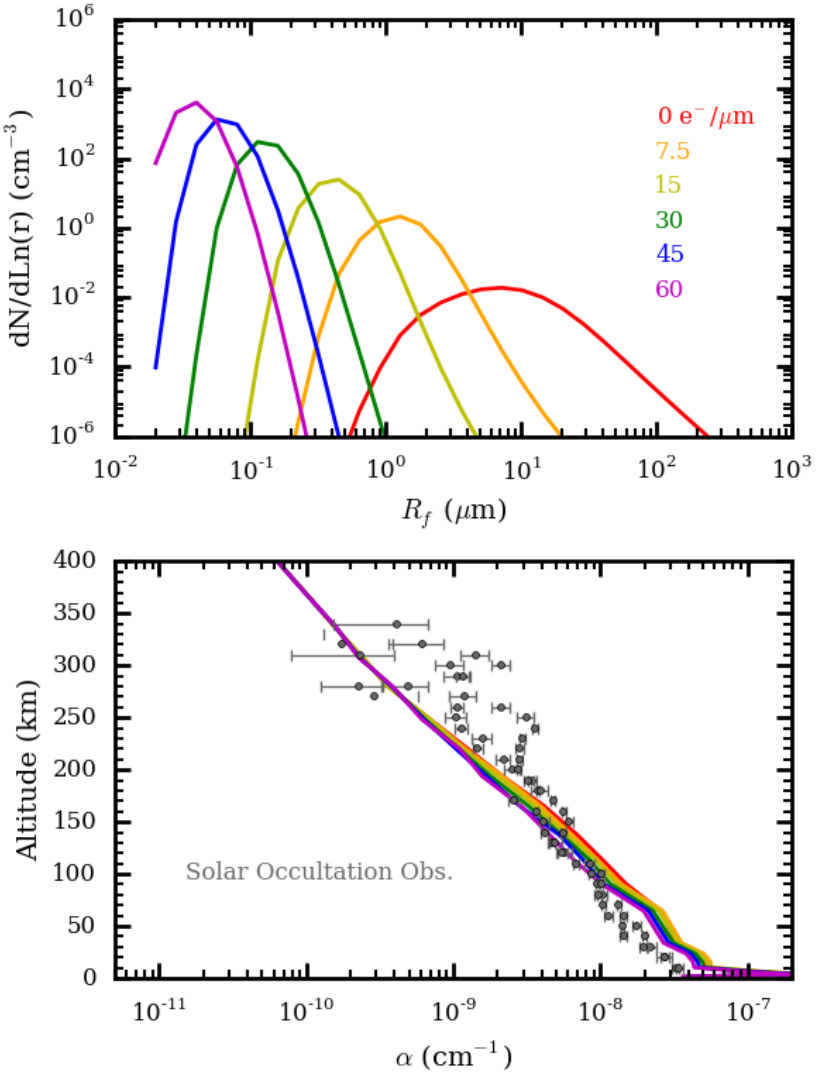

Figure 3.5: (Top) Particle size distributions for charge to particle radius ratios of 0 (red), 7.5 (orange), 15 (yellow), 30 (green), 45 (blue), and 60 e$^-$/μm (magenta). (Bottom) Extinction coefficients α corresponding to the different charge to particle radius ratios compared to the ingress and egress New Horizons solar occultation observations (gray points; ingress and egress data are not distinguished from each other).

similar way the extinction cross section and mass of an aggregate scale with radius, such that a small number of large aggregates would have nearly the same extinction cross section as a large number of small aggregates, provided their total masses were the same. Also, as the density of an aggregate with $D_f = 2$ is inversely proportional to the aggregate effective radius R_f, and Ω varies slowly with R_f (Lavvas, Yelle, and Griffith, 2010), the sedimentation velocity for aggregates in the kinet-

ics regime is largely independent of R_f. Thus, the small differences between the various particle charge to radius ratio cases stem from variations of the extinction efficiency with R_f.

Despite the general agreement between our model and data, it is clear that there are deficiencies. For example, the observations show a somewhat steeper α profile compared to what our models produce, characterized by nearly vertical "steps" in between gentler slopes, the latter of which appear to match the slope of our model α profiles (see, for example, the fit between the data and the 5 nm monomer aggregate curve between 150 and 200 km). One possible explanation is that Titan's haze is not a perfect analogy for that of Pluto. On Titan, haze production is effected by both solar UV photons and energetic particles from Saturn's magnetic field, whereas for Pluto this latter energy source either does not exist (Elliot, Dunham, et al., 1989), or is replaced by energetic particles from the solar wind, which could lead to different haze production schemes. In addition, Pluto's atmospheric chemistry may be sufficiently different from Titan such that more nitriles are incorporated into the haze particles by comparison Wong, Yung, and Gladstone (2015). Furthermore, the 10 times higher mixing ratio of CO in Pluto's atmosphere (~500 ppm; Lellouch et al., 2011) vis-á-vis Titan (~50 ppm; Kok et al., 2007) may result in more oxidized haze particles. These effects can lead to different refractive indices for the Pluto haze particles such that using those for Titan tholins may not be appropriate. Quantifying how these subtle differences in haze composition change their refractive indices will require laboratory measurements of analogous materials.

Another possible effect not considered in our model is that of dynamics. Gladstone et al. (2016) showed that vertical velocities of 20 cm s^{-1} at 200 km altitude and <10 cm s^{-1} below 75 km altitude are possible due to gravity waves arising from sublimation and orographic forcing, which are ~10 times larger than the sedimentation velocity above the gravity wave saturation altitude of ~10 km (Figure 3.2). Though these waves could cause the emergence of layering in the haze, it is unknown how they could affect the overall slope of the extinction profile, as the calculated velocities oscillate between upward and downward motion that may cancel out at longer length scales.

Finally, the fractal dimension of Pluto's hazes may not be exactly 2, considering the range in D_f, 1.75–2.5, estimated for Titan (Cabane et al., 1993). If $D_f > 2$, then the aggregate case would become more similar to the spherical case. If $D_f < 2$, then the increased porosity of the aggregates would decrease their sedimentation

velocities and increase their coagulation rates. As the cross sectional area of the aggregate now grows faster than its mass, this leads to an increase in extinction at lower altitudes, which is not seen in the New Horizons observations.

3.4.2 Effects of Condensation

Another possible cause for the discrepancies between model and data is condensation of hydrocarbons and nitriles onto the aggregates, which is necessary to explain the observed extinction due to these chemical species (Wong, Fan, et al., 2016). As mentioned in §3.3, our current photochemical and microphysical models are decoupled from each other, so a self-consistent treatment of condensation and its impact on both chemical species' mixing ratios and aerosol number density and size distributions is not possible. However, we can still estimate the effects of condensation on α due to changes in particle and monomer size and number density by using the net condensation rates calculated by the photochemical model of Wong, Fan, et al. (2016) (Figure 3.1), scaling relations, and mass balance.

Consider sedimenting particles composed of a condensed layer of hydrocarbons and nitriles around a "core" of tholin aggregate. From the net condensation rates, we find a total column-integrated condensation "flux" of $\sim 8.1 \times 10^{-15}$ g cm^{-2} s^{-1}, which is about 2/3 of the downward mass flux of haze particles. Thus, it is unlikely for the condensed material to completely inundate the aggregate such that the particle becomes non–porous; instead, it can be assumed that the condensed material merely fills in some of the pores within the aggregate. For simplicity we assume that the condensed mass contributes entirely to increasing the monomer size and/or fusing separate monomers together into single, larger monomers, while keeping R_f and D_f constant. In such a scenario, the mass flux of particles Φ_{ij} in mass bin j through an altitude level i in the atmosphere would be equal to

$$\Phi_{ij} = \rho_{ij} v_{ij} = \rho^a_{ij} v_{ij} + \Phi^c_{ij}, \tag{3.16}$$

where ρ_{ij} is the total mass density of particles in bin j at altitude i, equal to the mass of a single particle times their number density N_{ij}, ρ^a_{ij} is the total mass density of just the aggregate core in bin j at altitude i, v_{ij} is the sedimentation velocity of the composite particle in bin j at altitude i, and Φ^c_{ij} is the net column rate of condensation onto a haze particle in bin j at altitude i, calculated by multiplying the net condensation rates in Figure 3.1 by the thickness of altitude layer i. Expanding the mass densities according to Eq. 3.2 gives

$$N_{ij}\frac{4}{3}\pi\rho_p r'_{mij}R^2_{fij}v_{ij} = N_{ij}\frac{4}{3}\pi\rho_p r_{mij}R^2_{fij}v_{ij} + \Phi^c_{ij}, \tag{3.17}$$

where r'_{mij} is the monomer size after the particle passes through altitude i and has changed due to condensation, and r_{mij} is the monomer size before passing through altitude i. In other words, we assume that condensation at each altitude level happens instantaneously in the middle of that level, with a condensation rate depending on how fast the particle was traveling through that level. Thus, $r'_{mij} = r_{m(i+1)j}$, where i increases upwards. Isolating the r_m's gives

$$r_{mij} = r_{m(i+1)j} + \frac{3\Phi^c_{ij}}{4N_{ij}\pi\rho_p R^2_{fij}v_{ij}}. \tag{3.18}$$

In Wong, Fan, et al. (2016), the condensation rate is assumed to be proportional to the surface area of the haze particles, which were taken to be spheres with radius R_f as a compromise between the increased surface area of aggregates compared to spheres and the limited diffusive pathways a condensate molecule can take to get into the pore spaces of the aggregate. We thus calculate Φ^c_{ij} by scaling the total net column rate of condensation at altitude i by the total surface area of particles in bin j at that altitude

$$\Phi^c_{ij} = \Phi^c_i \frac{N_{ij}R^2_{fij}}{\sum_j N_{ij}R^2_{fij}}. \tag{3.19}$$

We have thus derived in Eqs. 3.18–3.19 an iterable expression that can calculate r_m for every altitude and particle bin given r_m at the top of the model and Φ^c_i. Eq. 3.18 is iterated multiple times per ij pair in order to assert self-consistency, as v_{ij} depends on r_{mij}. For a starting r_m = 10 nm for all bins at 500 km and Φ^c_i given by Figure 3.1, Figure 3.6 shows the change in the weighted mean of r_m as a function of altitude, weighted by the number density of aggregates, due to condensation by HCN (red), C_2H_2 (yellow), C_2H_4 (green), C_2H_6 (blue), and all of these species combined (black). Minor differences in altitude exist between where each chemical species condense the fastest (i.e. where r_m grows the fastest), but they are all within ~50 km of each other, and all occur above 200 km, which is consistent with Figure 3.1, while a minor amount of r_m growth also occurs down to 100 km. These two altitudes also coincide roughly with the bottoms of the upper two steep "steps" in the observed extinction profiles (Figure 3.4), suggesting some connection between

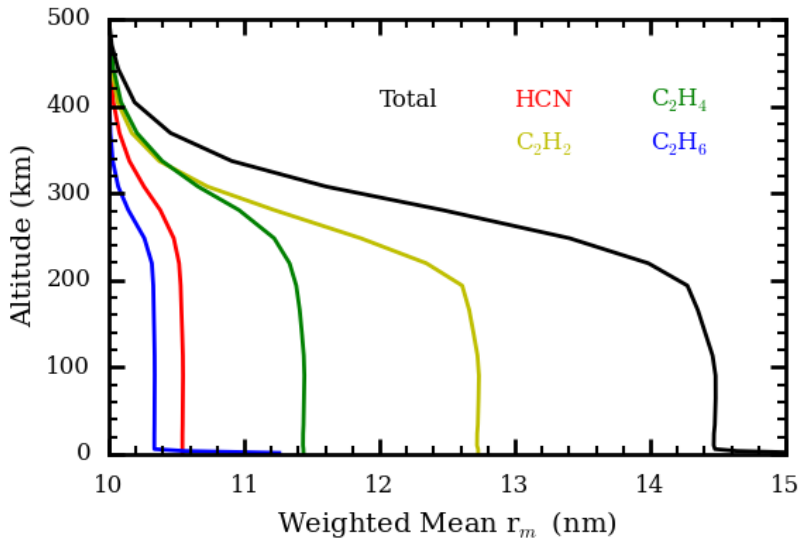

Figure 3.6: The change in mean monomer radius r_m for the 10 nm monomer aggregate case, weighted by the particle number density, as a function of altitude due to condensation of HCN (red), C_2H_2 (yellow), C_2H_4 (green), and C_2H_6 (blue). The total change in weighted mean r_m is shown in black.

condensation and extinction. The third "step" at ~75 km, which is more muted than the top two steps in the egress profile and is absent in the ingress profile correspond to a warmer region of the atmosphere (Figure 3.1), where the r_m growth curve reverses direction slightly due to net evaporation (not shown in Figure 3.1). The large increase in r_m occurring near the surface resulting mostly from C_2H_6 condensation and rainout is not in the altitude range of the data.

There are three ways in which condensation can affect α: (1) By changing the refractive index of the haze particles, (2) by increasing the mass of particles such that their sedimentation velocities change, which in turn affects the equilibrium number density and (3) by directly changing the cross sections of the aggregates and/or their monomers. The refractive indices of hydrocarbon and nitrile ices in the FUV are not well known (Bergh et al., 2008; Hendrix, Domingue, and Noll, 2013) and therefore we cannot speak to the validity of (1), though α is roughly linear with the imaginary part of the refractive index, and so altering its value by a factor of a few could improve the agreement between our model and the data. Options (2) and (3) can be evaluated using scaling relations. Consider again Eq. 3.16, but only the left and middle terms; expanding the latter out and combining with Eqs. 3.8, 3.10–3.12 gives

$$\Phi \propto N r_m^2, \tag{3.20}$$

where again we have assumed that R_f and D_f stay constant. A similar proportionality can be written for α,

$$\alpha \approx \sigma N \propto Q_e r_m^{2/3} N. \tag{3.21}$$

Combining Eqs. 3.20 and 3.21 thus gives

$$\alpha \propto Q_e r_m^{-4/3} \Phi. \tag{3.22}$$

Note that, were R_f not held constant, it would enter Eq. 3.22 as a factor $R_f^{-2/3}$. Using the aggregate scattering code of Tomasko et al. (2008) and fixing R_f to 20 nm and D_f to 2 while changing r_m shows that $Q_e \propto r_m^0.64$, so that

$$\alpha \propto r_m^{-0.69} \Phi. \tag{3.23}$$

Including condensation increases Φ by a factor of 5/3 over the flux corresponding to just sedimenting tholins, while r_m increases by a factor of 50%, resulting in an increase in α by ~26%. In other words, the increase in mass, and thus extinction efficiency of the particles dominates the decrease in the particle number density caused by an increased sedimentation velocity, resulting in greater extinction overall. This is the opposite of what is seen in the observations, though the effect is small in comparison to the magnitude of the "steps", which decrease α with respect to a smoothly, downward increasing profile by a factor of ~2–3 (see, for example, the difference between the data and the 5 nm monomer aggregate model curve at ~130 km).

The above calculation assumes that the condensed mass only contributes to increasing the aggregate monomer size. Several alternative scenarios exist, which include (1) condensation affecting both r_m and R_f, while keeping N_m and D_f fixed, corresponding to the condensate molecules depositing on all available aggregate surfaces equally, and (2) condensation affecting both R_f and N_m, while keeping r_m and D_f fixed, corresponding to the condensate forming a thin shell around the aggregate, leaving pore spaces unaffected. However, after repeating our above procedure (Eqs. 3.16–3.23) for these alternate scenarios, we find that none of them decrease α after

condensation occurs. The scenarios where D_f changes were not investigated, as the Tomasko et al. (2008) model has not been tested for $D_f \neq 2$. Nonetheless, the case where condensation affects both r_m and D_f and not R_f and N_m,, corresponding to the infilling of the pore spaces of the aggregate offers another likely possibility, but will require a more rigorous treatment of aggregate extinction.

The simplicity of Eqs. 3.16–3.23 begets several caveats. For example, coagulation of the composite particles is not taken into account, the rate of which would change due to the different mass, size, and number density of the particles. The condensation rates themselves could also change due to variations in aggregate surface area, sticking coefficient, and number density. In other words, a more realistic treatment of this problem would require a self-consistent aggregate microphysical model that takes into account coagulation and condensation, and that which feeds back on the photochemistry.

We have shown that the hazes of Pluto are likely composed of fractal aggregates similar to those of Titan, with their distribution shaped by sedimentation and coagulation. The mean haze particle sizes and extinction profiles calculated by our microphysical model are in general agreement with forward scattering and solar occultation observations obtained by New Horizons. Discrepancies between the model results and the observations could be due to subtle differences in composition between the Pluto hazes and the tholins derived in Earth laboratories caused by different chemistry, formation processes, and nucleation and condensation of HCN and C_2 hydrocarbons onto the haze particles.

This research was supported in part by a grant from the New Horizons Mission. YLY and RLS were supported in part by the Cassini UVIS program via NASA Grant JPL.1459109, NASA NNX09AB72G grant to the California Institute of Technology. PG was supported in part by an RTD grant from JPL.

References

Bardeen, C. G. et al. (2008). “Numerical simulations of the three dimensional distribution of meteoric dust in the mesosphere and upper stratosphere.” In: *Journal of Geophysical Research* 113, p. D17202.

Barth, E. L. (2014). “P33B-4036: Haze particles and condensation in Pluto’s atmosphere explored through microphysical modeling.” Presented at the *American Geophysical Union Fall Meeting 2014*, San Francisco, USA.

Barth, E. L. (2015). “300.02: Condensation of trace species to form ice layers in Titan’s stratosphere.” Presented at the *Division of Planetary Sciences Meeting 47*, National Harbor, USA.

Bergh, C. de et al. (2008). “Laboratory data on ices, refractory carbonaceous materials, and minerals relevant to transneptunian objects and centaurs.” In: *The Solar System beyond Neptune.* Ed. by M. A. Barucci et al. Tucson, USA: University of Arizona Press, pp. 483–506.

Cabane, M. et al. (1993). “Fractal aggregates in Titan’s atmosphere”. In: *Planetary and Space Science* 41, pp. 257–267.

Cheng, A. F., G. R. Gladstone, and M. and Summers (2015). “105.02: Discovery of hazes in Pluto’s atmosphere.” Presented at the *Division of Planetary Sciences Meeting 47*, National Harbor, USA.

Cravens, T. E. and D. F. Strobel (2015). “Pluto’s solar wind interaction: Collisional effects.” In: *Icarus* 246, pp. 303–309.

Cruikshank, D. P. and R. H. Brown (1986). “Satellites of Uranus and Neptune, and the Pluto-Charon system.” In: *Satellites*. Ed. by J. A. Burns and M. S. Matthews. Tucson, USA: University of Arizona Press, pp. 836–873.

Dias-Oliveira, A. et al. (2015). “Pluto’s atmosphere from stellar occultations in 2012 and 2013.” In: *The Astrophysical Journal* 811, p. 53.

Elliot, J. L., A. Ates, et al. (2003). “The recent expansion of Pluto’s atmosphere.” In: *Nature* 424, pp. 165–168.

Elliot, J. L., E. W. Dunham, et al. (1989). “Pluto’s atmosphere”. In: *Icarus* 77, pp. 148–170.

Fuch, N. A. (1964). *The Mechanics of Aerosols.* Pergamon Press, New York (translated by R.E. Daisley and M. Fuchs).

Gladstone, G. R. et al. (2016). “The atmosphere of Pluto as observed by New Horizons.” In: *Science* 351, p. 1280.

Grainger, R. G. et al. (2004). “Calculation of Mie derivatives”. In: *Applied Optics* 43, pp. 5386–5393.

Gulbis, A. A. S. et al. (2015). “Observations of a successive stellar occultation by Charon and graze by Pluto in 2011: Multiwavelength SpeX and MORIS data from the IRTF.” In: *Icarus* 246, pp. 226–236.

Hendrix, A. R., D. L. Domingue, and K. S. Noll (2013). “Ultraviolet properties of planetary ices.” In: *The science of Solar System ices.* Ed. by M. S. Gudipati and J. Castillo-Rogez. New York, USA: Springer-Verlag.

Jacobson, M. Z. and R. P. Turco (1994). “Modeling coagulation among particles of different composition and size.” In: *Atmospheric Environment* 28, pp. 1327–1338.

Kammer, J. A. et al. (2013). “Composition of Titan’s upper atmosphere from Cassini UVIS EUV stellar occultations”. In: *Planetary and Space Science* 88, pp. 86–92.

Khare, B. N. et al. (1984). “Optical constants of organic tholins produced in a simulated Titanian atmosphere: From soft X-ray to microwave frequencies.” In: *Icarus* 60, pp. 127–137.

Kok, R. de et al. (2007). “Oxygen compounds in Titan’s stratosphere as observed by Cassini CIRS.” In: *Icarus* 186, pp. 354–363.

Larson, E. J. L., O. B. Toon, and A. J. Friedson (2014). “Simulating Titan’s aerosols in a three dimensional general circulation model”. In: *Icarus* 243, pp. 400–419.

Larson, E. J. L., O. B. Toon, R. A. West, et al. (2015). “Microphysical modeling of Titan’s detached haze layer in a 3D GCM”. In: *Icarus* 254, pp. 122–134.

Lavvas, P., C. A. Griffith, and R. V. Yelle (2011). “Condensation in Titan’s atmosphere at the Huygens landing site”. In: *Icarus* 215, pp. 732–750.

Lavvas, P., R. V. Yelle, and C. A. Griffith (2010). “Titan’s vertical aerosol structure at the Huygens landing site: Constraints on particle size, density, charge, and refractive index”. In: *Icarus* 210, pp. 832–842.

Lellouch, E. et al. (2011). “High resolution spectroscopy of Pluto’s atmosphere: Detection of the 2.3 μm CH4 bands and evidence for carbon monoxide.” In: *Astronomy and Astrophysics* 530, p. L4.

Olkin, C. B. et al. (2014). “Pluto’s atmospheric structure from the July 2007 stellar occultation.” In: *Icarus* 239, pp. 15–22.

Owen, T. C. et al. (1993). “Surface ices and atmospheric composition of Pluto.” In: *Science* 261, pp. 745–748.

Person, M. J. et al. (2013). “The 2011 June 23 stellar occultation by Pluto: Airborne and ground observations.” In: *The Astronomical Journal* 146, p. 83.

Pruppacher, H. R. and J. D. Klett (1978). *Microphysics of clouds and precipitation*. D. Reidel Publishing Company, Dordrecht, Holland.

Stansberry, J. A., J. I. Lunine, W. B. Hubbard, et al. (1994). “Mirages and the nature of Pluto’s atmosphere”. In: *Icarus* 111, pp. 503–513.

Stansberry, J. A., J. I. Lunine, and M. G. Tomasko (1989). “Upper limits on possible photochemical hazes on Pluto.” In: *Geophysical Research Letters* 16, pp. 1221–1224.

Stern, S. A. et al. (2015). “The Pluto system: Initial results from its exploration by New Horizons.” In: *Science* 350, p. 292.

Tomasko, M. G. et al. (2008). “A model of Titan’s aerosols based on measurements made inside the atmosphere”. In: *Planetary and Space Science* 56, pp. 669–707.

Toon, O. B., C. P. McKay, et al. (1992). “A physical model of Titan’s aerosols”. In: *Icarus* 95, pp. 24–53.

Toon, O. B., R. P. Turco, et al. (1988). “A multidimensional model for aerosols: Description of computational analogs.” In: *Journal of the Atmospheric Sciences* 45, pp. 2123–2143.

Turco, R. P. et al. (1979). “A one-dimensional model describing aerosol formation and evolution in the stratosphere: I. Physical processes and mathematical analogs.” In: *Journal of the Atmospheric Sciences* 36, pp. 699–717.

West, R. A. and P. H. Smith (1991). “Evidence for aggregate particles in the atmospheres of Titan and Jupiter”. In: *Icarus* 90, pp. 330–333.

White, F. M. (1974). *Viscous Fluid Flow.* McGraw-Hill, New York, USA.

Wolf, E. T. and O. B. Toon (2010). “Fractal organic hazes provided an ultraviolet shield for early Earth”. In: *Science* 328, pp. 1266–1268.

Wong, M. L., S. Fan, et al. (2016). “Photochemical model of hydrocarbons on Pluto and comparison to New Horizons observations.” In: *Icarus*. Submitted. Preprint available from http://web.gps.caltech.edu/ yly/dmp/wong/.

Wong, M. L., Y. L. Yung, and G. R. Gladstone (2015). “Pluto’s implications for a snowball Titan.” In: *Icarus* 246, pp. 192–196.

Young, E. F. et al. (2008). “Vertical structure in Pluto’s atmosphere from the 2006 June 12 stellar occultation.” In: *The Astronomical Journal* 136, pp. 1757–1769.

Zhu, X., D. F. Strobel, and J. T. Erwin (2014). “The density and thermal structure of Pluto’s atmosphere and associated escape processes and rates.” In: *Icarus* 228, pp. 301–314.

Chapter 4

AGGREGATE PARTICLES IN THE PLUMES OF ENCELADUS

Gao, P. et al. (2016). "Aggregate particles in the plumes of Enceladus". In: *Icarus* 264, pp. 227–238. DOI: 10.1016/j.icarus.2015.09.030.

4.1 Abstract

Estimates of the total particulate mass of the plumes of Enceladus are important to constrain theories of particle formation and transport at the surface and interior of the satellite. We revisit the calculations of A. P. Ingersoll and Ewald (IE11), who estimated the particulate mass of the Enceladus plumes from strongly forward scattered light in Cassini ISS images. We model the plume as a combination of spherical particles and irregular aggregates resulting from the coagulation of spherical monomers, the latter of which allows for plumes of lower particulate mass. Though a continuum of solutions are permitted by the model, the best fits to the ISS data consist either of low mass plumes composed entirely of small aggregates or high mass plumes composed of mostly spheres. The high particulate mass plumes have total particulate masses of $(166 \pm 42) \times 10^3$ kg, consistent with the results of A. P. Ingersoll and Ewald (IE11). The low particulate mass plumes have masses of $(25 \pm 4) \times 10^3$ kg, leading to a solid to vapor mass ratio of 0.07 ± 0.01 for the plume. If indeed the plumes are made of such aggregates, then a vapor-based origin for the plume particles cannot be ruled out. Finally, we show that the residence time of the monomers inside the plume vents is sufficiently long for Brownian coagulation to form the aggregates before they are ejected to space.

4.2 Introduction

Enceladus' plumes provide an indirect way to study the subsurface. In particular, the ratio of ice particle to vapor mass can serve as an important constraint of ice particle formation and transport (IE11, henceforth IE11). IE11 examined Cassini Imaging Science System (ISS) images of the plumes at small scattering angles from 2.2–5.3°, where forward scattering is dominated by ice grains as opposed to water vapor. They then fit the resulting phase curves to various mass and shape distributions, assuming that the ice grains are solid spherical or ellipsoidal particles. However, the large particle to vapor mass ratio calculated by IE11 could not be easily

explained by any existing theoretical models. Furthermore, recent results from the Cassini Cosmic Dust Analyzer (CDA) (Kempf, S., Cassini Project Science Meeting, Jan 22, 2015, and private communication) indicate that the particulate mass may be a factor of ten lower than the estimates of IE11. Since the defining property of the plume particles is strong forward scattering, an alternative model for the plume is one made up of aggregates.

An aggregate is a particle of irregular shape composed of smaller subunits (or "monomers") stuck to each other. The monomers are usually composed of simpler shapes, such a spheres, plates, or columns, depending on the formation mechanisms. Aggregates form under many different settings. For example, the hazes in the atmospheres of Jupiter and Titan are thought to be composed of hydrocarbon aggregates (R. A. West and Smith, 1991; Tomasko, Doose, Engel, et al., 2008; Zhang et al., 2013); Saturn's F-ring is likely populated by ice aggregate particles (Vahidinia et al., 2011); and cirrus cloud particles on Earth take on a variety of non-spherical shapes, ranging from fernlike and fractal geometries to aggregates of irregular shapes (Yang and Liou, 1998). In particular, ice clouds that form as a result of strong vertical motions are dominated by aggregate particles (Baum et al., 2011; Heymsfield et al., 2002). Since aggregates form under such a wide variety of conditions, it is plausible that they could form in the plumes of Enceladus.

Thanks to the diversity of instruments on Cassini, the plumes are well studied. There are good estimates of water vapor mass from the Ultraviolet Imaging Spectrograph (UVIS) instrument (Tian et al., 2007; Hansen et al., 2011, for example), as well as that of other minor gaseous constituents, such as carbon dioxide, methane, ammonia, and argon from the Ion and Neutral Mass Spectrometer (INMS) (Waite Jr et al., 2009). Data from Cassini CDA suggests that the ice particles in the plumes can be broadly classified into two types: slow, large, salt-rich grains that tend to fall back onto the surface, and fast, salt-poor grains that escape into the E-ring (Postberg, Schmidt, et al., 2011). Ice particle velocity distributions were measured using the Visual and Infrared Mapping Spectrometer (VIMS) (Hedman, Nicholson, et al., 2009) and ISS (IE11). However, the shapes of the particles remain mostly unconstrained by observations and are usually assumed to be spherical or oblate/prolate, such as in C. C. Porco et al. (2006) and IE11. In this study, we derive estimates for the total particulate mass of the Enceladus plumes by extending the range of possible particle shapes to aggregates.

4.3 Aggregate Model

Aggregate particles are defined by two parameters: their fractal dimension D and their monomer radius r_m. These two quantities are related to the number of monomers that make up the aggregate N_m and the radius of the aggregate particle r by

$$N_m = \left(\frac{r}{r_m}\right)^D. \tag{4.1}$$

A typical value of D for aggregates in the Solar System is around 2. For example, it has been shown that $D = 2$ is a good approximation for the aggregate particles in the Titan hydrocarbon haze, where the actual dimension may vary between 1.75 and 2.5 (Cabane et al., 1993). $D = 2$ is also appropriate for snowflakes and cirrus cloud ice crystals on Earth, which have variations in D between 1.9 and 2.3 (Westbrook, Ball, and Field, 2006; Schmitt and Heymsfield, 2010). Zhang et al. (2013) further showed that $D = 2$ aggregates can be used to fit Cassini ISS observations of the Jupiter stratospheric aerosols. Such particles have masses that scale linearly with surface area, like a sheet, though the particle itself is a 3–dimensional object. As a result, these particles tend to have small masses associated with large scattering cross sections.

By comparison, r_m values vary considerably across different types of aggregates. For example, $r_m = 10$ nm for the stratospheric aerosols of Jupiter (Zhang et al., 2013) and 40 nm for Titan's haze aggregates (Tomasko, Doose, Dafoe, et al., 2009), but these values are easily dwarfed by that of Saturn's F ring particles, which can reach a few microns (Vahidinia et al., 2011), while ice crystal monomers on Earth can be hundreds of microns across (Kajikawa and Heymsfield, 1989). We will therefore leave r_m as a free parameter in our model that will be varied to best fit the data. As a simplification, we assume that all aggregates in the plume have monomers of the same r_m.

Equation 4.1 leads to a minimum size r_{min} for an aggregate of

$$r_{min} = 2^{\frac{1}{D}} r_m, \tag{4.2}$$

where we have chosen $N_m = 2$ as the minimum number of monomers an aggregate can have. Particles with $r < r_{min}$ are assumed to be spherical with radius r. To simplify the problem and reduce the number of free parameters, we further assume that both spherical and aggregate particles "share" the same particle size distribution

$$\frac{dN}{dlnr} = N_0 (r/r_0)^{f-3} / [1 + (r/r_0)^{2f}], \tag{4.3}$$

which is the number of particles in the natural log of radius interval $dln(r)$, with N_0 as a parameter that scales with the particle number density, f as a positive width factor, and r_0 as the median radius of the particle mass distribution given by

$$\frac{dM(r)}{dr} = \frac{2M_0}{\pi r_0} \frac{f(r/r_0)^{f-1}}{1 + (r/r_0)^{2f}}, \tag{4.4}$$

where

$$M(r) = \frac{2M_0}{\pi} \arctan\left[\left(\frac{r}{r_0}\right)^f\right] \tag{4.5}$$

is the total mass of particles with radius between 0 and r, and M_0 is the total mass of particles. r_0 splits the mass distribution into equal halves, with the width of the distribution governed by f; small f values indicate wide distributions while large f values indicate narrow distributions. M_0, r_0, and f are free to vary in the model during optimization of the fit to the data. Eqs. 4.3 - 4.5 are the same distribution functions given in IE11, which were chosen due to their relative simplicity and their ability to capture both sharply peaked and asymptotic functional forms with only two free parameters. Figure 4.1 shows a schematic of how the aggregate and spherical particles "share" the $dM(r)/dr$ distribution in our model. Particles with $r > r_{min}$ are assumed to be aggregates with radius r given in Eq. 4.1 and r_m defined by Eq. 4.2; they follow the size distribution of Eq. 4.3 with some given r_0 and f values. Particles with $r < r_{min}$ are assumed to be spheres of radius r that follow the same size distribution as the aggregates, with the same r_0 and f values. With these definitions, $dM(r)/dr$ has a discontinuity at $r = r_{min}$. This is caused by the different ways the mass of single particles (aggregate or spheres) scales with r while keeping N_0 fixed for both the aggregate and spherical sections of the size distribution. The discontinuity is not shown in Figure 4.1, and we avoid it in our calculations, as discussed below.

4.4 Observations and Model Setup

Following the procedure of IE11, we use the following relationship to estimate total plume particulate mass (Eq. 4 of that paper):

$$R(\theta) = \frac{M_0}{4\rho_{ice}} \int \frac{A_p Q_{sca} P(\theta)(dN/dln(r))dln(r)}{V_p(dN/dln(r))dln(r)}, \tag{4.6}$$

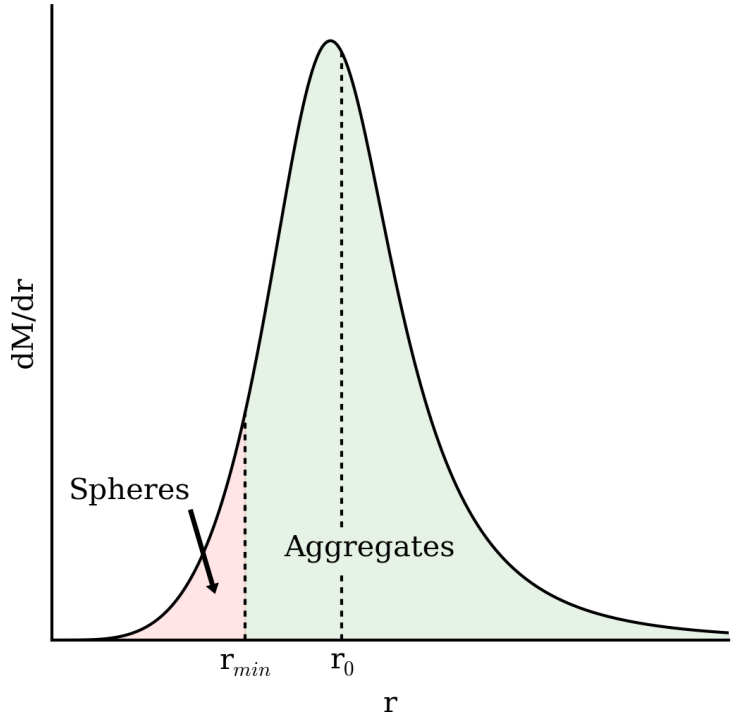

Figure 4.1: A schematic of the plume particle mass distribution dM/dr as a function of the particle radius r, with the median particle radius r_0 and minimum aggregate radius r_{min} labelled.

where M_0 is now the total particulate mass of the plume; $A_p Q_{sca}$ is the scattering cross section of the particle, which, for spherical particles, can be split into the geometric cross section of the particle $A_p = \pi r^2$ and the scattering efficiency Q_{sca}; $P(\theta)$ is the scattering phase function; θ is the scattering angle, which is given in Table 1 of IE11; V_p is the solid volume of each particle, given by $(4/3)\pi r^3$ for spheres and $(4/3)\pi r_m^3 N_m$ for aggregates; $\rho_{ice} = 0.917$ g cm^{-3} is the density of ice; and r is the particle radius, as given for aggregates and spheres in Section 4.3. $R(\theta)$ is defined as

$$R(\theta) = \int \frac{I}{F} dA, \tag{4.7}$$

where I is the measured radiance, πF is the solar irradiance, and the integral is taken over the area A of the image projected onto a plane at the distance of Enceladus to Cassini. The values and associated uncertainties of $R(\theta)$ are also listed in Table 1 of

IE11. Only the wide-angle camera (WAC) images are used. In order to remove the bias of the data towards scattering angles where more observations were taken, we repeat the procedure of IE11 and grouped the 18 brightness measurements into 10 data points by scattering angle, and averaged the brightness values and uncertainties within each group.

In order to sample multiple scattering angles the observations were taken at multiple orbital phases. However, Hedman, Gosmeyer, et al. (2013) showed that the brightness of the plumes varied as a function of orbital phase, even when scattering was taken into account, indicating variability in the intensity of the plumes. They showed that the plume brightness increased rapidly from an orbital phase of 90° to 180°, while below 90° the changes in brightness were much more gradual (see their Figure 4). Our observations, as given in Table 1 of IE11, were taken at orbital phases of 7.68° to 55.93°, well within the "gradual" part of the orbit. Therefore, while the intensity of the plume still changed during our observational period, we will assume that the changes are minor compared to brightness changes due to particle scattering.

We calculate the Mie scattering cross section and phase function of the spherical particles using Grainger et al. (2004), while those of the aggregates are calculated using the model of Tomasko, Doose, Engel, et al. (2008, henceforth T08), a detailed description of which can be found in the appendix of that paper. The T08 model is a fast parametrization valid only for $D = 2$ due to the computationally intensive calculations required for a model of aggregates of arbitrary dimension (Mishchenko, Travis, and Mackowski, 1996); as discussed in Section 4.3, $D = 2$ is valid for many types of aggregates in the Solar System, including ice particles in Earth clouds. A visual description of such particles is found in Figure 1 of R. A. West and Smith (1991). The aggregate scattering model considers each aggregate to be a collection of spherical monomers that scatter and absorb as Mie spheres; the total intensity of the scattered light from the aggregate is then the superposed intensity of scattered light from all the monomers in the aggregate. For more complex interactions, such as repeated scattering and absorption by multiple monomers, correction factors are added that are functions of N_m, the refractive index, and the size parameter of the monomers

$$x_m = \frac{2\pi r_m}{\lambda}, \tag{4.8}$$

where λ is the wavelength of the radiation being scattered. The correction factors are empirical and listed in Table A2 of Appendix A of T08. Only cases with x_m between 10^{-4} and 1.5 have currently been validated; and extrapolations to different x_m values become increasingly uncertain the farther they are from the tested range of values (see again Appendix A of T08). The T08 model has been used to fit observations of Titan's haze, as well as that of the stratospheric aerosols of Jupiter (Zhang et al., 2013) and aggregate particles created in laboratory experiments (Bar-Nun, Dimitrov, and Tomasko, 2008). We assume a real index of refraction of 1.31 and an imaginary index of refraction of 0.0005 for ice in our scattering calculations for the three Cassini ISS wavelength channels considered (VIO, 420 nm; CLR, 635 nm; IR3, 918 nm), as with IE11 (Meng et al., 2010).

In order to avoid the discontinuity in $dM(r)/dr$, we treat particles of different sizes separately by discretizing $dN/dlnr$ into 25 bins in our calculations, with a minimum particle radius of 80 nm and a particle volume ratio of 2 between successive bins. We then approximate the integrals in Eq. 4.6 as summations over the size bins, so that different forms of A_p, Q_{sca}, $P(\theta)$, and V_p can be used depending on whether the bin corresponds to spherical particles or aggregate particles. This enables each integral to sum over both types of particles across the entire size range, provided N_0 is a constant that drops out of Eq. 4.6, and ensures that M_0 is a constant that applies to the entire plume, as $M_0 = \rho_{ice} \int V_p(dN/dln(r))dln(r)$. The minimum particle size is set to prevent an infinite integral of $dN/dlnr$ for $f \leq 3$ in our numerical scheme, though the total mass and $R(\theta)$ are always finite for any positive value of f. This is because V_p scales as r^3 for spheres and r^2 for aggregates, and because Q_{sca} scales as r^4 when $r \to 0$. The value of the minimum particle radius was picked such that it is much lower than the likely range of favorable r_m values estimated by fitting the data by hand. We have also confirmed, through tests of our model, that particles smaller than 80 nm do not contribute signficantly to the forward scattering for all reasonable model parameter values.

4.5 Fitting to Data

We use the Markov Chain Monte Carlo (MCMC) method (Hastings, 1970) to optimize the fits to the data and obtain statistically significant confidence intervals for the optimized parameters, which consist of M_0, r_m, r_0, and f, with D fixed to 2. This is the same number of parameters as IE11, though they had a particle aspect ratio rather than r_m.

The MCMC explores parameter space by comparing the likelihood of a model defined by one set of parameters with that defined by a perturbed set of parameters. The likelihood L of a model is defined as

$$L = e^{\mathcal{L}}, \mathcal{L} = -\frac{1}{2}\sum_i \frac{(x_i - \mu_i)^2}{\sigma_i^2}, \tag{4.9}$$

where x_i is the ith data point, μ_i is the ith model point, and σ_i^2 is the variance of the ith data point, calculated from Table 1 of IE11. Models with high L values correspond to better fits to the data than models with low L values, and thus the sets of parameters that define the better-fit models are closer to the true values of these parameters than the sets of parameters that define the worse-fit models.

At every link of the MCMC, one of the four parameters is chosen randomly to be perturbed by adding onto the original parameter value a perturbation, the magnitude of which is drawn from normal distributions of certain standard deviations: 10^4 kg for M_0; 0.5 μm for r_m and r_0, and 1 for f. The likelihood of this perturbed set of parameters is then calculated according to Eq. 4.9. If the likelihood of the model defined by the perturbed set is greater than that of the original set, then the perturbed set of parameters are accepted as a new link in the chain and the new standard with which subsequent sets of perturbed parameters are compared; otherwise, the perturbed set is accepted if the ratio of the likelihood of the model defined by the perturbed set to that of the original set is greater than a random number drawn from a uniform distribution from 0 to 1. In other words, if the L value of the model defined by the perturbed set is very low, i.e. a very bad fit to the data and thus a very low probability that the data is described by this model, then it is highly unlikely that it will be accepted. By calculating the likelihood of models defined by different sets of parameters with a bias proportional to L, the MCMC method samples the probability density function (PDF) of the parameters. The PDF of each parameter is then the histogram of the accepted parameter values.

We use a total of 2×10^6 links in the MCMC, and the parameter PDFs are constructed from taking the histograms of the accepted values. Sensitivity tests are conducted by halving and doubling the widths of the normal distributions from which the perturbations at each step of the MCMC were drawn, with no major changes to our results.

We apply loose bounds to the parameters: M_0 is restricted to positive values; r_0 is bound between 0.2 and 20 μm and r_m is limited to values between 0.08 and

14 μm to ensure that the radius grid captures most of the size distribution; and f is constrained between 0 and 10 to avoid size distributions narrower than the resolution of the radius grid. The best fit parameters of IE11 are well within these bounds. If there arises a perturbation during a step of the MCMC that resulted in values of the parameters outside their bounds, then the perturbation is redrawn from its normal distribution until a value within the bounds results.

4.6 Results

Figure 4.2 shows the results of the MCMC calculations in the form of scatter plots of the accepted sets of parameters for each parameter pair. Areas of parameter space with more accepted values (points) correspond to places of higher likelihood, and thus better fits to data. It is immediately clear that there are multiple families of solutions, which have been assigned different colored points. For example, the M_0 vs. r_m plot shows at least seven local maxima of accepted parameter sets, though the local maximum with the lowest M_0 appears to be separate from the others. Conversely, the M_0 vs. r_0 and M_0 vs. f plots show only three local maxima at distinct locations in parameter space, one at low M_0 and two at high M_0. These two high M_0 families of solutions can be further split in terms of r_0 and f, with one at high r_0 and high f (and slightly lower M_0) and one at low r_0 and low f (and slightly higher M_0). From the r_m vs. r_0 and r_m vs. f plots we see that the local maximum with the second lowest r_m is resticted to high r_0 and high f values, and that it is the only local maximum out of the seven to exhibit this behavior. Therefore, the seven local maxima of r_m can be distributed among the three local maxima in the other plots as follows: the local maximum with $r_m < 0.8\ \mu m$ defines the low M_0 family of solutions (red); the local maximum with $0.8\ \mu m < r_m < 1.25\ \mu m$ defines the high M_0, r_0, and f family of solutions (blue); and the remaining local maxima with $r_m > 1.25\ \mu m$ defines the high M_0 and low r_0 and f family of solutions (green). In other words, the red points are solutions corresponding to low particulate mass plumes composed primarily of small aggregates with $N_m > 100$; the blue points are high particulate mass plume solutions consisting of large aggregates made up of large monomers, such that they also have $N_m > 100$; and the green points are also high particulate mass plume solutions, but they are comprised of a mixture of spheres and large aggregates composed of very few and very large monomers, which we term the "sphere-aggregate" solutions.

Despite the distinctiveness of these solutions in parameter space, most of their x_m values are >1.5, which is outside the validated range of the T08 model. Therefore,

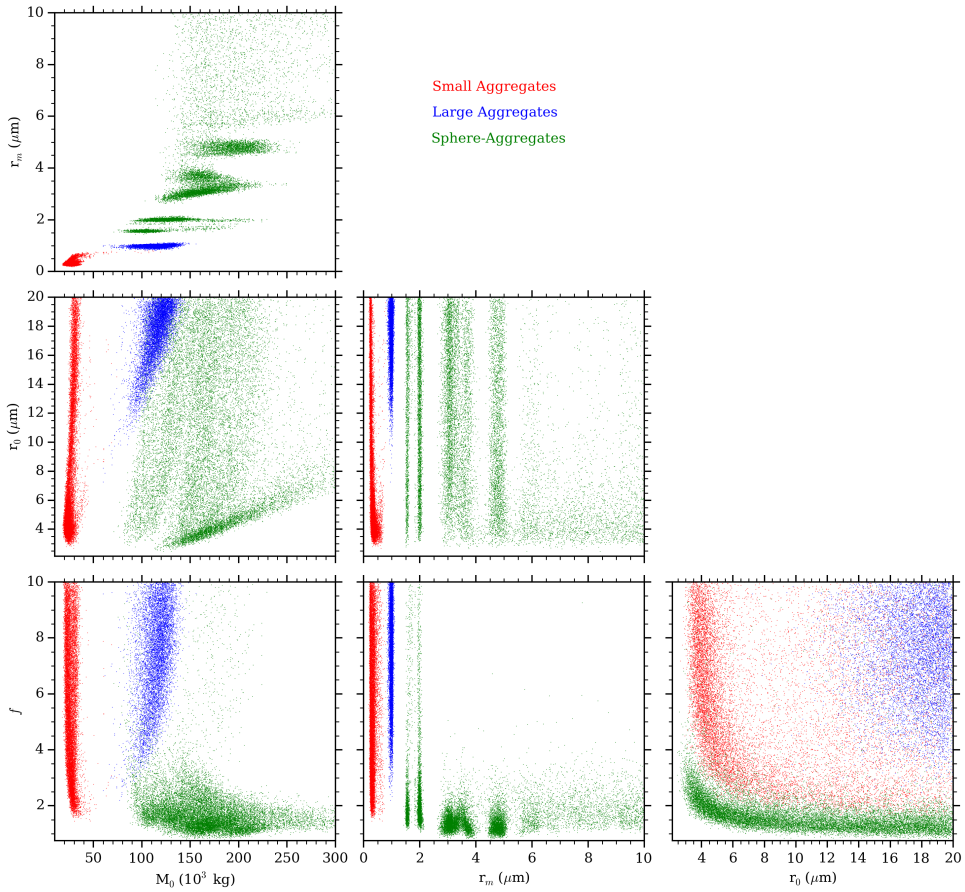

Figure 4.2: Scatter plots of the accepted sets of parameters from the MCMC calculations for each parameter pair. The regions with higher concentrations of points correspond to areas of higher likelihood. Red points correspond to the small aggregate family of solutions defined by $r_m < 0.8\ \mu m$, with low M_0; blue points correspond to the large aggregate family of solutions defined by $0.8\ \mu m < r_m < 1.25\ \mu m$, with high M_0, r_0, and f; and green points correspond to the sphere-aggregate family of solutions defined by $r_m > 1.25\ \mu m$, with high M_0 and low r_0 and f.

caution must be exercised when interpreting these results. As there are currently no quantitaive estimates of the divergence of this approximate model from the detailed T-matrix calculations outside the validated range (Mishchenko, Travis, and Mackowski, 1996), we compare our results to that of the fractal aggregate scattering model of Rannou, McKay, et al. (1999, henceforth R99). The R99 model is semi-empirical and derives particle scattering properties using interpolated values from the mean field approximation of Botet, Rannou, and Cabane (1997), which itself is based on an exact theory of scattering by aggregate particles (Xu, 1995). The R99 model has been validated to $x_m \sim 8$ (Coustenis et al., 2001; Rannou, Hour-

din, and McKay, 2002; Rannou, Hourdin, McKay, and Luz, 2004; Rannou, Cours, et al., 2010; Lavvas, Yelle, and Griffith, 2010, for e.g.) and shows good agreement with the T08 model within the latter's validated range. Thus, it can be used as an approximate fiducial to evaluate the accuracy of the T08 model beyond this range. Only rough agreement is necessary however, as the R99 model is more error-prone than the T08 model due to nonlinear effects in light scattering (T08).

Figure 4.3 shows the percent difference in the scattering efficiency Q_{sca} (top) and the phase function $P(\theta)$ (bottom) (see Eq. 4.6) between the R99 and T08 models for relevant scattering angles and size parameters. The comparison is done in the CLR wavelength channel with 300 monomers assumed for each case, which is expected for the small and large aggregate solutions given their r_m and r_0 values; the refractive indices used are those of water ice (Section 4.4) and the fractal dimension is set to 2. The x_m values of each of the colored phase curves in the bottom panel are indicated by the same colored points in the top panel. The comparison shows that the Q_{sca} and $P(\theta)$ values for the two models agree to within 20% for most $x_m < 3.5$, thereby extending the range of validity of the T08 model. For the small aggregates, $x_m \sim 3$ for the CLR channel (assuming $r_m \sim 0.3$ μm), and thus it is a valid family of solutions. Conversely, the large aggregates have $x_m \sim 10$ for the CLR channel (assuming $r_m \sim 1$ μm), which is well outside the extended validity range, and therefore calls into question the existence of this family of solutions. An additional issue with the large aggregate solutions is its high r_0 value (~ 20 μm), which goes against previous estimates of the sizes of the Enceladus plume particles of a few μm (Kieffer, Lu, McFarquar, et al., 2009; Hedman, Nicholson, et al., 2009). The sphere-aggregate solutions are largely independent of the limitations of the T08 model, as most of the forward scattering is due to spherical particles.

From this exercise it is clear that the small and sphere-aggregate solutions are likely real, but that the large aggregate solutions may not be. Therefore, we will ignore the large aggregates in the remainder of this work.

The left side of Figure 4.4 shows the PDFs of the four varied parameters for the small aggregate solution, generated by marginalizing the 2D distributions of Figure 4.2 along one dimension for the small aggregate solution only and normalizing the area of the resulting 1D histograms. The most probable values–the maximum likelihood estimates–correspond to the peaks of the PDFs, marked by the green lines. Models generated from these parameter values are most likely to describe the data. For the M_0, r_m, and r_0 PDFs, the 68% (1σ) confidence intervals are enclosed by the

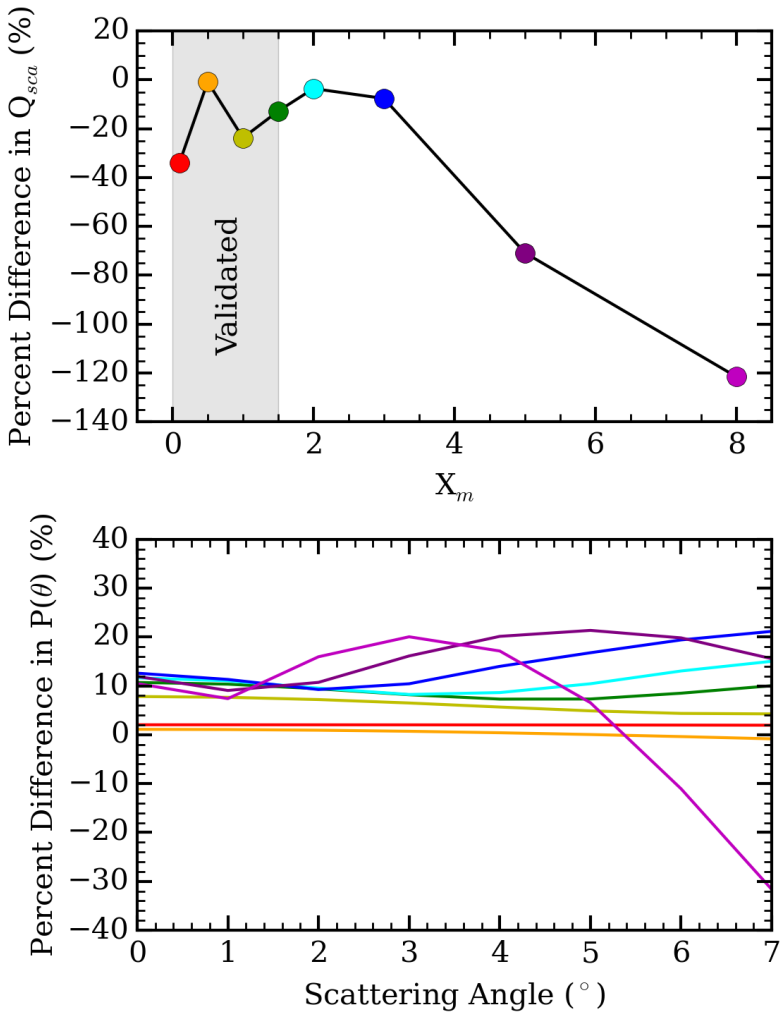

Figure 4.3: Percent difference in the scattering efficiency Q_{sca} (top) and the phase function P(θ) (bottom) between the models of Rannou, McKay, et al. (1999) and Tomasko, Doose, Engel et al. (2008) for relevant values of the size parameter x_m and scattering angle θ. The comparison is done in the CLR wavelength channel with 300 monomers assumed for each case. The refractive indices used are those of water ice (Section 4.4) and the fractal dimension is set to 2. The x_m values of each of the colored phase curves in the bottom panel are indicated by the same colored points in the top panel. The gray shaded region in the top panel indicates the range in $x_m$for which the model of Tomasko et al. (2008) has been validated.

blue lines, which indicate the smallest interval in parameter space that encloses 68% of the accepted values. The PDF of f does not have a well-defined peak, and thus a lower limit is given, with the 68% confidence interval now defined as the 68% of accepted values immediately below the most probable value. Table 4.1 gives these most probable values and the associated 68% confidence intervals, which we set to

be the ranges of uncertainty in our fit to data.

Parameter	Small Aggregates	Sphere-Aggregates
M_0 (10^3 kg)	25 (22 - 30)	166 (119 - 205)
r_m (μm)	0.27 (0.24 - 0.35)	–
r_0 (μm)	4.20 (3.11 - 10.51)	3.90 (3.34 - ∞)
f	2.5 (2.1 - ∞)	1.34 (1.05 - 1.89)

Table 4.1: Most probable values and (in brackets) 68% confidence intervals of the retrieved parameters, where M_0 = total mass of the plume, r_m = monomer radius, r_0 = median particle radius, and f = width of the size distribution for the small aggregate (left) and sphere-aggregate (right) particle plume solutions. The sphere-aggregate r_0 and the small aggregate f PDFs have unconstrained upper bounds and so only the lower bounds are given, defined as the lower limit of the 68% of the accepted values immediately below the most probable value. The monomer radius for the sphere-aggregate solution is omitted, as it is multimodal and thus does not have a well-defined most-probable value or confidence interval.

The small aggregate plume solution yields a most probable r_0 consistent with the r_0 of the spherical particles of IE11, but the total plume mass is ~ 6 times lower. Meanwhile, the PDF of f is very broad, meaning that this parameter is not well-constrained by the Cassini ISS data. The lack of a upper limit allows for large f values, leading to narrow size distributions centered at r_0, with low abundances of both smaller and larger particles. This is consistent with a scenario where the smaller monomers are depleted to form small aggregates of median radius r_0.

The right side of Figure 4.4 shows the PDFs of the sphere-aggregate solutions. As before, the 68% confidence intervals are shown for PDFs with well-defined peaks (M_0 and f), while for the r_0 PDF only the lower limits are given. The r_m PDF is multimodal and thus does not have a well-defined most-probable value or confidence interval. This is likely due to the limitations of the T08 model, as the corresponding x_m values are far greater than even the extended validity range given above. Beyond $r_m > 6$ μm, spherical particles dominate the particle population, and thus r_m becomes unconstrained.

The results of IE11 indicate that, for spherical particles, mass distributions with $f = 1$ to 2 best fit the data. This is consistent with our sphere-aggregate particle plume results. Our M_0 and r_0 estimates for the sphere-aggregate solutions are also consistent with IE11, though the PDF for r_0 has a significant tail towards larger values. This highlights a deficiency in forward scattering measurements, as more massive particles are difficult to observe due to their low surface to volume ratio.

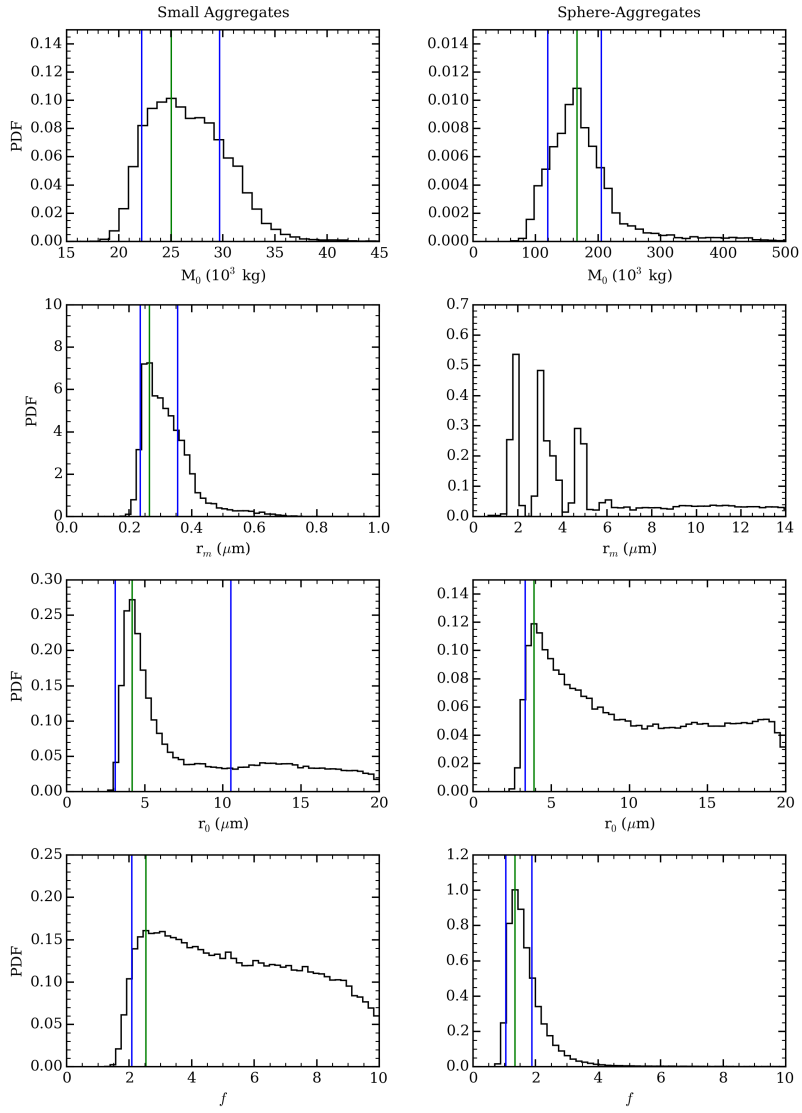

Figure 4.4: The probability density functions (PDFs) of the total mass of the plume M_0 (top), the monomer radius r_m (middle-top), the median particle radius r_0 (middle-bottom), and the width of the size distribution f (bottom) for the small aggregate (left) and sphere-aggregate (right) particle plume solutions. Note the different abscissa values between the r_0 and r_m plots. Each histogram contains 50 bins. The most probable value is marked by the green line. For the M_0, small aggregate r_m and r_0, and sphere-aggregate f PDF's, the 68% confidence intervals are enclosed by the blue lines, while for the small aggregate f and sphere-aggregate r_0 PDFs only the lower 68% confidence interval is marked. The sphere-aggregate r_m PDF is multimodal and thus does not have a well-defined most-probable value or confidence interval.

Therefore, the impact of massive particles on the phase curves is minimal, allowing the results to be poorly constrained at large particle sizes.

Figure 4.5 gives representative best fits to the VIO (top), CLR (middle), and IR3 (bottom) channels of the Cassini ISS data for the small aggregate (red) and sphere-aggregate (green) particle solutions, the latter of which reproduces the lower left panel of Figure 6 of IE11. In our case, the small aggregate solution provides the best fit, as defined by its reduced chi-square value

$$\chi_r^2 = \frac{1}{N-n-1}\sum_i \frac{(x_i-\mu_i)^2}{\sigma_i^2}, \tag{4.10}$$

where $N = 10$ is the number of data points being fitted to, $n = 4$ is the number of parameters, and the variables in the summation are the same as that of Eq. 4.9. Lower χ_r^2 values indicate better fits, though if $\chi_r^2 \ll 1$ then the error bars on the observations are likely overestimated. $\chi_r^2 = 0.71$ for the small aggregate solution fit and $\chi_r^2 = 1.5$ for the sphere-aggregate solution fit. Both solutions give similar fits for the VIO and CLR channels, but differ significantly in the IR3 channel at scattering angles $< 2°$. Whereas the small aggregate model curve features a broad forward scattering peak, the sphere-aggregate model curve's forward scattering peak is much narrower in IR3. The width of the forward scattering peak is related to r_0 (IE11), but also r_m in the case of aggregates (Lavvas, Yelle, and Griffith, 2010); large particles result in narrower/sharper peaks while smaller particles result in broader peaks. Therefore, as the small aggregate particles have small r_m values, their forward scattering peaks are the most broad, increasing $R(\theta)$ at larger scattering angles and prompting low M_0 values. Meanwhile, the lack of small monomers in the sphere-aggregate particles narrows the forward scattering peak, resulting in low values at large θ, and a higher M_0 than for the small aggregate solution.

It is interesting to note that only the IR3 channel offers a way to discriminate between the two solutions. This is caused by the strong dependence of the intensity of scattered light on the particle size parameter x_m. In our fits there are two ranges of particle sizes to consider: the small aggregate monomer radius ~ 0.3 μ m and the median particle radius for the small aggregate and sphere-aggregate solutions ~ 4 μm; the intensity of the scattered light will depend on a combination of the particle radius and the monomer radius, if applicable. For the VIO and CLR channels ($\lambda =$ 420 and 635 nm, respectively), both the small aggregate and sphere-aggregate particles are much larger than the wavelengths considered, leading to narrow forward scattering peaks. However, for the IR3 channel ($\lambda = 918$ nm), the small aggregate monomer radius is now much smaller than the wavelength, leading to a much

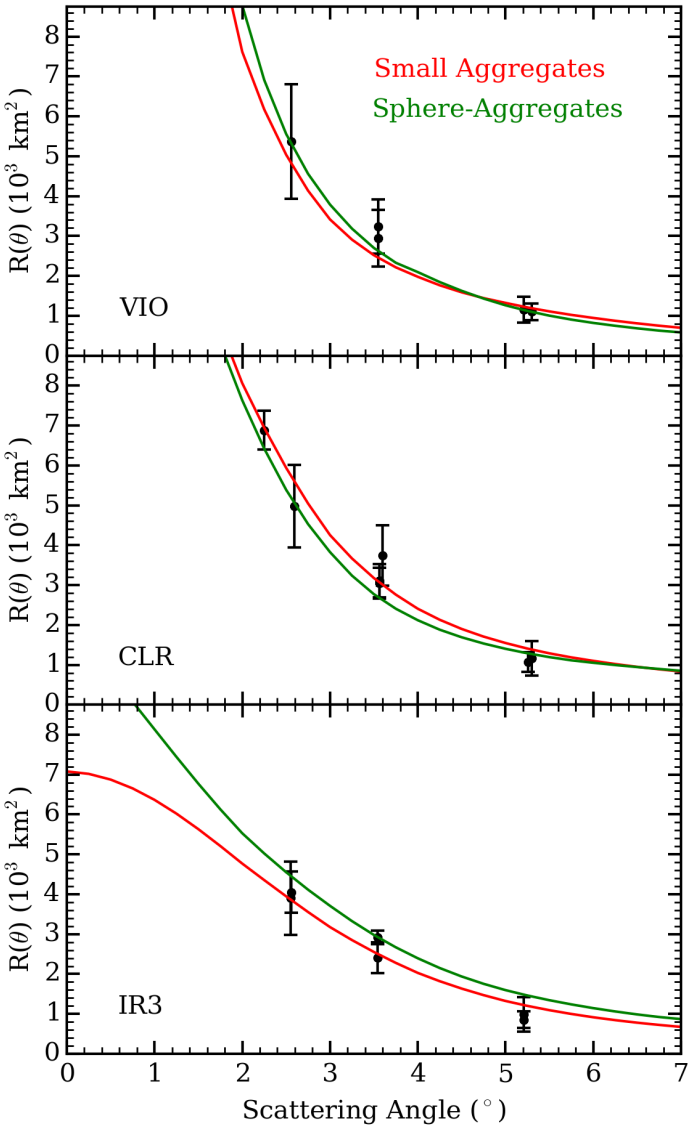

Figure 4.5: Representative best fits to the VIO (top), CLR (middle), and IR3 (bottom) wavelength channel data from Cassini ISS for the small aggregate (red) and sphere-aggregate (green) plume particle solutions. Parameters used for the small aggregate solution fit are: $M_0 = 22.58 \times 10^3$ kg, $r_m = 0.331$ μm, $r_0 = 3.9$ μm, and $f = 7.79$. Parameters used for the sphere-aggregate solution fit are: $M_0 = 172.42 \times 10^3$ kg, $r_m = 4.87$ μm, $r_0 = 4.81$ μm, and $f = 1.71$.

broader forward scattering peak. Similarly, the low f value of the sphere-aggregate solution means that there exists a great number of small particles that are responsible for much of the scattering, and which are now much smaller than the channel

wavelength, again leading to a wider forward scattering peak.

In obtaining two separate families of solutions, we have shown that degeneracy exists in the ISS data from IE11 when both spherical and aggregate particles are considered. This degeneracy can be broken by an independent mass measurement, such as from Cassini CDA.

4.7 Discussion

We can calculate the solid to vapor mass ratio of the plume for the small aggregate solution following the procedure described in IE11. We derive a value for the particulate column mass abundance M^p_{col} by relating it to the I/F values of the Cassini ISS NAC image from IE11 using their Eq. 8,

$$\frac{I}{F} = \frac{M^p_{col}}{M_0} R(\theta) = K_0(\theta) M^p_{col}, \tag{4.11}$$

where $R(\theta)$ is defined in Eq. 4.7. Dividing M^p_{col} by the vapor column mass abundance, M^v_{col}, at the same altitude above Enceladus then gives the solid to vapor mass ratio of the plume at that altitude. From the small aggregate curve (red) in Figure 4.5, we interpolate a $R(\theta)$ value of 6.4×10^3 km^2 for the CLR channel at $\theta = 2.38°$, the wavelength channel and scattering angle of the NAC image, respectively. This is slightly higher than the value given in IE11, 5.4×10^3 km^2, owing to the different model curves used for the interpolation. Setting M_0 to $(25 \pm 4) \times 10^3$ kg for the small aggregate solution and I/F to 0.07, the brightest pixel value of the NAC image above background (as with IE11), we find that $M^p_{col} = (2.7 \pm 0.4) \times 10^{-7}$ kg m^{-2} for that pixel, which is ~ 7 times lower than the M^p_{col} value calculated by IE11. The altitude above Enceladus that corresponds to that pixel is similar to that probed by the occultations carried out by Hansen et al. (2011) to measure M^v_{col} using Cassini UVIS. Therefore, the solid to vapor mass ratio can be obtained by dividing the M^p_{col} value derived here by the M^v_{col} value derived from averaging the second column of Table 1 of Hansen et al. (2011). This gives a solid to vapor mass ratio for the small aggregate plumes of

$$\frac{M^p_{col}}{M^v_{col}} = 0.07 \pm 0.01, \tag{4.12}$$

which is again 7 times lower than that of IE11. The error arises from uncertainties in both the solid and vapor column mass abundances and is likely underestimated,

as we have assumed zero uncertainty for the $R(\theta = 2.38^\circ)$ and I/F values. It should be noted that, while $K_0(\theta)$ is defined using all available WAC images, the comparison with UVIS requires that we use just the brightest pixel of the one NAC image to set the I/F value. In other words, the global I/F values of the plume in the WAC images are assumed to be the same as that of the brightest plume pixel in the NAC image, which is equivalent to assuming that the particle size distribution is independent of altitude above Enceladus. This is only an approximation, as evidence exists that the particle size distribution does change with altitude (Hedman, Nicholson, et al., 2009; Postberg, Schmidt, et al., 2011). However, for simplicity we do not consider this effect in this work.

Our calculated solid to vapor ratio is consistent with that of Kieffer, Lu, McFarquar, et al. (2009), who provided an upper bound of ~0.1–0.2 using observations from Cassini ISS and UVIS (C. C. Porco et al., 2006). It is also consistent with the lower end of the range of solid to vapor ratios ($\sim 0.01 - -100$) calculated by Hedman, Nicholson, et al. (2009) using Cassini VIMS observations and spherical and irregular particle scattering models, though aggregates were not considered.

The $K_0(\theta)$ quantity in Eq. 4.11 is extremely useful as it can readily convert an observed I/F value into the column mass abundance. It also varies depending on the particle scattering properties, wavelength of scattered light, and particle size distribution. Figure 4.6 shows the $K_0(\theta)$ values of the small (solid lines) and sphere-aggregate (dashed lines) solutions at scattering angles between 0° and 50° for the VIO (blue), CLR (green), and IR3 (red) wavelength channels. The small aggregate $K_0(\theta)$ values are, as expected, higher than that of the sphere-aggregate solution, since there is less mass for the same intensity of forward scattering. The sphere-aggregate $K_0(\theta)$ values are typically within 10% of those of IE11, further reinforcing the lack of dependence of the sphere-aggregate solutions on the limitations of the T08 model. A full set of $K_0(\theta)$ values for the two families of solutions and the best fit solution of IE11 at the Cassini WAC and NAC channel wavelengths can be found in the online supplemental material.

Aside from what can be retrieved from observations, it is also imperative that the particle solutions are physical and adhere to theoretical constraints of formation and evolution. As IE11 has already considered high mass plumes, we will focus on the low mass small aggregate solutions and their possible formation mechanisms for the remainder of this work.

Aggregate particles in the Solar System typically form through the coagulation of

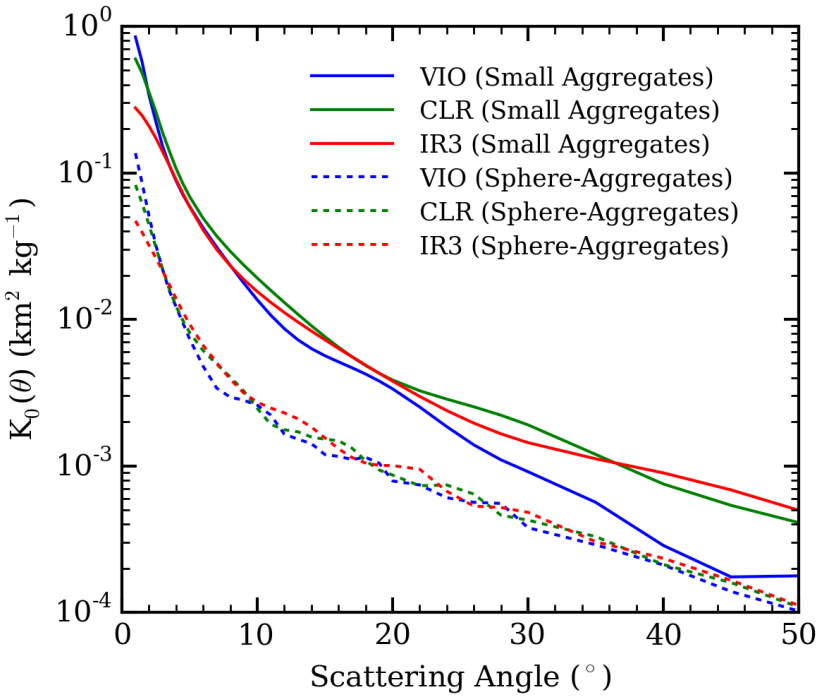

Figure 4.6: Variations of $K_0(\theta) = R(\theta)/M_0$ as a function of scattering angle for the VIO (blue), CLR (green), and IR3 (red) wavelength channels and the small aggregate (solid lines) and sphere-aggregate (dashed lines) solutions.

monomers, a process that depends heavily on the free-floating monomer number density (Lavvas, Yelle, and Griffith, 2010, for e.g.,), i.e. those not already incorporated into aggregates. Therefore, much of the coagulation process must take place within the plume vents, where the particle number density is higher. This is consistent with our small aggregate particle solution, which shows a low abundance of monomers compared to aggregates in the plume, as the monomers must have already coagulated to form aggregates before they were ejected into space. The residence time of particles inside the plume vents is of order D/v, where D is the depth of the liquid vapor interface and v is the average velocity of the particles. In order for complete coagulation of monomers within the plume vents, this residence time must be greater or equal to the coagulation time scale, approximated by

$$\tau_{coag} = \left(\frac{1}{n}\left|\frac{dn}{dt}\right|\right)^{-1} = \frac{1}{nK}, \tag{4.13}$$

where n is the free-floating monomer number density in the vent, and K is the coagulation kernel. In the free molecular limit (Knudsen number >> 1), the Brownian coagulation kernel for two spherical particles with radii r_1 and r_2 is

$$K = (r_1 + r_2)^2 \sqrt{\frac{6kT}{\rho_p}\left(\frac{1}{r_1^3} + \frac{1}{r_2^3}\right)}, \tag{4.14}$$

where k is the Boltzmann constant, T is temperature, and ρ_p is the solid particle density (0.917 g cm^{-3}). Setting $r_1 = r_2 = r_m$,

$$K = \sqrt{\frac{192kTr_m}{\rho_p}} \tag{4.15}$$

(Pruppacher and Klett, 1978). To find a value for the coagulation time scale, we consider the rate at which particulate mass is emerging from the vents, which can be expressed as

$$\frac{dM_p}{dt} = \frac{4}{3}\pi r_m^3 \rho_p n A v = \rho_m A v, \tag{4.16}$$

where ρ_m is the total mass of particulates per unit volume and A is the total vent area of the Enceladus plumes. IE11 gives this rate as dM_p/dt = 51 kg s^{-1}, but the reduced plume mass of the small aggregate solutions results in a smaller value. Rather than assuming that dM_p/dt is linearly proportional to M_0 however, we instead appeal to the solid to vapor mass ratio by considering the rate at which vapor is emerging from the vents, dM_v/dt, which has been determined by Hansen et al. (2011) to be $\sim$ 200 kg s^{-1} based on Cassini UVIS observations. Thus,

$$\frac{dM_v}{dt} = \rho_v A v = 200 \text{ kg s}^{-1}, \tag{4.17}$$

where ρ_v is the density of the vapor at the liquid-vapor interface, 4.85 $\times$ 10^{-3} kg m^{-3} at T = 273 K. Dividing Eq. 4.16 by Eq. 4.17 gives us the solid to vapor mass ratio $\sim$ [dM_p/dt / dM_v/dt] and allows us to eliminate A and v. Substituting the result into Eq. 4.13 then allows us to eliminate n. The necessary condition for the completion of monomer coagulation before exiting the vent then becomes

$$\frac{D}{v} > \tau_{coag} = \frac{1}{K}\left(\frac{4}{3}\pi r_m^3\right)\frac{\rho_p}{\rho_v}\frac{dM_v/dt}{dM_p/dt} \sim 20 \text{ s}, \tag{4.18}$$

where we use r_m = 0.3 μm and T = 273 K. For [dM_p/dt / dM_v/dt] we use the solid to vapor mass ratio derived in Eq. 4.12.

Several assumptions have gone into Eq. 4.18. One is that the particles and the vapor emanate from the same liquid-vapor interface, or at least very close above it in the vent. This is necessary to maintain high T and ρ_p values. If the particles form in flight higher up in the vent, as in a convective cloud, the reduction in ρ_p due to lower T and/or condensation on the vent walls would drastically increase τ_{coag}. The fact that some of the plume particles are Na-rich (Postberg, Kempf, et al., 2009; Postberg, Schmidt, et al., 2011) argues that they originate from the liquid, but we cannot rule out a vapor origin for the Na-poor particles. Another assumption is that the different parts of the erupting area A behave the same way whether they are a single crack running the length of each tiger stripe, a series of 100 discrete sources (C. Porco, DiNino, and Nimmo, 2014), or some combination of the two (Tian et al., 2007; Hansen et al., 2011; Postberg, Schmidt, et al., 2011; Spitale et al., 2015, for e.g.). A third assumption is that the solid to vapor mass ratio remains the same as the plumes vary with orbitial phase (Hedman, Gosmeyer, et al., 2013). These assumptions are difficult to test, but they seem reasonable.

A fourth assumption is that the relevant vapor density and velocity are close to those at the liquid-vapor interface and not those at the top of the vent where the particles and vapor exit to space. From the vertical distribution of particles exiting the vent, one infers velocities of order 60–90 m s^{-1} (Porco et al., 2006; IE11). However, the particles are accelerated to this speed within a few meters of the surface (Schmidt et al., 2008; A. P. Ingersoll and Pankine, 2010), so the exit speed underestimates the time spent in the vent during which coagulation takes place. Postberg, Kempf, et al. (2009) use 500 m s^{-1} for the speed of the vapor and the triple point value for its density, but Nakajima and A. . Ingersoll (Submitted) point out that these are overestimates. Their model includes friction with the walls of the crack as the gas flows upward. This produces backpressure at the liquid-vapor interface, and for a long, narrow crack the backpressure severely limits the evaporation rate and the upward velocity. For crack widths less than 0.1 m, the upward velocity is less than 10 m s^{-1} below depths of 1 km. If the evaporating surface is another 1 km below that level, the time spent in the vent is well over 100 s and the condition for coagulation of aggregates (Eq. 4.18) is comfortably satisfied. Crack width is an important parameter, since it affects the velocity. Nakajima and A. . Ingersoll (Submitted) derive their estimate by matching the ratio of the power released through latent heat to that released through infrared radiation, but one should remember that these numbers are uncertain by factors of 2 or more.

Our results favor a less violent source for the plumes than the earlier results of IE11. Here, "less violent" means steady, controlled evaporation rather than explosive boiling. For example, it could be that most of the ice particles condense directly from the expanding vapor above the liquid-vapor interface rather than erupt as a bubbly liquid, which then breaks up and freezes into small ice particles in the vacuum of space. Alternatively, the particles could be generated by bubbles of methane or CO_2 rising through liquid water and breaking at the surface, thereby sending up a fine spray of ice particles. C. C. Porco et al. (2006) mentioned two extremes: particles condensing directly from the vapor and particles forming from the breakup of a boiling liquid, the latter analogous to a cold Yellowstone geyser. The relatively large solid to vapor ratio of IE11 favors the violent source, while the lower ratio of our small aggregate solution allows for less violent sources. Thus, the present results make the ISS data compatible with a wider variety of sources than the IE11 results.

Schmidt et al. (2008) and A. P. Ingersoll and Pankine (2010) used hydrodynamic models to simulate the condensation of ice particles from water vapor, and obtained solid to vapor mass ratios of 0.05–0.06 and 0.015, respectively. The lower value calculated by A. P. Ingersoll and Pankine (2010) results from the condensation of vapor onto the vent walls, which Schmidt et al. (2008) did not consider. These values of the solid to vapor mass ratios are more consistent with our small aggregate solution than with the results of IE11. Kieffer, Lu, Bethke, et al. (2006) considered explosive decomposition of a hydrate clathrate that contains methane and other gases in much greater abundances than their solubility in liquid water would allow. The solid to vapor mass ratio of such an event is uncertain, but it could be lower than that quoted by IE11 and closer to the ratio derived here from the small aggregate solution. Meanwhile, Hsu et al. (2015) and Postberg, Kempf, et al. (2009) and Postberg, Schmidt, et al. (2011) showed that silica grains and sodium salts are present in both E ring and plume particles, which argues strongly for frozen droplets originating from a salty liquid rather than ice particles forming directly from vapor condensation. Postberg, Kempf, et al. (2009) suggested that ascending bubbles of plume gases (CO_2, N_2, CO, CH_4) can disperse the liquid droplets into the vapor, and that the evaporation of the boiling liquid source is taking place over a large horizontal area so that freezing of the vents is suppressed. Nakajima and A. . Ingersoll (Submitted) showed that the backpressure due to friction on the walls of the channel could severely limit the evaporation rate. A. P. Ingersoll and Nakajima (Submitted) argue that this "controlled boiling" allows bubbles of vapor to break at the surface

instead of throwing up large amounts of spray as in boiling into vacuum. All of this points to a relatively gentle source and a relatively low solid to vapor mass ratio.

Our small aggregate solution does not rule out a vapor-based source for the plume particles. Parkinson et al. (2008) showed that spherical particles with radii similar to r_m can form from water vapor nucleating on involatile grains in a few seconds, while spherical particles with radii up to 3 μm can form by condensation in about 100 s, though large condensation nuclei and/or a high density of water vapor may be necessary. Similarly, non-spherical ice crystals resembling aggregates, e.g. dendritic shapes, can form directly from condensation and nucleation of water vapor, with growth rates comparable to that of spherical particles (Pruppacher and Klett, 1978). Bullet rosettes – highly non-spherical, polycrystalline ice particles made up of clumps of hexagonal columns – can also yield high scattering cross sections for a small particle mass, but they are formed by the fracturing of ice during the freezing of a large water drop (Baum et al., 2011).

We have shown that forward scattering observations of the Enceladus plumes from Cassini ISS can be well-fit by plumes made up of ice aggregates and solid ice spheres. This results in a bifurcation in the allowed total particulate mass of the plumes: small aggregate plumes are six times less massive than plumes made of larger aggregates and spheres. The small aggregate plumes, in particular, lead to a solid to vapor mass ratio of 0.07 ± 0.01, which is suggestive of a "gentle source" for the plume particles.

We thank Y. L. Yung and H. Ngo for their valuable input. P. Gao and P. Kopparla were supported in part by an NAI Virtual Planetary Laboratory grant from the University of Washington to the Jet Propulsion Laboratory and California Institute of Technology under solicitation NNH12ZDA002C and Cooperative Agreement Number NNA13AA93A. X. Zhang was supported by the Bisgrove Scholar Program at the University of Arizona. A. P. Ingersoll was supported by the Cassini Project and NASA's Cassini Data Analysis Program.

References

Bar-Nun, A., V. Dimitrov, and M. G. Tomasko (2008). "Titan's aerosols: Comparison between our model and DISR findings". In: *Planetary and Space Science* 56, pp. 708–714.

Baum, B. A. et al. (2011). "Improvements in shortwave bulk scattering and absorption models for the remote sensing of ice clouds". In: *Journal of Applied Meteorology and Climatology* 50, pp. 1037–1056.

Botet, R., P. Rannou, and M. Cabane (1997). “Mean-field approximation of Mie scattering by fractral aggregates of identical spheres”. In: *Applied Optics* 36, pp. 8791–8797.

Cabane, M. et al. (1993). “Fractal aggregates in Titan’s atmosphere”. In: *Planetary and Space Science* 41, pp. 257–267.

Coustenis, A. et al. (2001). “Images of Titan at 1.3 and 1.6 μm with adaptive optics at the CFHT”. In: *Icarus* 154, pp. 501–515.

Grainger, R. G. et al. (2004). “Calculation of Mie derivatives”. In: *Applied Optics* 43, pp. 5386–5393.

Hansen, C. J. et al. (2011). “The composition and structure of the Enceladus plume”. In: *Geophysical Research Letters* 38.

Hastings, W. K. (1970). “Monte Carlo sampling methods using Markov chains and their applications”. In: *Biometrika* 57, pp. 97–109.

Hedman, M. M., C. M. Gosmeyer, et al. (2013). “An observed correlation between plume activity and tidal stresses on Enceladus”. In: *Nature* 500, pp. 182–184.

Hedman, M. M., P. D. Nicholson, et al. (2009). “Spectral observations of the Enceladus plume with Cassini-VIMS”. In: *The Astrophysical Journal* 693, p. 1749.

Heymsfield, A. J. et al. (2002). “A general approach for deriving the properties of cirrus and stratiform ice cloud particles”. In: *Journal of the atmospheric sciences* 59, pp. 3–29.

Hsu, H. W. et al. (2015). “Ongoing hydrothermal activities within Enceladus”. In: *Nature* 519, pp. 207–210.

Ingersoll, A. P. and S. P. Ewald (2011). “Total particulate mass in Enceladus plumes and mass of Saturn’s E ring inferred from Cassini ISS images”. In: *Icarus* 216, pp. 492–506.

Ingersoll, A. P. and M. Nakajima (Submitted). “Controlled boiling on Enceladus. 2. Model of the liquid-filled cracks”. In: *Icarus*.

Ingersoll, A. P. and A. A. Pankine (2010). “Subsurface heat transfer on Enceladus: Conditions under which melting occurs”. In: *Icarus* 206, pp. 594–607.

Kajikawa, M. and A. J. Heymsfield (1989). “Aggregation of ice crystals in cirrus”. In: *Journal of the Atmospheric Sciences* 46, pp. 3108–3121.

Kieffer, S. W., X. Lu, C. M. Bethke, et al. (2006). “A clathrate reservoir hypothesis for Enceladus’ south polar plume”. In: *Science* 314, pp. 1764–1766.

Kieffer, S. W., X. Lu, G. McFarquar, et al. (2009). “A redetermination of the ice/vapor ratio of Enceladus’ plumes: Implications for sublimation and the lack of a liquid water reservoir”. In: *Icarus* 203, pp. 238–241.

Lavvas, P., R. V. Yelle, and C. A. Griffith (2010). “Titan’s vertical aerosol structure at the Huygens landing site: Constraints on particle size, density, charge, and refractive index”. In: *Icarus* 210, pp. 832–842.

Meng, Z. et al. (2010). “Single-scattering properties of tri-axial ellipsoidal mineral dust aerosols: A database for application to radiative transfer calculations”. In: *Journal of Aerosol Science* 41, pp. 501–512.

Mishchenko, M. I., L. D. Travis, and D. W. Mackowski (1996). “T-matrix computations of light scattering by nonspherical particles: A review”. In: *Journal of Quantitative Spectroscopy and Radiative Transfer* 55, pp. 535–575.

Nakajima, M. and A .P. Ingersoll (Submitted). “Controlled boiling on Enceladus. 1. Model of the vapor-driven jets”. In: *Icarus*.

Parkinson, C. D. et al. (2008). “Habitability of Enceladus: Planetary conditions for life”. In: *Origins of Life and Evolution of Biospheres* 38, pp. 355–369.

Porco, C. C. et al. (2006). “Cassini observes the active south pole of Enceladus”. In: *Science* 311, pp. 1393–1401.

Porco, C., D. DiNino, and F. Nimmo (2014). “How the geysers, tidal stresses and thermal emission across the south polar terrain of Enceladus are related”. In: *The Astronomical Journal* 148, pp. 45–68.

Postberg, F., S. Kempf, et al. (2009). “Sodium salts in E-ring ice grains from an ocean below the surface of Enceladus”. In: *Nature* 459, pp. 1098–1101.

Postberg, F., J. Schmidt, et al. (2011). “A salt-water reservoir as the source of a compositionally stratified plume on Enceladus”. In: *Nature* 474, pp. 620–622.

Pruppacher, H. R. and J. D. Klett (1978). *Microphysics of clouds and precipitation*. D. Reidel Publishing Company, Dordrecht, Holland.

Rannou, P., T. Cours, et al. (2010). “Titan haze distribution and optical properties retrieved from recent observations”. In: *Icarus* 208, pp. 850–867.

Rannou, P., F. Hourdin, and C. P. McKay (2002). “A wind origin for Titan’s haze structure”. In: *Nature* 418, pp. 853–856.

Rannou, P., F. Hourdin, C. P. McKay, and D. Luz (2004). “A coupled dynamics-microphysics model of Titan’s atmosphere”. In: *Icarus* 170, pp. 443–462.

Rannou, P., C. P. McKay, et al. (1999). “Semi-empirical model of absorption and scattering by isotropic fractal aggregates of spheres”. In: *Planetary and Space Science* 47, pp. 385–396.

Schmidt, J. et al. (2008). “Slow dust in Enceladus’ plume from condensation and wall collisions in tiger stripe fractures”. In: *Nature* 451, pp. 685–688.

Schmitt, C. G. and A. J. Heymsfield (2010). “The dimensional characteristics of ice crystal aggregates from fractal geometry”. In: *Journal of the Atmospheric Sciences* 67, pp. 1605–1616.

Spitale, J. N. et al. (2015). “Curtain eruptions from Enceladus’ south-polar terrain”. In: *Nature* 521, pp. 57–60.

Tian, F. et al. (2007). “Monte Carlo simulations of the water vapor plumes on Enceladus”. In: *Icarus* 188, pp. 154–161.

Tomasko, M. G., L. Doose, L. E. Dafoe, et al. (2009). “Limits on the size of aerosols from measurements of linear polarization in Titan’s atmosphere”. In: *Icarus* 204, pp. 271–283.

Tomasko, M. G., L. Doose, S. Engel, et al. (2008). “A model of Titan’s aerosols based on measurements made inside the atmosphere”. In: *Planetary and Space Science* 56, pp. 669–707.

Vahidinia, S. et al. (2011). “Saturn’s F-ring grains: Aggregates made of crystalline water ice”. In: *Icarus* 215, pp. 682–694.

Waite Jr, J. H. et al. (2009). “Liquid water on Enceladus from observations of ammonia and 40Ar in the plume”. In: *Nature* 460, pp. 487–490.

West, R. A. and P. H. Smith (1991). “Evidence for aggregate particles in the atmospheres of Titan and Jupiter”. In: *Icarus* 90, pp. 330–333.

Westbrook, C. D., R. C. Ball, and P. R. Field (2006). “Radar scattering by aggregate snowflakes”. In: *Quarterly Journal of the Royal Meteorological Society* 132, pp. 897–914.

Xu, Y. I. (1995). “Electromagnetic scattering by an aggregate of spheres”. In: *Applied Optics* 34, pp. 4573–4588.

Yang, P. and K.-N. Liou (1998). “Single-scattering properties of complex ice crystals in terrestrial atmosphere”. In: *Beitrage zur Physik der Atmosphare-Contributions to Atmospheric Physics* 71, pp. 223–248.

Zhang, X. et al. (2013). “Stratospheric aerosols on Jupiter from Cassini observations”. In: *Icarus* 226, pp. 159–171.

PART III: STRANGE NEW WORLDS

Chapter 5

MICROPHYSICS OF KCL AND ZNS CLOUDS ON GJ 1214 B

5.1 Abstract

Clouds have been shown to be ubiquitous in warm exoplanet atmospheres, particularly Super Earths and Mini Neptunes, where they block the spectral signatures of key atmospheric molecules in the transmission spectra of exoplanets. Not only does this prevent us from gaining knowledge about their atmospheric composition, but also require that we include clouds in their atmospheric models in order to fully characterize them. The formation and evolution of clouds are controlled by microphysical processes, including nucleation, condensation/evaporation, and transport, which have not yet been incorporated into exoplanet cloud models that can simulate worlds smaller and cooler than Hot Jupiters. In this work, we apply a cloud microphysics model to simulate the potassium chloride (KCl) and zinc sulfide (ZnS) clouds of the Super Earth GJ 1214 b. We investigate the cloud distribution as a function of the degree of vertical mixing, as parameterized by eddy diffusion, and the atmospheric metallicity. We find that pure ZnS clouds do not form via homogeneous nucleation because of its high surface energy, and when it is allowed to heterogeneously nucleate onto KCl particles it remains a minor cloud component. Pure KCl cloud distributions are strongly influenced by the rates of homogeneous nucleation versus the rates of sedimentation/mixing and condensational growth. High eddy diffusivities promote high rates of nucleation due to increased upwelling of KCl vapor from depth and generate more massive, vertically extended clouds, while low eddy diffusivities lead to diminutive clouds that experience periodic bursts of nucleation. Higher metallicities drastically increase the cloud mass due to higher supersaturations leading to high nucleation rates, and as a result even moderately supersolar metallicities ($0 < [Fe/H] < 1$) may produce optically thick clouds at high altitudes. Possible cloud nucleation pathways are discussed, which will require laboratory work into exoplanet cloud material properties to be fully understood.

5.2 Introduction

Investigations of exoplanet atmospheres have unearthed a prevalence of clouds and hazes that impede understanding of atmospheric composition (Gibson, Aigrain,

Pont, et al., 2012; Gibson, Aigrain, Barstow, et al., 2013; Deming et al., 2013; Jordán et al., 2013; Mandell et al., 2013; Sing, Lecavelier des Etangs, et al., 2013; Chen et al., 2014; Schlawin et al., 2014; Wilkins et al., 2014; Fukui et al., 2014; Mallonn and Strassmeier, 2016). Their presence is typically revealed through a flattening of spectral features in the transmission spectrum, resulting from the inability of stellar photons to reach depths in the atmosphere below the cloud top due to scattering and absorption by the cloud particles. This phenomenon is observed across many exoplanets of various sizes, effective temperatures, and stellar irradiation levels. For example, while many super Earths and warm Neptunes appear cloudy (e.g. Crossfield et al., 2013; Kreidberg et al., 2014; Knutson, Benneke, et al., 2014; Knutson, Dragomir, et al., 2014), there exist exceptions (Fraine et al., 2014). Meanwhile, a continuum in cloudiness has been observed for hot Jupiters (Sing, Fortney, et al., 2016; Iyer et al., 2016), as determined from the magnitude of the spectral features of water, potassium, sodium, and Rayleigh scattering.

There are now some hints of correlations between cloudiness and other planetary properties, such as geometric albedo and equilibrium temperature (Heng and Demory, 2013; Stevenson, 2016), but the processes that control the formation and distribution of exoplanet clouds are still mostly unknown. This is a profound problem, as clouds are strongly coupled to the atmospheric radiation environment, chemical composition, and dynamics. For example, the presence of a cloud formed from condensation gives clues to the temperature structure and metallicity of an atmosphere, as cloud formation requires a supersaturation of the condensing species. In addition, clouds obfuscate investigations of exoplanet atmospheres by hiding molecular spectral features, and thus future exoplanet observing missions and programs would greatly benefit from a theoretical framework that can determine *a priori* whether an exoplanet is cloudy or clear.

Previous efforts in detailed modeling of exoplanet clouds can be split into two categories: Equilibrium condensation and grain chemistry. Equilibrium condensation presumes an atmosphere with a composition determined by thermochemical equilibrium, and that certain species can be in their condensed phase if it is energetically favorable. The resulting condensed material would be distributed vertically such that the sedimentation of cloud particles is balanced by vertical lofting due to eddy mixing (A. S. Ackerman and Marley, 2001). Using this framework, Morley, Fortney, Marley, Visscher, et al. (2012) showed that the formation of sulfide clouds (e.g. Na_2S) could explain the infrared colors of cooler Brown dwarfs, while Morley,

Fortney, Kempton, et al. (2013) was able to explain the flat transmission spectrum of the super Earth GJ 1214 b by appealing to the formation of KCl and ZnS clouds in a high (100–1000 times solar) metallicity atmosphere. Charnay, Meadows, and Leconte (2015) and Charnay, Meadows, Misra, et al. (2015) extended this scheme to 3D and found that submicron KCl and ZnS particles can be lofted to high enough altitudes such that the resulting transmission spectrum is flat within the uncertainties of the data. However, while these models have been successful in explaining the available data, they lack the physical processes that govern cloud formation and evolution on the scale of the particles, namely their initial nucleation and their subsequent growth/loss through microphysical processes. This deficiency dampens their predictive powers.

In contrast to the equilibrium condensation models, grain chemistry models assume that cloud formation is a kinetics process, characterized by the growth and shrinking of cloud particles with mixed compositions via heterogeneous chemical reactions on their surfaces. This framework has been developed in great detail for brown dwarf and hot Jupiter atmospheres, where the cloud formation processes is assumed to begin with the nucleation of TiO_2 clusters in the upper atmosphere that are then transported downwards and act as nucleation sites for an array of condensing species, including $MgSiO_3$, Mg_2SiO_4, SiO_2 ,Al_2O_3, and Fe (Helling, Oevermann, et al., 2001; Woitke and Helling, 2003; Woitke and Helling, 2004; Helling, Klein, et al., 2004; Helling and Woitke, 2006; Helling, A. Ackerman, et al., 2008; Helling, Woitke, and Thi, 2008; Witte, Helling, and Hauschildt, 2009; Witte, Helling, Barman, et al., 2011; Lee, Helling, Dobbs-Dixon, et al., 2015; Lee, Helling, Giles, et al., 2015; Helling, Lee, et al., 2016). These models have been compared favorably to brown dwarf emission spectra (Witte, Helling, Barman, et al., 2011), and have shown that a vertical gradient in cloud composition is likely in brown dwarf and hot exoplanet atmospheres. In addition, these models have also been recently extended to 3D (Lee, Helling, Dobbs-Dixon, et al., 2015; Helling, Lee, et al., 2016), and showed that HD 189733b and HD 209458b are enveloped by mineral clouds with vertical and latitudinal variations in composition due to dynamics and global temperature differences, with the former planet exhibiting a lower cloud deck, explaining the more pronounced molecular features in its transmission spectra. Though these models have greatly illuminated the complexities of brown dwarf/exoplanet cloud processes, they are difficult to generalize due to their reliance on the specific TiO_2 nucleation pathway for cloud formation. As a result, they have not yet been used to investigate cooler, smaller exoplanets.

In this work we explore the formation and evolution of exoplanet clouds from a perspective especially applicable to cooler atmospheres: cloud microphysics. On Earth, water clouds form through condensation of preexisting water molecules onto condensation nuclei (heterogeneous nucleation) or, less frequently, by homogeneous nucleation where no seeds are necessary; these cloud particles can then grow by condensation and coagulation/coalescence, or shrink by evaporation, and are transported through sedimentation, advection, and turbulent mixing. These processes are likely at work across the Solar System, controlling the sulfuric acid clouds of Venus (Gao et al., 2014), the CO_2 and water clouds of Mars (Michelangeli et al., 1993; Colaprete, Toon, and Magalhães, 1999), the ammonia clouds of Jupiter and Saturn (Rossow, 1978; Carlson, Rossow, and Orton, 1988), and the hydrocarbon clouds of Titan, Uranus, and Neptune (Moses, Allen, and Yung, 1992; Barth and Toon, 2003; Barth and Toon, 2004; Barth and Toon, 2006). Cloud microphysics is a variation on grain chemistry in that it also treats cloud formation as a kinetics process, but it presumes that the condensing material already exists as free floating molecules, whereas in grain chemistry many of the condensed species form on the grains themselves.

We use the 1–dimensional Community Aerosol and Radiation Model for Atmospheres (CARMA), which calculates the rates of particle growth and loss due to the aforementioned cloud microphysics processes. We apply our model to GJ 1214 b, as it has the highest precision observations for planets in its size and temperature range (Kreidberg et al., 2014), and simulate the formation of KCl and ZnS clouds. Not only does this allow us to test our model in an exoplanet framework, but we will also be able to investigate the assumptions and results of previous studies that have targeted this world (Morley, Fortney, Kempton, et al., 2013; Charnay, Meadows, and Leconte, 2015; Charnay, Meadows, Misra, et al., 2015).

In §5.3, we describe our cloud microphysics model, including the augmentations needed to simulate exoplanet clouds. We discuss our results in §5.4, where we show how the cloud distribution varies with atmospheric mixing and metallicity, and when composite cloud particles are allowed. We present our conclusions and make recommendations for future investigations in §5.6.

5.3 Model

5.3.1 Model Description & Setup

CARMA is a 1–dimensional Eulerian forward model that solves the discretized continuity equation for aerosol particles subject to vertical transport and production and loss due to particle nucleation (homogeneous and heterogenous), condensation, evaporation, and coagulation (Turco et al., 1979; Toon et al., 1988; Jacobson and Turco, 1994; Bardeen et al., 2008). Starting from some initial state, CARMA time steps towards an equilibrium particle distribution by balancing the rates of the aforementioned processes. As such, perturbations to the particle distribution due to changes in the background atmosphere, such as temperature variations, can be investigated. CARMA resolves the particle size distribution using mass bins, thus avoiding assumptions of analytical particle size distributions (e.g. lognormal), which may lead to false conclusions when the actual size distribution is irregular.

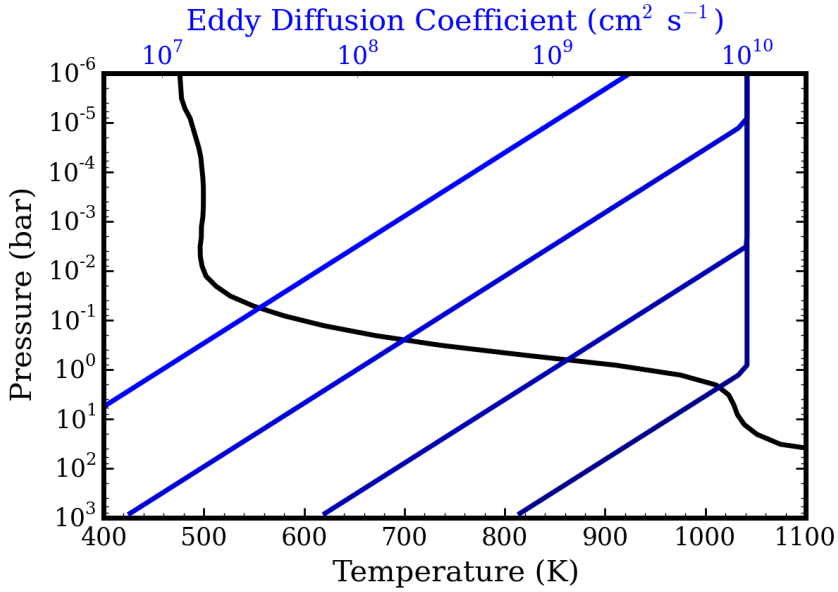

Figure 5.1: Pressure–temperature profile for GJ 1214 b calculated by SCARLET (black) and K_{zz} profiles for different K^o_{zz} values (blue).

A key input to CARMA is the background atmosphere's pressure–temperature profile, which we calculate for GJ 1214 b using the SCARLET code Benneke and Seager (Self-Consistent Atmospheric Retrieval framework for ExoplaneTs; 2013). SCARLET is capable of generating fully self-consistent 1D atmospheres given a metallicity, C/O ratio, stellar insolation, and internal heat, while taking into account thermochemistry, photochemistry, and radiative–convective heat transport. For GJ

1214 b we generated pressure–temperature profiles for a clear, H/He-dominated atmosphere in radiative–convective equilibrium, which we split into 80 levels (Figure 5.1). The atmospheric compositions is assumed to be in thermochemical equilibrium with solar C/O ratios and metallicities of 1×, 10×, and 100× solar metallicity (i.e. [Fe/H] = 0, 1, 2). Morley, Fortney, Kempton, et al. (2013) showed that increasing metallicity leads to cloud decks of higher optical depth, and we will test this result using our model, and evaluate how cloud optical depth scales with metallicity. In addition, we test multiple values for the eddy diffusivity, K_{zz} , parameterized according to Charnay, Meadows, and Leconte (2015),

$$K_{zz} = K^o_{zz} P^{-0.4}, \tag{5.1}$$

where P is the atmospheric pressure in bars, and K^o_{zz} is set to 10^7, 10^8, 10^9, and 10^{10} cm^2 s^{-1} in our tests. Figure 5.1 shows these K_{zz} profiles. Note that we limited itheir values to below 10^{10} cm^2 s^{-1} at all pressure levels. For comparison, Charnay, Meadows, and Leconte (2015) found values for K^o_{zz} between 7×10^6 and 3×10^7 cm^2 s^{-1} in their GCM simulations.

Abundances of the condensates, KCl and ZnS, were assumed to correspond to those of K and Zn at the designated metallicities, as they are both the least abundant element in their molecules. In other words, we assume that all K is tied up in KCl and all Zn in ZnS. The volume mixing ratios of K and Zn in an atmosphere of H_2 and He at solar metallicity are 0.22 and 0.076 ppmv, respectively Lodders (2010).

All simulations are initiated in an atmosphere devoid of particles, and with constant KCl and ZnS volume mixing ratios at all pressure levels corresponding to their 1×, 10×, or 100× metallicity abundances. Both species are then allowed to homogeneously nucleate to produce cloud particles, and evolve towards equilibrium. For one simulation we allow ZnS to both homogeneously nucleate and heterogeneously nucleate on homogeneously nucleated KCl cloud particles, producing layered, mixed clouds. Once formed, the cloud particles are transported via eddy diffusion and sedimentation under gravity, with a gravitational acceleration for GJ 1214 b of 8.93 m s^{-2} (Charbonneau et al., 2009). We set a zero–flux top boundary condition, corresponding to a lack of significant loss of condensing/condensed material to space. For the bottom boundary, we hold the abundances of KCl and ZnS vapor to their initial values, and set the particle abundance to zero, as the condensate vapors are vastly undersaturated there.

Condensational growth in CARMA takes into account latent heating of particles due to the addition of vapor molecules. This heat is removed from the particle by conduction. We set the thermal conductivity κ of the atmosphere to be that of pure H_2, given by

$$\kappa(ergs\, s^{-1}\, m^{-1}\, K^{-1}) = 7148.57 + 39.12T + 3.1607 \times 10^{-3} T^2, \tag{5.2}$$

where T is temperature (in K) and the numerical coefficients are obtained by fitting to data from Lemmon (2016). For the heat capacity of the atmosphere C_p, which is used to correct for κ in the kinetics limit, we use a constant value of 1.3×10^8 ergs g^{-1} K^{-1}, appropriate for a H_2–dominated atmosphere (Kataria et al., 2015). The viscosity of the atmosphere is given by the Sutherland equation

$$\eta(Poise) = 8.76 \times 10^{-5} \left(\frac{293.85 + 72}{T + 72}\right) \left(\frac{T}{293.85}\right)^{1.5}, \tag{5.3}$$

where the numerical constants are those for H_2 taken from White (1974). The atmospheric viscosity is needed to calculate the sedimentation velocity of cloud particles in the continuum limit.

5.3.2 Microphysical Properties of KCl & ZnS

Another set of key inputs to CARMA are the material properties that define each condensing species, including their densities (1.98 g cm^{-3} for KCl and 4.09 g cm^{-3} for ZnS), saturation vapor pressures, surface tensions/energies, latent heats, and molecular diffusion coefficients.

The saturation vapor pressures P_x^s for KCl and ZnS have been estimated from by Morley, Fortney, Marley, Visscher, et al. (2012) to be

$$\log P^s_{KCL} = 7.611 - 11382/T \tag{5.4}$$

$$\log P^s_{ZnS} = 12.812 - 15873/T - [Fe/H], \tag{5.5}$$

where P_x^s is in bars. These saturation vapor pressures can then be used in conjunction with the Clausius–Clapeyron equation

$$\frac{d \ln P_x^s}{dT} = \frac{L}{RT^2} \tag{5.6}$$

to calculate the latent heats L, where R is the universal gas constant. For KCl and ZnS, L is found to be 2.923×10^{10} ergs g^{-1} and 3.118×10^{10} ergs g^{-1}, respectively (Charnay, Meadows, Misra, et al., 2015).

The surface tension γ_x of molten KCl is (Janz and Dijkhuis, 1969)

$$\gamma_{KCl}(ergs\,cm^{-2}) = 160.4 - 0.07T. \tag{5.7}$$

This value is similar to that found for the {100} face of solid KCl crystals (Westwood and Hitch, 1963), which is reassuring since it is unknown what phase KCl would be in exoplanet atmospheres. No data exists regarding the surface tension of liquid ZnS, so we use the surface energy of ZnS solid, $\gamma_{ZnS} = 1672$ ergs cm^{-2} (Celikkaya and Akinc, 1990). Note the one order of magnitude difference between KCl and ZnS; as the particle nucleation and condensation rates scale exponentially with surface energy to the third power, this will likely have a large impact on the resulting cloud structure.

Condensation of trace gases in an atmosphere depends strongly on the diffusion rate of gas molecules to the cloud particles. The molecular diffusion coefficient D can be expressed using Chapman–Enskog theory as (Jacobson, 2005)

$$D = \frac{5}{16Ad^2\rho_a\Omega_c}\sqrt{\frac{RT\mu_a(\mu_c + \mu_a)}{2\pi\mu_c}}, \tag{5.8}$$

where A is Avogadro's number, ρ_a is the atmospheric mass density, μ_a and μ_c are the mean molecular weight of the atmosphere and molecular weight of the condensing species, respectively, Ω_c is the collision integral of the condensing species with the main atmospheric components and is of order unity, and d is the collision diameter of the condensing species. We estimate the collision diameters for KCl and ZnS to be 2.67 Å and 2.0464 Å, respectively, from their equilibrium bond lengths (Sanderson, 1976; Zack and Ziurys, 2009).

For our test case where ZnS is allowed to nucleate on KCl, an additional set of physical quantities that relate the two species must be known. These include the contact angle made by the surface of a ZnS "droplet" on the surface of a KCl grain, which is related to the surface energies of the two species against the atmosphere and the interfacial energy of the two species together; the desorption energy of a ZnS molecule on a KCl surface; and the oscillation frequency associated with said

desorption energy. None of these quantities are known at present, and would require laboratory investigations to measure. We have thus made approximations for their values. The desorption energy and associated oscillation frequency have been set to that of water over silicate surfaces, 0.18 eV and 10^{13} Hz, respectively (Lavvas, Griffith, and Yelle, 2011). The contact angle is completely unknown, and so we have set it to a small value of 2° to promote formation of layered clouds. Increasing this angle would decrease the rate at which ZnS nucleate onto KCl, and vice versa. Once ZnS has nucleated onto the KCl particle, it is assumed to completely cover it, thereby cutting off KCl vapor from condensing onto the KCl "core". This is different from the approach of Helling and Woitke (2006) and similar models, where multiple condensates can condense on a particle simultaneously.

5.4 Results

5.4.1 The Lack of Pure ZnS Clouds

No pure ZnS clouds resulted from our microphysical calculations due to its low homogeneous nucleation rates stemming from its high surface energy. Thus, the equilibrium cloud distributions we present in §5.4.2 and §5.4.3 are those of KCl only. Our results are in contrast with the results of equilibrium condensation cloud models, which show ZnS to be a major cloud component on warm super Earths (Morley, Fortney, Kempton, et al., 2013; Morley, Fortney, Marley, Zahnle, et al., 2015). We will discuss how ZnS can still manifest as a cloud material in §5.4.4.

5.4.2 Variations with $\mathbf{K}_{zz}$

Figure 5.2 shows the total particle number density (solid) and total condensed mass density (dashed) for the resulting cloud distribution at equilibrium subject to eddy diffusion coefficients at 1 bar of 10^7 (red), 10^8 (yellow), 10^9 (green), and 10^{10} cm^2 s^{-1} (blue). Solar metallicity is assumed. Both the number of cloud particles and the condensed mass generally increase with increasing eddy diffusion coefficient, but the increase is not linear, suggesting contributions from processes beyond vertical transport (see below). Furthermore, the peaks in the particle number density curves occur higher in the atmosphere than the peaks of the mass density curves, suggesting that most of the mass contribution comes from large particles at the cloud base.

Figure 5.3 shows the particle size distribution at 0.1 bar in the atmosphere corresponding to the four eddy diffusion cases (same colors as in Figure 5.2). None of the distributions are strictly lognormal, as has been proposed for previous exoplanet cloud models (e.g. A. S. Ackerman and Marley, 2001), and they evolve further away

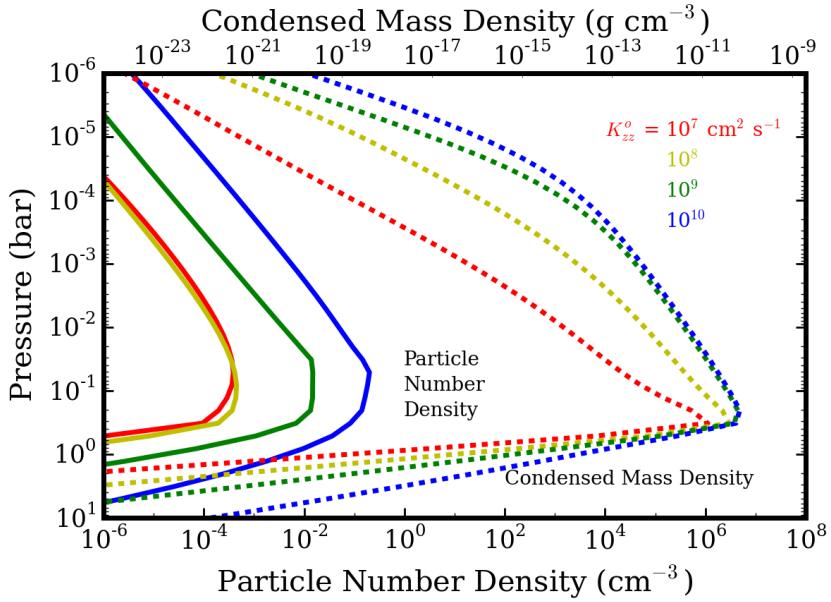

Figure 5.2: Particle number density (solid) and mass density of condensed material (dashed) as a function of atmospheric pressure level for K_{zz}^o values of 10^7 (red), 10^8 (yellow), 10^9 (green), and 10^{10} cm^2 s^{-1} (blue). Solar metallicity is assumed.

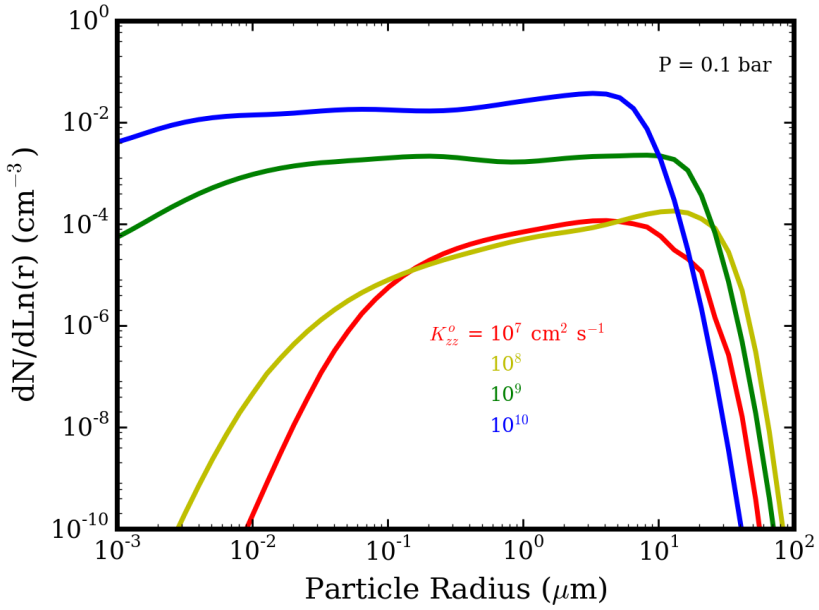

Figure 5.3: Particle size distributions at 0.1 bars in the atmosphere. The colors indicate the same K_{zz}^o values as in Figure 5.2.

from lognormal as K_{zz} is increased. At the highest K_{zz} , the distribution is nearly flat from 10 nm to several microns. This is indicative of a blending of two or more

particle populations, each with their own processes of formation and evolution (Seinfeld and Pandis, 2006).

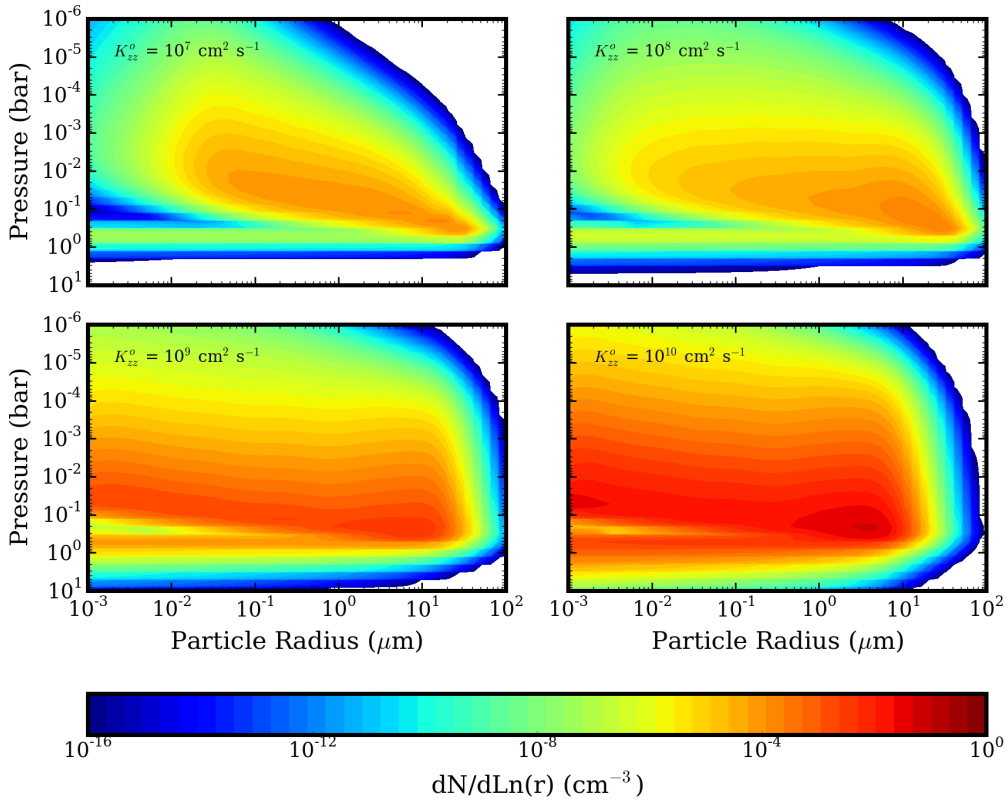

Figure 5.4: Particle number density as a function of particle radius and atmospheric particle level for the four K_{zz}^o cases.

Figure 5.4 summarizes our results for KCl clouds in the atmosphere of GJ 1214 b as K_{zz} is varied by showing the particle number density (in the form of $dN/dLn(r)$) as a function of particle radius and atmospheric pressure level. The characteristic "bar–like" feature at the bottom of the clouds show the evaporation (and thus decreasing size) of cloud particles as they sediment past the cloud base. Above this feature, a maximum in the particle number density can be discerned at ~0.3 bars that corresponds to ~20 μm for the lowest K_{zz} , decreasing to ~2 μm for the highest K_{zz} case. At lower pressures, the particle number density drops exponentially, while the mean particle radius varies differently depending on the K_{zz} .

The results shown in Figs. 5.2–5.4 paint a detailed picture of how KCl clouds evolve as K_{zz} changes. For example, Figure 5.2 shows that, while the two lowest–K_{zz} cases show similar particle number densities and different mass densities, the two higher K_{zz} cases show different particle number densities but similar mass densi-

ties. Meanwhile, Figure 5.3 shows that the lowest K_{zz} case has a nearly lognormal size distribution, while the higher K_{zz} cases have particle size distributions more extended towards smaller radii. Finally, Figure 5.4 show that, for the lowest K_{zz} case, the mean particle radius drops precipitously to smaller values higher up in the cloud, while higher K_{zz} cases maintain a healthy supply of large particles even at high altitudes. These results suggest that there are two regimes of cloud formation in this system, and it is likely related to the interplay between transport and particle formation via homogeneous nucleation.

In the first regime, corresponding to low K_{zz} values, the upwelling rate of KCl vapor from depth is low, producing small supersaturations in the cloud–forming region right above the cloud base, which in turn leads to low rates of particle production via homogeneous nucleation. The main particle population is therefore an "aged" population sustained by upward lofting and condensation growth, while undergoing sedimentation at the same time. These processes combined result in lognormal size distributions. The two lowest–K_{zz} cases correspond to this regime.

As K_{zz} is increased, the rate at which KCl vapor is upwelled from depth into the cloud forming region near the cloud base also increases. This leads to higher supersaturations and higher rates of particle nucleation, which preferentially produce numerous smaller particles, leading to the extension of the particle size distributions to smaller particle radii and higher particle number densities. These smaller particles take longer to sediment, thus increasing the cloud mass as well. At the same time, increased mixing leads to higher lofting of large particles, thereby increasing the presence of large particles at higher altitudes. The two higher K_{zz} cases correspond to this regime, which is sustained by homogeneous nucleation and mixing.

The two lowest–K_{zz} cases have a further property not shown in the previous figures, in that their cloud distributions oscillate in time. This is shown in Figure 5.5, where we present the time evolution of the cloud mass density (top 2 plots), particle number density (middle two plots), and KCl vapor saturation radio (= the ratio of the KCl partial pressure to its saturation vapor pressure; bottom two plots). A major difference between the two lowest–K_{zz} cases is the period of this oscillation, with the higher K_{zz} case (lower plot of each pair) oscillating ~7 times faster. This oscillation likely results from the homogeneous nucleation occurring in this regime of cloud formation.

At equilibrium, most of the cloud particles are growing by condensation and sedimenting out of the cloud deck, with very low rates of homogeneous nucleation

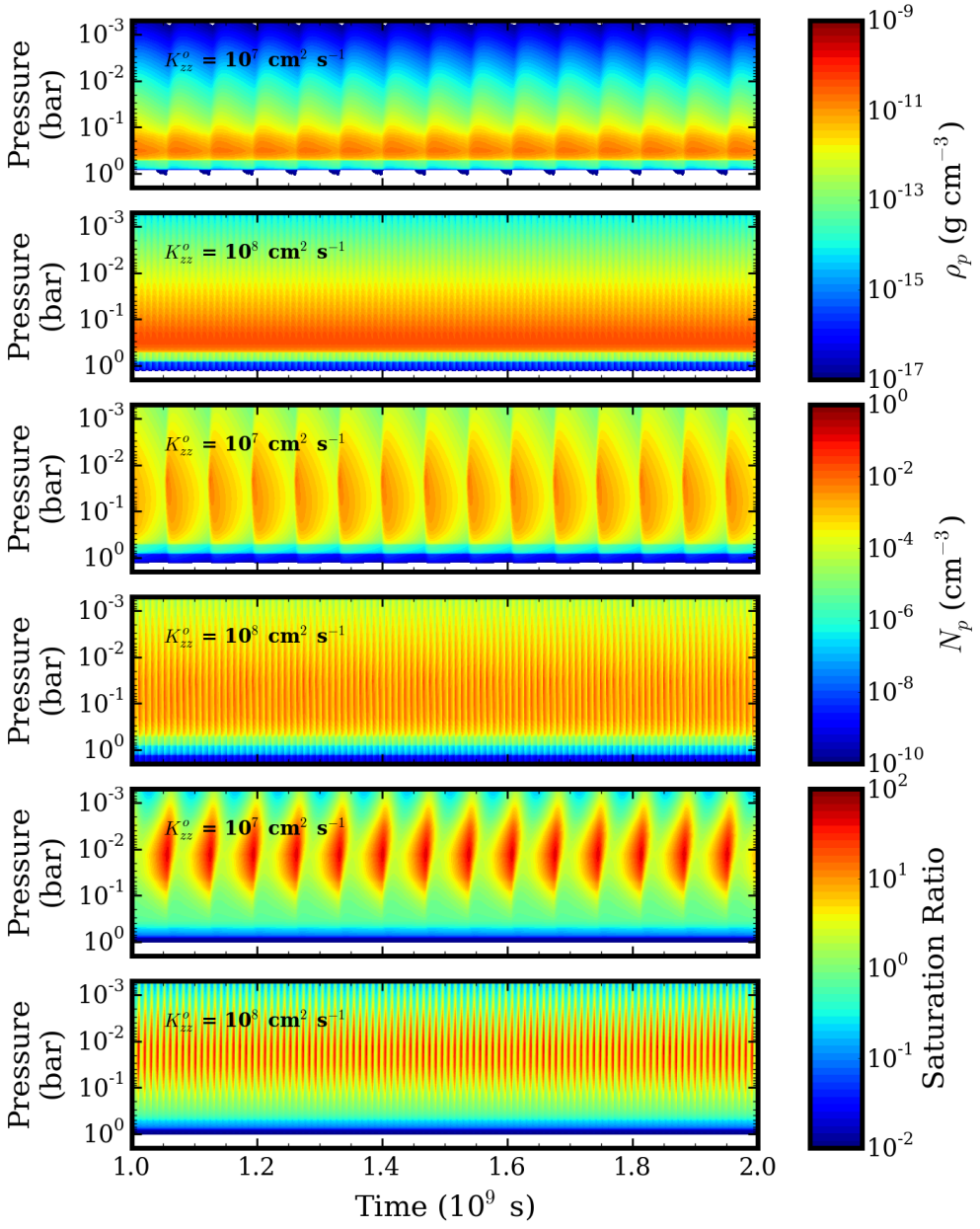

Figure 5.5: Time evolution of the condensed mass density (top two), particle number density (middle two), and KCl saturation ratio (bottom two) for the $K_{zz}^o = 10^7$ (top of each pair) and 10^8 (bottom of each pair) cases.

creating new particles. The cloud can eventually be depleted in this manner, as the K_{zz} is not high enough to sustain large particles, which all particles eventually evolve towards due to constant condensational growth resulting from a steady supply of KCl vapor from depth. However, as the cloud is depleted, the rate of KCl vapor uptake by the particles also decrease. Eventually, the condensation rate be-

comes lower than the KCl vapor upwelling rate, and the vapor mixing ratio begins to increase. Though this may lead to increased growth, the resulting larger particles will simply sediment faster, further decreasing the vapor uptake by the cloud particles. At the same time, as the KCl vapor increases in the cloud forming region, the rate of homogeneous nucleation increases exponentially, eventually reaching a critical value (i.e. the rate of vapor uptake due to particle formation balances the influx of vapor from depth) where the increased particle formation depletes the KCl vapor. Particle formation then decreases to very low values once more, and the newly created particles begin growing by condensation eventually sediment out of the cloud, thus completing the cycle.

The above sequence can be seen in Figure 5.5 by tracing how the KCl saturation ratio correlates with the particle number density and condense mass density. For example, in the lowest K_{zz} case, the saturation ratio reaches a maximum in the cloud formation region (~0.01 bar) at $\sim 1.05 \times 10^9$ s, at which time both particle densities make sudden jumps to their maximum values. The KCl vapor is then quickly depleted while the particle densities begin a slow decline as the new particles grow and sediment out of the cloud. Eventually, as the condensation centers are depleted, the KCl saturation ratio begins to increase again.

The processes described above is heavily dependent on the rate at which KCl is supplied to the cloud forming regions. Increasing this rate leads to increased rates of particle growth and depletion, and thus increased frequency of oscillation, which is what is seen in our results when the two lowest K_{zz} cases are compared. However, this sequence eventually breaks down when the "background" homogeneous nucleation rate becomes comparable to the particle growth and sedimentation rates. In other words, this oscillatory behavior should be significantly reduced for the higher K_{zz} regimes. Figure 5.6 shows that this is indeed the case, though oscillations with comparatively tiny amplitudes still persist.

It is useful to evaluate whether this oscillatory behavior is important for exoplanet clouds. The time scales are long: 7 Earth years for the lowest K_{zz} case and 1 Earth year for the next highest K_{zz} case. This is far longer than timescales associated with atmospheric dynamics (e.g. Charnay, Meadows, and Leconte, 2015), which can potentially produce local pockets of supersaturation that causes high homogeneous nucleation rates (Helling, Oevermann, et al., 2001). Two possibilities exist: (1) the oscillations seen here occur over a long time scale, on top of the short timescale cloud variations due to dynamics, or (2) atmospheric dynamics disrupt

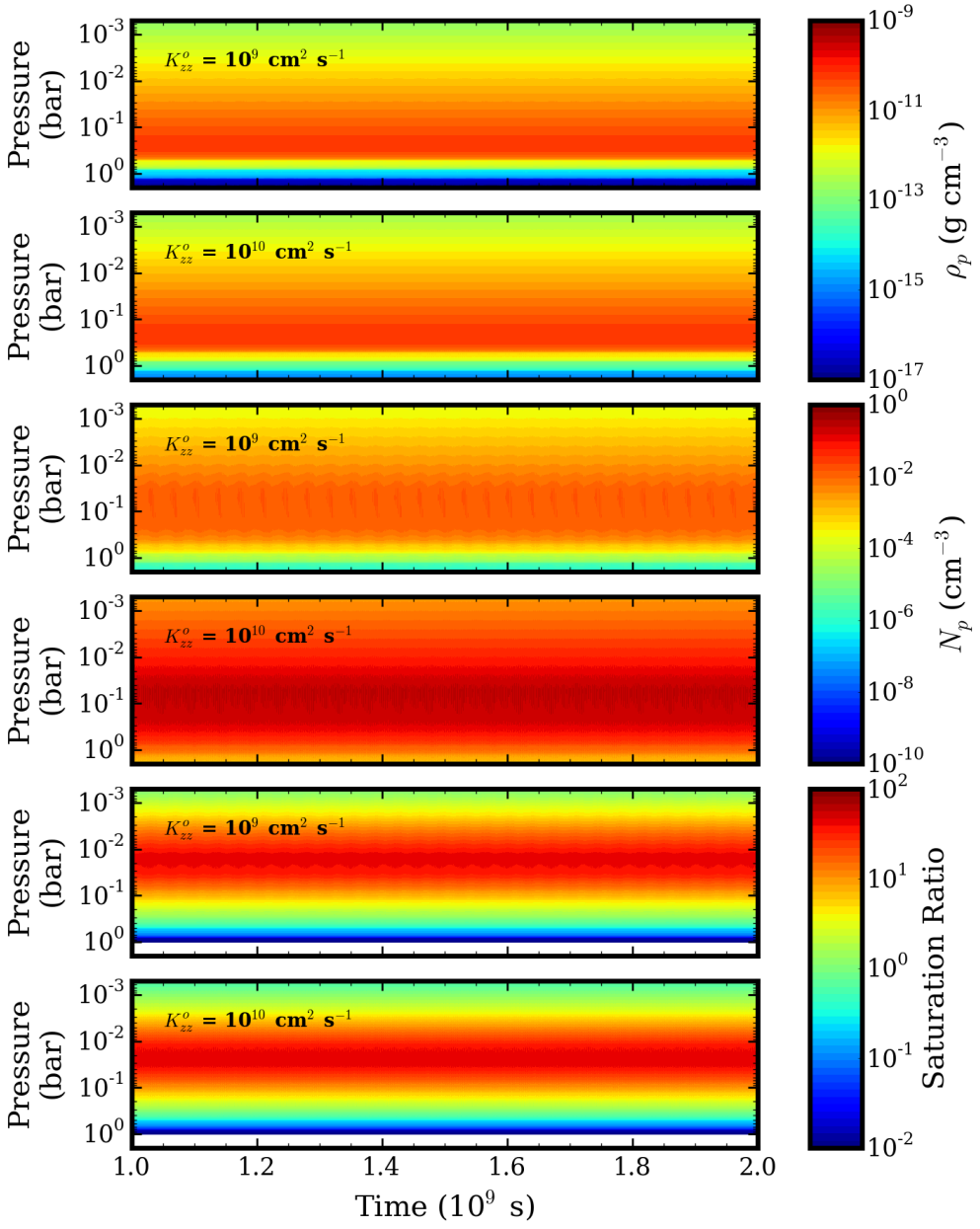

Figure 5.6: Same as Figure 5.5 for the $K_{zz}^o = 10^9$ (top of each pair) and 10^{10} (bottom of each pair) cases.

the cycle such that it does not occur. A coupled dynamics–microphysical model will be needed to ascertain which possibility is more likely.

5.4.3 Variations with Metallicity

Figure 5.7 shows the total particle number density (solid) and total condensed mass density (dashed) for the resulting cloud distribution at equilibrium in atmospheres

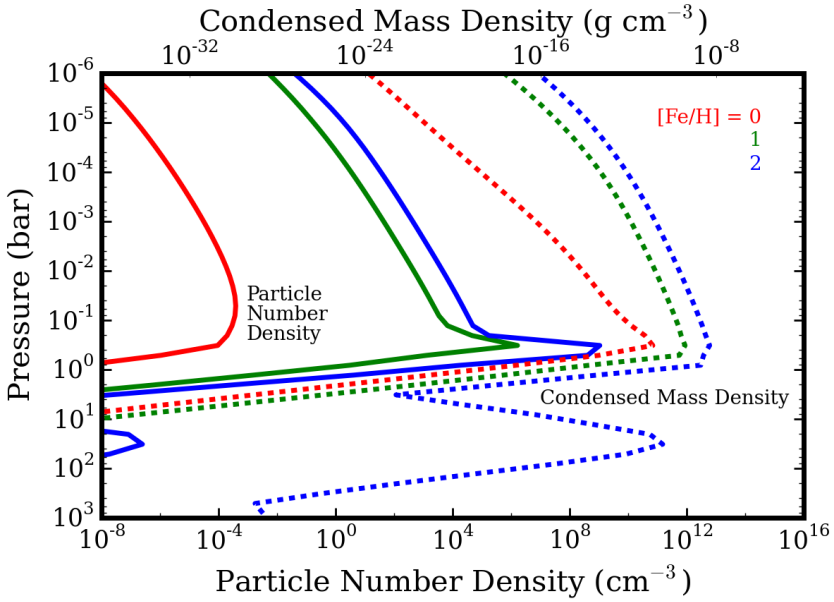

Figure 5.7: Particle number density (solid) and mass density of condensed material (dashed) as a function of atmospheric pressure level for solar (red), 10x solar (green), and 100x solar (blue) metallicity. A K_{zz}^{o} value of 10^{7} cm^{2} s^{-1} is assumed.

with metallicities of 1x (red), 10x (green), and 100x (blue) solar metallicity. A K_{zz}^{o} value of 10^{7} cm^{2} s^{-1} has been assumed. As expected, increasing the metallicity increases the cloud mass, but the magnitude of the increase is not linear–the increase between the solar and 10x solar cases is much greater than between the 10x and 100x solar cases (which is about 1 order of magnitude, in line with the increase in metallicity) The shapes of the curves are also different, with the higher metallicity cases having a large abundance of smaller particles at the cloud base (i.e. their presence is seen in the number density curves but not the mass density curves). Furthermore, the 100x solar case has a secondary cloud formation at a depth of a few tens of bars, caused by a local minimum in the saturation vapor pressure corresponding to a nearly isothermal region of the atmosphere (Figure 5.1).

Figure 5.8 shows the particle size distributions at 0.1 bar in the atmosphere for the same metallicity cases as in Figure 5.7. Again, the distributions are not lognormal, but they are more similar to a lognormal distributions than the flat distributions from the high K_{zz} cases. This is not surprising since K_{zz} is low for all of these cases. As with the number and mass densities, the two higher metallicity cases are vastly different from the solar metallicity case–whereas the latter peaks at a few microns, the former peak at 0.1 μm, feature extensions to smaller particles, and are

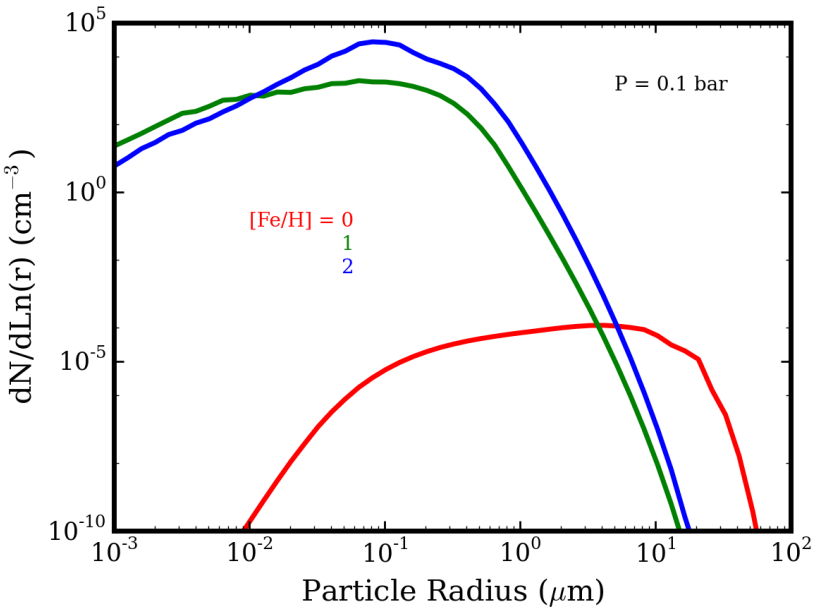

Figure 5.8: Particle size distributions at 0.1 bars in the atmosphere. The colors indicate the same metallicities as in Figure 5.7.

low in particles >1 μm. This allows for a comparison to the results of Charnay, Meadows, Misra, et al. (2015), which prescribed several particle sizes to their KCl clouds, including 0.1 μm. Indeed, the condensate mass mixing ratio of our 100x solar metallicity case (Figure 5.7) is within a factor of two of their results for the same mean particle radius and metallicity.

Figure 5.9 summarizes our metallicity results. It is here that the large difference between the solar and higher metallicity cases truly manifests: the distribution of particles with size and atmospheric pressure level are clearly dissimilar. This difference can again be attributed to the impact of homogeneous nucleation, as can be inferred by the large abundance of small particles (<0.1 μm) at ~0.3 bar in the higher metallicity cases. This is due to the higher upward flux of KCl vapor from depth into the cloud forming region attributed to the higher metallicity. As with the higher K_{zz} cases, the increased KCl vapor flux leads to increased supersaturations, and thus higher rates of homogeneous nucleation and production of smaller particles. The difference between the higher metallicity and the higher K_{zz} cases is that the KCl vapor mixing ratio can never be higher than what they are at the cloud base, and so the higher metallicity cases are able to produce a higher supersaturation even at low K_{zz} compared to the solar metallicity case at high K_{zz} , thereby producing many more particles from homogeneous nucleation. The high nucleation rates

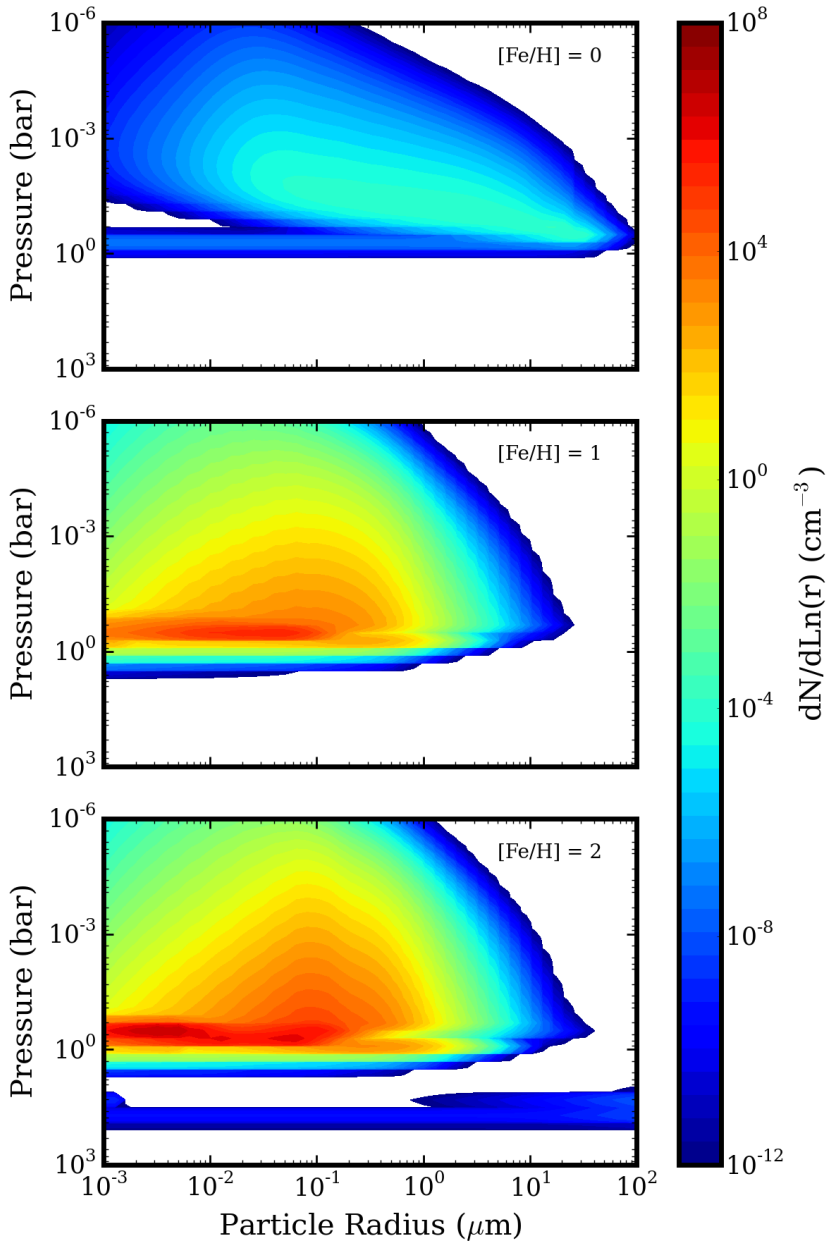

Figure 5.9: Particle number density as a function of particle radius and atmospheric particle level for the three metallicity cases.

overwhelm the condensational growth and sedimentation of particles, and thus no oscillatory behavior is observed. The high number of particles also means that the KCl vapor is distributed among more particles, and so growth of particles to larger sizes (>1 μm) is discouraged.

The secondary cloud can be seen in the 100x solar plot as being composed of very

large particles, even to the extent that they have hit the maximum size allowable in our model. This is likely due to them being at depth, where sedimentation velocities are low.

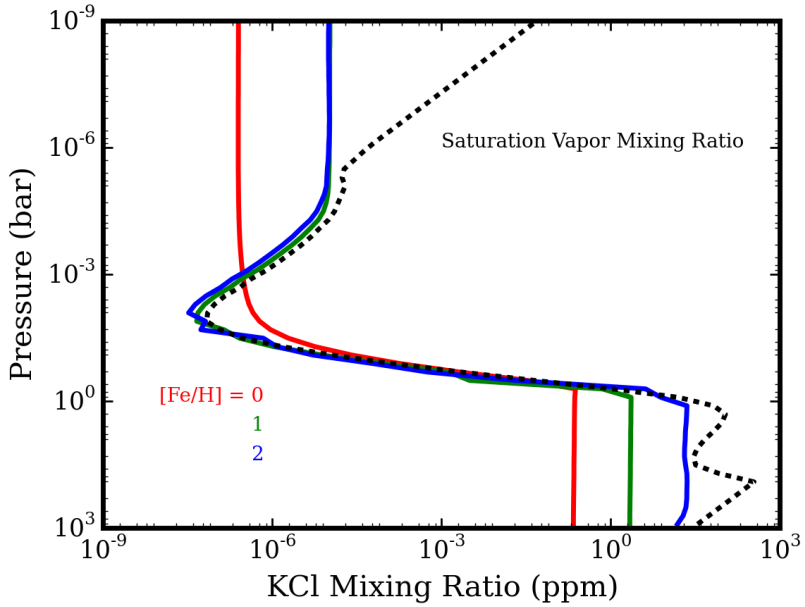

Figure 5.10: KCl mixing ratio for the solar (red), 10x solar (green), and 100x solar (blue) metallicity cases, compared to the KCl saturation vapor mixing ratio (black, dashed).

Figure 5.10 shows the KCl vapor mixing ratio from the three metallicity cases and compares them to the KCl saturation vapor mixing ratio (black, dashed). The solar metallicity curve is taken from a point in time during the depletion of the cloud and charging of the cloud forming region with KCl vapor. In contrast, the consistently high rate of particle formation in the high metallicity cases keeps the KCl vapor pressure close to saturation at all times. The higher metallicity cases also feature a higher KCl mixing ratio above the saturated region, where the vapor is constantly being replenished by evaporating cloud particles lofted into that region, balanced by depleted due to downward mixing of vapor into the cloud forming region. The KCl mixing ratio curve can be seen to approach the local minimum in the saturation vapor mixing ratio curve at around a few tens of bars, thereby generating the secondary cloud at depth.

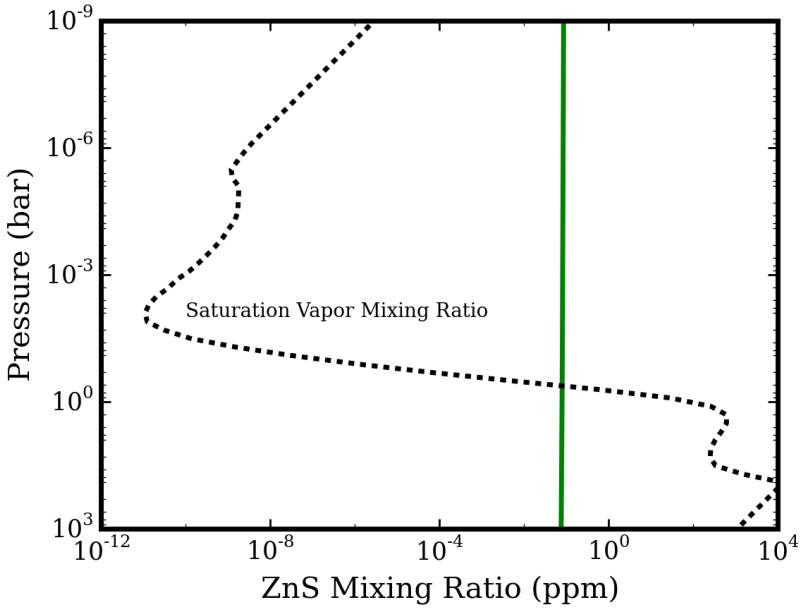

Figure 5.11: Equilibrium ZnS mixing ratio for the solar metallicity case with K^o_{zz} = 10^7 cm^2 s^{-1} (green) compared to the ZnS saturation vapor mixing ratio (black, dashed), where only homogeneous nucleation of KCl and ZnS are allowed.

5.4.4 Mixed Clouds

Figure 5.11 shows the ZnS vapor mixing ratio for the solar metallicity, lowest K_{zz} case and compares it to the ZnS saturation vapor mixing ratio (black, dashed). As previously stated, the high surface energy of ZnS prevented particles from forming through homogeneous nucleation. This is manifested here by the equilibrium ZnS vapor mixing ratio curve being well–mixed instead of being close to saturation due to particle formation, even when the supersaturation is extremely high ($\sim 10^{10}$). We thus investigate the formation of ZnS clouds by heterogeneous nucleation, where ZnS is allowed to nucleate onto pure KCl particles formed from homogeneous nucleation.

Figure 5.12 shows the total particle number density (solid) and total condensed mass density (dashed) for the resulting cloud distribution at equilibrium, where a pure KCl (red) and a mixed ZnS/KCl cloud (gray) have formed. We assume a K^o_{zz} value of 10^7 cm^2 s^{-1} and solar metallicity. The mixed cloud develops near the cloud base of the KCl cloud, and visibly depletes the KCl cloud by converting KCl particles to KCl cores at ~0.2 bars. At higher altitudes, the mass density of mixed clouds remains similar to that of the pure KCl clouds despite rapidly falling number densities, indicating that the mixed particles are on average larger than the pure KCl

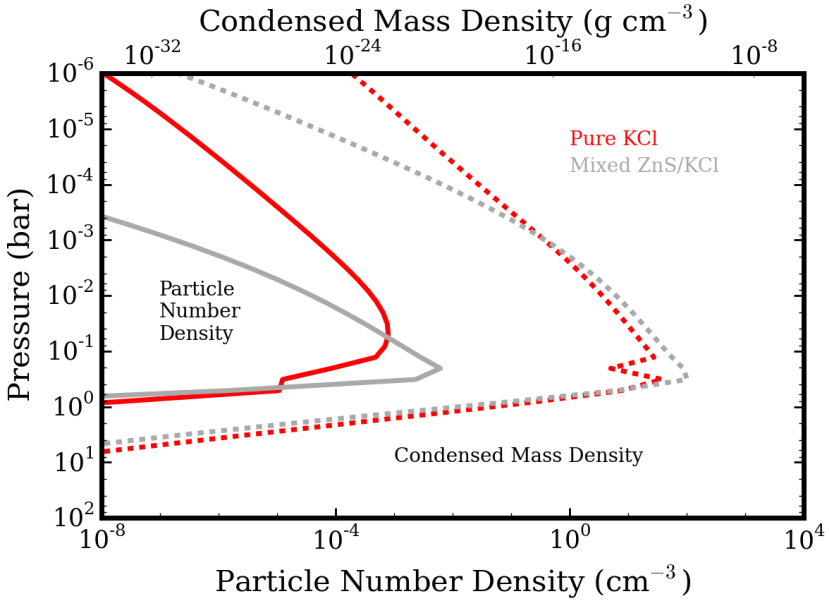

Figure 5.12: Particle number density (solid) and mass density of condensed material (dashed) as a function of atmospheric pressure level for pure KCl (red) and mixed (ZnS shell covering a KCl core; gray) particles. Solar metallicity and a K_{zz}^{o} value of 10^{7} cm^{2} s^{-1} is assumed.

particles.

Figure 5.13 shows the particle number density as a function of particle radius and atmospheric pressure level, plotted at the same scale as in Figure 5.4. The formation of the mixed clouds results in a decrease in ~10 μm KCl particles at ~0.2 bars. We can also confirm that, above ~0.01 bar, the mean mixed particle is larger than the mean pure KCl particle, suggesting that the opacity of the mixed cloud may dominate over that of the pure KCl cloud.

Figure 5.14 compares the ZnS vapor mixing ratio (green) to its saturation vapor mixing ratio (black, dashed) and shows that allowing heterogeneous nucleation depletes ZnS to saturation above the cloud base. Like the KCl vapor mixing ratio curve in Figure 5.10, the ZnS vapor becomes well mixed above the cloud, with a mixing ratio set by the minimum in the saturation vapor mixing ratio curve.

Figure 5.15 shows the ZnS mass fraction in the mixed cloud particles as a function of particle radius and atmospheric pressure level. The white areas are regions of the parameter space with particle number densities lower than 10^{-8} cm^{-3}. Most of the ZnS–rich particles are concentrated near the cloud base, but there is a clear preference for ZnS to nucleate onto KCl particles of a few microns in radius. The

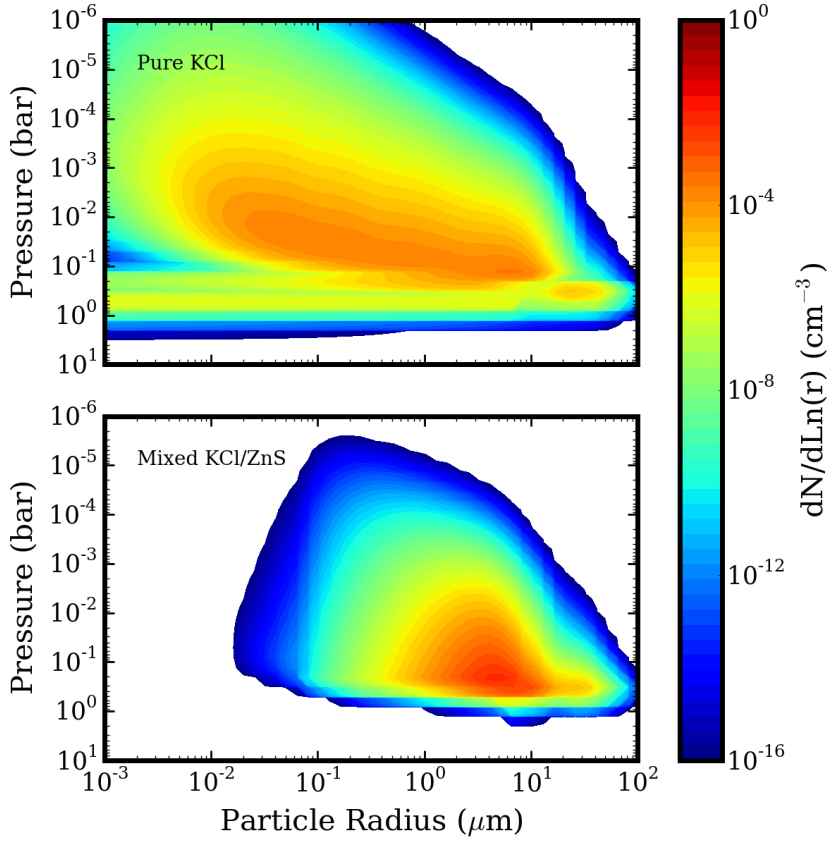

Figure 5.13: Particle number density as a function of particle radius and atmospheric particle level for the pure KCl and mixed cloud cases.

ZnS fraction decreases at larger particle radii, though that is due to the particles having larger KCl cores rather than a lower rate of ZnS deposition.The ZnS mass fraction integrated over the particle size distribution is shown in Figure 5.16. ZnS mass fractions are <0.5 for most of the cloud deck, but peaks at 0.3 bars with a value of 0.7. Despite this peak, however, KCl appears to dominate ZnS as the main cloud component on GJ 1214 b.

5.5 Discussion

The application of cloud microphysics to exoplanet clouds have revealed their potential complexity beyond equilibrium condensation. Accounting for additional properties of the cloud materials beyond their saturation vapor pressures, for example, has shown that a widely accepted cloud component, ZnS, may in fact contribute very little to the atmospheres of super Earths on account of their high surface energies. This raises the question of whether any other proposed cloud materials, such as Na_2S, MnS, Cr, enstatite/forsterite, and Fe, may also possess high surface ener-

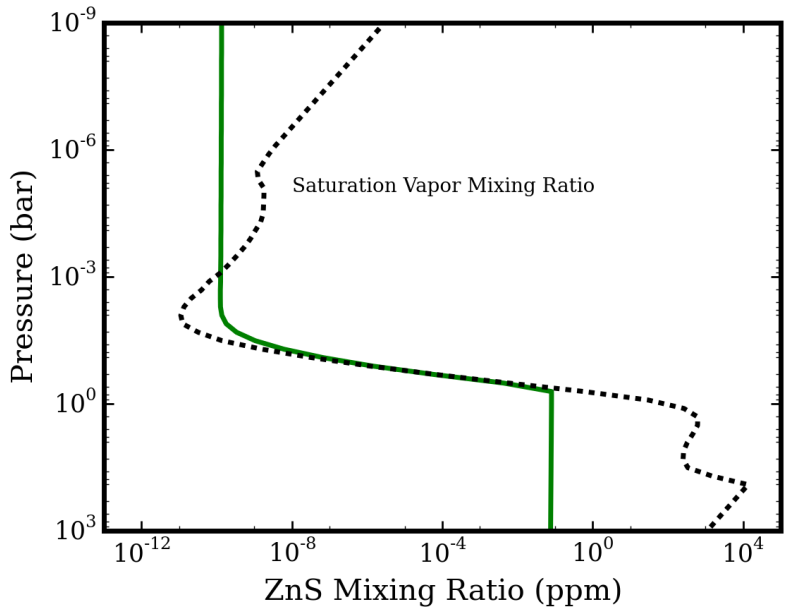

Figure 5.14: Same as Figure 5.11 but allowing for heterogeneous nucleation of ZnS onto KCl particles.

gies that reduce their nucleation rates. Forsterite, for example, has a surface energy of 1280 ergs cm^{-2} (Miura et al., 2010), which is only slightly less than that of ZnS, and thus is unlikely to form in its pure form via homogeneous nucleation. This is consistent with the "dirty grains" from grain chemistry, where condensates such as forsterite are part of multi-component particles, formed from heterogeneous reactions on the grains themselves (e.g. Helling and Woitke, 2006). If surface energies like ZnS are the norm, then most exoplanet clouds are likely of mixed composition, which would further complicate our attempts to characterize them.

Alternatively, homogeneous nucleation may be superseded by heterogeneous nucleation onto meteoric dust formed from the condensation of vapor shed by ablating meteorites. On Earth, meteoric dust can potentially act as nucleation sites for high altitude water ice clouds (Hunten, Turco, and Toon, 1980). If such processes occur in exoplanet atmospheres, then the particle number density of clouds there would be controlled by the flux of meteoric dust particles rather than the rate of homogeneous nucleation, assuming exoplanet cloud materials favor nucleation onto the surfaces of meteoric dust (i.e. the contact angles between meteoric dust and cloud condensates are small).

Another possible set of nucleation sites are the surfaces of sedimenting photochem-

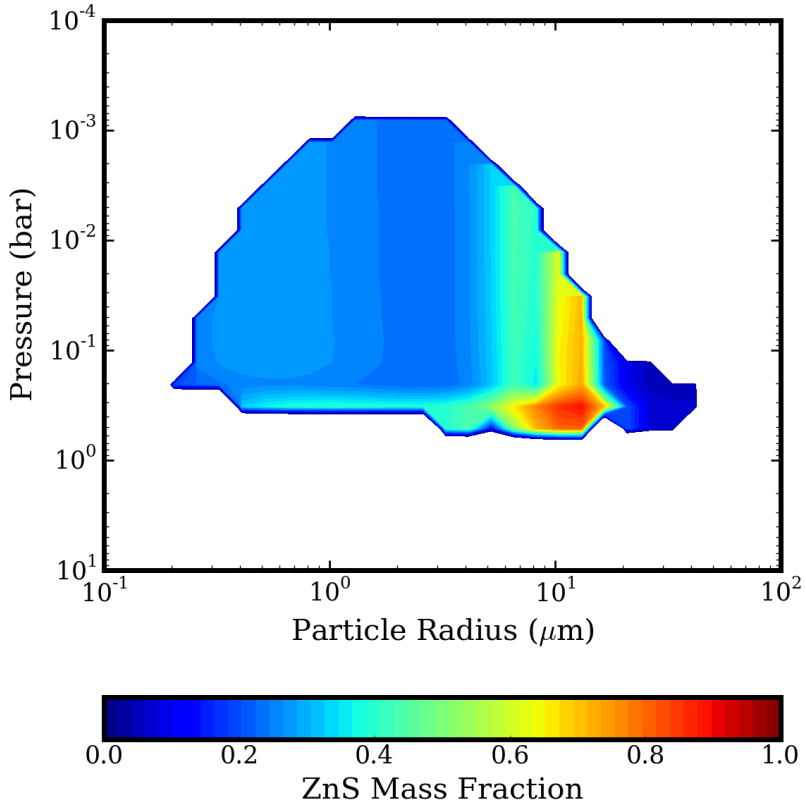

Figure 5.15: ZnS mass fraction of mixed cloud particles as a function of mixed particle radius and atmospheric pressure level. The white regions are parts of parameter space with fewer than 10^{-8} cloud particles per cm^3.

ical haze particles, which form at high altitudes from photochemistry and polymerization of photolysis products. Such hazes pervade many worlds in the Solar System (e.g. Yung, Allen, and Pinto, 1984; Zhang et al., 2012), and similar hazes have been proposed for exoplanets (Morley, Fortney, Kempton, et al., 2013; Zahnle et al., 2016). As these hazes sediment to deeper atmospheric layers, they can potentially become nucleation sites for supersaturated cloud condensates (again, subject to contact angle considerations). Thus, there may exist a strong link between clouds composed of materials derived from equilibrium chemistry and hazes formed from disequilibrium chemistry.

The above discussions show that there exists great uncertainty surrounding the way in which exoplanet clouds form. While we have relied mostly on homogeneous nucleation, heterogeneous nucleation on foreign surfaces can also occur. At higher temperatures, grain chemistry models envision TiO_2 clusters as the condensation nuclei (Helling and Woitke, 2006). Knowing which process(s) dominate exoplanet

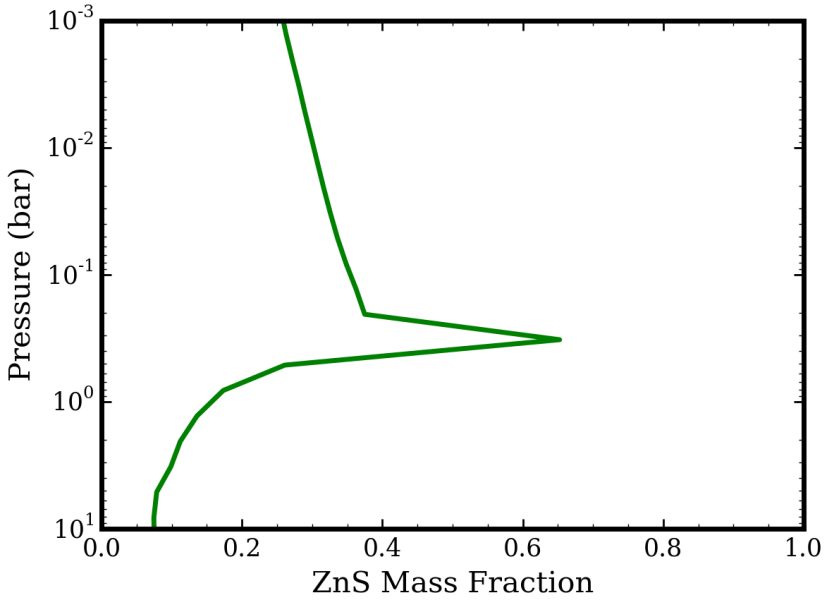

Figure 5.16: ZnS mass fraction of mixed cloud particles integrated over all particle mass bins, as a function of atmospheric pressure level.

cloud formation will require laboratory investigations into the materials in question, especially on how they interact with each other. Furthermore, given the disparity between how cloud formation proceeds at low temperatures (i.e. condensation of water vapor on Earth) versus at high temperatures (formation of condensate molecules on mixed mineral grains), there may exist a transition regime in between where cloud microphysics as we have defined it competes with grain chemistry. The two processes can also be unified in a sense, by removing the distinction in our model between a cloud "core" and the condensed shell around it. In other words, instead of assuming that ZnS completely covers the KCl particles it nucleates on, both materials can condense on the same particle simultaneously, forming "dirty grains".

The uncertainty regarding how exoplanet clouds form will certainly impact predictions of exoplanet "cloudiness". If homogeneous nucleation (and heterogenous nucleation of material on top of homogeneously nucleated particles) dominate, as they do in our current model, then the cloud distribution would be extremely sensitive to the supersaturation of vapor of low surface energy condensates, which in turn means sensitivity to temperature, metallicity, and the cloud material itself. In the extreme case where all other condensates have much higher surface energies than KCl, increasing temperatures and reducing metallicity would result in signif-

icantly less massive clouds, possibly populated with larger particles on account of the reduced rates of homogeneous nucleation, and vice versa for decreasing temperatures and increasing metallicities. These clouds would also be dominated by KCl. In contrast, if the clouds form from heterogeneous nucleation onto foreign surfaces, then high surface energy condensates may become important cloud components, and the cloud mass will be less dependent on supersaturation and material properties and more dependent on the influx of condensation nuclei. Both of these factors will likely result in more massive clouds with mixed compositions.

One microphysical process that we did not consider is coagulation/coalescence, where cloud particles collide with each other and stick. We chose to ignore this process because of the uncertainty involving the outcome of such an interaction, in that the combined particle can be either roughly spherical (usually when the particles are liquid or otherwise amorphous), or be a loose, extended aggregate, which would greatly affect their transport timescales. Given their low densities, aggregates would be able to stay aloft to higher altitudes much longer then spherical, compact grains (e.g. Lavvas, Yelle, and Griffith, 2010). If coagulation is important in exoplanet atmospheres and the resulting particles are preferentially aggregates in nature, then that may explain the high altitude aerosols seen in some exoplanet transmission spectra (Kreidberg et al., 2014). An improved microphysical model that can take into account aggregation and condensational growth of aggregates will be needed to treat this problem.

5.6 Conclusions

We have investigated the formation and evolution of KCl and ZnS clouds in the atmosphere of GJ 1214 b by taking into account microphysical processes, such as homogeneous/heterogeneous nucleation, growth by condensation, loss by evaporation, and transport by sedimentation and eddy diffusion. By varying the magnitude of eddy mixing and the planet's metallicity, as well as allowing for mixed composition clouds, we can make the following conclusions:

- The high surface energy of ZnS forbids formation of pure ZnS clouds via homogeneous nucleation. ZnS can only condense if a favorable nucleation surface exists, such as cloud particles of other compositions, meteoric dust, or photochemical haze particles, in which case the condensed ZnS abundance is beholden to the abundance of the condensation nuclei. The contact angle between a nucleating germ of ZnS and any of these surfaces is not known

but is crucial for calculating the rates of nucleation, necessitating laboratory investigations of these materials.

- The behavior of ZnS suggests that other proposed exoplanet cloud compositions with high surface energies, such as forsterite, may also be unable to form pure grains, which is consistent with the results of grain chemistry models.

- For low degrees of eddy mixing (K_{zz} = 10^7–10^8 cm^2 s^{-1} at 1 bar), the cloud distribution is controlled by condensation growth and sedimentation, with periodic spikes in new particle generation via homogeneous nucleation. At higher values of K_{zz}, the cloud distribution is controlled by homogeneous nucleation and mixing and is more stable. Increasing K_{zz} leads to more vertically extended, more massive clouds.

- Increasing metallicity past solar values drastically increases the cloud mass while decreasing the mean particle size due to the increased importance of new, small particles produced by homogeneous nucleation. This suggests that even planets with moderately supersolar metallicities may possess optically thick clouds.

Our results reveal the inherent complexities involved in determining the distribution of exoplanet clouds. Their dependence on various aspects of the background atmosphere and their own material properties not only increases the difficulty in generalizing their behaviors across planetary parameter space, but also strongly ties them to the rest of the atmosphere. Therefore, models that capitalize on those ties, such as ours, will be indispensable in understanding these exotic atmospheres as we face the onslaught of new exoplanet observations from JWST, WFIRST, and ground–based observatories. In addition, the importance of laboratory studies into the proposed exoplanet cloud materials cannot be overstated, as they are instrumental in informing models like ours by providing necessary material properties, as well as observations by providing the optical properties of these materials. As investigations of exoplanets focus more and more on smaller, cooler worlds, insight into the clouds, hazes, and aerosols that are sure to pervade their atmospheres will become more and more important in understanding them as a whole.

References

Ackerman, A. S. and M. S. Marley (2001). "Precipitating Condensation Clouds in Substellar Atmospheres". In: *The Astrophysical Journal* 556, pp. 872–884. arXiv: 0103423 [astro-ph].

Bardeen, C. G. et al. (2008). "Numerical simulations of the three dimensional distribution of meteoric dust in the mesosphere and upper stratosphere." In: *Journal of Geophysical Research* 113, p. D17202.

Barth, E. L. and O. B. Toon (2003). "Microphysical modeling of ethane ice clouds in Titan's atmosphere". In: *Icarus* 162, pp. 94–113.

– (2004). "Properties of methane clouds on Titan: Results from microphysical modeling". In: *Geophysical Research Letters* 31, L17S07.

– (2006). "Methane, ethane, and mixed clouds in Titan's atmosphere: Properties derived from microphysical modeling". In: *Icarus* 182, pp. 230–250.

Benneke, B. and S. Seager (2013). "How to Distinguish between Cloudy Mini-Neptunes and Water/Volatile-dominated Super-Earths". In: *The Astrophysical Journal* 778, p. 153.

Carlson, B. E., W. B. Rossow, and G. S. Orton (1988). "Cloud microphysics of the giant planets". In: *Journal of Atmospheric Sciences* 45, pp. 2066–2081.

Celikkaya, A. and M. Akinc (1990). "Preparation and Mechanism of Formation of Spherical Submicrometer Zinc Sulfide Powders". In: *Journal of the American Ceramic Society* 73, pp. 2360–2365.

Charbonneau, D. et al. (2009). "A super-Earth transiting a nearby low-mass star". In: *Nature* 462, pp. 891–894.

Charnay, B., V. Meadows, and J. Leconte (2015). "3D Modeling of GJ1214b's Atmosphere: Vertical Mixing Driven by an Anti-Hadley Circulation". In: *The Astrophysical Journal* 813, p. 15.

Charnay, B., V. Meadows, A. Misra, et al. (2015). "3D Modeling of GJ1214b's Atmosphere: Formation of Inhomogeneous High Clouds and Observational Implications". In: *The Astrophysical Journal Letters* 813, p. L1.

Chen, G. et al. (2014). "Broad-band transmission spectrum and K-band thermal emission of WASP-43b as observed from the ground". In: *Astronomy & Astrophysics* 563, A40. arXiv: 1401.3007.

Colaprete, A., O. B. Toon, and J. A. Magalhães (1999). "Cloud formation under Mars Pathfinder conditions". In: *Journal of Geophysical Research* 104, pp. 9043–9054.

Crossfield, I. J. M. et al. (2013). "Warm ice giant GJ 3470b: I. A flat transmission spectrum indicates a hazy, low-methane, and/or metal-rich atmosphere". In: *Astronomy & Astrophysics* 559, A33.

Deming, D. et al. (2013). “INFRARED TRANSMISSION SPECTROSCOPY OF THE EXOPLANETS HD 209458b AND XO-1b USING THE WIDE FIELD CAMERA-3 ON THE HUBBLE SPACE TELESCOPE”. In: *The Astrophysical Journal* 774, p. 95. arXiv: 1302.1141.

Fraine, J. et al. (2014). “Water vapour absorption in the clear atmosphere of a Neptune-sized exoplanet”. In: *Nature* 513, pp. 526–529.

Fukui, A. et al. (2014). “MULTI-BAND, MULTI-EPOCH OBSERVATIONS OF THE TRANSITING WARM JUPITER WASP-80b”. In: *The Astrophysical Journal* 790, p. 108. arXiv: arXiv:1406.3261v1.

Gao, P. et al. (2014). “Bimodal distribution of sulfuric acid aerosols in the upper haze of Venus”. In: *Icarus* 231, pp. 83–98. DOI: 10.1016/j.icarus.2013.10.013.

Gibson, N. P., S. Aigrain, J. K. Barstow, et al. (2013). “A gemini ground-based transmission spectrum of WASP-29B: A featureless spectrum from 515 to 720 NM”. In: *Monthly Notices of the Royal Astronomical Society* 428, pp. 3680–3692. arXiv: 1210.7798.

Gibson, N. P., S. Aigrain, F. Pont, et al. (2012). “Probing the haze in the atmosphere of HD 189733b with Hubble Space Telescope/WFC3 transmission spectroscopy”. In: *Monthly Notices of the Royal Astronomical Society* 422, pp. 753–760. arXiv: 1201.6573.

Helling, C., A. Ackerman, et al. (2008). “A comparison of chemistry and dust cloud formation in ultracool dwarf model atmospheres”. In: *Monthly Notices of the Royal Astronomical Society* 391, pp. 1854–1873.

Helling, C., R. Klein, et al. (2004). “Dust in brown dwarfs. IV. Dust formation and driven turbulence on mesoscopic scales”. In: *Astronomy & Astrophysics* 423, pp. 657–675.

Helling, C., G. Lee, et al. (2016). “The mineral clouds on HD 209458b and HD 189733b”. In: *Monthly Notices of the Royal Astronomical Society* 460, pp. 855–883.

Helling, C., M. Oevermann, et al. (2001). “Dust in brown dwarfs. I. Dust formation under turbulent conditions on microscopic scales”. In: *Astronomy & Astrophysics* 376, pp. 194–212.

Helling, C. and P. Woitke (2006). “Dust in brown dwarfs. V. Growth and evaporation of dirty dust grains”. In: *Astronomy & Astrophysics* 455, pp. 325–338.

Helling, C., P. Woitke, and W.-F. Thi (2008). “Dust in brown dwarfs and extra-solar planets. I. Chemical composition and spectral appearance of quasi-static cloud layers”. In: *Astronomy & Astrophysics* 485, pp. 547–560.

Heng, K. and B.-O. Demory (2013). “Understanding Trends Associated with Clouds in Irradiated Exoplanets”. In: *The Astrophysical Journal* 777, p. 100.

Hunten, D. M., R. P. Turco, and O. B. Toon (1980). "Smoke and dust particles of meteoric origin in the mesosphere and stratosphere." In: *Journal of the Atmospheric Sciences* 37, pp. 1342–1357.

Iyer, A. R. et al. (2016). "A Characteristic Transmission Spectrum Dominated by H_2O Applies to the Majority of HST/WFC3 Exoplanet Observations". In: *The Astrophysical Journal* 823, p. 109.

Jacobson, M. Z. (2005). *Fundmentals of Atmospheric Modeling*. Cambridge University Press, Cambridge, UK.

Jacobson, M. Z. and R. P. Turco (1994). "Modeling coagulation among particles of different composition and size." In: *Atmospheric Environment* 28, pp. 1327–1338.

Janz, G. J. and C. G. M. Dijkhuis (1969). *NSRDS-NBS 28 Report, Molten Salts: Volume 2*. Natl. Bur. Standards, Washington, D. C., USA.

Jordán, A. et al. (2013). "A GROUND-BASED OPTICAL TRANSMISSION SPECTRUM OF WASP-6b". In: *The Astrophysical Journal* 778, p. 184. arXiv: 1310.6048 [astro-ph.EP].

Kataria, T. et al. (2015). "The Atmospheric Circulation of the Hot Jupiter WASP-43b: Comparing Three-dimensional Models to Spectrophotometric Data". In: *The Astrophysical Journal* 801, p. 86.

Knutson, H. A., B. Benneke, et al. (2014). "A featureless transmission spectrum for the Neptune-mass exoplanet GJ436b". In: *Nature* 505, p. 66. arXiv: 1401.3350.

Knutson, H. A., D. Dragomir, et al. (2014). "Hubble Space Telescope Near-Ir Transmission Spectroscopy of the Super-Earth Hd 97658B". In: *The Astrophysical Journal* 794, p. 155. arXiv: 1403.4602.

Kreidberg, L. et al. (2014). "Clouds In The Atmosphere Of The Super-Earth Exoplanet GJ1214b". In: *Nature* 505, pp. 69–72. arXiv: arXiv:1401.0022v1.

Lavvas, P., C. A. Griffith, and R. V. Yelle (2011). "Condensation in Titan's atmosphere at the Huygens landing site". In: *Icarus* 215, pp. 732–750.

Lavvas, P., R. V. Yelle, and C. A. Griffith (2010). "Titan's vertical aerosol structure at the Huygens landing site: Constraints on particle size, density, charge, and refractive index". In: *Icarus* 210, pp. 832–842.

Lee, G., C. Helling, I. Dobbs-Dixon, et al. (2015). "Modelling the local and global cloud formation on HD 189733b". In: *Astronomy & Astrophysics* 580, A12.

Lee, G., C. Helling, H. Giles, et al. (2015). "Dust in brown dwarfs and extra-solar planets. IV. Assessing TiO_2 and SiO nucleation for cloud formation modelling". In: *Astronomy & Astrophysics* 575, A11.

Lemmon, E. W. (2016). "Thermophysical Properties of Fluids". In: *CRC Handbook of Chemistry and Physics, 94th Edition*. Ed. by W. M. Haynes. Boca Raton, Florida, USA: CRC Press, pages.

Lodders, K. (2010). “Solar System Abundances of the Elements”. In: *Astrophysics and Space Science Proceedings* 16, p. 379.

Mallonn, M. and K. G. Strassmeier (2016). “Transmission spectroscopy of HAT-P-32b with the LBT: confirmation of clouds/hazes in the planetary atmosphere”. In: *Astronomy & Astrophysics* 100, pp. 1–15. arXiv: 1603.09136.

Mandell, A. M. et al. (2013). “Exoplanet Transit Spectroscopy Using WFC3: WASP-12 b, WASP-17 b, and WASP-19 b”. In: *The Astrophysical Journal* 779, p. 128. arXiv: 1310.2949.

Michelangeli, D. V. et al. (1993). “Numerical simulations of the formation and evolution of water ice clouds in the Martian atmosphere”. In: *Icarus* 102, pp. 261–285.

Miura, H. et al. (2010). “Formation of Cosmic Crystals in Highly Supersaturated Silicate Vapor Produced by Planetesimal Bow Shocks”. In: *The Astrophysical Journal* 719, pp. 642–654.

Morley, C. V., J. J. Fortney, E. M.-R. Kempton, et al. (2013). “QUANTITATIVELY ASSESSING THE ROLE OF CLOUDS IN THE TRANSMISSION SPECTRUM OF GJ 1214b”. In: *The Astrophysical Journal* 775, p. 33. arXiv: 1305.4124.

Morley, C. V., J. J. Fortney, M. S. Marley, C. Visscher, et al. (2012). “Neglected Clouds in T and Y Dwarf Atmospheres”. In: *The Astrophysical Journal* 756, p. 172.

Morley, C. V., J. J. Fortney, M. S. Marley, K. Zahnle, et al. (2015). “Thermal Emission and Reflected Light Spectra of Super Earths With Flat Transmission Spectra”. In: *The Astrophysical Journal* 815, p. 110.

Moses, J. I., M. Allen, and Y. L. Yung (1992). “Hydrocarbon nucleation and aerosol formation in Neptune’s atmosphere”. In: *Icarus* 99, pp. 318–346.

Rossow, W. B. (1978). “Cloud microphysics - Analysis of the clouds of Earth, Venus, Mars, and Jupiter”. In: *Icarus* 36, pp. 1–50.

Sanderson, R. T. (1976). *Chemical Bonds and Bonds Energy*. Academic Press, New York, New York, USA.

Schlawin, E. et al. (2014). “A 0.8-2.4 μm TRANSMISSION SPECTRUM OF THE HOT JUPITER CoRoT-1b”. In: *The Astrophysical Journal* 783, p. 5. arXiv: 1401.3337.

Seinfeld, J. H. and S. N. Pandis (2006). *Atmospheric chemistry and physics: From air pollution to climate change, 2nd edition.* John Wiley & Sons, Inc. Hoboken, New Jersey, USA.

Sing, D. K., J. J. Fortney, et al. (2016). “A continuum from clear to cloudy hot-Jupiter exoplanets without primordial water depletion”. In: *Nature* 529, pp. 59–62.

Sing, D. K., A. Lecavelier des Etangs, et al. (2013). “HST hot-Jupiter transmission spectral survey: evidence for aerosols and lack of TiO in the atmosphere of WASP-12b”. In: *Monthly Notices of the Royal Astronomical Society* 436, pp. 2956–2973.

Stevenson, K. B. (2016). “Quantifying and Predicting the Presence of Clouds in Exoplanet Atmospheres”. In: *The Astrophysical Journal Letters* 817, p. L16.

Toon, O. B. et al. (1988). “A multidimensional model for aerosols: Description of computational analogs.” In: *Journal of the Atmospheric Sciences* 45, pp. 2123–2143.

Turco, R. P. et al. (1979). “A one-dimensional model describing aerosol formation and evolution in the stratosphere: I. Physical processes and mathematical analogs.” In: *Journal of the Atmospheric Sciences* 36, pp. 699–717.

Westwood, A. R. C. and T. T. Hitch (1963). “Surface Energy of {100} Potassium Chloride”. In: *Journal of Applied Physics* 34, pp. 3085–3089.

White, F. M. (1974). *Viscous Fluid Flow.* McGraw-Hill, New York, USA.

Wilkins, A. N. et al. (2014). “THE EMERGENT 1.1-1.7 μm SPECTRUM OF THE EXOPLANET COROT-2B AS MEASURED USING THE HUBBLE SPACE TELESCOPE”. In: *The Astrophysical Journal* 783, p. 113. arXiv: 1401.4464.

Witte, S., C. Helling, T. Barman, et al. (2011). “Dust in brown dwarfs and extrasolar planets. III. Testing synthetic spectra on observations”. In: *Astronomy & Astrophysics* 529, A44.

Witte, S., C. Helling, and P. H. Hauschildt (2009). “Dust in brown dwarfs and extrasolar planets. II. Cloud formation for cosmologically evolving abundances”. In: *Astronomy & Astrophysics* 506, pp. 1367–1380.

Woitke, P. and C. Helling (2003). “Dust in brown dwarfs. II. The coupled problem of dust formation and sedimentation”. In: *Astronomy & Astrophysics* 399, pp. 297–313.

– (2004). “Dust in brown dwarfs. III. Formation and structure of quasi-static cloud layers”. In: *Astronomy & Astrophysics* 414, pp. 335–350.

Yung, Y. L., M. Allen, and J. P. Pinto (1984). “Photochemistry of the atmosphere of Titan - Comparison between model and observations”. In: *The Astrophysical Journal Supplemental Series* 55, pp. 465–506.

Zack, L. N. and L. M. Ziurys (2009). “The pure rotational spectrum of ZnS (χ^1 σ^+)”. In: *Journal of Molecular Spectroscopy* 257, pp. 213–216.

Zahnle, K. et al. (2016). “Photolytic Hazes in the Atmosphere of 51 Eri B”. In: *The Astrophysical Journal* 824, p. 137.

Zhang, X. et al. (2012). “Sulfur chemistry in the middle atmosphere of Venus.” In: *Icarus* 217, pp. 714–739.

Chapter 6

SULFUR HAZES IN GIANT EXOPLANET ATMOSPHERES: IMPACTS ON REFLECTED LIGHT SPECTRA

6.1 Abstract

Knowing the composition of the pervasive clouds and hazes shrouding warm exoplanets will greatly inform our knowledge of the atmospheric processes that lead to their formation and evolution. Proposed compositions include clouds of salts and sulfides and photochemical hazes composed of hydrocarbon "soots". Recent work has shown that elemental sulfur and its allotropes may arise in reducing atmospheres due to photolysis of H_2S, and their condensation could result in the formation of sulfur hazes. We investigate the impact such a haze would have on a temperate giant exoplanet's geometric albedo spectrum using a suite of established radiative–convective, cloud, and albedo models in order to inform future direct imaging missions. Photochemical destruction of H_2S results in the production of ~1 ppmv of S_8 between 100 and 0.1 mbar. The S_8 mixing ratio is largely independent of the stellar UV flux, vertical mixing rates, and atmospheric temperature for appropriate ranges of those values, such that the S_8 haze mass is dependent only on the S_8 supersaturation, controlled by the local temperature. Nominal haze masses are found to drastically alter a planet's geometric albedo spectrum: whereas a clear atmosphere is dark at wavelengths between 0.5 and 1 μm due to molecular absorption, the addition of a sulfur haze boosts the albedo there to ~0.7 due to its purely scattering nature. Strong absorption by the haze shortward of 0.4 μm results in albedos <0.1, contrasting the high albedos produced by Rayleigh scattering in a clear atmosphere. The albedo change due a sulfur haze is largely independent of the location of the haze in the atmosphere in the range between 100 and 0.1 mbar, but is a strong function of the haze optical depth as controlled by its column number density and mean particle size, though the absorption feature at short wavelengths remains robust. Detection of such a haze by future direct imaging missions like WFIRST is possible, though discriminating between a sulfur haze and any other reflective material, such as water ice, will require observations shortward of 0.4 μm, which is currently beyond WFIRST's grasp.

6.2 Introduction

Observations of exoplanet atmospheres have revealed a ubiquity of clouds and hazes that impede understanding of atmospheric composition (Gibson, Aigrain, Pont, et al., 2012; Gibson, Aigrain, Barstow, et al., 2013; Deming et al., 2013; Jordán et al., 2013; Mandell et al., 2013; Sing et al., 2013; Chen et al., 2014; Schlawin et al., 2014; Wilkins et al., 2014; Fukui et al., 2014; Mallonn and Strassmeier, 2016). Their presence is typically shown by a flattening of spectral features in the transmission spectrum, resulting from the inability of stellar photons to reach depths in the atmosphere below the cloud and haze layers. Such flat transmission spectra have been seen across many exoplanets of different sizes, effective temperatures, and stellar irradiation levels (e.g. Crossfield et al., 2013; Kreidberg et al., 2014; Knutson, Benneke, et al., 2014; Knutson, Dragomir, et al., 2014), suggesting that the processes governing cloud and haze formation in exoplanet atmospheres are complex.

One key unknown is whether the particulates blocking the stellar photons are part of a cloud, which condensed from atmospheric gases and are typically supported in an atmosphere by turbulent mixing, or part of a haze, which are produced high in the atmosphere, usually via photochemistry. Morley, Fortney, Kempton, et al. (2013) showed that, for the super Earth GJ 1214 b, photochemical hazes may be preferred as a solution to its flat transmission spectra, as it is formed high up in the atmosphere. By contrast, cloud particles must be lofted by turbulent mixing, and a high metallicity may be required to ensure enough material gets to the pressure levels probed by transmission spectroscopy to make a difference.

Knowing whether a planet is shrouded by clouds or hazes (or both) is important despite the flat transmission spectra that both types of aerosols generate, as more discriminating features may appear in direct imaging, which is receiving more priority in upcoming missions such as JWST and WFIRST (Beichman et al., 2014; Robinson, Stapelfeldt, and Marley, 2016). Morley, Fortney, Marley, Zahnle, et al. (2015) showed, for example, that there are large differences in the reflected light spectra of super Earths depending on whether the planet is cloudy or hazy, and what kind of clouds/hazes are present. Specifically, they showed that cooler planets may be more reflective due to KCl, ZnS, and water clouds, while planets with complex hydrocarbon, "soot" hazes resulting from methane photolysis and polymerization tend to be very dark. Additionally, hazes composed of tholins–thought to be the composition of Titan's hazes (Khare et al., 1984)–are dark at the blue end

of the visible range and more reflective at the red end.

An alternative set of compounds that are known to form hazes in planetary atmospheres are those derived from sulfur chemistry. In oxidizing atmospheres, SO_2, OCS, and H_2S from volcanic outgassing is transformed into sulfuric acid through photolysis and reactions with water. Condensation of sulfuric acid can then form clouds and hazes, such as the global cloud deck of Venus (Hansen and Hovenier, 1974) and the Junge layer in the upper stratosphere of Earth (Junge, 1963; Crutzen, 1976). In reducing atmospheres, photolysis of H_2S can lead to the formation of elemental sulfur. Hu, Seager, and Bains (2013), for example, showed that terrestrial worlds with H_2–dominated atmospheres can be enveloped in optically thick sulfur hazes resulting from volcanic outgassing of H_2S.

More recent work by Zahnle et al. (2016) showed that rich sulfur photochemistry could potentially take place in the atmospheres of temperate giant exoplanets (250 K $< T <$ 700 K), generating sulfur allotropes that may form hazes at lower temperatures. As these planets are the targets of current and planned direct imaging campaigns, it is essential that the optical characteristics of elemental sulfur hazes be known in order to inform these future observations. In this paper we investigate the geometric albedo spectra of elemental sulfur hazes and their variations with haze properties, such as the location of the haze in the atmosphere and the haze optical depth. We also address the observability of a sulfur haze for the upcoming space–based direct imaging campaigns of WFIRST (Spergel et al., 2013).

In §6.3, we give an overview of the sulfur chemistry elaborated upon in Zahnle et al. (2016), with a focus towards the formation of sulfur hazes, as well as sulfur's optical properties. In §6.4 we describe in brief the suite of models used in this study. In §6.5 we present our results showing how the geometric albedo varies with different haze properties and whether a clear planet can be distinguished from a hazy planet using proposed instruments onboard WFIRST. Finally, in §6.6 we discuss the impact of our assumptions, the implications of our results, and potential avenues of investigation for future missions and observation campaigns.

6.3 Sulfur in Giant Exoplanets

In temperate and warm giant exoplanet atmospheres sulfur is found mostly in the form of H_2S. Transport of H_2S to the tropopause by turbulent mixing and advection then allows for its destruction by photolysis and reactions with atomic H resulting from photolysis of CH_4, NH_3, and H_2O

$$H_2S + H \longrightarrow HS + H_2 \quad \text{[R6.1]}$$

The resulting HS radical quickly reacts to free sulfur and form S_2

$$HS + H \longrightarrow S + H_2 \quad \text{[R6.2]}$$

$$HS + S \longrightarrow H + S_2 \quad \text{[R6.3]}$$

This begins the polymerization process to form higher sulfur allotropes, eventually creating the stable allotrope, S_8. Transport of S_8 into the deep atmosphere then results in its destruction via thermal decomposition

$$S_8 + M \longrightarrow 2S_4 + M \quad \text{[R6.4]}$$

the products of which go on to decompose further before reforming H_2S, thus completing the cycle. In the event that the equilibrium S_8 partial pressure is above the saturation vapor pressure P_{sat} of S_8 somewhere in the atmosphere, given by

$$P_{sat} = \begin{cases} \exp\left(20 - 11800/T\right) & T < 413\text{K} \\ \exp\left(9.6 - 7510/T\right) & T > 413\text{K} \end{cases} \quad (6.1)$$

then an S_8 haze may form.

Figure 6.1 shows the temperature profile (blue), saturation mixing ratio of S_8 (saturation vapor pressure divided by total atmospheric pressure, in yellow), and the equilibrium mixing ratios of numerous chemical species in a temperate giant exoplanet atmosphere (see §6.4.1) as a result of photochemistry and transport by eddy diffusion. The equilibrium mixing ratio of S_8 peaks at ~1 ppmv, and crosses the S_8 saturation mixing ratio curve between 100 and 1 mbar (the yellow region). This allows for a rough estimate of the total mass of the haze, assuming that all S_8 that is supersaturated condenses. For example, 1 ppmv of S_8 at the 100 mbar level with T ~ 250 K results in a number density of S_8 molecules of $\sim 3 \times 10^{12}$ cm^{-3}. Assuming

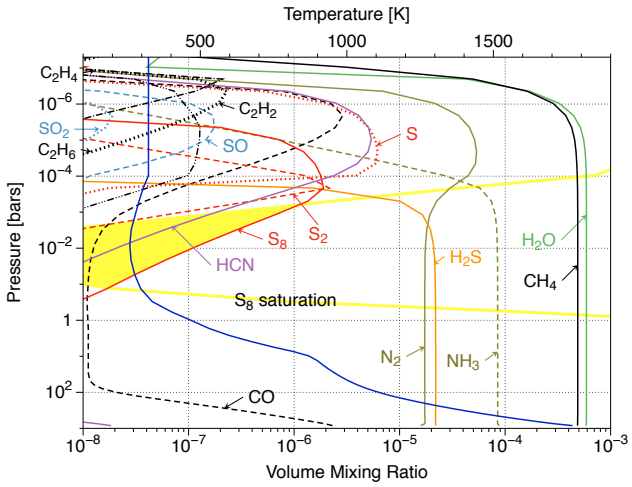

Figure 6.1: The temperature profile (blue), S_8 saturation vapor mixing ratio (yellow), and equilibrium mixing ratios of several important and/or sulfur–derived chemical species in a model giant exoplanet atmosphere subject to photochemistry and eddy diffusion. The shaded yellow region indicates where S_8 is supersaturated.

a column height equaling one scale height (~20 km at 100 mbar for this atmosphere), then the column integrated number density of S_8 is $\sim 6 \times 10^{18}$ cm^{-2}, which translates to a haze particle column number density of $\sim 3 \times 10^{11}$ cm^{-3} assuming a particle size of 0.1 μm and a mass density of 2 g cm^{-3}.

The ultimate haze mass will depend on the degree to which S_8 is supersaturated, which in turn depends on the equilibrium S_8 mixing ratio and the S_8 saturation vapor mixing ratio. Zahnle et al. (2016) showed that, for a wide range in stellar UV fluxes and eddy diffusivities, the peak equilibrium S_8 mixing ratio remained close to 1 ppmv to within a factor of 2, though its vertical profile became more extended/compressed when the eddy diffusivity increased/decreased, respectively. The S_8 mixing ratio is largely independent of stellar UV fluxes because the fluxes experienced by temperate giant exoplanets are such that the photochemistry is limited by H_2S upwelling, rather than the supply of UV photons. The S_8 mixing ratio is also independent of the eddy diffusivity because, in the event that S_8 does not condense, the upward mixing of H_2S is balanced by the downward mixing of S_8, and thus changing the rate of mixing should not change the size of the reservoirs from which material is exchanged by mixing. Furthermore, as Figure 6.1 shows, changing the temperature does not alter the S_8 mixing ratio a large degree either. This likely results from the stability of S_8, such that it can act as an ultimate sink for sulfur above the region where it thermally decomposes. In other words, though

varying the temperature changes the rates of reactions, all reactions eventually lead to the transformation of H_2S to S_8 above the tropopause.

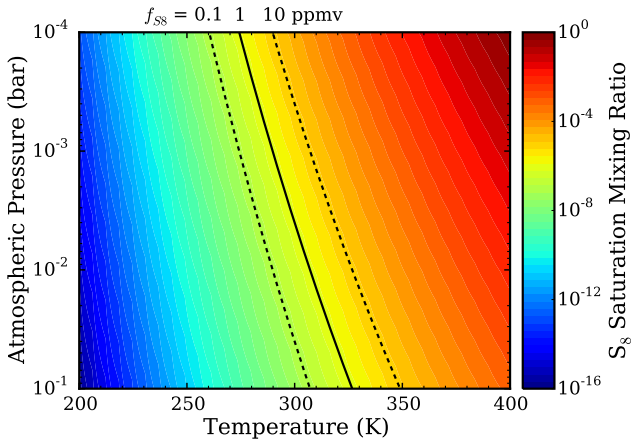

Figure 6.2: S_8 saturation vapor mixing ratio as a function of temperature and background atmospheric pressure. The solid line indicates where the S_8 saturation vapor mixing ratio equals 1 ppmv, while the dotted lines to the left and right indicate 0.1 and 10 ppmv, respectively.

Given the stability of the equilibrium S_8 mixing ratio, the haze mass will largely depend on the saturation vapor mixing ratio, which is a function of temperature. Figure 6.2 shows the S_8 saturation vapor mixing ratio as a function of temperature and pressure level in the atmosphere, where the range in pressure level denotes where S_8 tends to be abundant (Zahnle et al., 2016). The solid line indicates a saturation vapor mixing ratio of 1 ppmv, while the dashed lines to the left and right side of it indicate 0.1 and 10 ppmv, respectively. Thus, if an exoplanet atmosphere contains 1 ppmv of S_8 , then condensation can occur (S_8 is supersaturated) for temperatures and atmospheric pressure levels to the left of the 1 ppmv line, while to the right the abundance of S_8 is too low to condense. A complication arises at low temperatures however, due to the condensation of NH_3, which reacts with H_2S to form NH_4SH clouds. This process has been hypothesized to occur in the atmospheres of Jupiter and Saturn (e.g. Atreya et al., 1999). Once H_2S is lost to NH_4SH it will no longer be available as a sulfur source to photochemically form S_8. Therefore, we can conclude that sulfur hazes may arise on temperate giant exoplanets with stratospheric temperatures <325K but warmer than Jupiter, given that their metallicity is solar. Increased metallicity leads to a wider temperature range in which sulfur can condense, and vice versa for lower metallicity.

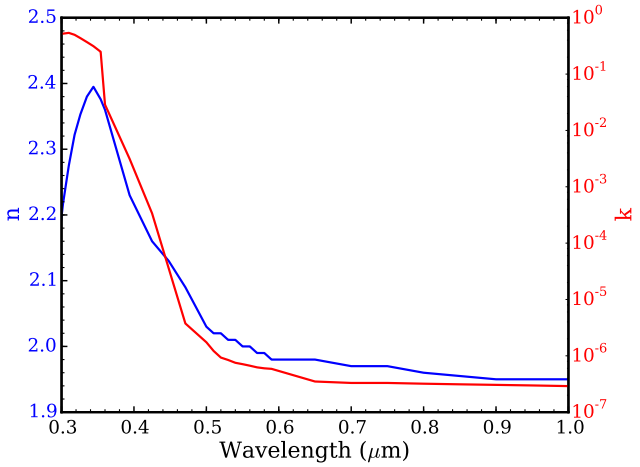

Figure 6.3: Real (blue) and imaginary (red) components of S_8's complex refractive index (Fuller, Downing, and Querry, 1998)

The effect of a sulfur haze on a planet's geometric albedo depends heavily on sulfur's optical properties, stemming primarily from its complex refractive index. Figure 6.3 shows the real (n) and imaginary (k) indices of refraction for orthorhombic crystals of sulfur, a form of solid sulfur composed mainly of S_8. Orthorhombic sulfur is the most stable form of solid sulfur for the temperatures relevant here, though an alternative form, monoclinic sulfur, exists transiently with conversion rates to orthorhombic sulfur decreasing with decreasing temperature (Fuller, Downing, and Querry, 1998), though conversion of orthorhombic sulfur to monoclinic sulfur becomes preferred above 368 K (Meyer, 1976). A key feature of orthorhombic sulfur's complex refractive index is the increase in k at shorter wavelengths caused by vibrational modes in the S_8 molecules, which tend to become more populated at higher temperatures, thereby shifting the increase in k to longer wavelengths (Meyer et al., 1972). Increased absorption at shorter wavelengths will lead to sulfur haze–enveloped exoplanets being yellowish to reddish in color.

6.4 Methods

6.4.1 Model Atmosphere

We evaluate the effect a sulfur haze would have on a planet's geometric albedo spectrum by introducing a sulfur haze into a 1–dimensional model background atmosphere, which we initially assume to be devoid of clouds or hazes. The pressure–temperature profile of the model atmosphere is set by asserting radiative–convective equilibrium, and its molecular composition is determined by assuming thermo-

chemical equilibrium. The planetary parameters are chosen to be that of Gamma Cephei Ab, a warm giant exoplanet discovered via radial velocities (Campbell, Walker, and Yang, 1988; Hatzes et al., 2003) with a minimum mass of 1.6 Jupiter masses, and which orbits its host star, a K1IVe subgiant, at a semimajor axis of 2 AU. Figure 6.1 shows the model atmosphere pressure–temperature profile in blue, where only the regions below 0.1 mbar are in radiative–convective equilibrium. Extension of the PT profile upwards was necessary to investigate the abundance of S_8 produced in this model atmosphere due to photochemistry, but we do not consider the regions above 0.1 mbar in our geometric albedo calculations. We chose Gamma Cephei Ab due to its moderate stratospheric temperatures, which could be conducive to sulfur haze formation.

The PT profile of our atmosphere is generated using the iterative radiative–convective model developed in McKay, Pollack, and Courtin (1989), and extended by Marley, Saumon, et al. (1996), Marley and McKay (1999), Marley, Seager, et al. (2002), Burrows et al. (1997), Fortney, Marley, Lodders, et al. (2005), Fortney, Marley, Saumon, et al. (2008), and Saumon and Marley (2008). Given an internal heat flux and incident flux from the host star, the PT profile is adjusted until (1) the net flux between the plane–parallel atmospheric layers is zero and (2) the profile adheres to convective stability. The radiative transfer is treated via the two–stream source function method described in Toon et al. (1989), with opacities of molecular species provided by Freedman, Marley, and Lodders (2008) with updates from Saumon, Marley, et al. (2012) and combined using the correlated–k method (Goody et al., 1989).

We assume solar metallicity for the model atmosphere (Lodders, 2003), and calculate its molecular composition by minimizing the Gibbs free energy to ensure thermochemical equilibrium. The major chemical species that are abundant and/or optically active include H_2, H, VO, TiO, CO_2, He, H_2O, CH_4, CO, NH_3, N_2, PH_3, H_2S, Fe, Na, and K. In the event that a species becomes supersaturated, it is assumed to be depleted via condensation above the crossing point between its partial pressure and its saturation vapor pressure (Lodders, 1999). The thermochemical equilibrium composition is used to calculate the planet's geometric albedo, and serve as initial conditions for the time–stepping photochemical model, the results of which are shown in Figure 6.1.

6.4.2 Cloud Model and Haze Treatment

The PT profile of our model atmosphere is such that KCl and ZnS can potentially condense and form clouds (Morley, Fortney, Marley, Visscher, et al., 2012). To include clouds in our model we use the approach of Ackerman and Marley (2001), where the cloud mass and mean particle size is determined by balancing vertical mixing due to eddy diffusion and sedimentation of cloud particles:

$$K_{zz}\frac{\partial q_t}{\partial z} + f_{sed} w q_c = 0, \tag{6.2}$$

where q_t is the total mixing ratio of the condensing species, q_c is the mixing ratio of the condensed form of the condensing species only, w is the convective velocity, f_{sed} is a tunable parameter and a measure of the sedimentation efficiency of the cloud particles that we set to 3, appropriate for Jupiter–like words (Ackerman and Marley, 2001; Saumon and Marley, 2008; Morley, Fortney, Marley, Visscher, et al., 2012), and K_{zz} is the eddy diffusion coefficient, calculated by assuming that the convective mass transport is equivalent to convective heat transport. A minimum value $K_{zz}^{min} = 10^5$ cm^2 s^{-1} is set in regions that are convectively stable, as eddy diffusion does not only represent convective turbulence. w is then calculated via mixing length theory: $w = K_{zz}/L$, where L is the mixing length given by

$$L = H \max(0.1, \Gamma/\Gamma_{ad}), \tag{6.3}$$

where H is the atmospheric scale height, Γ and Γ_{ad} are the local and dry adibatic lapse rates, and 0.1 is the minimum scaling for L when the atmosphere is convectively stable.

For both the clouds and sulfur haze, we assume that the particle size distribution dn/dr is lognormal, given by

$$\frac{dn}{dr} = \frac{N}{r\sqrt{2\pi}\ln\sigma}\exp\left[-\frac{\ln^2\left(r/r_g\right)}{2\ln^2\sigma}\right], \tag{6.4}$$

where N is the total number density of particles, r is the particle radius, r_g is the mean particle radius, and σ is a measure of the width of the distribution and is fixed to 2 in the cloud model.

While the Ackerman and Marley (2001) model is appropriate for clouds that are supported by vertical mixing, it cannot be used to simulate photochemical hazes that

have an in situ source. Therefore, we prescribe a sulfur haze with a set location in the atmosphere, particle number density, and mean particle radius. We position our nominal sulfur haze layer at the 10 mbar level in the model atmosphere, consistent with the results of Zahnle et al. (2016) and our Figure 6.1; the column number density of the haze is set to 10^{11} cm^{-2}, in agreement with our calculations of the haze mass in §6.3; and the mean particle radius is set to 0.1 μm, similar to mode 1 particles in the clouds of Venus, which may be composed of elemental sulfur (Knollenberg and Hunten, 1980).

The optical properties of the clouds and the sulfur haze, such as their optical depth, single scattering albedo, and asymmetry parameter (a measure of their degree of forward scattering) are calculated by the cloud model using Mie theory assuming homogeneous spheres. As with the sulfur haze, the optical properties of the clouds are determined by their complex indices of refraction, which for KCl and ZnS are provided by Querry (1987).

In a self–consistent atmosphere, the formation of clouds and hazes would perturb the PT profile, which will in turn lead to different molecular abundances. However, for this exercise we do not ensure this self-consistency. Instead, the PT profile is fixed to that of a clear atmosphere (though the molecular abundances do reflect condensation), with condensate clouds and the prescribed sulfur haze layer added to it afterwards. We discuss the consequences of this assumption in §6.6.

6.4.3 Geometric Albedo Model

The geometric albedo of a planet is defined as the ratio of the reflected flux of that planet at full phase to the reflected flux from a perfect Lambert disk with the same radius as the planet located at the same distance from its host star (Cahoy, Marley, and Fortney, 2010). The reflecting hemisphere of our cloudy/hazy planet is split into individual 1–dimensional atmospheric columns with plane–parallel layers, and radiative transfer calculations for each column is performed separately following Toon et al. (1989), relating incident fluxes to reflected fluxes. Due to the curvature of the reflecting hemisphere, each column will possess a different observing angle and reflect differently depending on their latitudinal and longitudinal coordinates. The geometric albedo spectrum is then calculated by averaging over the reflected flux from each column weighted by viewing geometry (Cahoy, Marley, and Fortney, 2010).

Opacity sources considered when calculating the geometric albedo spectrum in-

clude molecular absorption as previously mentioned (including collision–induced absorption of H_2–H, H_2–H_2, H_2–He, and H_2–CH_4), as well as Rayleigh scattering (Cahoy, Marley, and Fortney, 2010) and Raman scattering (Pollack et al., 1986). The optical depths, single scattering albedos, and asymmetry parameters calculated by the cloud model are used to account for the opacity of the condensate clouds and the sulfur haze.

6.4.4 WFIRST Noise Model

WFIRST (Wide Field Infrared Survey Telescope) is a planned space–based, coronagraph–equipped observational platform with a 2.4 m diameter primary aperture, an operational wavelength range from ~0.4 to 1 μm, and a spectral resolution of 70 (Spergel et al., 2013). Robinson, Stapelfeldt, and Marley (2016) showed, using a state–of–the–art noise model, that given a coronagraph capable of achieving a planet–star contrast ratio of 10^{-9} and appropriate levels of read noise, dark current, leaked stellar light, and zodiacal light from the Solar System and the exoplanetary system, a giant exoplanet located at 2 AU from a sun–like star is readily detectable and characterizable with integration times of several tens of hours, provided that the exoplanetary system is located (~10 pc) such that the exoplanet is between the inner and outer working angles.

We investigate the observability of a sulfur haze using an updated version of this noise model, which includes specific coronagraph designs that have been proposed for WFIRST, such as the Shaped–Pupil Coronagraph (capable of both broadband imaging and spectroscopy; Kasdin et al., 2004) and the Hybrid Lyot Coronagraph (imaging mode only; Trauger et al., 2016). The baseline telescope and instrument parameter values corresponding to these coronagraphs are different from that of Robinson, Stapelfeldt, and Marley (2016) (see their Table 3): We use a telescope diameter of 2.4 m rather than 2 m; the read noise counts per pixel has been adjusted to 0.2 from 0.1; the telescope and instrument throughput has been set to 0.037, changed from 0.05; and the coronagraph inner working angle is now $2.7\lambda/D$ rather than $2\lambda/D$.

To use the noise model, we position our exoplanetary system at 8 pc so that the full wavelength range under consideration can be observed without going beyond the inner or outer working angles (the real Gamma Cephei Ab is located 14 pc away). In addition, we assume that (1) the exozodi brightness is the same as zodiacal light in our own Solar System, (2) our model planet orbits a sun–like star, and (3) our

model planet has the same radius as Jupiter. As the observation would likely be made while the exoplanet is at quadrature rather than at full phase, we multiply the contrast ratio calculated from the (full phase) geometric albedo by a correction factor $1/\pi$, roughly simulating the drop in brightness at quadrature versus full phase. However, this does not take into account the changes in geometric albedo due to non–uniform scattering phase functions of the clouds and hazes in the atmosphere.

6.5 Results

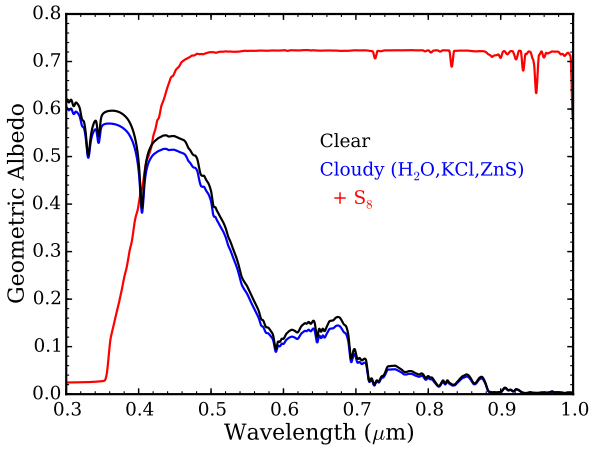

Figure 6.4: Geometric albedo spectra for a clear (black), cloudy (blue), and hazy (red) giant exoplanet atmosphere. The cloudy case includes KCl and ZnS clouds. The hazy case includes all aforementioned clouds, and the nominal sulfur haze layer located at 10 mbar with a column number density of 10^{11} cm^{-2} and a mean particle size of 0.1 μm.

Figure 6.4 shows the geometric albedo spectra of a clear Gamma Cephei Ab atmosphere (black), an atmosphere with KCl and ZnS clouds included (blue), and our nominal hazy model including both the aforementioned clouds and a sulfur haze (red). Absorption features due to H_2O and CH_4 can be clearly discerned at longer wavelengths in the clear case, which makes the planet especially dark there. At shorter wavelengths Rayleigh scattering increases the geometric albedo, with absorption dominated by alkali metals such as potassium (Cahoy, Marley, and Fortney, 2010). Adding condensation clouds does not change the geometric albedo significantly, as the metallicity is not high enough to produce optically thick KCl and ZnS clouds. The resulting cloudy geometric albedo spectrum is simply less bright than the clear case due to decreased Rayleigh scattering caused by decreased path lengths for photons in the atmosphere resulting from the presence of diminutive

KCl and ZnS clouds.

In contrast, adding a sulfur haze layer drastically alters the geometric albedo spectrum; the planet is now much brighter at longer wavelengths due to the purely scattering sulfur haze there, while at wavelengths <0.45 μm the albedo drops precipitously due to increased sulfur absorption. These features are the exact opposite of the clear case, where the planet is darker at long wavelengths and bright at short wavelengths. The shape of the geometric albedo spectrum also contrasts with those produced by hazes composed of other materials. Soots, for example, darken the planet across the entire wavelengths range studied here, while tholins are more similar to sulfur in that it also brightens a planet at long wavelengths while darkening it short wavelengths, though the transition from high to low albedo for a tholin haze is considerably more gradual (Morley, Fortney, Marley, Zahnle, et al., 2015).

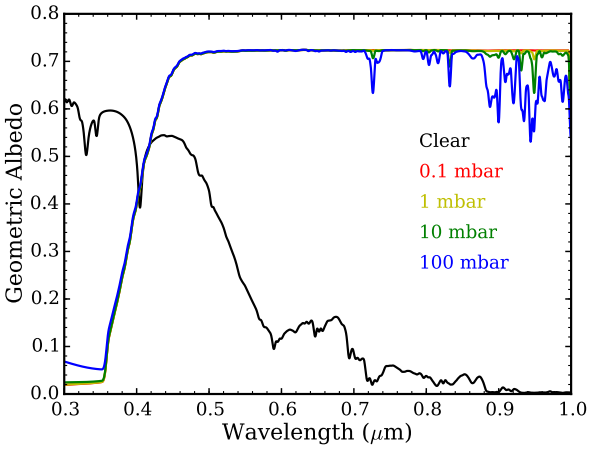

Figure 6.5: Geometric albedo of a giant exoplanet with a sulfur haze located at 0.1 (red), 1 (yellow), 10 (green), and 100 mbar (blue). The geometric albedo of a clear atmosphere (black) is shown for comparison.

Figure 6.5 shows the variations in the geometric albedo spectrum as the sulfur haze layer is placed at different pressure levels, within the range of pressure levels where S_8 is abundant. The location of the sulfur haze layer can be variable since it depends on where the S_8 mixing ratio curve intercepts the S_8 saturation vapor mixing ratio curve, which in turn is a function of the atmospheric temperature structure and intensity of vertical mixing. There is very little difference between the different cases, with the only variations due to increased absorption by CH_4 and H_2O as the haze is lowered in the atmosphere, thereby increasing the optical depth of these gases above the haze.

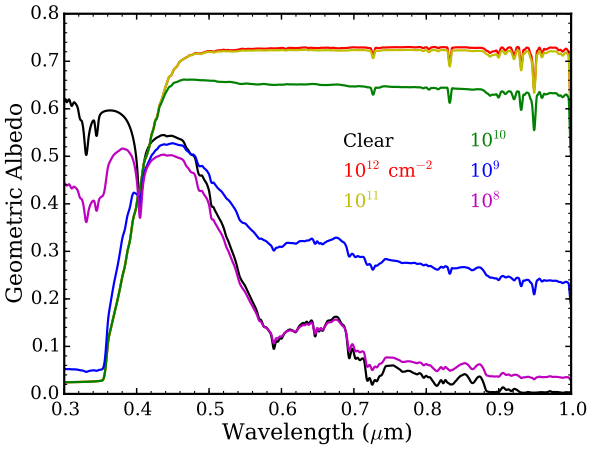

Figure 6.6: Geometric albedo of a giant exoplanet with a sulfur haze with column number densities of 10^{12} (red), 10^{11} (yellow), 10^{10} (green), 10^{9} (blue), and 10^{8} cm^{-2} (magenta). The geometric albedo of a clear atmosphere (black) is shown for comparison.

Figure 6.6 shows the changes in the geometric albedo spectrum as the column number density of sulfur haze particles is varied. The column number density is strongly related to the degree of supersaturation of S_8 vapor and is controlled largely by the microphysics of sulfur haze formation. Increasing the column number density from our nominal case does not change the geometric albedo spectrum to any large degree, indicating that the effect of the sulfur haze has already "saturated" for our nominal haze abundance. This is not surprising since the optical depth of our nominal case is already >1. Decreasing the column number density past an optical depth of 1 reduces the effect of the haze on the geometric albedo. In particular, the brightness of the planet is reduced significantly longward of 0.45 μm until it begins to match the clear case. By contrast, the geometric albedo shortward of 0.45 μm remains largely unchanged even at very low sulfur haze optical depths, only approaching the clear case for optical depths 1000 times less than that of the nominal case.

Figure 6.7 shows the changes in the geometric albedo spectrum as the mean sulfur haze particle size is varied, while keeping the total haze mass the same (i.e. increasing particle size leads to a lower column number density). Like the column number density, the particle size depends on the microphysics of sulfur haze formation and growth by condensation of S_8 vapor. Varying the particle size is seen to have different effects depending on whether the particles are mostly scattering (longward of

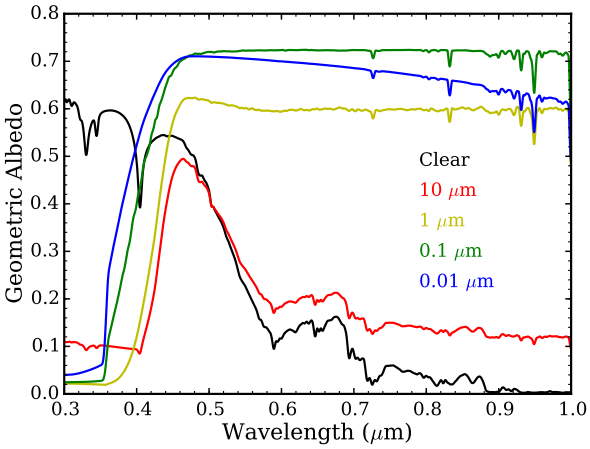

Figure 6.7: Geometric albedo of a giant exoplanet with a sulfur haze with a mean particle radius of 0.01 (red), 0.1 (yellow), 1 (green), and 10 μm (blue). The total haze mass is kept constant for cases. The geometric albedo of a clear atmosphere (black) is shown for comparison.

0.45 μm) or absorbing (shortward of 0.45 μm). In the scattering region, decreasing the particle size such that it becomes much smaller than the wavelength results in a Rayleigh slope developing at longer wavelengths, darkening the planet slightly. Increasing the particle size past the considered wavelength range leads to a decrease in the geometric albedo due to the decrease in haze optical depth. This results from the consolidation of haze mass in larger particles, since optical depth is proportional to the square of the particle radius, while particle mass is proportional to the cube of the particle radius, and the scattering efficiency is largely independent of the particle radius for radii much greater than the wavelength (Hulst, 1957). The geometric albedo is largely unchanged in the absorbing part of the spectrum. This can be explained by the roughly linear relationship between particle size and the absorption efficiency (Hulst, 1957); in other words, the decrease in haze optical depth due to consolidating mass in larger particles is balanced by an increase in absorption by those larger particles. In addition, the wavelength at which the geometric albedo drops abruptly moves to longer wavelengths with increasing particle size. This is caused by the increasing importance of absorption for larger particles, and also that the smallest particles are more Rayleigh scattering, thereby increasing the albedo at shorter wavelengths.

Using the WFIRST noise model from Robinson, Stapelfeldt, and Marley (2016), we can assess whether the drastic changes to a giant exoplanet's geometric albedo

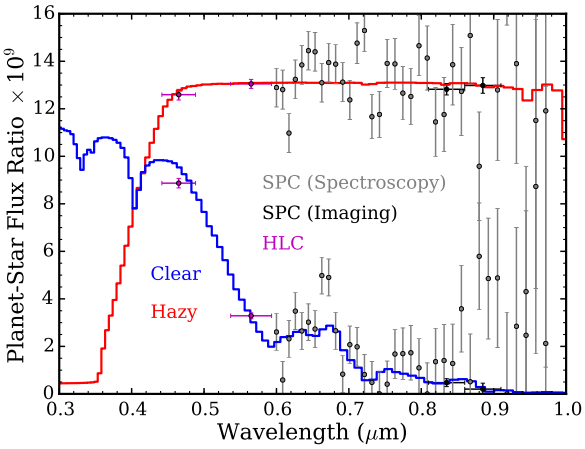

Figure 6.8: Planet–star flux ratio $\times$ 10^9 for a clear (blue) and hazy (red) giant exoplanet with a radius of 1.6 Jupiter radii, located 8 pc away, and orbiting a sun–like star at 2 AU. Synthetic data from the shaped pupil coronagraph (SPC) in imaging (black) and spectroscopy (gray) mode and the hybrid Lyot coronagraph (HLC; magenta), possible instruments onboard WFIRST, are overplotted. Integration time for each exposure is set to 20 hours, with the SPC in spectroscopy mode needing 3 exposure to cover the full wavelength range presented in the figure.

caused by a sulfur haze layer is detectable. Figure 6.8 shows the low resolution (R = 70) planet–star flux ratio multiplied by 10^9 for the clear atmosphere case (blue) and the nominal hazy case (red). Superimposed on the spectra are synthetic observations taken by the shaped pupil coronagraph (SPC) in imaging (black) and spectroscopy (gray) mode, and the hybrid Lyot coronagraph (HLC; magenta), each with a 20 hour integration time per observation. Note that the shaped pupil coronagraph in spectroscopy mode requires three exposures to capture its full wavelength range, so the full observation time to obtain SPC spectra is 60 hours.

There is a clear difference between the clear and the hazy cases. For the wavelength range WFIRST is able to observe, the hazy planet is brighter by a factor of ~6, and thus easier to detect. With the added HLC channel at 0.465 μm, a clear Rayleigh slope is discernible in the clear case, whereas the hazy case is flat for all observed wavelengths. However, the same can be said of high water ice clouds in a colder atmosphere, the albedo spectrum of which is nearly identical to our nominal hazy case for wavelengths >0.465 μm (Morley, Fortney, Marley, Zahnle, et al., 2015). Thus, without being able to observe the strong absorption at wavelengths <0.45 μm, it would be difficult to confirm that the high albedo is caused by a sulfur haze versus a brightly reflecting water ice cloud.

6.6 Discussion

We have shown that the existence of a sulfur haze can significantly alter the geometric albedo spectrum of a temperate giant exoplanet. However, our results depend greatly on the properties of the haze, such as the mean particle size and column number density, both of which are determined by microphysical processes, such as nucleation of aerosols, growth by condensation and coagulation, loss through evaporation and collisional breakup, and transport by sedimentation, mixing, and advection (Pruppacher and Klett, 1978). Although the modeling of these processes is beyond the scope of this work and will be treated in a future paper, we can speculate on how a sulfur haze subject to microphysics differ from the simple slab model we have used. A major difference would be the vertical profile of the haze. Vertical mixing will loft sulfur particles to higher altitudes, where the lower atmospheric pressure and S_8 mixing ratio may result in evaporation of haze particles and a decrease in mean particle size. A haze layer with a vertical gradient in mean particle size would generate a different geometric albedo spectrum than a layer with the same size distribution at all altitudes.

Given that the sulfur haze would have a source of new particles at or near the altitude where S_8 is photochemically produced, there exists the possibility of multi–modal particle size distributions. The situation is similar to that of Venus, where large, $\sim$1 μm sulfuric acid cloud particles coexist with $\sim$0.1 μm particles of photochemical origins, possibly composed of elemental sulfur or sulfuric acid as well e.g. Knollenberg and Hunten, 1980; Imamura and Hashimoto, 2001; Gao et al., 2014. In our case, freshly nucleated sulfur haze particles may coexist with larger, "aged" sulfur particles that have grown by the condensation of S_8 and other sulfur allotropes, resulting in more complex geometric albedo spectra than those presented here.

In addition to the microphysics of the haze itself, the effect of the haze on the rest of the atmosphere must be considered. The chemical abundances presented in Figure 6.1 does not take condensation into account. Indeed, if S_8 condenses then all other sulfur allotropes may condense on the S_8 particles as well, as their saturation vapor pressures are all significantly lower (Lyons, 2008; Zahnle et al., 2016). This will have the effect of not only changing the sulfur chemistry in the atmosphere, possibly removing all sulfur species above the haze layer, but also introduce/increase contamination of the haze particles by smaller sulfur allotropes such as the metastable S_3 and S_4, thereby changing the optical properties of the haze and its geometric albedo spectrum (Meyer et al., 1972). Furthermore, as H_2S is key in forming sulfide

clouds in exoplanet atmospheres (Morley, Fortney, Marley, Visscher, et al., 2012), including the ZnS clouds in our model, and sulfur haze particles can potentially form condensation nuclei for cloud formation, perturbations to the sulfur chemistry and emergence of sulfur hazes could impact condensation clouds as well.

The strong absorption of UV photons by sulfur hazes is also likely to affect the rest of the atmosphere. On Venus, absorption of UV by an unknown agent in the mesosphere, possibly sulfur (Mills, Esposito, and Yung, 2007), leads to several K day^{-1} of heating (Crisp, 1986; Haus, Kappel, and Arnold, 2015; Haus, Kappel, Tellmann, et al., 2016). Such heating in a giant exoplanet atmosphere may increase temperatures, affecting the sulfur haze abundance. Increasing the haze temperature also increases the wavelength of sulfur's UV absorption edge, though the change is small over the temperature range of relevance ($\sim$0.23 nm K^{-1}; Meyer et al., 1972).

The current configuration of WFIRST cannot observe the strong absorption of sulfur hazes shortward of 0.45 μm, which is its defining feature between 0.3 and 1 μm. Future telescopes capable of direct imaging, such as the LUVOIR (Large UV-Optical-InfraRed) telescope, could potentially probe down to such short wavelengths. Alternatively, sulfur hazes may be discerned in the infrared. The compilation of orthorhombic sulfur complex refractive indices provided by Fuller, Downing, and Querry (1998) show a gap in the imaginary component between 2 and 7 μm, likely indicating that it was too low to be measured precisely; beyond 7 μm, k increases steadily from 10^{-6} to 10^{-2} with punctuating spikes up to as high as 0.1, suggesting that JWST may be able to distinguish the signatures of sulfur hazes using MIRI (Mid–Infrared Instrument; Beichman et al., 2014). We will investigate how a sulfur haze changes a giant exoplanet's emission spectrum in the infrared in a future publication.

We have demonstrated that sulfur photochemistry in temperate giant exoplanets with solar metallicity inexorably generates $\sim$1 ppmv of S_8 vapor for large swaths of planetary parameter space. Therefore, a sulfur haze could form if the stratospheric temperature is low enough such that S_8 becomes supersaturated. The effect of such a sulfur haze on the planet's geometric albedo is significant: pure scattering sulfur particles boost the albedo longward of 0.45 μm to $\sim$0.7, while strong absorption shortward of 0.45 μm lowers the albedo to near zero. This is the opposite trend to a clear atmosphere, where deep molecular absorption darkens a planet at long wavelengths while Rayleigh scattering brightens the planet at short wavelengths. The impact of the sulfur haze on the geometric albedo is largely independent of where

the haze is located in the atmosphere within the range where S_8 vapor is abundant, as most of the molecular absorption occurs at depth. In contrast, changing the optical depth of the haze by varying the particle column number density or the mean particle size does drastically change the resulting geometric albedo spectrum, though the absorption at short wavelengths remains robust even at optical depths 1/1000th that of our nominal case. Physically constraining the optical depth of sulfur hazes will require more detailed, coupled photochemical–microphysical models that feedback on the atmospheric thermal structure due to sulfur haze UV heating.

Sulfur hazes on giant exoplanets may be detectable by the next generation of space–based observatories like WFIRST, though discriminating whether the high albedo is caused by sulfur or by other reflective materials (e.g. water ice) will require wavelength coverage shortward of the absorption edge at 0.45 μm, which is not currently planned for WFIRST. Alternatively, sharp features in sulfur's complex refractive index in the mid– to far–infrared may allow for the detection and characterization of sulfur hazes by instruments aboard JWST.

We thank the Kavli Summer Program in Astrophysics and its sponsors for providing the opportunity and funding to conduct this research. We thank the Scientific Organizing Committee (J. Fortney, D. Abbot, C. Goldblatt, R. Murray–Clay, D. Lin, A. Showman, and X. Zhang) for putting together an enlightening series of lectures and activities that bolstered our research efforts both at Kavli and at home. We thank P. Garaud, the program coordinator, and others in the Local Organizing Committee (J. Scarpelli, Z. Kornberg, and S. Nasab) for ensuring that our stay at UC Santa Cruz was an amazing experience, being both conducive to research and fun. We thank the senior participants in the Kavli program, in particular D. Catling, K. Menou, and J. Bean, for giving such illuminating and interesting talks to start off our days. Last but far from the least, we thank the Kavli Fellows, A. Baker, C. Leung, C. Cadiou, D. Powell, G. McDonald, K. Feng, K. Ohno, L. Mayorga, M. Malik, N. Batalha, N. Espinoza, R. Garland, R. MacDonald, T. Komacek, T. Louden, and Y. Kawashima for creating an incredible atmosphere of camaraderie, friendship, adventure, and cake by the ocean.

References

Ackerman, A. S. and M. S. Marley (2001). "Precipitating Condensation Clouds in Substellar Atmospheres". In: *The Astrophysical Journal* 556, pp. 872–884. arXiv: 0103423 [astro-ph].

Atreya, S. K. et al. (1999). “A comparison of the atmospheres of Jupiter and Saturn: deep atmospheric composition, cloud structure, vertical mixing, and origin”. In: *Planetary and Space Science* 47, p. 1243.

Beichman, C. et al. (2014). “Observations of Transiting Exoplanets with the James Webb SpaceTelescope (JWST)”. In: *Publications of the Astronomy Society of the Pacific* 126, p. 1134.

Burrows, A. et al. (1997). “A Nongray Theory of Extrasolar Giant Planets and Brown Dwarfs”. In: *The Astrophysical Journal* 491, pp. 856–875.

Cahoy, K. L., M. S. Marley, and J. J. Fortney (2010). “Exoplanet Albedo Spectra and Colors As a Function of Planet Phase, Separation, and Metallicity”. In: *The Astrophysical Journal* 724, pp. 189–214. arXiv: 1009.3071.

Campbell, B., G. A. H. Walker, and S. Yang (1988). “A search for substellar companions to solar-type stars”. In: *The Astrophysical Journal* 331, pp. 902–921.

Chen, G. et al. (2014). “Broad-band transmission spectrum and K-band thermal emission of WASP-43b as observed from the ground”. In: *Astronomy & Astrophysics* 563, A40. arXiv: 1401.3007.

Crisp, D. (1986). “Radiative forcing of the Venus mesosphere”. In: *Icarus* 514, pp. 484–514.

Crossfield, I. J. M. et al. (2013). “Warm ice giant GJ 3470b: I. A flat transmission spectrum indicates a hazy, low-methane, and/or metal-rich atmosphere”. In: *Astronomy & Astrophysics* 559, A33.

Crutzen, P. J. (1976). “The possible importance of CSO for the sulfate layer of the stratosphere”. In: *Geophysics Research Letters* 3, pp. 73–76.

Deming, D. et al. (2013). “INFRARED TRANSMISSION SPECTROSCOPY OF THE EXOPLANETS HD 209458b AND XO-1b USING THE WIDE FIELD CAMERA-3 ON THE HUBBLE SPACE TELESCOPE”. In: *The Astrophysical Journal* 774, p. 95. arXiv: 1302.1141.

Fortney, J. J., M. S. Marley, K. Lodders, et al. (2005). “Comparative Planetary Atmospheres: Models of TrES-1 and HD 209458b”. In: *The Astrophysical Journal* 627, pp. L69–L72.

Fortney, J. J., M. S. Marley, D. Saumon, et al. (2008). “Synthetic Spectra and Colors of Young Giant Planet Atmospheres: Effects of Initial Conditions and Atmospheric Metallicity”. In: *The Astrophysical Journal* 683, pp. 1104–1116.

Freedman, R. S., M. S. Marley, and K. Lodders (2008). “Line and Mean Opacities for Ultracool Dwarfs and Extrasolar Planets”. In: *The Astrophysical Journal Supplement Series* 174, pp. 504–513.

Fukui, A. et al. (2014). “MULTI-BAND, MULTI-EPOCH OBSERVATIONS OF THE TRANSITING WARM JUPITER WASP-80b”. In: *The Astrophysical Journal* 790, p. 108. arXiv: arXiv:1406.3261v1.

Fuller, K. A., H. D. Downing, and M. R. Querry (1998). "Orthorhombic Sulfur (α–S)". In: *Handbook of Optical Constants of Solids III*. Ed. by E. D. Palik. San Diego, USA: Academic Press, pp. 899–922.

Gao, P. et al. (2014). "Bimodal distribution of sulfuric acid aerosols in the upper haze of Venus". In: *Icarus* 231, pp. 83–98. DOI: 10.1016/j.icarus.2013.10.013.

Gibson, N. P., S. Aigrain, J. K. Barstow, et al. (2013). "A gemini ground-based transmission spectrum of WASP-29B: A featureless spectrum from 515 to 720 NM". In: *Monthly Notices of the Royal Astronomical Society* 428, pp. 3680–3692. arXiv: 1210.7798.

Gibson, N. P., S. Aigrain, F. Pont, et al. (2012). "Probing the haze in the atmosphere of HD 189733b with Hubble Space Telescope/WFC3 transmission spectroscopy". In: *Monthly Notices of the Royal Astronomical Society* 422, pp. 753–760. arXiv: 1201.6573.

Goody, R. et al. (1989). "The correlated-k method for radiation calculations in non-homogeneous atmospheres". In: *Journal of Quantitative Spectroscopy and Radiative Transfer* 42, pp. 539–550.

Hansen, J. E. and J. W. Hovenier (1974). "Interpretation of the polarization of Venus." In: *Journal of the Atmospheric Sciences* 21, pp. 1137–1160.

Hatzes, A. P. et al. (2003). "A Planetary Companion to γ Cephei A". In: *The Astrophysical Journal* 599, pp. 1383–1394.

Haus, R., D. Kappel, and G. Arnold (2015). "Radiative heating and cooling in the middle and lower atmosphere of Venus and responses to atmospheric and spectroscopic parameter variations". In: *Planetary and Space Science* 117, pp. 262–294.

Haus, R., D. Kappel, S. Tellmann, et al. (2016). "Radiative energy balance of Venus based on improved models of the middle and lower atmosphere". In: *Icarus* 272, pp. 178–205.

Hu, R., S. Seager, and W. Bains (2013). "PHOTOCHEMISTRY IN TERRESTRIAL EXOPLANET ATMOSPHERES. II. H 2 S AND SO 2 PHOTOCHEMISTRY IN ANOXIC ATMOSPHERES". In: *The Astrophysical Journal* 769, p. 6.

Hulst, H. C. van de (1957). *Light Scattering by Small Particles*. John Wiley & Sons, Inc. New York, New York, USA.

Imamura, T. and G. L. Hashimoto (2001). "Microphysics of Venusian clouds in rising tropical air." In: *Journal of the Atmospheric Sciences* 55, pp. 3597–3612.

Jordán, A. et al. (2013). "A GROUND-BASED OPTICAL TRANSMISSION SPECTRUM OF WASP-6b". In: *The Astrophysical Journal* 778, p. 184. arXiv: 1310.6048 [astro-ph.EP].

Junge, C. E. (1963). “Sulfur in the atmosphere”. In: *Journal of Geophysical Research* 65, p. 227.

Kasdin, N. J. et al. (2004). “The shaped pupil coronagraph for planet finding coronagraphy: optimization, sensitivity, and laboratory testing”. In: *Proceedings of SPIE* 5487, p. 1312.

Khare, B. N. et al. (1984). “Optical constants of organic tholins produced in a simulated Titanian atmosphere: From soft X-ray to microwave frequencies.” In: *Icarus* 60, pp. 127–137.

Knollenberg, R. G. and D. M. Hunten (1980). “The microphysics of the clouds of Venus: Results of the Pioneer Venus particle size spectrometer experiment.” In: *Journal of Geophysical Research* 85, pp. 8039–8058.

Knutson, H. A., B. Benneke, et al. (2014). “A featureless transmission spectrum for the Neptune-mass exoplanet GJ436b”. In: *Nature* 505, p. 66. arXiv: 1401.3350.

Knutson, H. A., D. Dragomir, et al. (2014). “Hubble Space Telescope Near-Ir Transmission Spectroscopy of the Super-Earth Hd 97658B”. In: *The Astrophysical Journal* 794, p. 155. arXiv: 1403.4602.

Kreidberg, L. et al. (2014). “Clouds In The Atmosphere Of The Super-Earth Exoplanet GJ1214b”. In: *Nature* 505, pp. 69–72. arXiv: arXiv:1401.0022v1.

Lodders, K. (1999). “Alkali element chemistry in cool dwarf atmospheres”. In: *The Astrophysical Journal* 519, p. 793.

– (2003). “Solar System Abundances and Condensation Temperatures of the Elements”. In: *The Astrophysical Journal* 591, pp. 1220–1247. arXiv: 1409.7398.

Lyons, J. R. (2008). “An estimate of the equilibrium speciation of sulfur vapor over solid sulfur and implications for planetary atmospheres.” In: *Journal of Sulfur Chemistry* 29, pp. 269–279.

Mallonn, M. and K. G. Strassmeier (2016). “Transmission spectroscopy of HAT-P-32b with the LBT: confirmation of clouds/hazes in the planetary atmosphere”. In: *Astronomy & Astrophysics* 100, pp. 1–15. arXiv: 1603.09136.

Mandell, A. M. et al. (2013). “Exoplanet Transit Spectroscopy Using WFC3: WASP-12 b, WASP-17 b, and WASP-19 b”. In: *The Astrophysical Journal* 779, p. 128. arXiv: 1310.2949.

Marley, M. S. and C. P. McKay (1999). “Thermal structure of Uranus’ atmosphere.” In: *Icarus* 138, pp. 268–286.

Marley, M. S., D. Saumon, et al. (1996). “Atmospheric, evolutionary, and spectral models of the brown dwarf Gliese 229 B.” In: *Science (New York, N.Y.)* 272, pp. 1919–1921. arXiv: 9606036 [astro-ph].

Marley, M. S., S. Seager, et al. (2002). “Clouds and Chemistry: Ultracool Dwarf Atmospheric Properties from Optical and Infrared Colors”. In: *The Astrophysical Journal* 568, pp. 335–342.

McKay, C. P., J. B. Pollack, and R. Courtin (1989). "The thermal structure of Titan's atmosphere". In: *Icarus* 80, pp. 23–53.

Meyer, B. (1976). "Elemental sulfur". In: *Chemical Reviews* 76, pp. 367–387.

Meyer, B. et al. (1972). "The Spectrum of Sulfur and its Allotropes". In: *Sulfur Research Trends*. Ed. by D. J. Miller and T. K. Wiewiorowski. Washington, D. C., USA: American Chemical Society Publishing, pp. 53–72.

Mills, F. P., L. W. Esposito, and Y. L. Yung (2007). "Atmospheric composition, chemistry, and clouds." In: *Exploring Venus as a Terrestrial Planet*. Ed. by L. W. Esposito, E. R. Stofan, and T. E. Cravens. Washington D.C., USA: American Geophysical Union, pp. 73–100.

Morley, C. V., J. J. Fortney, E. M.-R. Kempton, et al. (2013). "QUANTITATIVELY ASSESSING THE ROLE OF CLOUDS IN THE TRANSMISSION SPECTRUM OF GJ 1214b". In: *The Astrophysical Journal* 775, p. 33. arXiv: 1305.4124.

Morley, C. V., J. J. Fortney, M. S. Marley, C. Visscher, et al. (2012). "Neglected Clouds in T and Y Dwarf Atmospheres". In: *The Astrophysical Journal* 756, p. 172.

Morley, C. V., J. J. Fortney, M. S. Marley, K. Zahnle, et al. (2015). "Thermal Emission and Reflected Light Spectra of Super Earths With Flat Transmission Spectra". In: *The Astrophysical Journal* 815, p. 110.

Pollack, J. B. et al. (1986). "Estimates of the bolometric albedos and radiation balance of Uranus and Neptune". In: *Icarus* 65, pp. 442–466.

Pruppacher, H. R. and J. D. Klett (1978). *Microphysics of clouds and precipitation*. D. Reidel Publishing Company, Dordrecht, Holland.

Querry, M. R. (1987). *Optical Constants of Minerals and Other Materials from the Millimeter to the Ultraviolet*. U.S. Army Armament, Munitions Chemical Research, Dover, New Jersey, USA.

Robinson, T. D., K. R. Stapelfeldt, and M. S. Marley (2016). "Characterizing Rocky and Gaseous Exoplanets with 2-meter Class Space-based Coronagraphs". In: *Publications of the Astronomical Society of the Pacific* 128, p. 39. arXiv: 1507.00777.

Saumon, D. and M. S. Marley (2008). "The Evolution of L and T Dwarfs in Color–Magnitude Diagrams". In: *The Astrophysical Journal* 689, pp. 1327–1344.

Saumon, D., M. S. Marley, et al. (2012). "NEW H 2 COLLISION-INDUCED ABSORPTION AND NH 3 OPACITY AND THE SPECTRA OF THE COOLEST BROWN DWARFS". In: *The Astrophysical Journal* 750, p. 74.

Schlawin, E. et al. (2014). "A 0.8-2.4 μm TRANSMISSION SPECTRUM OF THE HOT JUPITER CoRoT-1b". In: *The Astrophysical Journal* 783, p. 5. arXiv: 1401.3337.

Sing, D. K. et al. (2013). “HST hot-Jupiter transmission spectral survey: evidence for aerosols and lack of TiO in the atmosphere of WASP-12b”. In: *Monthly Notices of the Royal Astronomical Society* 436, pp. 2956–2973.

Spergel, D. et al. (2013). “Wide-Field InfraRed Survey Telescope-Astrophysics Focused Telescope Assets WFIRST-AFTA Final Report”. In: p. 190. arXiv: 1305.5422.

Toon, O. B. et al. (1989). “Rapid calculation of radiative heating rates and photodissociation rates in inhomogeneous multiple scattering atmospheres”. In: *Journal of Geophysical Research* 94, p. 16287.

Trauger, J. et al. (2016). “Hybrid Lyot coronagraph for WFIRST-AFTA: coronagraph design and performance metrics”. In: *Journal of Astronomical Telescopes, Instruments, and Systems* 2, p. 011013.

Wilkins, A. N. et al. (2014). “THE EMERGENT 1.1-1.7 μm SPECTRUM OF THE EXOPLANET COROT-2B AS MEASURED USING THE HUBBLE SPACE TELESCOPE”. In: *The Astrophysical Journal* 783, p. 113. arXiv: 1401.4464.

Zahnle, K. et al. (2016). “Photolytic Hazes in the Atmosphere of 51 Eri B”. In: *The Astrophysical Journal* 824, p. 137.

Appendix A

CARMA OVERVIEW

A.1 A Brief History of CARMA

The Community Aerosol and Radiation Model for Atmospheres (CARMA) is a 1–dimensional Eulerian time–stepping forward model written in FORTRAN that calculates the rates of particle formation via a suite of nucleation processes, including homogeneous and heterogeneous nucleation (as well as aerosol freezing, droplet activation, etc.), particle growth by condensation and coagulation, particle loss by evaporation, and particle transport via sedimentation, diffusion, and advection. It discretizes the particle distribution into bins, and the vertical extent of the atmosphere into layers. It was initial conceived at NASA Ames to model Earth's stratospheric sulfate aerosols (Turco et al., 1979; Toon, Turco, Hamill, et al., 1979), and has since been generalized to a variety of applications both on Earth and in other planetary atmospheres, including modeling polar stratospheric clouds to inform ozone depletion (Toon, Turco, Westphal, et al., 1988), the characteristics of the particles stemming from the eruption of Mount Pinatubo (Zhao, Turco, and Toon, 1995), various tropospheric cloud features on Earth (Jensen et al., 1994; Ackerman, Toon, and Hobbs, 1993), the sulfuric acid clouds of Venus (James, Toon, and Schubert, 1997; McGouldrick and Toon, 2007; Gao et al., 2014), water ice clouds on Mars (Colaprete, Toon, and Magalhães, 1999), aerosols on titan (Toon, McKay, et al., 1992), and organic hazes on ancient Earth (Wolf and Toon, 2010). Extension of the model to 3 dimensions (Toon, Turco, Jordan, et al., 1989) has allowed for the study of Martian dust storms (Murphy et al., 1993) and meteoric dust in Earth's mesosphere (Bardeen et al., 2008), among others. Updates to CARMA includes the addition of new coagulation routines (Jacobson and Turco, 1994), new sulfate microphysics (English et al., 2011), and conversion of the model to Fortran 90/95 (CARMA 3.0). In the subsequent sections, I review the structure of CARMA and the physical equations and numerical methods it uses to calculate the rates of the aforementioned microphysical processes.

A.2 CARMA Machinery

CARMA simulates aerosols by categorizing them into groups and elements. In the simple case where the microphysics of only a single type of homogeneous particle

is evaluated, then only one group, composed of one element, is necessary. Inhomogeneous particles, such as layered particles with a core and an outer mantle of another material, is characterized by two elements in a single group. Multiple groups are needed for different types of particles, e.g. condensation nuclei and the cloud particles that form from them. Gases are also added one by one. Microphysical processes are applied to different elements and groups and often institute specific mapping arrays between them, e.g. a nucleation process that transforms a condensation nuclei into a cloud core maps the masses of the condensation nuclei element to the cloud core element.

CARMA operates within a background atmosphere characterized by a pressure profile, a temperature profile, an altitude profile, and an eddy diffusion coefficient profile, which will all tend to be unique for each specific case. Less unique are the atmospheric properties needed for the microphysical calculations, including profiles of atmospheric viscosity and thermal conductivity, which will only change if the main atmospheric constituent is different, i.e. simulations taking place in the Venus and Mars atmospheres would have the same parameterizations for these two profiles since they're both composed of mainly CO_2. The condensing materials themselves are characterized by specific properties within CARMA, such as their saturation vapor pressure, surface energy/tension, latent heat of vaporization, and molecular diffusivity through the background atmosphere. The universality of the microphysical processes handled by CARMA allows it to simulate virtually any condensate in any atmosphere, provided their physical properties are known.

Running CARMA requires a set of initial conditions (e.g. initial concentrations of particles and gases) and a set of boundary conditions (e.g. concentration or flux of material at the top and bottom boundaries). The model then runs for a fixed number of time steps set by the user, though it may not always reach equilibrium by the end of the run–back of the envelope estimations may be needed to evaluate how many time steps are ultimately necessary.

A.3 Nucleation

For this thesis, classical theories of homogeneous and heterogeneous nucleation are used for computing the rates of new particle generation (Pruppacher and Klett, 1978; Lavvas, Griffith, and Yelle, 2011). For homogeneous nucleation, the rate J_{hom} in units of new particles per volume per unit time is given as

$$J_{hom} = 4\pi a_c^2 \Phi Z n \exp\left(-F/kT\right), \tag{A.1}$$

where n is the number density of condensate vapor molecules, k is the Boltzmann constant, and T is the temperature. a_c is the critical particle radius defined as

$$a_c = \frac{2M\sigma}{\rho_p RT \ln S}, \tag{A.2}$$

where M, σ, ρ_p, and S are the molecular weight, surface tension/energy, mass density, and saturation ratio of the condensate, respectively, and R is the universal gas constant. F is the energy of formation of a particle with radius a_c, given by

$$F = \frac{4}{3}\pi\sigma a_c^2. \tag{A.3}$$

In other words, classical homogeneous nucleation theory relates the rate of particle formation with the energy of formation. The greater the energy (i.e. the lower the supersaturation), the lower the production rate. The energy of formation is defined as the balance between the increase in energy associated enlarging a particle's surface to add vapor molecules and the decrease in energy due to the increase in the volume of the particle. Particles with a radius of a_c is at the cusp of this balance, where further growth leads to a net decrease in energy of formation, and therefore continued existence. Φ is the diffusion rate of vapor molecules to the forming particle, since a key bottleneck in particle formation is the rate at which vapor molecules can diffuse through the background atmosphere and come together; it is defined as

$$\Phi = \frac{p}{\sqrt{2\pi mkT}}, \tag{A.4}$$

where p is the atmospheric pressure and m is the mass of a vapor molecule. Finally, Z is the Zeldovich factor, which takes into account nonequilibrium effects, such as the evaporation of just–formed particles occurring at the same time as particle formation. Z is given by

$$Z = \sqrt{\frac{F}{3\pi kTg^2}}, \tag{A.5}$$

where g is the number of molecules in particles with radius a_c. Because CARMA splits the particle size distribution into discrete bins, the size of the particles actually

produced will correspond to the bin with a size that is closest to a_c, with the total mass produced conserved (i.e. if a_c is smaller than the size to which the appropriate bin corresponds, then fewer, larger particles will be produced).

The rate of heterogeneous nucleation, J_{het} is defined similarly in CARMA,

$$J_{het} = 4\pi^2 r^2 a_c^2 \Phi c_{surf} Z \exp\left(-Ff/kT\right), \tag{A.6}$$

where a_c is the critical radius of the initial cluster of condensate molecules ("germ") on the nucleating surface, r is the radius of the condensation nuclei, f is a shape factor given by

$$2f = 1 + \left(\frac{1-\mu x}{\phi}\right)^3 + x^3\left(2 - 3f_0 + f_0^3\right) + 3\mu x^2\left(f_0 - 1\right), \tag{A.7}$$

where μ is the cosine of the contact angle between the condensate the and the nucleating surface, and

$$x = r/a_c \tag{A.8}$$

$$\phi = \sqrt{1 - 2\mu x + x^2} \tag{A.9}$$

$$f_0 = (x - \mu)/\phi \tag{A.10}$$

and c_{surf} is the number density of condensate molecules on the nucleating surface, given by

$$c_{surf} = \frac{\Phi}{\nu} \exp\left(F_{des}/kT\right), \tag{A.11}$$

where ν is the oscillation frequency of adsorbed vapor molecules on the nucleating surface and F_{des} is the desorption energy of that molecule. Heterogeneous nucleation differs from homogeneous nucleation in that surface interactions must be taken into account, such as the effect of the surface curvature due to the Kelvin effect, and the probability that an adsorbed condensate molecule may break off before forming a critical germ. The units of J_{het} is critical germs per condensation nucleus, and thus to get the number of newly nucleated particles per volume per

unit time J_{het} must be multiplied by the number density of condensation nuclei. In CARMA, the newly nucleated particles are mapped from the condensation nuclei group to the cloud particle group assuming that the mass of the particles have not changed significantly, despite the appearance of a critical germ on its surface. This is acceptable since the successive bins double in mass, and the critical germs are usually much smaller than the condensation nuclei.

A.4 Condensation/Evaporation

Condensational growth and evaporation in CARMA takes into account the diffusion of condensate molecules to and away from the cloud particle, such that the rate of change in mass m of the particle is

$$\frac{dm}{dt} = 4\pi R_d^2 D \frac{d\rho_v}{dR_d}, \tag{A.12}$$

where R_d is the distance away from the center of the particle, D is the molecular diffusion coefficient of the condensate vapor through the background atmosphere, and ρ_v is the mass density of the condensate vapor. Addition of molecules to a particle releases latent heat, and vice versa for the removal of molecules. The rate of change in temperature of the particle, T_p arising from condensation and evaporation is

$$mC_p \frac{dT_p}{dt} = L\frac{dm}{dt} - \frac{dQ}{dt}, \tag{A.13}$$

where C_p is the heat capacity of the particle, L is the latent heat of evaporation of the condensate, and dQ/dt is the cooling rate of the particle given by

$$\frac{dQ}{dt} = -4\pi R_d^2 \kappa_a \frac{dT}{dR_d}, \tag{A.14}$$

where κ_a is the thermal conductivity of the atmosphere. Combining Eqs. A.12–A.14, along with the ideal gas law and the Clausius–Clapeyron equation,

$$\frac{dm}{dt} = \frac{4\pi r D p_{sat}(S-1)}{\frac{RT}{M} + \frac{DLp_{sat}}{\kappa_a T}\left(\frac{LM}{RT} - 1\right)}, \tag{A.15}$$

where p_{sat} is the saturation vapor pressure of the condensate (Jacobson, 2005). CARMA makes the assumption that $LM/RT - 1 \sim LM/RT$, and takes into account several additional effects, such that Eq. A.15 becomes

$$\frac{dm}{dt} = \frac{4\pi r D' p_{sat}(S - A_k)}{\frac{RT}{MF_v} + \frac{D'ML^2 p_{sat}}{\kappa'_a RT^2 F_t}}, \tag{A.16}$$

where A_k is the Kelvin factor, which takes into account the curvature of the particle surface, and is given by

$$A_k = \exp\left(\frac{2M\sigma}{\rho_p RTr}\right). \tag{A.17}$$

D' and κ'_a are the molecular diffusional coefficient of the condensate vapor through the atmosphere and the thermal conductivity of the atmosphere, respectively, modified to account for gas kinetics effects near the surface of the particle, and are expressed as

$$D' = \frac{D}{1 + \lambda Kn^c} \tag{A.18}$$

$$\kappa'_a = \frac{\kappa_a}{1 + \lambda_t Kn^c_t}, \tag{A.19}$$

where λ and λ_t are given by

$$\lambda = \frac{1.33Kn^c + 0.71}{Kn^c + 1} + \frac{4(1 - \alpha_s)}{3\alpha_s} \tag{A.20}$$

$$\lambda_t = \frac{1.33Kn^c_t + 0.71}{Kn^c_t + 1} + \frac{4(1 - \alpha_t)}{3\alpha_t}, \tag{A.21}$$

where α_s and α_t are the sticking coefficient and the thermal accommodation coefficient, respectively, which are set to 1, and Kn^c and Kn^c_t are Knudsen numbers of the condensing gas with respect to the particle, define as

$$Kn^c = \frac{3D}{r}\sqrt{\frac{\pi M}{8RT}} \tag{A.22}$$

$$Kn^c_t = \frac{Kn^c \kappa_a}{rD\rho\left(C_p - \frac{R}{2M_a}\right)}, \tag{A.23}$$

where ρ is the atmospheric mass density and M_a is the mean molecular weight of the atmosphere. Finally, F_v and F_t are the ventilation factors that account for the air density variations around a particle as it sediments in an atmosphere, which

increases density in front of it and lowers the density behind it (Toon, Turco, Jordan, et al., 1989; Lavvas, Griffith, and Yelle, 2011).

CARMA uses the piecewise parabolic method for treating advection of particles (Colella and Woodward, 1984) to apply the rate of change in mass dm/dt to evolving the binned particle distribution. In other words, CARMA treats the fluxes between mass bins as if they were fluxes between altitude levels.

A.5 Coagulation/Coalescence

Coagulation of particles occurs when the particles bump into each other due to Brownian motion and stick. The rate of coagulation of particles from two populations is given by the product of the coagulation kernel, K_b, the number density of one of the groups of particles, and the number density of the other group of particles. Given particle populations 1 and 2, the coagulation kernel is defined by

$$K_b = \frac{4\pi(D_1 + D_2)(r_1 + r_2)}{\frac{r_1+r_2}{r_1+r_2+\sqrt{\delta_1^2+\delta_2^2}} + \frac{4(D_1+D_2)}{(r_1+r_2)\sqrt{V_1^2+V_2^2}}}, \tag{A.24}$$

where D_x, r_x, V_x, and δ_x, x = 1,2 are the molecular diffusion coefficients, radii, thermal velocities, and interpolation factors of particles from populations 1 and 2, respectively. D_x is defined as

$$D_x = \frac{kTC}{6\pi\eta r_x}, \tag{A.25}$$

where C is the Cunningham slip correction factor (see §A.6) and η is the dynamic viscosity. V_x is given by

$$V_x = \sqrt{\frac{8kT}{\pi M_x}}, \tag{A.26}$$

where M_x, x = 1,2 is the mass of the particle. Finally, δ_x is expressed as

$$\delta_x = \frac{(2r_x + \lambda_x)^3 - (4r_x^2 + \lambda_x^2)^{3/2}}{6r_x\lambda_x} - 2r_x, \tag{A.27}$$

where λ_x is the particle mean free path and is given by

$$\lambda_x = \frac{8D_x}{\pi V_x}. \tag{A.28}$$

δ_x interpolates between the continuum and kinetic regimes (Lavvas, Yelle, and Griffith, 2010).

A.6 Vertical Transport

The sedimentation velocity v of a spherical particle of radius r is given by Stoke's fall velocity,

$$v = \frac{2}{9}\frac{\rho_p g r^2 C}{\eta}, \tag{A.29}$$

where g is the gravitational acceleration and C is the Cunningham slip correction factor given by

$$C = 1 + 1.246Kn + 0.42Kne^{-0.87/Kn}, \tag{A.30}$$

where Kn is the Knudsen number of the particle defined as the ratio of the atmospheric mean free path l to r, where l can be written as

$$l = \frac{2\eta}{\rho}\sqrt{\frac{\pi M_a}{8RT}}. \tag{A.31}$$

Note that Kn is different from Kn^c and Kn_t^c defined in Eqs. A.22–A.23. $C \sim 1$ in the continuum regime ($Kn \ll 1$). In the kinetics regime, C is large and mostly linear with Kn. Taking this into account, the sedimentation velocity becomes

$$v = A\frac{\rho_p g r_p}{\rho}\sqrt{\frac{\pi\mu}{2RT}}, \tag{A.32}$$

where A is a constant that is ~0.5.

The velocity associated with advection is calculated from a user defined wind speed via the piecewise parabolic method (Colella and Woodward, 1984). Diffusive velocities, meanwhile, is split into molecular diffusion and eddy diffusion, with the latter usually dominating the former. Eddy diffusion velocities are given by

$$v_{ed} = -K_{zz}\frac{d\ln f_r}{dz}, \tag{A.33}$$

where K_{zz} is the eddy diffusion coefficient and f_r is the mixing ratio of the constituent being transported (particles and condensate vapor). All the transport velocities are brought together and used to solve for the new particle and gas distribution

following Toon, Turco, Westphal, et al. (1988), which implicitly takes into account molecular diffusion.

References

Ackerman, A. S., O. B. Toon, and P. V. Hobbs (1993). "A model for particle microphysics, turbulent mixing, and radiative transfer in the stratocumulus-topped marine boundary layer and comparisons with measurements". In: *Journal of the Atmospheric Sciences* 52, pp. 1204–1236.

Bardeen, C. G. et al. (2008). "Numerical simulations of the three dimensional distribution of meteoric dust in the mesosphere and upper stratosphere." In: *Journal of Geophysical Research* 113, p. D17202.

Colaprete, A., O. B. Toon, and J. A. Magalhães (1999). "Cloud formation under Mars Pathfinder conditions". In: *Journal of Geophysical Research* 104, pp. 9043–9054.

Colella, P. and P. R. Woodward (1984). "The Piecewise Parabolic Method (PPM) for gas-dynamical simulations". In: *Journal of Computational Physics* 54, pp. 174–201.

English, J. M. et al. (2011). "Microphysical simulations of new particle formation in the upper troposphere and lower stratosphere." In: *Atmospheric Chemistry and Physics* 11, pp. 9303–9322.

Gao, P. et al. (2014). "Bimodal distribution of sulfuric acid aerosols in the upper haze of Venus". In: *Icarus* 231, pp. 83–98. DOI: 10.1016/j.icarus.2013.10.013.

Jacobson, M. Z. (2005). *Fundmentals of Atmospheric Modeling*. Cambridge University Press, Cambridge, UK.

Jacobson, M. Z. and R. P. Turco (1994). "Modeling coagulation among particles of different composition and size." In: *Atmospheric Environment* 28, pp. 1327–1338.

James, E. P., O. B. Toon, and G. Schubert (1997). "A numerical microphysical model of the condensational Venus cloud." In: *Icarus* 129, pp. 147–171.

Jensen, E. J. et al. (1994). "Microphysical modeling of cirrus: 1. Comparison with 1986 FIRE IFO measurements". In: *Journal of Geophysical Research* 99, pp. 10421–10442.

Lavvas, P., C. A. Griffith, and R. V. Yelle (2011). "Condensation in Titan's atmosphere at the Huygens landing site". In: *Icarus* 215, pp. 732–750.

Lavvas, P., R. V. Yelle, and C. A. Griffith (2010). "Titan's vertical aerosol structure at the Huygens landing site: Constraints on particle size, density, charge, and refractive index". In: *Icarus* 210, pp. 832–842.

McGouldrick, K. and O. B. Toon (2007). “An investigation of possible causes of the holes in the condensational Venus cloud using a microphysical cloud model with a radiative-dynamical feedback.” In: *Icarus* 191, pp. 1–24.

Murphy, J. R. et al. (1993). “Martian global dust storms: Zonally symmetric numerical simulations including size-dependent particle transport”. In: *Journal of Geophysical Research* 98, pp. 3197–3220.

Pruppacher, H. R. and J. D. Klett (1978). *Microphysics of clouds and precipitation*. D. Reidel Publishing Company, Dordrecht, Holland.

Toon, O. B., C. P. McKay, et al. (1992). “A physical model of Titan’s aerosols”. In: *Icarus* 95, pp. 24–53.

Toon, O. B., R. P. Turco, P. Hamill, et al. (1979). “A one-dimensional model describing aerosol formation and evolution in the stratosphere: II. Sensitivity studies and comparison with observations”. In: *Journal of the Atmospheric Sciences* 36, pp. 718–736.

Toon, O. B., R. P. Turco, J. Jordan, et al. (1989). “Physical processes in polar stratospheric ice clouds.” In: *Journal of Geophysical Research* 94, pp. 11359–11380.

Toon, O. B., R. P. Turco, D. Westphal, et al. (1988). “A multidimensional model for aerosols: Description of computational analogs.” In: *Journal of the Atmospheric Sciences* 45, pp. 2123–2143.

Turco, R. P. et al. (1979). “A one-dimensional model describing aerosol formation and evolution in the stratosphere: I. Physical processes and mathematical analogs.” In: *Journal of the Atmospheric Sciences* 36, pp. 699–717.

Wolf, E. T. and O. B. Toon (2010). “Fractal organic hazes provided an ultraviolet shield for early Earth”. In: *Science* 328, pp. 1266–1268.

Zhao, J., R. P. Turco, and O. B. Toon (1995). “A model simulation of Pinatubo volcanic aerosols in the stratosphere”. In: *Journal of Geophysical Research* 100, pp. 7315–7328.